核理研研究報告　第36巻　2003年

ISSN 0385-2105

TOHOKU

RESEARCH REPORT OF LABORATORY OF NUCLEAR SCIENCE

Vol.36 2003

TOHOKU UNIVERSITY

Editors

TAMAE, Tadaaki

OHTSUKI, Tsutomu

HAMA, Hiroyuki

Laboratory of Nuclear Science

Tohoku University

1-2-1 Mikamine, Taihaku, Sendai 982-0826

Japan

Pone: +81, 22-743-3400

Fax: +81, 22-743-3401

Web site: http://www.lns.tohoku.ac.jp/

982-0826 仙台市太白区三神峯1-2-1

東北大学大学院理学研究科

附属原子核理学研究施設

電話　022-743-3400

Fax　022-743-3401

Preface

This issue of Research Report of Laboratory of Nuclear Science reports research activities of the LNS performed in the 2002 academic/fiscal year (April 2002 - March 2003). Major research activities are based on the electron accelerator complex consisting of the 300-MeV LINAC and the 1.2-GeV STB ring. The accelerators have altogether provided a beam time of about 1,600 hours for various experiments through the year.

In order to use the STB ring more effectively, a new experimental hall which is called GeV γ-ray experimental hall was built next to the experimental hall 2. The construction started in February 2002, and ended in August 2002. The beam could not be delivered to the experimental hall 2 in this period. The beam was back to the hall 2 in late October, after a legal inspection on the radiation safety. Thus, the beam time for the experimental use of this year was obliged to be much less than those of the previous years. In the experimental hall 2, the measurements of the C(γ,K^0) reaction were continued, and the construction of a tagged photon beam line for the new experimental hall began. In addition, a few experiments using low energy tagged photons were performed as well as radioactive isotope production.

We hope that this Report will serve as a quick overview of the present LNS activities over a variety of nuclear research fields.

Jirohta KASAGI
Director

Research Report of Laboratory of Nuclear Science
Volume 36, 2003

Contents

核理研研究報告　第36巻　目　次

Ⅰ．原子核物理

Ⅱ. 放射化学

Ⅲ. 加速器・放射光・測定装置

Ⅳ. 平成14年度加速器報告

Ⅴ. 論文リスト

Ⅵ. 課題採択結果

Ⅰ. Nuclear Physics

(LNS Experiment : #2350)

Cross Sections and Angular Distributions for the ^{10}B(e, e′n)^{9}B Reaction in the Giant Resonance Region

H. Ueno[1], T. Suzuki[1], T. Saito[2]*, T. Nakagawa[2]†, K. Kino[2]§, T. Nakagawa[3]‡, Y. Matsuura[4], T. Kawamura[4] and M. Higuchi[4]

[1]*Department of Physics, Yamagata University, Kojirakawa, Yamagata 990-8560*
[2]*Laboratory of Nuclear Science, Tohoku University, Mikamine, Taihaku-ku, Sendai 982-0826*
[3]*Department of Physics, Tohoku University, Aramaki, Aoba-ku, Sendai 980-8578*
[4]*Faculty of Engineering, Tohoku Gakuin University, Chuo, Tagajo 985-8537*

The cross sections and angular correlations for neutron emission to various states in the residual nucleus, following the ^{10}B(e, e′n) reaction, have been measured over the excitation energy range 18-33 MeV at the effective momentum transfer of 0.49 fm^{-1}. In the giant resonance, neutron emission leads predominant population of two higher excited states: (6.97 MeV 7/2$^-$ (n_5), 11.70 MeV 7/2$^-$+12.06 MeV 3/2$^-$ ($n_{6,7}$)). This is the first observation for neutron population of these states. The angular distributions for each transition were fitted with Legendre polynomials. The angular distributions for n_0 indicate an interference of a transition with the opposite parity to E1. The angular distributions for n_5 and $n_{6,7}$ have a peak at about 50°; they are quite different patterns from that for n_0. It might reflect lower E1 amplitude comparing to other multipole ones. It was confirmed that neutron emission from the giant resonance in ^{10}B leaves the residual nucleus ^{9}B not at the ground state but mainly at 6.97 MeV 7/2$^-$ and 11.70 MeV 7/2$^-$+12.06 MeV 3/2$^-$ states as predicted by shell model calculations with intermediate coupling.

§ 1. Introduction

The giant resonance of ^{10}B was investigated using the (γ, n) reaction [1-4]. Ahsan *et al.* [1] observed a split E1 giant resonance region with maxima at 20.2 and 23.0 MeV as in the earlier studies [2-4]. They interpreted it as being due to an asymmetry in analogy to the splitting of the giant resonance in deformed nuclei. The observed giant resonance is consistent with the shell model calculations by Gol′tsov and Goncharova [5] and Shackleton [6], but a peak predicted at ≈ 11 MeV [5] was not observed. On the other hand, data for the (γ, p) reaction are few [7-9]. In our previous study [9], the giant resonance for the odd-odd nucleus ^{10}B has been investigated using the (e, p) and (e, d_0) reactions. From the ^{10}B(e, p) reaction, the cross sections for (γ, p_0) and (γ, p_2) were obtained separately. However, cross

*Present address: Faculty of Engineering, Tohoku Gakuin University, Chuo, Tagajo 985-8537
†Present address: Toshiba Co. Shibaura 1-1-1, Minato-ku, Tokyo 105
§Present address: Research Center for Nuclear Physics, Osaka University, Mihogaoka, Ibaraki, Osaka 567-0047
‡Present address: Tohoku Institute of Technology, Kasumicho, Taihaku-ku, Sendai 982-8577

sections for decay protons to the high-lying states in the residual nucleus could not be obtained because of oxygen contamination in the thin boron target. The integrated cross section for the sum of (γ, p_0) and (γ, p_2) cross sections up to 27 MeV is measured to be 6.1±0.2 MeV mb, which represents about 4.1± 0.2% of the classical sum rule value [9]. On the other hand, the integrated cross section for (γ, n) up to 24.5 MeV represents 30% of the classical sum rule value [1]. The small sum rule value for (γ, $p_{0,2}$) might arise from the missing of the transition to the high-lying states as predicted by the shell model calculations by Gol'tsov and Goncharova [5]. In the (e, e'n) reaction, a thick target can be used and it sets oxygen contamination free.

In this paper we report the measurements of the cross sections and angular distributions for the ^{10}B (e, e'n)^{9}B reaction and compare the results with those of the ^{10}B(γ,n) and ^{10}B(γ, p) reactions and of the shell model calculations.

§ 2. Experimental Procedure

The ^{10}B(e, e'n) experiment was performed using the continuous electron beam from the stretcher-booster ring at Tohoku University. A ^{10}B-enriched target (96.5%) of thickness 340 mg/cm^2 in the form of a disk of compressed granular boron was bombarded with electrons of energy 200 MeV. The beam current was 150-200 nA with an 80% duty factor. Scattered electrons were momentum analyzed at θ_e= 28° by a magnetic spectrometer, and detected using a vertical drift chamber and three layers of plastic scintillators. The spectrometer has a solid angle of 5 msr, and a momentum resolution of 0.05% within the accepted momentum bite of 5.3%. Neutrons emitted from the target were measured using eight NE213 liquid scintillator neutron detectors.

These were placed in the electron scattering plane at θ_n = 58°, 83°, 108°, 133°, 158°, 213°, 238°, and 263° relative to the electron beam direction. Each detector was placed 85 cm from the center of the scattering chamber allowing the neutron energy to be determined by the time-of-flight method. The neutron detectors were shielded with lead, paraffin, and concrete, and lead collimators were placed in front of 4-cm-thick bismuth plates to absorb scattered electrons and soft γ-rays from the target. The neutron detectors were calibrated using γ-rays from ^{22}Na, ^{137}Cs, ^{60}Co, and ^{88}Y sources. The Compton edge of the ^{137}Cs γ-ray was utilized to set the detection threshold. The neutron efficiency for the detectors was determined using a ^{252}Cf source and an analytical calculation code. The details of electronics, data acquisition, and detection efficiency are described elsewhere [10].

In order to remove γ-ray events, pulse shape discrimination (PSD) modules and the charge comparison method were used. A typical n/γ discrimination is shown in Fig.1.

§ 3. Results and Discussion

3.1 Missing energy spectrum

Data has been taken for the excitation energy range of 18-33 MeV. Figure 2 shows the missing energy spectrum for the ^{10}B(e, e'n) reaction. In the figure the energies corresponding to transitions to the ground and excited states in ^{9}B are shown by the arrows. A peak at 8.4 MeV corresponds to the ground-state transition, which does not have strong neutron population as seen in the (e, e'n) reaction

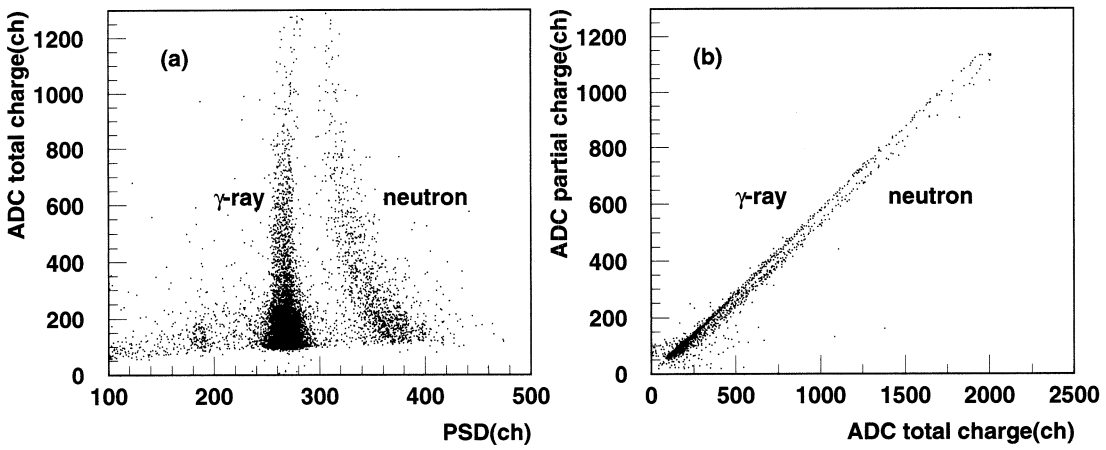

Fig.1. n/γ discrimination by the (a) PSD module and (b) charge comparison method.

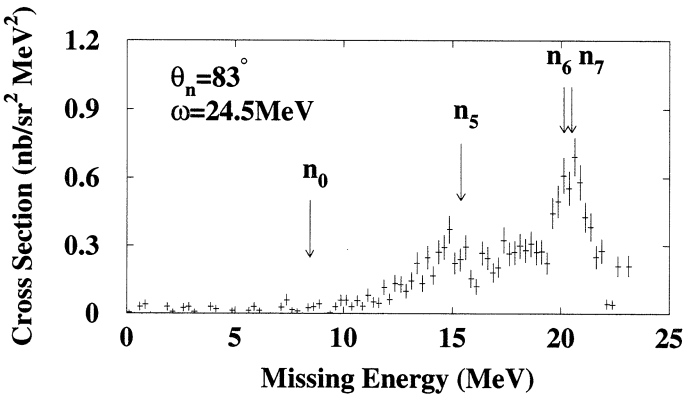

Fig.2. Missing energy spectrum for the ^{10}B(e, e′n)^{9}B reaction at ω = 24.5 MeV and $\theta_n = 83^\circ$.

for even-even light nuclei. In the spectrum, two prominent peaks are seen at approximately at 15 and 21 MeV. They correspond to the population of the 6.97 MeV $7/2^-$ state and 11.70 MeV $7/2^- + 12.06$ MeV $3/2^-$ states in ^{9}B. These groups will be identified as n_5 and $n_{6,7}$.

3.2 Cross section and angular correlation

The cross section magnitudes were determined by summing the yield within a range of ±1.5 MeV for each missing energy peak. The background was subtracted making use of the region in which true events do not contribute. The resultant differential cross sections for the (e, e′n_0), (e, e′n_5), (e, e′$n_{6,7}$), and (e, e′n_{total}) reactions were obtained.

The angular correlations for these decay channels were obtained from the differential cross sections. Angular correlations for each neutron group and total neutrons are shown in Figs.3-6 with the best fit curves of Legendre polynomials described below.

The angular distributions for the (e, e′n_0) reaction show a strong forward-backward asymmetry, which suggests an interference of a transition with the opposite parity to E1. The angular distributions for (e, e′$n_{6,7}$) is strikingly similar to ones for (e, e′n_5). It suggests that the n_6 decay to the $7/2^-$ state is main in the (e, e′$n_{6,7}$) reaction. The angular distributions for n_5 and $n_{6,7}$ have a peak at about 50°. The

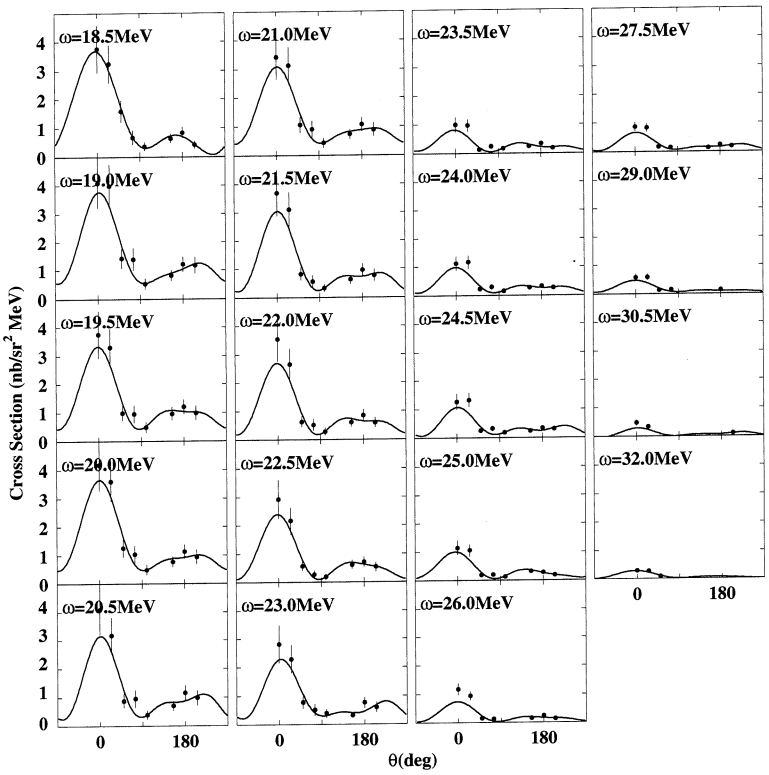

Fig.3. Angular correlations for the n_0 neutron group. Solid curves are best fits of Legendre polynomials. Angles are relative to the momentum-transfer direction.

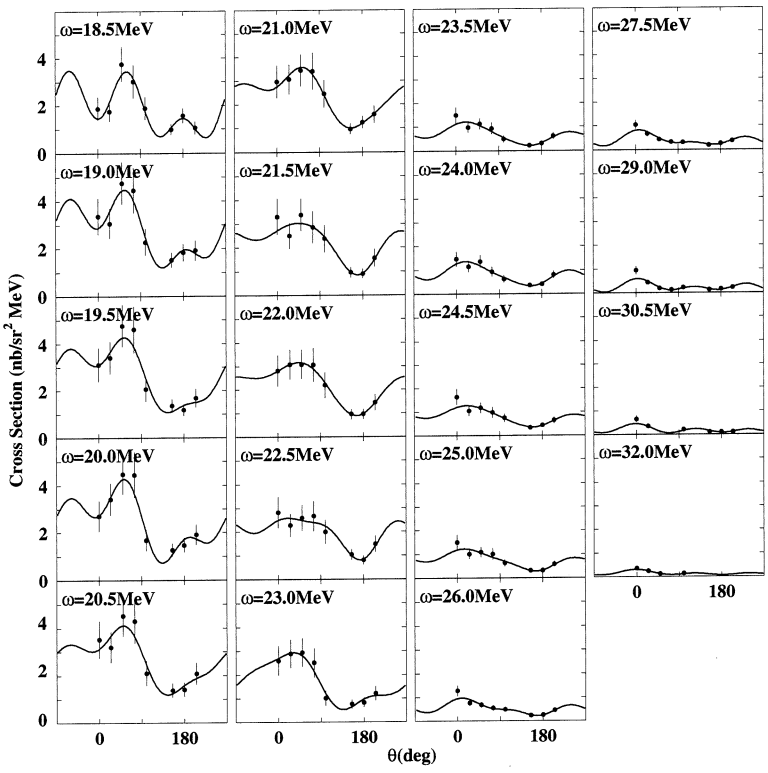

Fig.4. Angular correlations for the n_5 neutron group. The legend is the same as in Fig.3

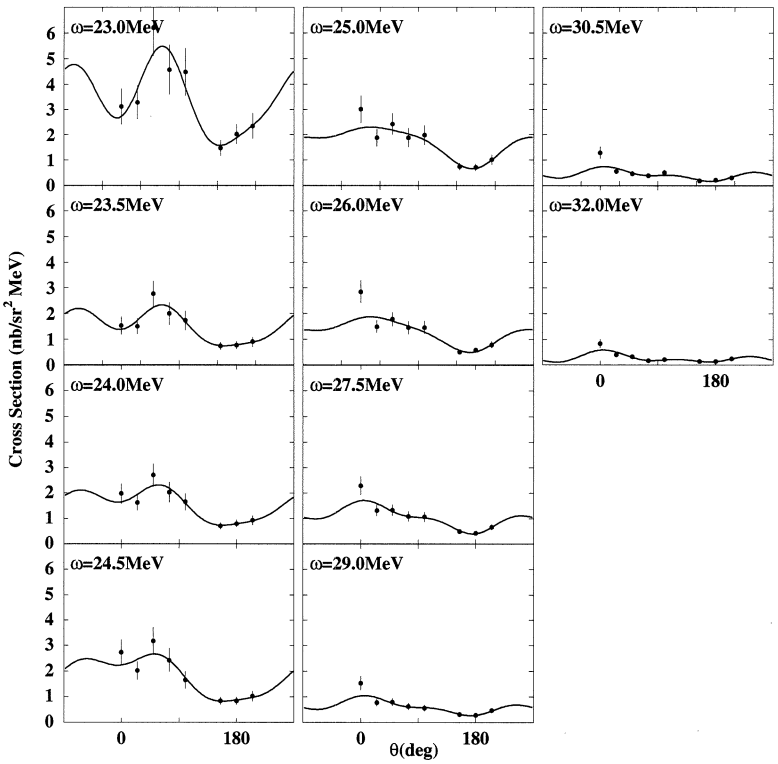

Fig.5. Angular correlations for the $n_{6,7}$ neutron group. The legend is the same as in Fig.3

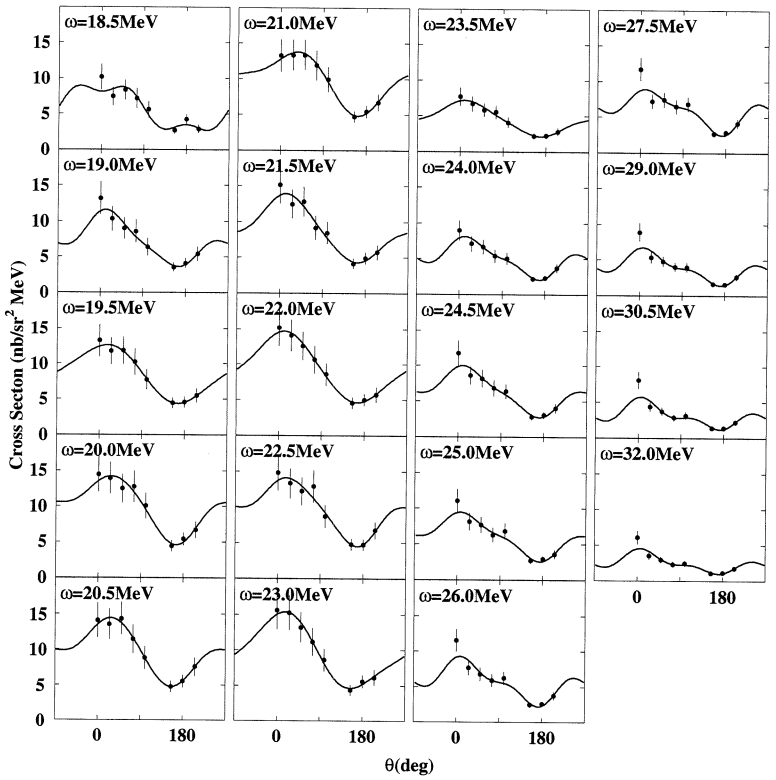

Fig.6. Angular correlations for total neutrons. The legend is the same as in Fig.3

peak approaches 0° with increasing the excitation energy. The angular distributions for n_5 and $n_{6,7}$ are quite different from for n_0. These angular correlations were analyzed in the following way. The theoretical cross section can be written as [11, 12]

$$d^3\sigma/d\Omega_e\, d\omega\, d\Omega_n = \sigma_M \{V_L R_L + V_T R_T + V_{LT} R_{LT} \cos\phi_n + V_{TT} R_{TT} \cos 2\phi_n\}, \quad (1)$$

where σ_M is the Mott cross section for scattering on a point nucleus, and V_i are the leptonic kinematic factors. The response functions R_i contain all the nuclear structure information. Under the present experimental conditions, namely for forward scattering ($\theta_e = 28°$) and low momentum transfer (q_{eff} = 0.57 fm^{-1}), the giant dipole resonance (GDR) is excited predominantly via the longitudinal interaction ($C1$); the transverse component ($T1$) and other multipoles ($C2$) may be weakly excited. Under these conditions the longitudinal and transverse response functions R_L and R_T can be expressed by $|C1|^2$, $C1^*C2$, and $|T1|^2$. The interference terms R_{LT} can be expressed by $C1^*T1$ and $C2^*T1$, and R_{TT} by $|T1|^2$. The present response functions are approximated by a set of third-order Legendre polynomials and associated Legendre polynomials;

$$\begin{aligned} V_L R_L + V_T R_T &= A_0 [1 + b_1 P_1(x_n) + b_2 P_2(x_n) + b_3 P_3(x_n)], \\ V_{LT} R_{LT} &= C_2 [c_1 P_1^1(x_n) + P_2^1(x_n) + c_3 P_3^1(x_n)], \\ V_{TT} R_{TT} &= D_2 P_2^2(x_n), \\ x_n &= \cos\theta_n. \end{aligned} \quad (2)$$

In making a fit to the data, the following approximations were assumed. From the Goldhaber-Teller model (G-T model) [13], the ratio of the transverse to longitudinal strength was estimated to be 1% at E_x = 10 MeV increasing to 12% at E_x = 30 MeV. The transverse term was less than the C1 term, so that the c_1, c_3, and D_2 terms were neglected. Consequently, the cross section can be expressed by five terms:

$$d^3\sigma/d\Omega_e\, d\omega\, d\Omega_n = A_0 \sigma_M [1 + b_1 P_1(x_n) + b_2 P_2(x_n) + b_3 P_3(x_n)] - (C_2/A_0) P_2^1(x_n)], \quad (3)$$

where A_0, b_1, b_2, b_3, and C_2 are fitting parameters.

The experimental angular correlations for each excitation energy region were fitted with Eq. (3), and the Legendre polynomial coefficients were obtained. The $4\pi A_0$, b_1, b_2, b_3, and C_2/A_0 parameters were obtained for the (e, e′n_0), (e, e′n_5), (e, e′$n_{6,7}$), and (e, e′n_{total}) reactions on ^{10}B. The parameters $4\pi A_0$, b_1, b_2, b_3, and C_2/A_0 for n_0, n_5, and $n_{6,7}$ neutron groups are shown in Figs.7-9, respectively. The cross section ($4\pi A_0$) for total neutrons is shown in Fig.10.

A shift of the forward peak from 0° for the n_5 and $n_{6,7}$ transitions is usually explained by an interference between the longitudinal and transverse terms, namely C_2/A_0 [14]. However, C_2/A_0 values for the n_5 and $n_{6,7}$ transitions are small as seen in Figs.8 and 9. The shift might arise from that the interference terms (b_1 and b_3) are comparable or larger than an E1 amplitude (b_2) comparing to b_i values for n_0.

The angular coefficient b_i relates to longitudinal matrix elements in the static limit of resonance approximation [11] assuming that only E0, E1, and E2 excitations contribute. The angular coefficient b_2 is expressed as [15]

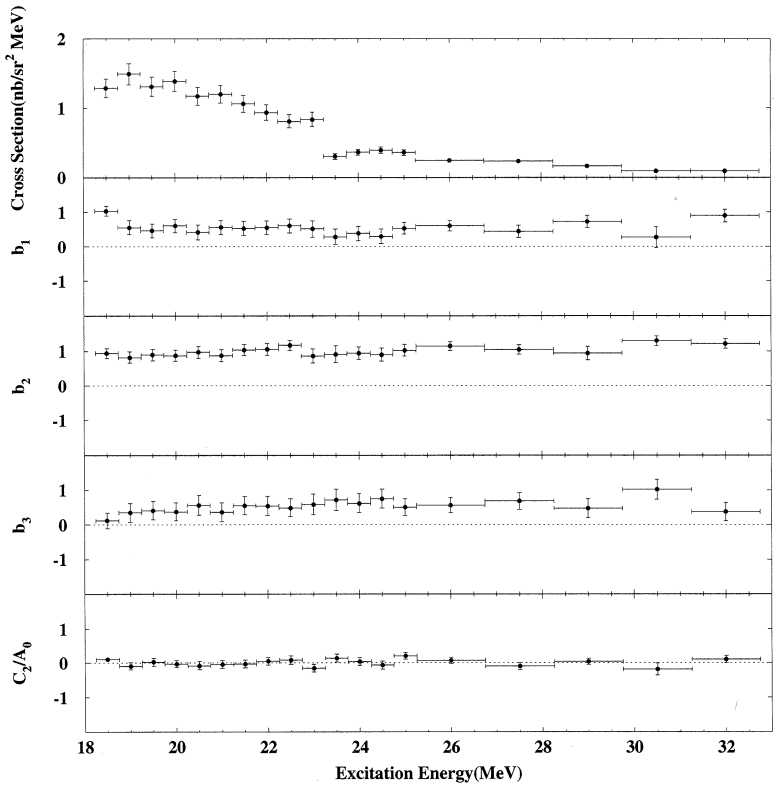

Fig.7. Cross section ($4\pi A_0$) and angular coefficients b_i and C_2/A_0 for the n_0 neutron group.

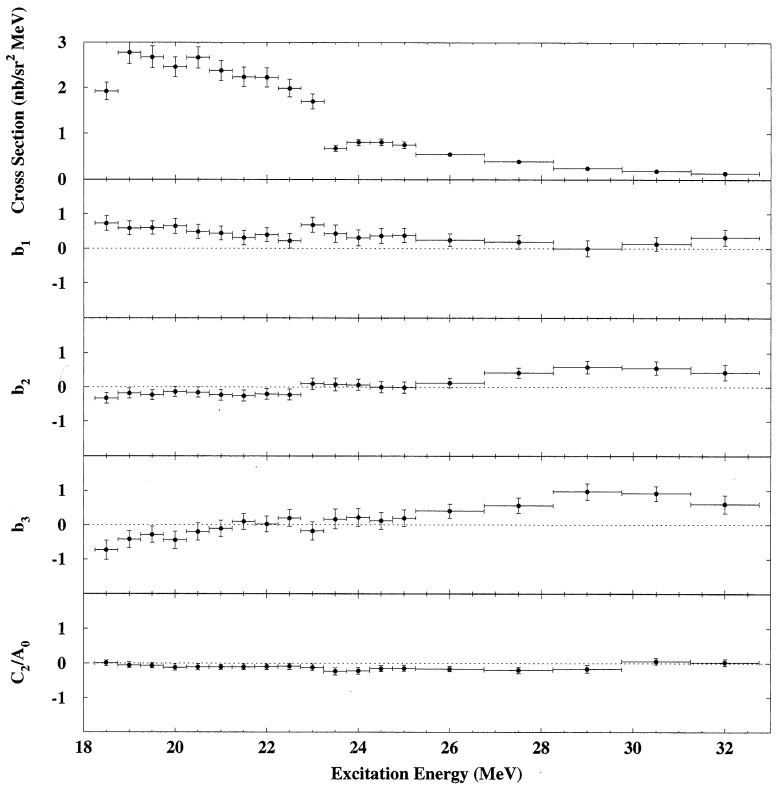

Fig.8. Cross section ($4\pi A_0$) and angular coefficients b_i and C_2/A_0 for the n_5 neutron group.

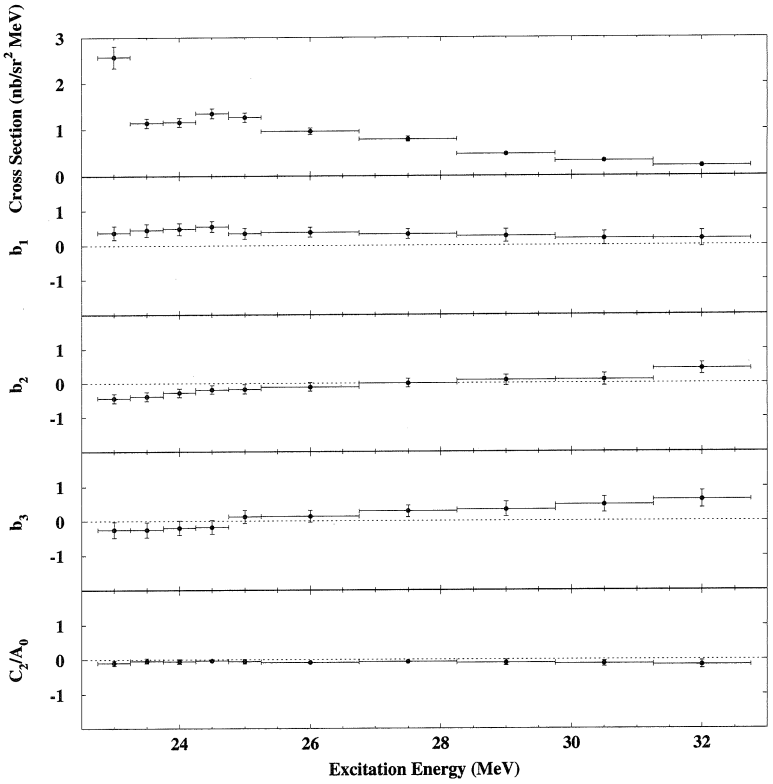

Fig.9. Cross section ($4\pi A_0$) and angular coefficients b_i and C_2/A_0 for the $n_{6,7}$ neutron group.

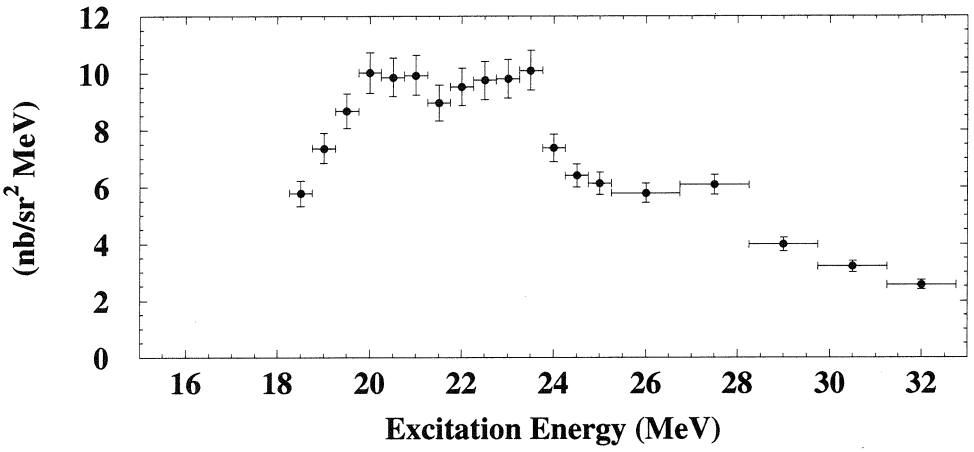

Fig.10. Cross section for the $^{10}B(e,e'n)^9B$ reaction.

$$b_2 = \frac{1}{A_0}\left\{3C1^2 - \frac{15}{2}C2^2 + 3\sqrt{5}\,C0\,C2\cos\delta_{20}\right\} \quad (4)$$

were $C0$ and δ_{20} represent the monopole matrix element and phase difference between E2 and E0 excitationns, respectively. The change of the sign of b_2 seen in the (e, e′n_5) and (e, e′$n_{6,7}$) reactions can be supposed to depend on a relative magnitude of $C2$ and/or $C1$ from Eq. (4). In these reactions decaying to the high spin state 1f 7/2$^-$, an E2 (E0) excitation might be enhanced comparing to the (e, e′n_0) reaction.

3.3 Comparison with the photoneutron reaction

The cross section for the photoneutron reaction [1] has been transformed into the form factor by the usual method [16], which assumes that the photoneutron cross section is completely an E1 transition. It is compared with the present data in the upper part of Fig.11. The ^{10}B(e, e′n) cross section agrees fairly well the ^{10}B(γ,n) cross section. A disagreement of the magnitude of the second peak might be due to the missing of low energy neutrons in the (e, e′n) reaction.

3.4 Comparison with the photoproton reaction

A comparison between the ^{10}B(e, e′n) and ^{10}B(γ, $p_{0,2}$) cross sections [9] is shown in Fig.11. The (γ, $p_{0,2}$) cross sections are the sum of cross sections to the p_0 and p_2 transitions. It indicates a broad peak at about 15 MeV, which is larger than the peak of the giant resonance at about 21 MeV seen in the (e, e′n) reaction. The small cross section might reflect the missing of the transition to the high-lying states as observed in the (e, e′n) reaction.

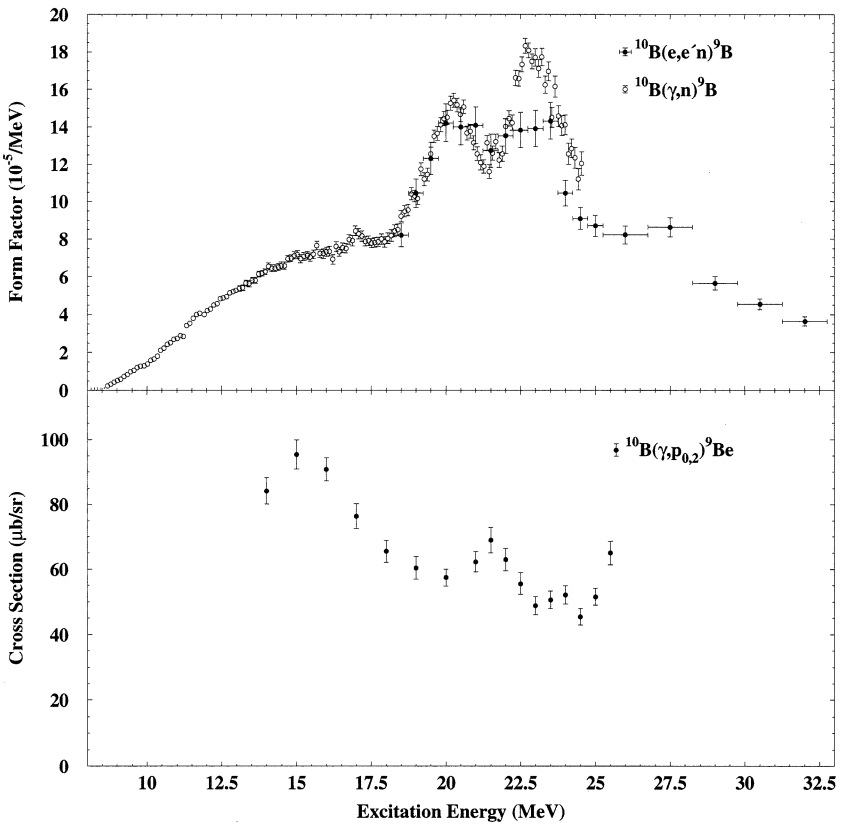

Fig.11. Comparison of the cross sections. Upper part: ^{10}B(e, e'n)^{9}B and ^{10}B(γ,n)^{9}B from Ref. [1]. Lower part: ^{10}B(e, e'$p_{0,2}$)^{9}Be from Ref. [9].

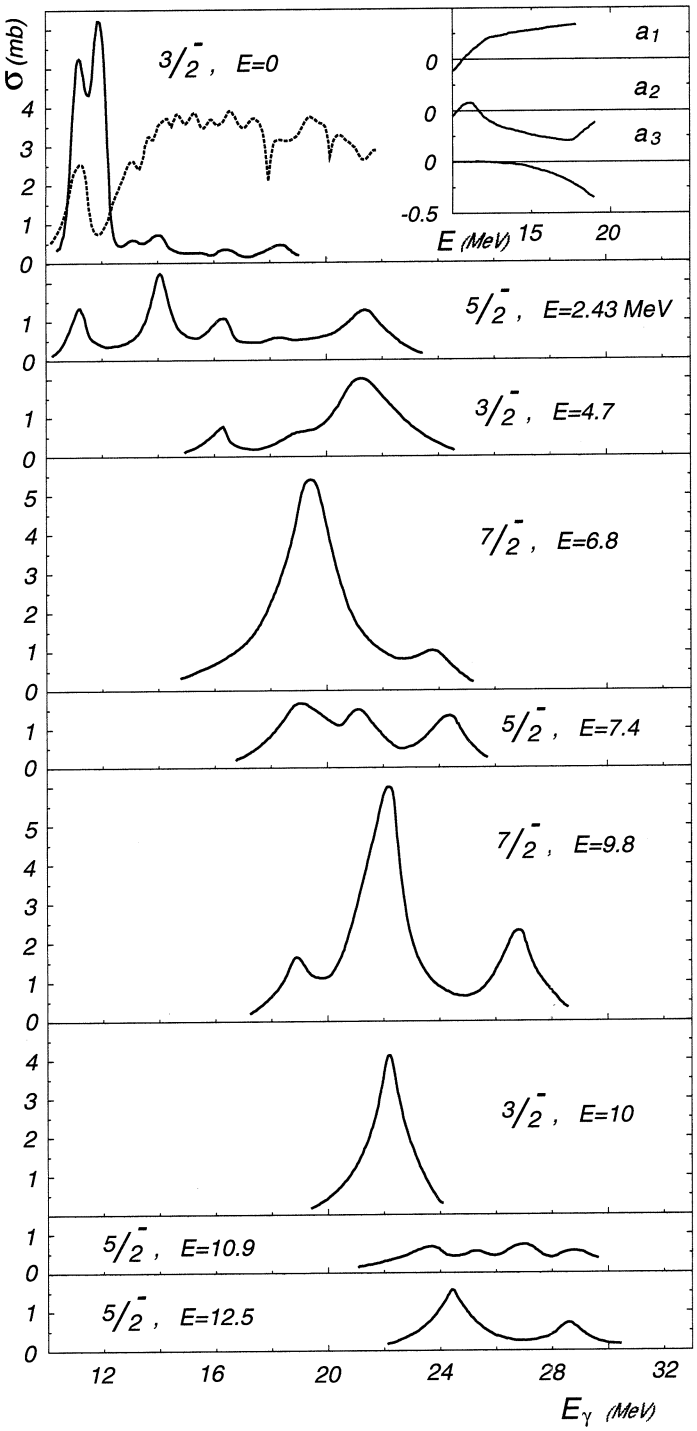

Fig.12. Calculated partial cross sections for the photoproton channels of the ^{10}B disintegration (solid curves) and experimental data [8] (dashed curve) for ^{9}Be (p, γ_0)^{10}B from Ref. [5].

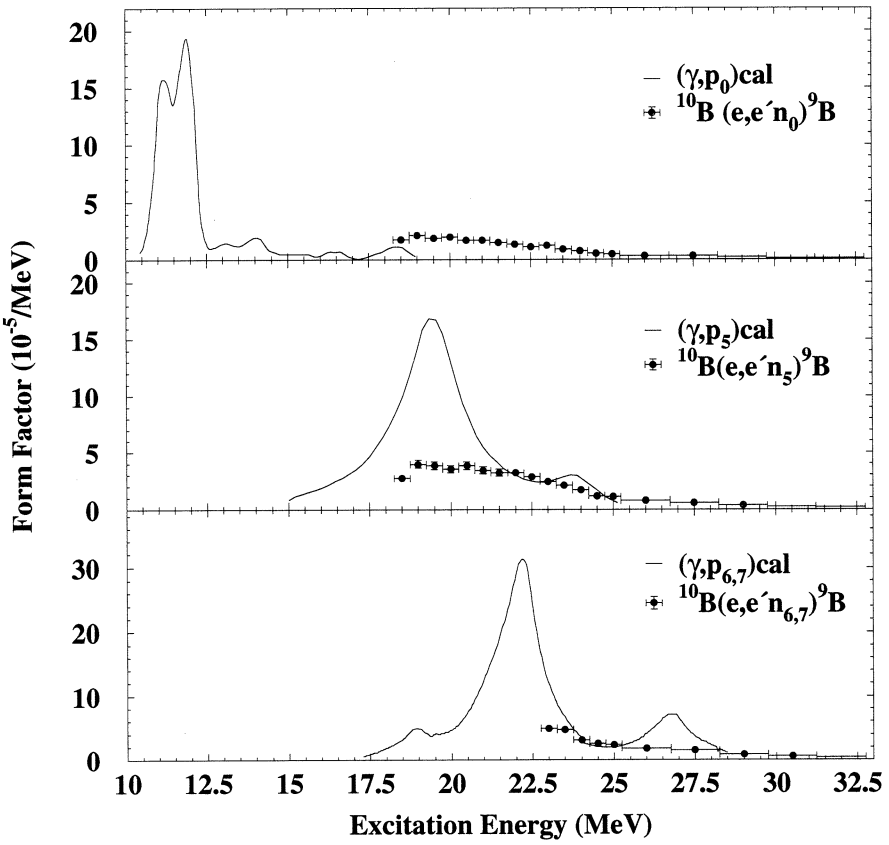

Fig.13. Comparison with the shell model calculations [5] for the n_0, n_5, and $n_{6,7}$ transitions.

3.5 Comparison with the shell model calculations

The partial and total cross sections for the photodisintegration of the nucleus are calculated in the framework of the shell model with intermediate coupling by Gol'tsov and Goncharova [5]. The calculated cross section for the photoproton channels are shown in Fig.12. The partial cross sections for photoneutron channels are similar to the photoproton ones [5]. Therefore, the present data for the n_0, n_5, and $n_{6,7}$ transitions are compared with the calculations in Fig.13. In the experiment, the (e, e′n_0) cross section was observed over 24 MeV. The calculations for (e, e′n_0) fail to reproduce the cross section in the excitation energy region of 19-24 MeV. For the n_5 transition, a pronounced peak in the cross section was not observed, but the magnitude of the cross section agrees well with the calculated cross section in the tail region. For the $n_{6,7}$ transition, the measured and calculated cross sections are consistent in the tail of the main peak. It was confirmed that neutrons from the giant resonance in ^{10}B have decayed mainly not to the ground state but the high-lying states in ^{9}B in the cross section, too.

§ 4. Summary

The cross section and angular correlations to several residual states following the ^{10}B(e, e′n) reaction have been measured in the excitation energy region of about 18-33 MeV at the effective momentum transfer of 0.49 fm^{-1}. The states observed clearly to be populated are the ground (n_0), 6.97 MeV $7/2^-$ (n_5) and 11.70 MeV $7/2^-$+12.06 MeV $3/2^-$ ($n_{6,7}$) states. The cross sections for each transition were compared with the shell model calculations. The cross section for n_0 was measured up to 32 MeV

beyond the predictions. For the n_5 transition, a pronounced peak in the cross section was not observed, but the measured and calculated cross sections agree well in the tail region. For the $n_{6,7}$ transition, the measured cross sections are consistent with calculated ones in the tail of the main peak of the prediction. The angular distributions for n_0 show a strong forward-backward asymmetry, which suggests an interference of a transition with the opposite parity to E1. The angular distributions for n_5 and $n_{6,7}$ show a peak at about 50° not at 0°. It might reflect not an interference between the longitudinal and transverse components, but a lower E1 amplitude from an analysis of the Legendre polynomial expansion of the angular distributions. The ^{10}B(e, e'n) cross section was compared with ^{10}B(γ, n) cross section. Both cross sections agree fairly well. It was confirmed that neutrons from the giant resonance in ^{10}B have decayed mainly not to the ground state but the 6.97 MeV $7/2^-$ and 11.70 MeV $7/2^-$ +12.06 MeV $3/2^-$ states in ^{9}B as predicted.

References

[1] M.H. Ahsan, S.A. Siddiqui and H.H. Thies : Nucl. Phys. **A469** (1987) 381.

[2] E. Hayward and T. Stovall : Nucl. Phys. **69** (1965) 241.

[3] R.J. Hughes and E.G. Muirhead : Nucl. Phys. **A215** (1973) 147.

[4] U. Kneissl, K.H. Leister, H.O. Neidel and A. Weller : Nucl. Phys. **A264** (1976) 30.

[5] A.N. Gol'tsov and N.G. Goncharova : Sov. J. Nucl. Phys. **38** (1983) 857.

[6] R. Shackleton : Ph.D Thesis, University of Melbourne, 1971 (unpublished).

[7] A.Kh. Shardanov and B.A. Yuryev : J. Nucl. Phys. **8** (1961) 424.

[8] G. Fisher : Thesis, Stanford Univ., 1970 (unpublished).

[9] H. Ueno, H. Taneichi, Y. Takahashi, T. Suzuki, K. Shoda, T. Saito and T. Tsukamoto : (unpublished).

[10] S. Suzuki *et al.* : Nucl. Instr. Meth. **A314** (1992) 547.

[11] W.E. Kleppinger and J.D. Walecka : Ann. Phys. (N. Y.) **146** (1983) 349.

[12] G. Co' and S. Krewald : Nucl. Phys. **A433** (1985) 392.

[13] M. Goldhaber and E. Teller : Phys. Rev. **74** (1948) 1046.

[14] M. Cavinato, D. Drechsel, E. Fein, M. Marangoni and A.M. Saruis : Nucl. Phys. **A444** (1985) 13.

[15] M. Span, Th. Kihm and K.T. Knöpfle : Z. Phys. A **330** (1988) 345.

[16] C. Takakuwa *et al.* : Phys. Rev. C **50** (1994) 845.

(LNS Experiment : #2414, #2447)

Total Nuclear Photon Absorption Cross Section for ^{27}Al

M. Inoue[1], K. Hirose[2], H. Kanda[2], K. Maeda[2], M. Mutoh[1],
T. Ohtsuki[1], T. Terasawa[1] and Y. Yamaguchi[2]

[1]*Laboratory for Nuclear Science, Tohoku University, Sendai 982-0826*
[2]*Physics Department, Graduate School of Science, Tohoku University, Sendai 980-8578*

We have developed a new technique to measure the total photon absorption cross section. We found that this method shows the possibility of quick data acquisition of the total photoabsorption cross section. We demonstrate the measurement of the total photon absorption cross section of ^{27}Al.

The total nuclear photon absorption cross section is a sum of all nuclear photo-reaction channels. It is one of the most sensitive quantity to the nuclear structure information. Ahrens *et. al.* [1] reported the measurements of the total photon absorption cross sections $\sigma(E_\gamma)$ for Li, Be, C, O, Al, Si and Ca nuclei from E_γ = 10 MeV to the meson threshold. They used bremsstrahlung photons produced by pulsed electrons from the Mainz linear accelerator with a duty factor of 0.45×10^{-3}. A pair of Compton spectrometers was used to count the photons before and after the absorption target. A lot of beam time was required to achieve sufficient statistics owing to not only the low duty electron beam but also the inefficient spectrometer system. Several small fluctuations are seen above the giant dipole resonance. Recently, they have noticed as possibilities of the double giant resonance [2].

In this report, we show the development of a new method to measure the total photon absorption cross section $\sigma(E_\gamma)$. The preliminary data for ^{27}Al in an energy range of E_γ = 40~110 MeV are presented.

The experimental setup is shown in Fig. 1. The 140 MeV electrons from the pulsed beam stretcher were transported to the photon tagger. Bremsstrahrung photons were produced in a gold radiator of 1/1000 radiation length. We employed a 3 cm $\phi\times$ 15 cm lead glass Cherenkov counter to detect photons. The recoil electrons were momentum-analyzed by a magnetic field and detected by a 64-channel tagging counter (TC). The momentum width of each counter was 1.4 MeV. We used a 5.0 cm $\phi\times$12.0 cm aluminum rod as the absorber. The rod included 5% magnesium and the specific gravity was 2.65 g/cm^3. The absorber was mechanically putting in and out of the photon beam every 10 seconds. The timing signals for the measurement are shown in Fig. 2. Single and coincidence counts of the tagging counters were registered in scalers. The background was measured without the radiator and found to be negligibly small.

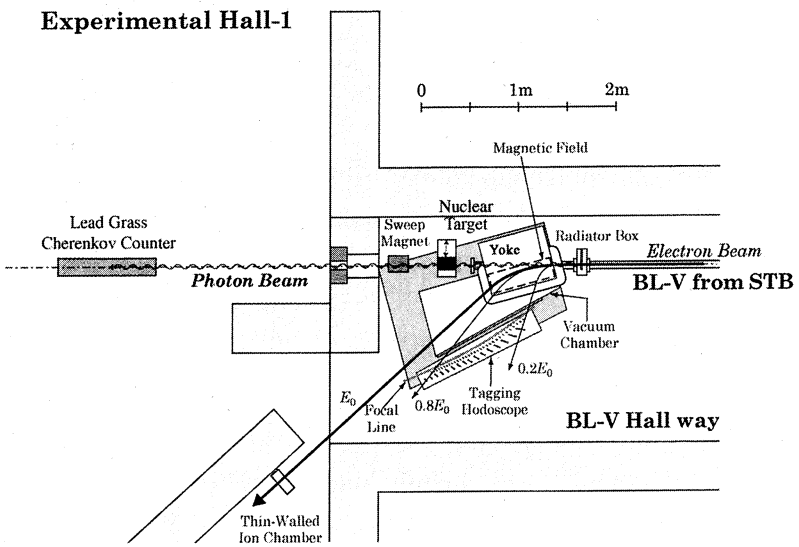

Fig.1. Layout of the photon tagging system and the setting for this experiment.

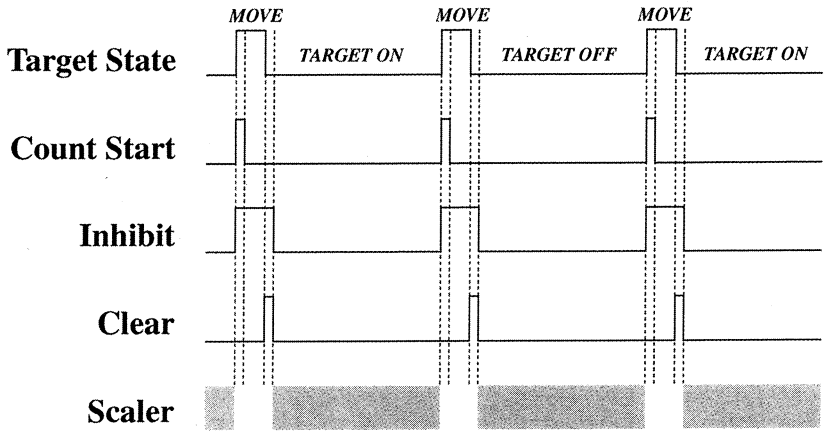

Fig.2. Timing chart of absorber movement.

The energy of photon (E_γ) is defined by the energy of electron (E_e) which is determined by tagging counters as,

$$E_\gamma = E_0 - E_e,$$

where E_0 is the energy of the incident electron. The tagging counters are consisted of 64-channel thin plastic scintillators lining up on the focal plane of the tagging magnet from $0.2\,E_0$ to $0.8\,E_0$ at an interval of $0.094\,E_0$. The energy of the tagged photon at the ith channel becomes,

$$E_\gamma = E_0 - (0.2\,E_0 + 0.094\,E_0^{(i-1)})$$

The low energy side of E_γ deviates from this equation because of non-uniform fringing field of the magnet. This deviation was investigated by T. Suda using the measurement of ^{2}H (γ , n_0) reaction. They were tabulated by P. Harty [3].

The total photon absorption cross section $\sigma_{tot}(E_\gamma)$ as a function of the photon energy E_γ can be deduced from the absorption law,

$$N(E_\gamma)=N_0(E_\gamma)\exp(-n\sigma_{tot}(E_\gamma)),$$

where N and N_0 are the number of photons in a certain energy bin with and without the absorption, respectively. Here, n is the number of nuclei per cm^2 in the absorber. The coincidence counts between tagging counters and the Cherenkov counter were normalized by a sum of counts in each cycle with or without the absorber. Obtained $\sigma_{tot}(E_\gamma)$ is shown in Fig. 3. The curve in the figure shows the calculated photon absorption cross section of the atomic process. The calculation overstimates the data at high energies.

During the measurement, the beam intensity was kept at low enough to avoid the pile-up of the coincidence counts. However, a slight influence of the pile-up, which depends on the beam intensity, was observed. The beam intensities measured as the sum of tagging electrons distributed from 30 kHz to 100 kHz. Because the coincidence count without absorber is about twice of that with absorber, the pile-up of the coincidence count without and with absorber is not same. Since the $\sigma_{tot}(E_\gamma)$ does not depend much on E_γ at E_γ = 30～110 MeV, we summed N_0 and N for all tagging channels. The experimental results of N_0/N divided into 7 intensities are shown in Fig. 4. The best fitted curve showed that N_0/N at zero intensity was $2.118\pm(0.425\times10^{-3})$. The obtained value was 2.110. The correction factor for $\sigma_{tot}(E_\gamma)$ was ln(2.118) /ln(2.110) = 1.005, irrespective of the photon energy.

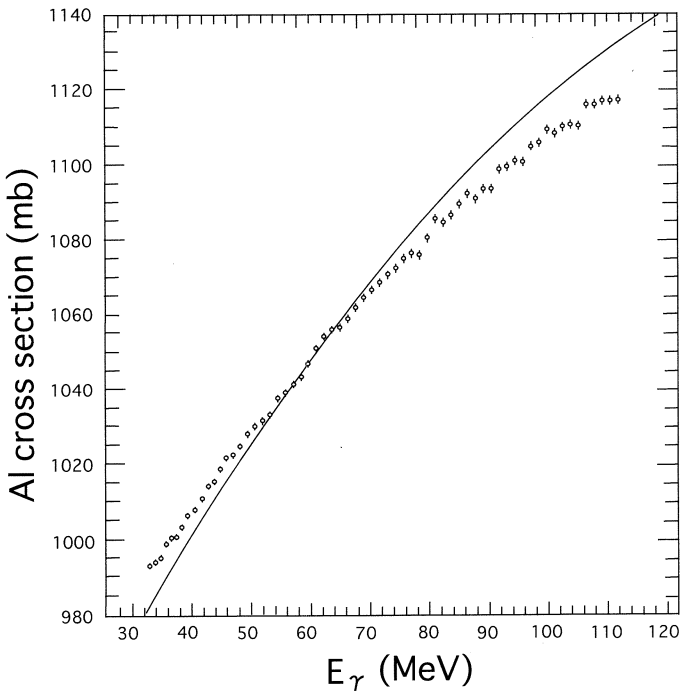

Fig.3. Total photon absorption cross section for Al. The curve is the theoretical prediction of the atomic process.

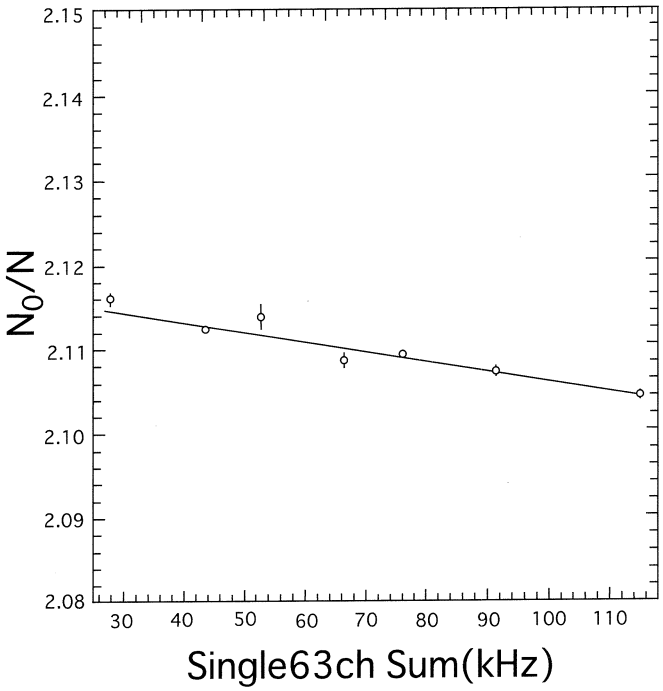

Fig.4. The beam intensity dependence of N_0/N.

Absorption of photons produces electrons, positrons and secondary bremsstrahlung photons in the absorber. These particles are detected in the Cherenkov counter. We calculated these electrons, positrons, and photons using GEANT3. We calculated the correction factor (r) due to those processes at 11 photon energies (Fig. 5). The photon energy dependence of r was obtained with the best fitted curve as shown in the figure.

We corrected the data in Fig. 3 for the pile-up and the mixing of the secondary bremsstrahlung. The result is shown in Fig. 6. By subtracting the calculated atomic cross section [4], we obtained the total nuclear photon absorption cross section as shown in Fig. 7. The magnitude of the cross section roughly agrees with the previous measurement [1]. In the present measurement a peak is obserbed at E_γ = 62 MeV. This peak was also observed by Ahrens et al. [1] together with two peaks at E_γ = 56 MeV and E_γ = 76 MeV. We did not observe the latter two peaks. We checked present ^{27}Al data by dividing runs into 4 sections, and the peak at E_γ= 62 MeV was observed in all sections. Just after the ^{27}Al measurement, we measured the cross section for ^{12}C. The peak at E_γ= 62 MeV was not seen in the ^{12}C data. Additional measurements are needed to confirm the peaks.

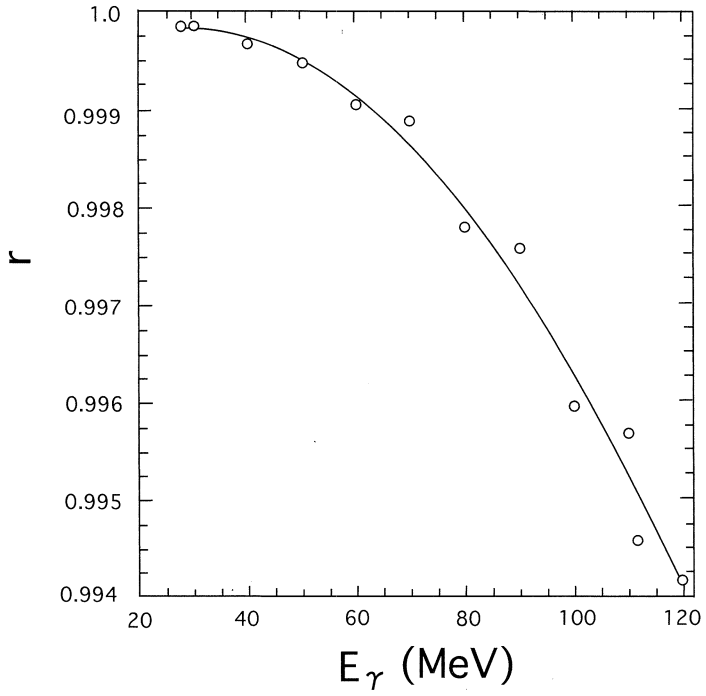

Fig.5. Photon energy dependence a correction factor due to secondary bremsstrahlung.

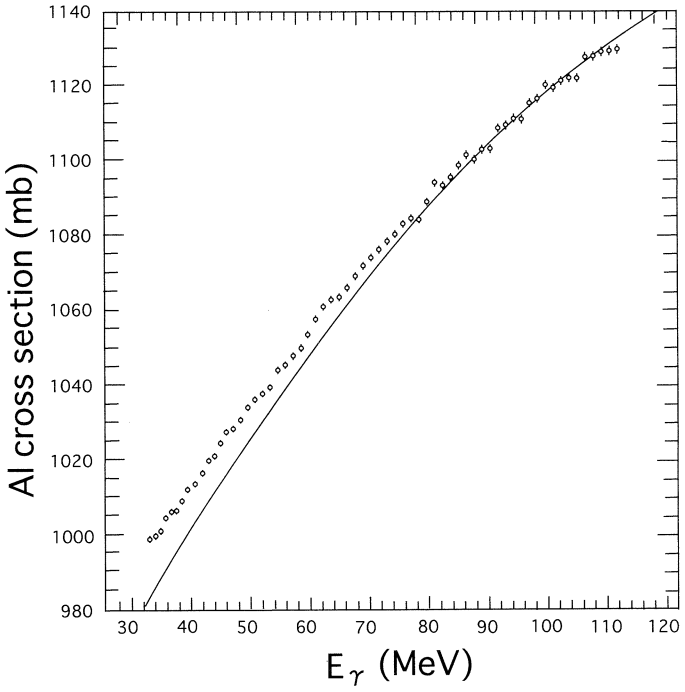

Fig.6. Total photon absorption cross section corrected for the pile-up and secondary bremsstrahlung. The curve is the calculated atomic cross section [4].

We wish to thank Mr. K. Matsuda for the guidance to make the target mover. We also thank the accelerator crew of the Laboratory of Nuclear Science for providing stable beam.

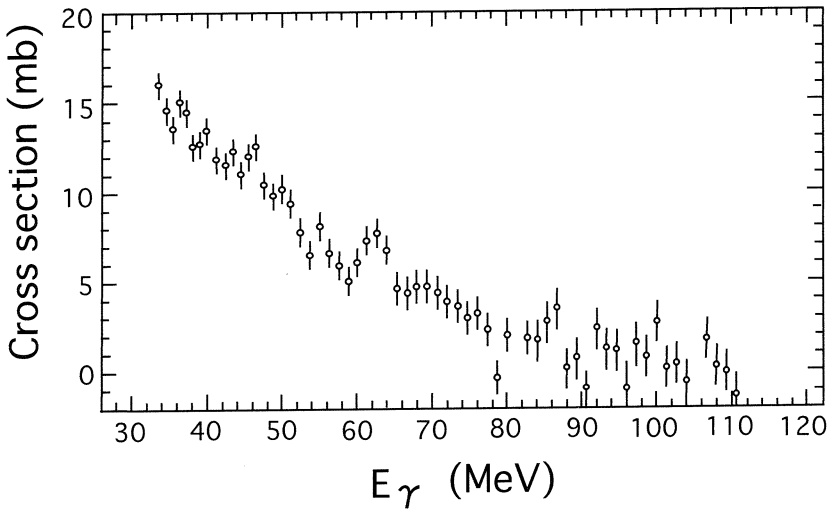

Fig.7. Total nuclear photon absorption cross section for ^{27}Al.

References

[1] J. Ahrens et al.: Nuclear Physics **A251** (1975) 479.

[2] E. Emling : Prog. Part. Nucl. Phys. **33** (1994) 729.

[3] P. Harty : thesis, University of Melbourne 1986.

[4] J. Hubbell : NSRDS-NBS 29, US Government Printing Office, Washington 1969.

(LNS Experiment : #2276, #2330)

Comparison of the ^{12}C(e, e′p) Cross Sections at Low Momentum Transfer with Relativistic Calculations

T. Tamae[1], Y. Sato[1], T. Yokokawa[1]*, Y. Asano[1]†, M. Kawabata[1], R. Kimura[2], O. Konno[1]‡, H. Miyase[2], I. Nakagawa[1]§, Nishikawa[1], K. Hirota[1]**, H. Tsubota[2] and H. Yamazaki[1]

[1]*Laboratory of Nuclear Science, Tohoku University, Mikamine, Taihaku-ku, Sendai 982-0826*
[2]*Department of Physics, Graduate School of Science, Tohoku University, Aramaki, Aoba, Sendai 980-8578*

The (e, e′p_0) cross section of ^{12}C previously measured using a 197.5 MeV continuous electron beam is compared with theoretical calculations based on the relativistic distorted-wave impulse approximation (RDWIA). The theoretical values overestimate the experimental ones by a factor of two. The contribution of meson exchange current (MEC) effects is important in the high missing momentum region.

We compared in a previous report [1] the reduced cross section obtained from the ^{12}C(e, e′p_0) experiment with results of a non-relativistic distorted-wave impulse approximation (DWIA). In this report, the reduced cross section is compared with theoretical calculations based on the relativistic distorted-wave impulse approximation (RDWIA) with and without MEC effects.

Recently the (e, e′p) and (γ, p) reactions have been investigated extensively in a fully relativistic DWIA (RDWIA) framework [2-8]. The relativistic calculations for the direct knock-out (DKO) mechanism appears to describe well measured (γ, p) cross sections in light nuclei at photon energies below 80 MeV, as well as the quasi-elastic (e, e′p) reaction. It means that the contribution of the MEC may not be large for the (γ, p) reaction in the relativistic framework. Actually, it was shown [8, 9] that the two-body contribution corresponding to the seagull term affects the (γ, p) cross section less than in non-relativistic calculations. The choice of the electromagnetic operator is a longstanding problem [7, 8]. Usually-used current-conserving operators (cc1, cc2, cc3) are equivalent each other for on-shell particles due to Gordon identity. However, for an off-shell nucleon, different choices of the prescriptions give very different (γ, p) cross sections.

In the plane-wave impulse approximation (PWIA) the (e, e′p) cross section can be factorized in the

* Present address: Iwanami Shoten Publishers, 2-5-5, Hitotsubashi, Chiyoda-ku, Tokyo 101-8002
† Present address: CATENA Corp., CATENA Tama Center Bldg. 1-15-2, Ochiai, Tama-Shi, Tokyo 206-0033
‡ Present address: Department of Electrical Engineering, Ichinoseki National College of Technology, Hagiso, Ichinoseki 021-8511
§ Present address: Department of Physics & Astronomy, University of Kentucky, Lexington, KY 40506, USA
** Present address: SPring-8, JASRI, Sayo-gun, Hyogo 679-5198

form;

$$\sigma_{e,e'p} \equiv \frac{d^3\sigma}{d\omega d\Omega_p d\Omega_p} = K\sigma_{e,p} S(E_m, p_m), \quad (1)$$

where K is a kinematic factor, and $\sigma_{e,p}$ is the off-shell electron-proton scattering cross section. In the PWIA the spectral function $S(E_m, p_m)$ is referred as a momentum distribution of the proton in the nucleus. From the measured coincidence cross section $\sigma_{e,e'p}$, the reduced cross section is defined by

$$\rho_{e,e'p}(p_m) = \frac{\sigma_{e,e'p}}{K\sigma_{e,p}}. \quad (2)$$

The reduced cross sections was obtained using the cc1 current [10]. The results with cc2 or cc3 currents are not different more than 2% from that with the cc1 prescription. The present data are compared with RDWIA calculations [11]. The RDWIA treatment is the same as in Refs. [7, 8]. The bound state wave function is calculated using parameters of the set NLSHT [12]. The relativistic bound state wave functions are solutions of a Dirac equation with scalar and vector potentials. The spectroscopic factor Z (p3/2) = 0.56 has been applied, which was obtained from the analysis [4] of the quasi-elastic (e, e'p_0) reaction. As the choice of the electromagnetic operator is, to some extent, arbitrary and no rigorous justification exists, three expressions (cc1, cc2, cc3) [7, 8, 10, 13] were used in the calculation in order to assess the effect. Figure 1 shows the calculations compared with the present data. The calculations overestimate the experimental data by about two times at low missing momenta. The enhancement factor is same to the (γ, p_0) reaction reported in Refs. [4, 6, 7]. A difference of the calculated results using different expressions of the current operator is larger than that in PWIA [10], and it becomes larger at high missing momenta. The measured cross section decreases a little slowly than the calculations with increasing missing momentum.

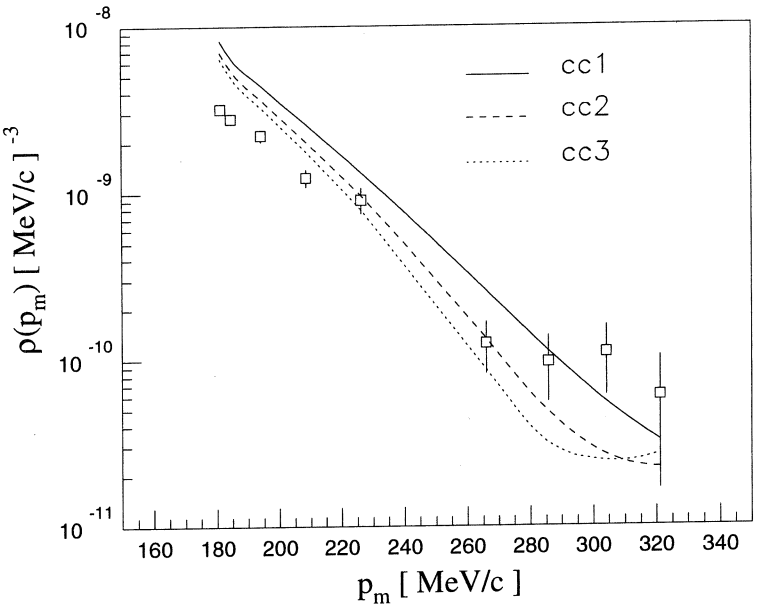

Fig.1. Reduced cross section of the present ^{12}C (e, e'p_0) measurement, compared with relativistic calculations including no MEC. Solid, dashed, and dotted lines represent the RDWIA results with cc1, cc2, and cc3 prescriptions for the one-body current, respectively.

In Fig.2 we compare the present data with the calculated results including the two-body seagull current [8, 14]. The calculations are multiplied by 0.5 in order to normalize them to the data at the lowest missing momentum. Although all of three calculations overestimate the data, the slope is similar to the data. The calculated result without the seagull term is also shown in Fig.2. It is clear that the calculation including the seagull term is in better agreement with the data at high missing momentums. The reduction factors for the cc2 and cc3 currents are almost same to that in the (γ , p_0) reaction. In the (γ , p_0) reaction the calculated result obtained with the cc1 current is enhanced above the data by an order of magnitude [7], while the overestimation is mild for the present (e, e'p_0) reaction. In the non-relativistic calculation for the (γ , p_0) reaction, a substantial reduction is obtained when the pion-in-flight diagram is added [8]. It is expected that the inclusion of the term may improve agreement between our data and calculations.

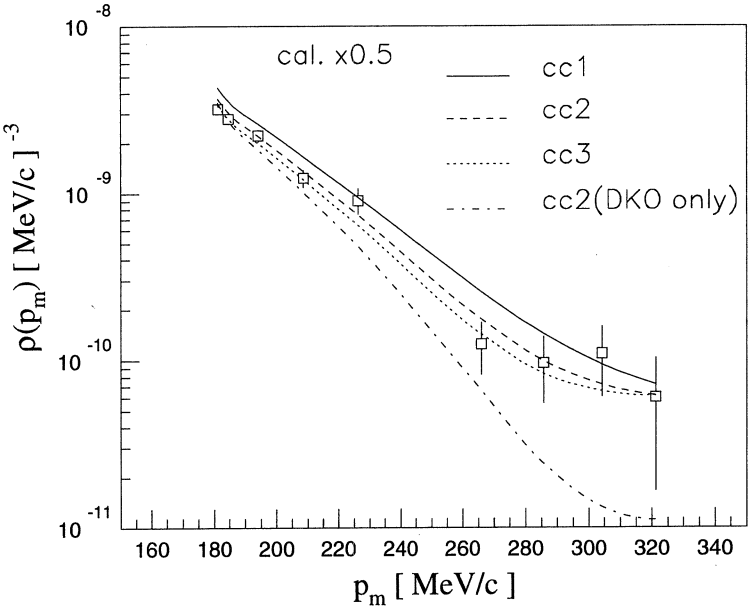

Fig.2. The reduced cross section compared with the RDWIA results calculated with the seagull contribution. Solid, dashed, and dotted lines represent the RDWIA result including the MEC, with cc1, cc2, and cc3 prescriptions for the one-body current, respectively. A dashed-dotted line shows the RDWIA result of the cc2 prescription without the MEC. Calculations are multiplied with a factor 0.5.

Any satisfactory theoretical model should simultaneously describe the (e, e'p) reaction in both of the quasi-elastic and low momentum transfer regions, and also (γ , p) and (γ , n) reactions. A consistent analysis of these reactions will disentangle the longstanding question about reaction mechanisms. The present investigation has firstly compared a relativistic calculation with the (e, e'p) reaction in the low momentum transfer region. The target nucleus of the present experiment, ^{12}C, is the one on which the RDWIA calculation overestimates the (γ , p_0) cross section at 60 MeV by a factor of 2. Obviously, successive investigations are needed on various nuclei such as ^{16}O and ^{40}Ca, for which the RDWIA calculation agrees well with the experiment in the (γ , p) reaction [4-9].

We wish to thank Prof. C. Giusti for providing calculations specific to the kinematic conditions of

the present experiment. This work has been supported by Grant-in-Aid for Scientific Research (KAKENHI) (No. 14540239) from Japan Society for the Promotion of Science (JSPS).

References

[1] Y. Sato *et al.* : Research Report of LNS, Tohoku Univ., **33** (2000) 7.

[2] J.M. Udias, J.A. Caballero, E. Moya de Guerra, J.E. Amaro and T.W. Donnelly: Phys. Rev. Lett. **83** (1999) 5451.

[3] A. Meucci, C. Giusti, and F.D. Pacati : Phys. Rev. C**64** (2001) 014604 .

[4] J. I. Johansson, H.S. Sherif and G. M. Lots : Nucl. Phys. A**605** (1996) 517.

[5] M. Hedayati-Poor and H.S. Sherif : Phys. Lett. B**326** (1994) 9.

[6] J.I. Johansson and H.S. Sherif : Phys. Rev. C**56** (1997) 328.

[7] A. Meucci, C. Giusti and F.D. Pacati : Phys. Rev. C**64** (2001) 064615.

[8] A. Meucci, C. Giusti and F.D. Pacati : Phys. Rev. C**66** (2002) 034610.

[9] C. Giusti and F.D. Pacati : Phys. Rev. C**67** (2003) 044601.

[10] T. de Forest, Jr.: Nucl. Phys. A**392** (1983) 232.

[11] C. Giusti : private communication.

[12] M.M. Sharma, M.A. Nagarajan and P. Ring : Phys. Lett. B**312** (1993) 377.

[13] J.J. Kelly : Phys. Rev. C**56** (1997) 2672 ; **60** (1999) 044609.

[14] G. Benenti, C. Giusti and F.D. Pacati : Nucl. Phys. A**574** (1994) 716.

Li+D Reaction in Pd and Au for $30 < E_d < 75$ keV

H. Yuki[1], J. Kasagi[1], T. Baba[1], T. Noda[1], A. Taguchi[1], M. Shimokawa[1] and W. Galster[2]

[1]*Laboratory of Nuclear Science, Tohoku University, Mikamine, Sendai 982-0826*
[2]*School of Engineering, Tohoku University, Aramaki-Aoba, Sendai 980-8579*

Thick target yields of α particles emitted in the ^{6,7}Li (d, α)^{4,5}He reactions in $PdLi_x$ and $AuLi_x$ were measured as a function of the bombarding energy between 30 and 75 keV. It was found that the reaction rate in Pd at lower energies is enhanced strongly over the one predicted by the cross section for the reaction with bare nuclei, but no enhancement is observed in Au. A screening energy is introduced to reproduce the excitation function of the thick target yield for each metal. The deduced value for Pd amounts to 1500±310 eV, whereas it is only 60±150 eV for Au. The enhancement in the Pd case cannot be explained by electron screening alone but suggests the existence of an additional and important mechanism of screening in metal.

Recently, the screening energy of the D+D reaction in various materials has been measured by several authors[1-7]. Surprisingly, some metals provide anomalously large size screening effects for the D+D reaction, while others exhibit normal electron screening enhancement. The enhancement of the reaction rate strongly depends on the host material, and deduced values of the screening energy vary from several tens of eV to 800 eV. Although Riola *et al.* [6] have discussed several possibilities to interpret such large screening in materials, no satisfactory explanation could be given. Yuki *et al.* [3] and Kasagi *et al.* [7] have proposed that high fluidity of deuterons in the host may be responsible for the enhancement.

In order to explore the mechanism of enhanced screening, we have studied other nuclear reactions in metal hosts. In the present work, we have investigated the ^{6,7}Li (d, α)^{4,5}He reactions in metal, for the first time. Two host metals were selected in which the Li+d reactions occur, Pd and Au. The screening energy of the D+D reaction in Pd is confirmed to be very large, although two reported values are not in good agreement with each other; U_s = 250~310 eV in Refs. [10, 14] and ~800 eV in Ref. [13]. On the other hand, the normal value of screening obtained for the D+D reaction in Au is U_s = 20~70 eV in Refs. [10, 14] and ~60 eV in Ref. [13]. Thus, a naive and natural question is whether the Li+D reaction in Pd is also strongly enhanced compared to Au.

The experiments were performed using a low-energy ion beam generator [1] at the Laboratory of Nuclear Science of Tohoku University, designed to produce deuteron beams with several 100 μA from 2 to 100 keV. The target used was a foil of Pd-Li alloy, which was prepared by arc melting Pd and Li as described in Ref. [8]. The atomic ratio Li/Pd obtained was 5~7% in a foil of 13×13×0.3 mm^3. A foil of

Au-Li alloy was obtained from Tanaka Metal Co. Its atomic ratio Li/Au was ~10% and the size of the foil was 20×20×1 mm^3. In addition, a 2-mm thick LiF foil was bombarded to deduce the excitation function of the ^{7}Li (d, α)^{5}He reaction as reference of non-metallic targets, since no measurement was reported so far in this low energy region. During the bombardment, the target was kept at low temperature between −80 and −70 ℃ to minimize the possible thermal diffusion of Li contained in the target alloy from the beam spot.

In order to detect α particles emitted in the ^{6,7}Li (d, α)^{4,5}He reactions, a ΔE-E counter telescope consisting of 30- and 100-μm thick Si surface barrier detectors was used. The front face of the ΔE detector was covered with a 2 μm thick Al foil to prevent electrons and scattered deuterons from hitting the detector. The counter telescope was placed at 125° to the beam direction and subtended a solid angle of 0.14 sr.

Figure.1(a) shows a scatter plot of ΔE vs. E measured during the bombardment on $AuLi_x$. Alpha particles are identified clearly as the events on a locus between the dashed lines; events A correspond to those from the ^{7}Li(d, α)^{5}He reaction and events B are from the ^{6}Li(d, α)^{4}He reaction. Events with ΔE < 400 ch were assigned as originating from the D+D reaction, in which the incident deuterons interact with the ones implanted by the beam in the target. In Fig.1(b), the projected energy spectrum of α-particles is shown, in which two peaks are clearly seen; one for the ^{6}Li(d, α)^{4}He reaction and the other for ^{7}Li(d, α)^{5}He. Although the lower energy peak of the ^{7}Li(d, α)^{5}He reaction does not possess a symmetric shape, we simply fixed the low energy side of the gate by using the same channel number of

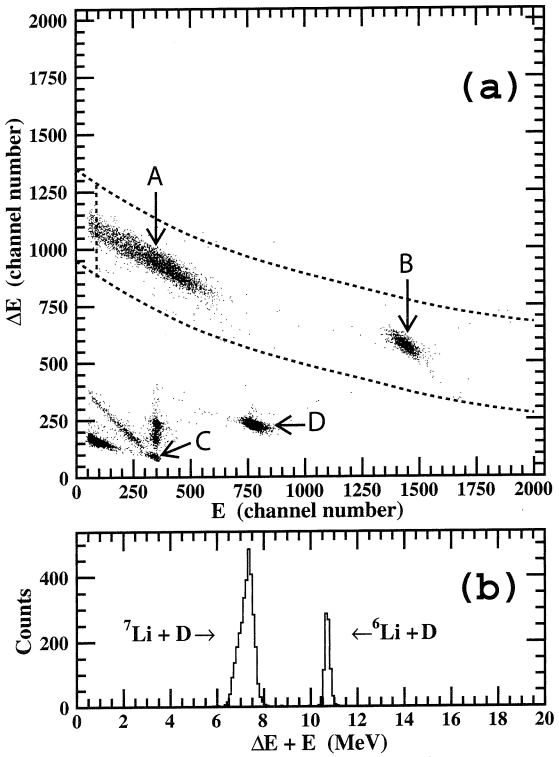

Fig.1. Measured spectra for the deuteron bombardment on $AuLi_x$; (a) two-dimensional scatter plot of ΔE vs E with α-particle events indicated between the dashed lines and (b) energy spectrum of α particles emitted in the ^{6,7}Li(d, α)^{4,5}He reaction in Au.

the E spectra for all the measurements, indicated by a vertical line in Fig.1(a).

The target Li in the metal host was present in form of an alloy, i.e., $PdLi_x$ or $AuLi_x$ with x = 0.05～0.10, and the number of Li atoms was found to decrease during the measurements. Thus, in the present work, we employed a method to obtain the relative yields; the α particle yield at 75 keV was repeatedly measured at frequent intervals to average out small fluctuations, and the yield at energy E_d was divided by the averaged yield at 75 keV measured just before and after each measurement at E_d. Figure 2 shows α-particle yields (sum yields of both channels, ^{6}Li+d and ^{7}Li+d) measured at E_d = 75 keV for the $PdLi_x$

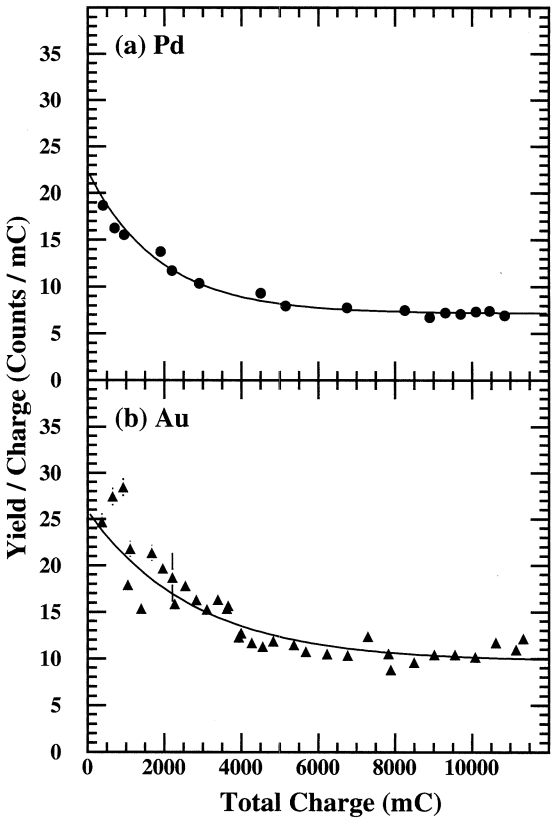

Fig.2. Summed yields of α particles emitted in the ^{6}Li+d and ^{7}Li+d reaction, measured at E_d = 75 keV for (a) $PdLi_x$ and (b) $AuLi_x$ as a function of the dose of the deuteron beam.

and $AuLi_x$ target as a function of the accumulated dose of deuteron beam. As can be seen, the yield decreases initially and becomes stable later on. For the LiF target, the yield at E_d = 75 keV was also measured frequently, although this yield remained more or less constant.

No measurement has been reported for the ^{7}Li(d, α)^{5}He reaction, so far. Thus, in the present work, the thick target yields of both the ^{6}Li(d, α)^{4}He and the ^{7}Li(d, α)^{5}He reactions were measured using LiF target. The purpose of this measurement was not to deduce the S-factor of the ^{7}Li(d, α)^{5}He reaction, but to obtain the ratio of the α-particle yield in the gate employed in the ^{7}Li(d, α)^{5}He reaction to the yield in the ^{6}Li(d, α)^{4}He reaction. Figure 3 shows results of the such measurement, i.e., the relative thick target yield for the LiF target as a function of the bombarding energy; (a) for the ^{6}Li(d, α)^{4}He reaction and (b) for the ^{7}Li(d, α)^{5}He reaction.

First, we analyze the excitation function of the ^{6}Li(d, α)^{4}He reaction. Since incident deuterons slow down in the target and the reaction can occur until the deuterons stop, the observed α-particle yield Y

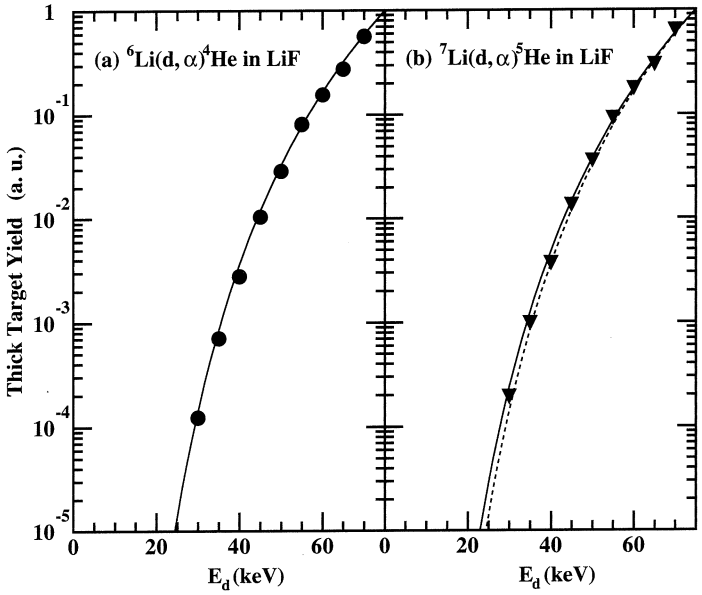

Fig.3. Relative yield of α particles emitted in the ^{6,7}Li(d, α)^{4,5}He reaction in LiF as a function of the bombarding energy of deuterons.

(E_d) at the bombarding energy E_d is given by

$$Y(E_d) = (\text{constant}) \times N_{Li} \int_0^{E_d} d\sigma_{^6Li}(E_{cm})/d\Omega_{cm} \, (d\Omega_{cm}/d\Omega_{lab}) \, (dE/dx)^{-1} \, dE. \quad (1)$$

Here, N_{Li} is the number of target Li, $d\Omega_{cm}/d\Omega_{lab}$ is the ratio of the solid angle in the center-of-mass to laboratory system, and dE/dx is the energy dependent stopping power for deuterons in LiF. Since the detector is placed at 125° with respect to the beam direction, $d\sigma_{^6Li}(E_{cm})/d\Omega_{cm}$ can be replaced as $\sigma(E_{cm})/4\pi$. For the calculation of the relative yield $Y(E_d)$ / Y(75 keV), N_{Li} cancels out. The parameterization by Anderson and Ziegler [9] is employed for the stopping power of deuterons and the S-factor in Ref. [10] is used for the cross section of the ^{6}Li(d, α)^{4}He reaction. The result of this calculation is given by the solid line in Fig.3(a). It is seen that the calculation with the standard parameter set reproduces the experimental data reasonably well.

The relative yield for the ^{7}Li(d, α)^{5}He reaction is then calculated in the same way using the cross section of the ^{6}Li+d reaction and is compared with the data. In this case, however, the calculation indicated by the dashed line in Fig.3(b) deviates increasingly from the experimental data as the bombarding energy decreases. We have measured the yield of the ^{7}Li(d, α)^{5}He reaction with a common gate setting for all the target. Thus, an effective excitation function corresponding to the present gate was deduced as the energy dependent yield function, $G_7(E) = \sigma_{^6Li}(E) \times (1.576 - 0.00712E)$, and have re-calculated the thick target yield for the ^{7}Li(d, α)^{5}He reaction by replacing $\sigma_{^6Li}(E)$ with $G_7(E)$ in Eq.(1). The result of the calculation is shown in Fig.3(b) by the solid line, which reproduces the data very well. Thus, we have obtained the standard excitation function, corresponding to the ^{7}Li(d, α)^{5}He reaction without the effect of the surroundings to be $G_7(E)$.

The results for the PdLi$_x$ and AuLi$_x$ targets are shown in Fig.4: Fig.4(a) for PdLi$_x$ and Fig.4(b) for AuLi$_x$. The upper part of Fig.4 shows the excitation functions of the ^{6,7}Li(d, α)^{4,5}He reactions relative to the yield at E_d = 75 keV. The standard calculations are carried out with Eq.(2), by using the stopping

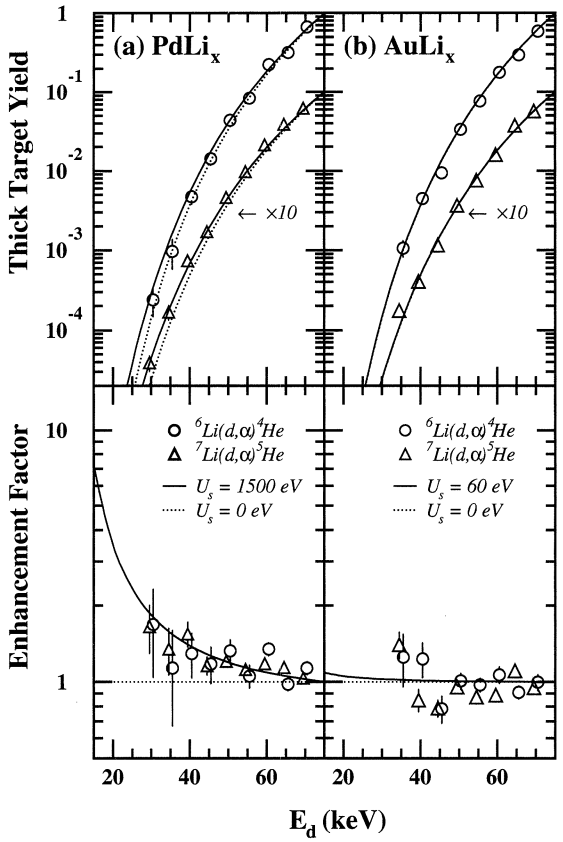

Fig.4. Relative yield of α particles emitted in the ^{6,7}Li(d, α)^{4,5}He reaction as a function of the bombarding energy of deuterons; (a) for PdLi$_x$ and (b) for AuLi$_x$. In the upper part, the data normalized to the yield at 75 keV are plotted. In the lower part, the experimental yields divided by those presented with the dotted curve are shown. The dotted curves correspond to the relative yields calculated without screening. Solid curves correspond to calculations with the screening energy indicated in each section.

power parameterized in Ref. [9] for Pd and Au together with $\sigma_{^6Li}(E)$ and $G_7(E)$. The results are plotted with dotted lines in Fig.4 (the dotted line in Fig.4(b) is covered by the solid line). Relative to the dotted line, the yield of the Li+d reaction in PdLi$_x$ is larger at the lower energies.

In the lower part of Fig.4, we plot the ratio of the experimental yields to the standard calculations in order to make the comparison easier. As seen, the reaction rate in Pd is systematically enhanced for both reactions. On the other hand, the deduced enhancement is negligibly small in Au and scatters around 1.0. In order to explain the observed enhancement, thick target yields have been calculated using the enhanced cross section with the screening energy U_s as described in Ref. [1]. The value of U_s for the ^{6}Li(d, α)^{4}He and the ^{7}Li(d, α)^{5}He reactions is searched for by fitting the experimental relative yields in Fig.4. The calculations with screening energy U_s are shown by the solid lines in the upper and lower parts of Fig.4. The results obtained are U_s = 1500±310 and 60±150 eV for the Li+d reactions in Pd and Au, respectively. The errors shown are statistical errors only. The systematic errors are considered to originate mainly from the uncertainty in the bombarding energy (±25 eV) and from fluctuations in the Li density (±100 eV) in the target.

The present work shows, for the first time, that, in the metallic environment, the size of the

screening effect in the Li+d reaction depends strongly on the metal host. The obtained value of the screening energy in Pd is about 4 times larger than those reported in Ref. [10] for the gas target and LiF target. In metals, the screening effect due to conduction electrons should also be considered. The screened electrostatic potential of the nucleus with atomic number Z existing in the sea of conduction electrons is given [11] as $\phi_s(r) = Ze/r \cdot \exp(-k_e r)$; $k_e = (6\pi e^2 n_e/E_F)^{1/2}$, n_e is the number density of electrons and E_F is the Fermi energy of the electrons. The corresponding screening energy is approximated as $U_{ce} = Ze^2 k_e$. For the Li+d reaction in Pd metal, E_F = 2.66 eV and $n_e = 1.97\times10^{22}$ cm^{-3} [12], thus U_{ce} = 61 eV is expected. The effect of the bound electron should be added, since the Li atom is considered to remain in metal in the form of Li^+. Summing up the values of the screening energy due to conduction electrons and bound electrons, we obtain a value of about 230 eV. Even if the experimental value in Ref. [10] is used for the bound electrons, the summed value is 410~480 eV. Therefore, the large screening energy of ~1500 eV obtained for the Li+D reaction in Pd cannot be due to electron screening alone.

Of particular interest is the fact that the Pd metal provides a large screening effect not only for the Li+d reaction but also for the D+D reaction (U_s = 250~310 eV [3,7] and 800 eV [6]), whereas the Au metal host does not in both cases. Thus the mechanism of enhanced screening in metal might have the same origin in the D+D and Li+d reactions. Although the enhanced screening is not fully understood, we have previously discussed the possibility that the large screening effect might originate from fluid deuterons in Pd [3,7]. If the same argument is applied to both reactions, the electrostatic potential of the nucleus with atomic number Z is also screened by mobile D^+ ions and by conduction electrons. In this case, the screened potential due to D^+ is given as $\phi_s(r) = Ze/r \cdot \exp(-k_d r)$, where $k_d = (4\pi e^2 n_d/k_B T)^{1/2}$ and n_d is the deuteron density. When we use the experimental values $n_d = 3\times10^{21}$/cm^3 [3,7] and T = 200° K, k_d = 56.5 nm^{-1} is deduced. This corresponds to the screening energy of ~240 eV for the Li+d reaction, which is similar in size to the electron screening but is still not sufficient to explain the observed screening energy. Thus, at present, we can only deduce that the enhanced screening observed in Pd depends on the atomic number Z of the implanted target nucleus; the value for implanted Li is 1.9 ~4.8 times larger than the one for implanted D, or a scaling form of $Z^{0.58\sim1.43}$.

The present work reveals a non negligible effect of the environment surrounding the nuclei on the cross section. Thus, low-energy nuclear reactions at energies far below the Coulomb barrier should be explored under various conditions, experimentally as well as theoretically.

References

[1] H. Yuki, T. Sato, T. Ohtsuki, T. Yorita, Y. Aoki, H. Yamazaki, J. Kasagi and K. Ishii : J. Phys. Soc. Jpn. **66** (1997) 73.

[2] H. Yuki, T. Sato, T. Ohtsuki, T. Yorita, Y. Aoki, H. Yamazaki and J. Kasagi : J. Phys. **G23** (1997) 1459.

[3] H. Yuki, J. Kasagi, A.G. Lipson, T. Ohtsuki, T. Baba, T. Noda, B.F. Lyakhov and N. Asami : JETP Lett. **68** (1999) 765.

[4] K. Czerski, A. Huke, A. Biller, P. Heide, M. Hoeft and G. Ruprecht : Europhys. Lett. **54** (2001) 449.

[5] F. Raiola *et al.* : Eur. Phys. J. **A13** (2002) 377.

[6] F. Raiola *et al.* : Phys. Lett. **B547** (2002) 193.

[7] J. Kasagi, H. Yuki, T. Baba, T. Noda, T. Ohtsuki and A.G. Lipson : J. Phys. Soc. Jpn. **71** (2002) 277.

[8] Y. Sakamoto, T. Hisamoto, M. Ura and R. Nakamura : J. Alloys Comp. **200** (1993) 141.

[9] H.H. Anderson and J.F. Ziegler : Hydrogen Stopping Powers and Ranges in All Elements (Pergamon, New York, 1977).

[10] S. Engstler *et al.* : Phys. Lett. **B279** (1992) 20.

[11] C. Kittel : Introduction to Solid State Physics (John Wiley & Sons, Inc., New York, 1976)

[12] M.J. Mehl and D. A. Papaconstantopoulos : Computer code STATIC (http://cst-www.nrl.navy.mil/bind/static/)

Measurement of Branching Ratio of the d+d Reaction in Metals below 12 keV

T. Shimizu[1], W. Galster[2], J. Kasagi[1], T. Hayakawa[1], H. Yonemura[1], T. Nakabayashi[1] and F. Miyahara[1]

[1]*Laboratory of Nuclear Science, Tohoku University, Mikamine, Taihaku-ku, Sendai 982-0826*
[2]*School of Engineering, Tohoku University, Aoba-ku, Sendai 980-8579*

We have measured the branching ratio of the d(d, p)^{3}He and d(d, p)t reactions in metal hosts for deuteron incident energies between 3.8 and 12.0 keV. Protons, tritons, and ^{3}He particles emitted in deuteron bombardment on Be, Ti, Pd, Sm and Au foils were observed simultaneously. We have succeeded in measuring the d+d branching ratio in several metals for the first time at such low energies. The measured cross section ratios show a dependence on the host metal.

§ 1. Introduction

Nuclear reactions at energies far below the Coulomb barrier are affected by the environment. One well-known effect is the screening of the Coulomb potential at large distances caused by electrons surrounding the interacting nuclei, resulting in an enhancement of the fusion cross section.Many authors have studied electron screening both experimentally and theoretically in order to obtain a better understanding of the underlying mechanism.

Recently, an anomalously large enhancement of the d(d, p)t reaction rate was observed in some metals, and large values of the screening energy U_e compared to D_2 gas target measurements and to theoretical predictions have been reported [1-4]. Such large values cannot be explained by a simple electron screening model but suggest the existence of important additional mechanisms, significantly increasing the fusion reaction rates in solids. In order to better understand this effect of the metallic environment, it is necessary to investigate low energy nuclear reactions in metals on various sides.

In the present work, we have measured the neutron to proton branching ratio of the d+d reaction in Be, Ti, Pd, Sm, Au at bombarding energies between 3.8 and 12 keV. As the cross section of the reaction decreases exponentially with decreasing bombarding energy, it becomes increasingly difficult to separate ^{3}He events in the d(d, n)^{3}He reaction from background events due to cosmic rays at a few tens of keV signal equivalent. Thus there are few reports on the measurement of d(d, n)^{3}He reaction yields in the low energy region. However, using thin Si detectors, the background could be reduced drastically and we have succeeded in measuring the d+d branching ratio at such low energies for the first time. In this report, the experimental technique and results are shown and the metallic environment effect is discussed.

§ 2. Experimental Procedure

The measurements were performed using the low-energy ion beam generator [5] at the Laboratory of Nuclear Science of Tohoku University. A deuteron beam of 100 μA intensity was collimated by two apertures in order to fix the beam position and size. The beam spot size at the target position was about 5 mm in diameter and deuterons were implanted continuously, while the d+d reaction was measured simultaneously.

The target host metals were commercially available high purity Be, Ti, Pd, Sm, Au foils of 100 to 250 μm thickness. During the bombardments, the targets were cooled by the liquid nitrogen and target temperature was monitored at ~120 K.

In order to simultaneously detect tritons, protons and ^{3}He emitted in the d(d, p)t and d(d, n)^{3}He reactions at low energies, 50-μm-thick Si surface barrier detectors were used. The front face of the detector was covered with a C foil of 50 μg/cm^2 thickness, to prevent elastically scattered and sputtered deuterons from hitting the detector. A negative voltage of 200 V was applied to the detector holder (including the C foil) for suppression of secondary electrons. The detector was placed at a distance of 3 cm from the target at 116° with respect to the beam direction. The target was placed towards to the detector at 50° with respect to the beam direction.

§ 3. Results and Discussion

3.1 Energy spectrum

Figure 1(a) shows a typical charged particle spectrum obtained at E_d = 8.0 keV. The three peaks shown in the figure correspond to ^{3}He-particles, tritons and protons emitted in the d+d reactions in Ti, and ^{3}He and tritons are stopped in the 50 μm detector. However, the proton in the d(d, p)t reaction has about 3 MeV, which is 3 times larger than the triton's energy. The energetic proton punches through the 50 μm detector, providing an energy loss signal of about 1 MeV, and consequently the proton peak appears just above the triton peak in the spectrum of Fig.1(a). As we consider the proton+triton sum yield, we are unconcerned even if the proton and triton peaks overlap. This spectrum was obtained in a 1 hour measurement, and Fig.1(b) shows the background spectrum obtained without deuteron beam normalized to the same measuring time. In the region of the three charged particle peaks, there is no background in the integration region. Figure 1(c) shows the spectrum after subtracting (b) from (a), and dashed lines indicate the gates of integration for ^{3}He and proton+triton events. The systematic error in the cross section ratio due to setting the gate positions is about 0.4 %. The peak close to channel zero is due to detector noise plus beam related background.

Figure 2(a) shows the charged particle spectrum obtained in Ti at E_d = 3.8 keV, which is the lowest energy in the present work. In spite of such a very low energy, the ^{3}He peak is clearly observed. It took about 56 hours to obtain this spectrum and Fig.2 (b) shows the result of a background run without deuteron beam, over the same measuring time. It is evident that there are very few background events.

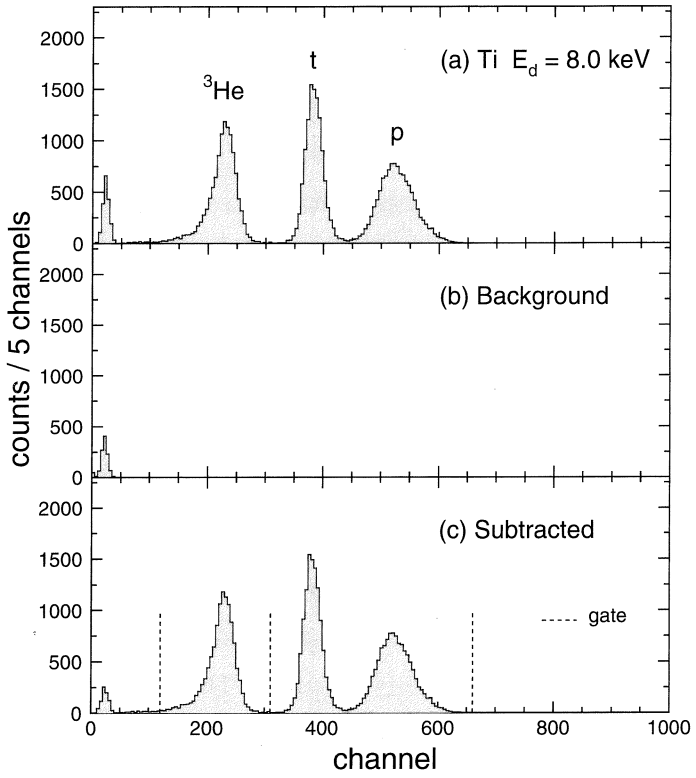

Fig.1. (a) Typical charged particle spectrum obtained for the d+d reaction in Ti at E_d = 8.0 keV. (b) Background spectrum for the same measuring time. (c) Spectrum obtained after subtracting (b) from (a). Dashed lines are event integration gates.

Figure 2(c) is the spectrum obtained after subtracting (b) from (a), and dashed lines are event integration gates.

The thick target yields, Y_{He} and Y_{p+t}, were obtained by integrating the ^{3}He and p+t events in the respective gates and by subtracting the time-normalized background events.

3.2 Cross section ratio

We have obtained the cross section ratio, $R = \sigma_n / \sigma_p$, from the measured ^{3}He and p+t yields, where σ_n and σ_p correspond to the d(d, n)^{3}He and d(d, p)t reaction cross section, respectively. As the deuteron energies in this experiment are low enough, angular distributions are expected to be isotropic [6]. Thus the cross section ratio R is obtained after correcting the measured yield ratio $2Y_{He}/Y_{p+t}$ for the solid angle ratio in the center-of-mass/laboratory system.

Figure 3 shows the result of cross section ratios in different metals, as a function of incident energy. The data points are the results of a weighted average of all runs with one standard deviation error in the incident energy range of $E_d \leq 5$ keV, $5 < E_d \leq 6$ keV, $6 < E_d \leq 7$ keV, ..., $11 < E_d \leq 12$ keV. Dashed lines are the results of fitting with a linear function in E_d. The cross section ratio data in Ti are consistent with those of Greife *et al.* [7] within the quoted errors.

3.3 Host metal dependence of cross section ratio

It is seen in Fig.3 that the cross section ratio in metals shows systematic differences, in particlular Ti and Au data exhibit different trends from other metals. That is, the branching ratio of the d+d reactions depends on the metallic environment, where the reactions between implanted and beam

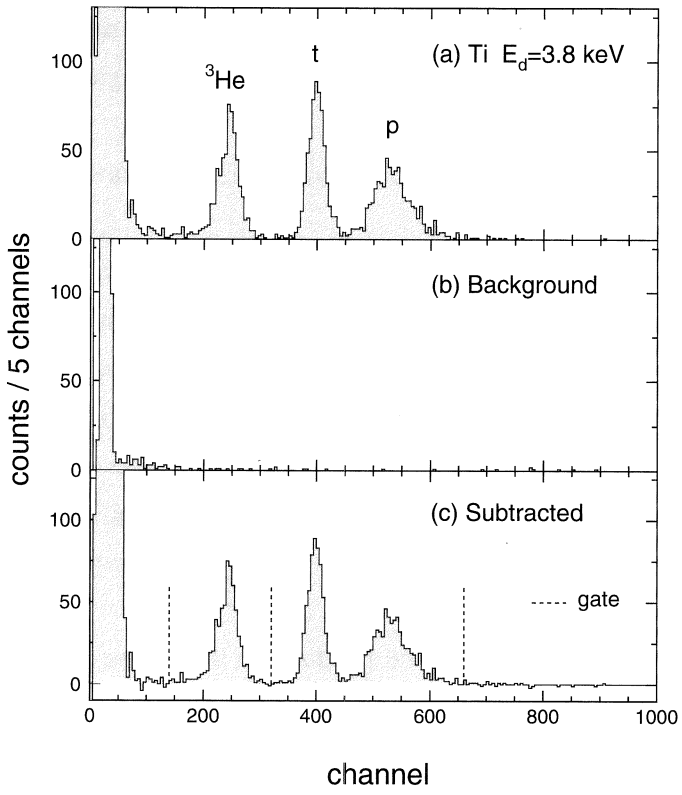

Fig.2. (a) Charged particle spectrum obtained for the d+d reaction in Ti at E_d = 3.8 keV. (b) Background spectrum without deuteron beam for the same measuring time. (c) Spectrum obtained after subtracting (b) from (a). Dashed lines are event integration gates.

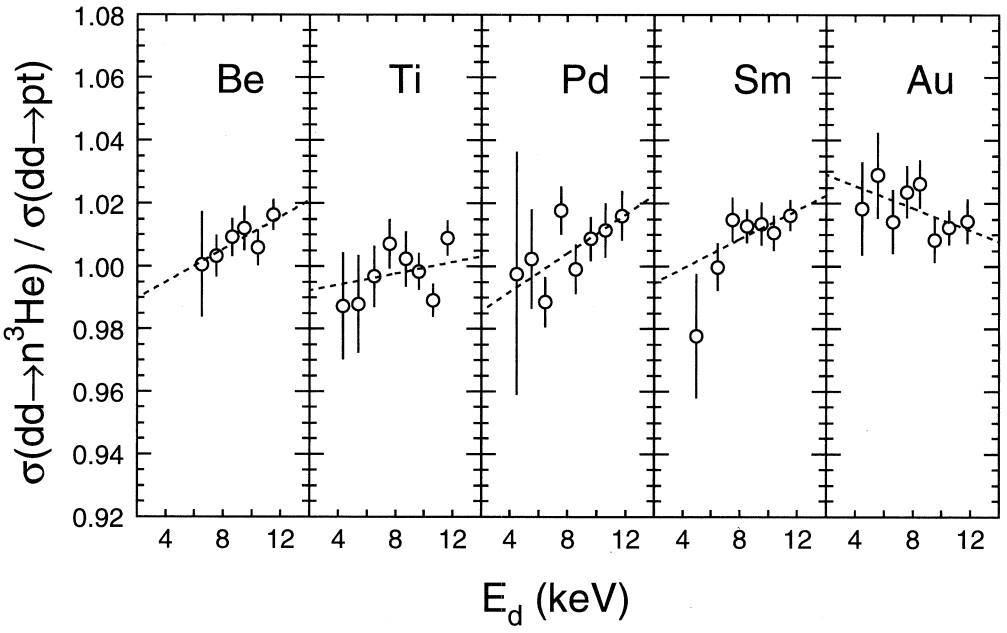

Fig.3. Cross section ratio of the d(d, n)^{3}He and d(d, p)t reactions in metals as a function of incident energy. Dashed lines are the results of fitting with a linear function in E_d.

particles occur.

Fitting the cross section ratio data in metals with linear functions in incident energy (as shown in Fig.3 by dashed lines), we have obtained the result that the cross section ratios in Be, Pd and Sm exhibit the same trends, and the averaged fitting function at low energies is given by

$$R=0.985+2.66\times10^{-3}E_{\mathrm{d}}, \tag{1}$$

whereas, the ratios in Ti and Au deviate significantly with higher than 99% confidence level from the trend described by eq. (1).

The study of muon catalyzed fusion provides a hint at how one might be able to explain this effect of the host environment. Petitjean *et al.* [8] reported on branching ratio measurements of muon catalyzed d+d reactions under different environment below room temperature. It is observed that the cross section ratio is about 1.4 for angular momentum $J = 1$, and about 0.8 if $J = 0$. In the d+d fusion reaction this $J = 1$ state corresponds to fusion with negative parity and $J = 0$ to fusion with positive parity. It is conceivable that metallic environments act differently on the incoming wave function of d+d and affect the parity before the fusion reaction takes place. Then the branching ratio varies in different metal host materials.

We are continuing the measurement of the d+d reaction branching ratio in different host materials to obtain a better understanding of the mechanism.

3.4 *S*(*E*) factor of d(d, n)^{3}He reaction

The astrophysical $S(E)$ factor of the d(d, p)t reaction at low energies has been studied by many authors, on the other hand, there are very few reports of $S(E)$ of the d(d, n)^{3}He reaction at low energies, due to the difficulty of measuring the ^{3}He yields. In the present work, we have obtained the cross section ratio data at very low energies with high precision. Thus we can deduce the parameters for the $S(E)$ factor of the d(d, n)^{3}He reaction from our data at low energy and compare to compilations, which extracted the ratio from cross sections measured at relatively high energies.

The cross section ratio data we used for this analysis are the results of D_2 gas target experiments from Krauss *et al.* [6] (E_{d} = 13.3 - 325 keV) and Greife *et al.* [7] (E_{d} = 29.7 - 256 keV). As the screening potential energy in Ti is very low, like in a gas target [1, 4], we also used the data from Greife *et al.* [7] (E_{d} = 4.8 - 26.2 keV in Ti) and our own experimental results in Ti (E_{d} = 3.8 - 11.9 keV). Our data have been weight averaged in energy steps of 0.5 keV. Further, we added the CD_2 target data from Cecil *et al.* [10] (E_{d} = 6 - 30 keV) and fitted the experimental data using a quadratic energy dependence:

$$R=\frac{\sigma_{\mathrm{n}}(E)}{\sigma_{\mathrm{p}}(E)}=\frac{S_{\mathrm{n}}(E)}{S_{\mathrm{p}}(E)}=\frac{a+bE+cE^2}{S_{\mathrm{p}}(E)}, \tag{2}$$

where $S_{\mathrm{n}}(E)$ and $S_{\mathrm{p}}(E)$ are the astrophysical $S(E)$ factors of the d(d, n)^{3}He and d(d, p)t reaction, respectively. E indicates the energy in the center-of-mass system. The astrophysical $S(E)$ factor is a weakly energy dependent function proportional to the cross section. As the d(d, p)t reaction has been studied extensively and there are much more data at low energies with good precision, compared to the d(d, n)^{3}He reaction, we adopted the recently reported $S_p(E)$ of Barker [11] as a known function:

$$S_{\mathrm{p}}(E)=57.8+0.0219E+1.066\times10^{-3}E^2 \ \ (\mathrm{keV\cdot b}). \tag{3}$$

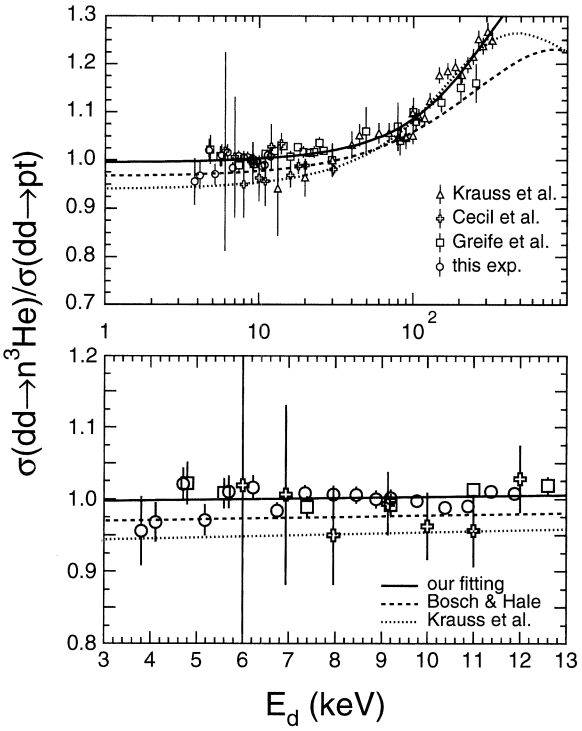

Fig.4. The results of fitting to the experimental branching ratios. Triangles, crosses, squares, and circles are the data from Krauss *et al.* [6], Cecil *et al.* [10], Greife *et al.* [7], and from our experiment (in Ti), respectively. The solid line indicates the result of fitting in the present work, dashed and dotted lines are from Bosch and Hale [9] and Krauss *et al.* [6], respectively. The low energy region is shown in linear scale.

The $S_p(0)$ = 57.8 keV·b of Barker [11] is slightly higher than the $S_p(0)$ = 56 keV·b of the NACRE compilation [12], which includes a fit to data at relatively high energies, E_d > 1 MeV. The $S_n(E)$ was obtained from fitting the experimental data:

$$S_p(E)=57.5+0.1160E+1.417\times10^{-3}E^2 \quad (\text{keV}\cdot\text{b}). \tag{4}$$

x^2 = 99.7, with a number of degrees of freedom of 75.

The result is shown by the full line in Fig.4. The experimental branching ratios are plotted as a function of deuteron incident energy. Triangles, crosses, squares, and circles are the data from Krauss *et al.* [6], Cecil *et al.* [10], Greife *et al.* [7], and from our experiment (in Ti), respectively. The solid line indicates the result of fitting in the present work, dashed and dotted lines are from Bosch and Hale [9] and Krauss *et al.* [6], respectively. The expanded low energy region of Fig.4 is shown in linear scale. The fit of the branching ratio using our parameters reproduces the data well from 4 to 300 keV.

The accurate determination of $S_n(E)$, based on experimental data at very low energies constitutes a significant improvement over previous data and we expect that $S_n(E)$ plays an important role in understanding the d+d reaction in different environments at ultra-low energies.

References

[1] H. Yuki *et al.* : JETP Lett. **68** (1998) 823.

[2] J. Kasagi *et al.* : J. Phys. Soc. Jpn. **71** (2002) 2881.

[3] K. Czerski *et al.* : Europhys. Lett. **54** (2001) 449.

[4] F. Raiola *et al.* : Phys. Lett. B **547** (2002) 193.

[5] H. Yuki *et al.* : J. Phys. Soc. Japan **66** (1997) 73.

[6] A. Krauss *et al.* : Nucl. Phys. A **465** (1987) 150.

[7] U. Greife *et al.* : Z. Phys. A **351** (1995) 107.

[8] C. Petitjean *et al.* : Hyp. Interact. **118** (1999) 127.

[9] H.S. Bosch and G.M. Hale, Nucl. Fusion **32** (1992) 611.

[10] F.E. Cecil *et al.* : Phys. Rev. C **47** (1993) 1178.

[11] F.C. Barker : Nucl. Phys. A **707** (2002) 277.

[12] C. Angulo *et al.* : Nucl. Phys. A **656** (1999) 3.

(LNS Experiment : #2465)

Experimental Study of Photonuclear Reactions of ^{4}He below Pion Threshold

T. Shima[1], N. Maehara[1], K. Takahisa[1], Y. Nagai[1], H. Makii[1], K. Maeda[2], T. Kobayashi[2], H. Ohtsu[2], H. Kanda[2], K. Abe[2], K. Hirose[2], Y. Yamaguchi[2], Y. Matsuda[2], Y. Seki[2], T. Terasawa[3], T. Tamae[3], T. Ohtsuki[3], M. Inoue[3] and Y. Hayashi[3]

[1]*Research Center for Nuclear Physics, Osaka University, 10-1, Mihogaoka, Ibaraki 567-0047*
[2]*Department of Physics, Tohoku University, Aramaki, Aoba, Sendai 980-8578*
[3]*Laboratory of Nuclear Science, Tohoku University, 1-2-1, Mikamine, Taihaku, Sendai 982-0826*

An experimental method for the precise measurement of the photonuclear reactions of ^{4}He below the pion threshold has been tested. We used a tagged photon beam and a time projection chamber containing helium gas, which served as an active target. It was proved that the chamber could successfully detect the tracks of the charged particles from the photonuclear reactions in a high radiation level due to the irradiation of a high-intensity photon beam. It was found that the background was mainly due to the noise of the chamber, and could be suppressed by taking coincidence of the signals from the chamber and the tagging counter.

§ 1. Introduction

The photonuclear reactions of ^{4}He provide important information on basic properties of the nuclear force as well as the dynamics of few-nucleon systems. For example, the self-conjugate ^{4}He nucleus is supposed to have a giant-dipole resonance (GDR) state with a pure $T = 1$ component at around the excitation energy of 20～30 MeV, and the cross sections of the ^{4}He(γ,p)^{3}H and ^{4}He(γ,n)^{3}He reactions should be almost equal, if there is no effect of the charge symmetry breaking (CSB) in nuclear forces. Therefore, the precise comparison of the ^{4}He(γ,p)^{3}H cross section and the ^{4}He(γ,n)^{3}He cross section can be used as a stringent test of the nuclear charge symmetry [1]. For that purpose the photonuclear reactions of ^{4}He in the GDR energy region have been studied extensively both experimentally and theoretically. However, the previous experimental data have been in severe discrepancy, and that has caused a long-standing problem as described below. Namely, most of the old experimental data [2－8] suggested the ^{4}He(γ,p)^{3}H and ^{4}He(γ,n)^{3}He cross sections had the maximum values of 1.5～2 mb and 1～1.5 mb near E_γ= 25 MeV, respectively. From those data, Calarco *et al.* recommended the ratio R_γ of the (γ,p) cross section to the (γ,n) cross section of 1.7±0.2 [9], which implied an extremely large effect of CSB. Those data were supported by a theoretical calculation based on the resonating group method (RGM) [10]. However, later measurements of ^{4}He(γ,n)^{3}He [11], ^{3}He(n,γ)^{4}He [12,13], ^{4}He(γ,p)^{3}H [14] and ^{3}H(p,γ)^{4}He [15] gave rather small cross sections of ～1.1 mb for both (γ,p) and (γ,n) reaction channels, and leaded to the value of R_γ near unity. Those new data were supported with a new

theoretical calculation by Unkelbach and Hofmann [16], which took into account the contributions of meson-exchange currents (MEC) beyond Siegert's theorem by using Ohta's method [17] together with the refined RGM. Therefore, the anomalous CSB effect seemed to be ruled out at that time. But the problem revived with the later experiments on ^{4}He(γ,p)^{3}H [18] and ^{3}H(p,γ)^{4}He [19], which give the cross sections as large as about 1.8 mb in the region of E_γ = 25～30 MeV. In addition, the total photoabsorption cross section of 2.86±0.12 mb has been obtained at E_γ= 25～26 MeV from the elastic photon scattering measurement [20]. Since the contributions from the reactions other than two-body channels are supposed to be small enough in this energy region, the total cross section is not consistent with the sum of the (γ,p) and (γ,n) cross sections around 1.1 mb. Recently, Efros *et al.* applied a new theoretical method, called the Lorentz integral transform, and succeeded in performing the calculation for the E1 photoabsorption cross section of ^{4}He, fully taking into account the effects of the final-state interaction (FSI) [21]. They claimed that the peak energy of the cross section should be at around 30 MeV, rather than the previously adopted value of about 25 MeV. Also they pointed out that the integrated cross sections obtained from the previous data and calculations exhaust only 60% of the value expected from the E1 sum rule. On the other hand, their calculation is consistent with the sum rule. To solve the above problems, a more precise experiment on the photonuclear reactions of ^{4}He will be demanded. In addition to the importance of the photonuclear reactions of ^{4}He in nuclear physics, they also play crucial roles in astrophysics. It is known that the radiative capture processes of light nuclei play crucial roles in the big-bang nucleosynthesis [22], and the information about the photonuclear reactions of ^{4}He at low energies are useful to establish microscopic theories for those processes. The photonuclear reaction of ^{4}He can be applied to investigate analogous processes of ^{4}He caused by the weak interaction [23] like the ^{3}He(p,$e^+\nu_e$)^{4}He and ^{4}He(ν,ν') reactions, which are relevant to the solar *hep* neutrino production [24] and the stellar nucleosynthesis by r-process in neutrino-driven wind [25], respectively.

For the above reasons, recently we have started a new experiment on the photonuclear reactions of ^{4}He by means of a real photon beam and a time projection chamber (TPC). We have already measured the cross sections in the region of E_γ from 22 MeV to 32 MeV, and the result was in nice agreement with the recent theoretical calculations. But the integrated total cross section below E_γ= 32 MeV was about 30% smaller than the value expected from the E1 sum rule. Therefore, it is quite interesting to make a systematic measurement up to higher energies in order to search for the missing transition strength. For that purpose we planned a new measurement using the tagged photon beam at LNS, Tohoku University. The present work was aimed at an experimental check for stable operation of TPC and the possible backgrounds under high radiation environment due to a high-energy (up to 120 MeV) and high-intensity (up to a few 10^6 photons/s) incident γ-ray beam.

§ 2. Experimental Method

The experiment was performed at the BL-V beam line at the Laboratory of Nuclear Science (LNS) of Tohoku University. The experimental set up is schematically shown in Fig. 1. For the γ-ray beam we employed the LNS tagged photon beam. The γ-ray beam impinged upon the ^{4}He gas target contained

in TPC, and caused photonuclear reactions. The charged particles emitted from the reactions were detected with TPC. To obtain the timing signal for measurement of the drift times in TPC, the trigger counters (TR) made of 30mm thick plastic scintillators were installed on four side walls of TPC [26]. The timing signals from TR were also used to determine the γ-ray energies event by event, by taking coincidence with the tagging counters (TAG). The details of the experimental method are described in the following.

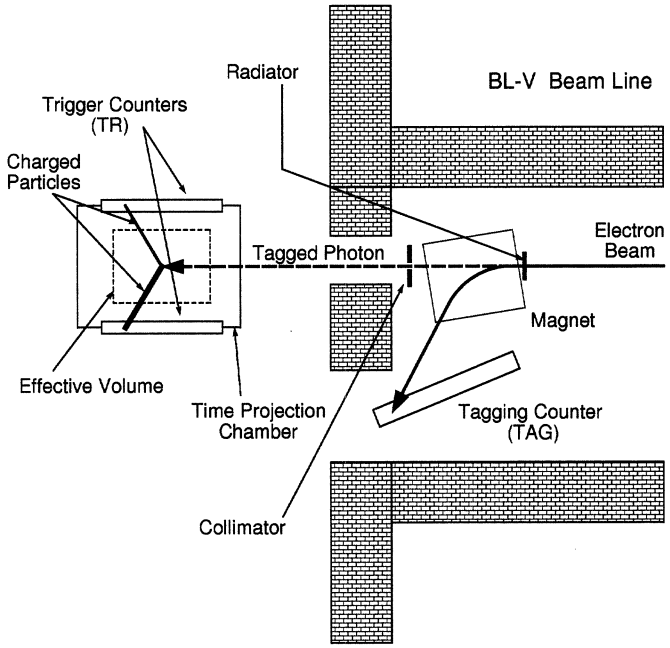

Fig.1. Experimental set up for ^{4}He photodisintegration measurement. The long-dashed line indicates the path of the tagged photon beam.

2.1 Tagged photon beam

The tagged photons were generated via the bremsstrahlung process of the 150 MeV electron beam on a 10 μm thick platinum target, where the primary electron beam was provided from the stretcher-booster ring at LNS, Tohoku University [27]. The energy range of the tagged photons was from 30 MeV to 120 MeV. The average intensity of the photon beam was 2×10^5 photons/s.

2.2 ^{4}He target and time projection chamber

The reaction events were detected with TPC filled with a mixture of 80% natural He gas and 20% CD_4 gas, where the ^{4}He nuclei contained in the counter gas were used as the target. This method has following advantages;

i) Since TPC serves as an active target, an acceptance of 4π and a detection efficiency of nearly 100% are achieved.

ii) TPC has a capability of measuring the track shapes and the energies of the charged particles produced in the reactions, and such information is useful for identification of the reaction events and rejection of backgrounds.

iii) The angular distributions and asymmetries of the emitted particles can be measured, and thus the transition strengths can be determined accurately depending on multipolarities and parities of the transitions.

TPC has an sensitive volume of 120 mm(W)×120 mm(H)×250 mm(D). The electrons ionized by the passage of a charged particle are drifted along the direction of the depth of TPC. The tagged photon beam was injected in the central axis of TPC along the drift direction. The effective depth of TPC was defined so that the detection efficiency ε of TPC was better than 99%, and actually it was 200 mm. The effective thickness of the ^{4}He target was determined from the temperature and the pressure of the counter gas, which were monitored during the measurement. The temperature and the pressure of the counter gas were in average 19.9±0.1 ℃ and 430±2 Torr, respectively. Thus the effective thickness of ^{4}He was determined as $(1.13\pm0.02)\times10^{-5}$ atoms/b. The spatial resolutions of TPC were 2 mm for directions parallel to and perpendicular to the photon beam axis. To monitor the response of TPC during the experiment, an α-ray source (^{241}Am) was installed at the head of the drift region.

2.3 Data acquisition system

The data acquisition was performed by using standard NIM and CAMAC circuits. The signals from the cathode wires were amplified, and converted to logic signals with discriminators. Those logic signals were sent to 32channel multi-hittable TDC's (LeCroy 2277), and were used to measure the drift times of the ionized electrons. The signals from the anode wires were summed, and their pulse shapes were recorded with 100 MHz flash ADC's (REPIC RPC-081). The summed anode signals were also discriminated and converted to anode-logic signals. The pulse heights and the timings of the signals from TR were recorded with current-sensitve ADC's (LeCroy 2249W) and TDC's (LeCroy 2228), respectively. The timing signals from TAG were recorded with TDC's (LeCroy 2228). The data acquisition was carried out when an anode-logic signal of TPC and a signal of TR were obtained in coincidence within a time interval of 70 μs, which was chosen to be sufficiently longer than the maximum drift time of TPC (~40 μs). The data from the CAMAC modules were acquired by an IBM-AT personal computer with the Linux operating system. For the CAMAC device driver, we employed the UNIDAQ system [28].

§ 3. Result

3.1 Event selection and background

With the above trigger condition for the data acquisition, 401,638 events were acquired as the raw data during the measurement time of 42,300 s. To select the candidates of the true events of the photonuclear reactions, we rejected the events in which the signals of TR and TAG were not detected in coincidence within the time width of 100 ns. Here the time width of 100 ns for the coincidence condition was defined from the distribution of the time difference between TR and TAG. 19,975 events survived after this requirement, and then those events were inspected event by event, by checking the tracks of the charged particles emitted by the reactions. The events could be categorized to seven types as listed in Table 1. Figures 2(a)~(g) show the examples of the tracks of the events of Type-1~7, respectively.

In Fig. 2, tracks are indicated as the areas surrounded by dots, which correspond to the timing of the drift electrons in TPC. Here, the pulses from the cathode wires of TPC were converted to logic signals with the discriminators, and both the leading edge and the trailing edge of the logic signals were recorded with TDC's. Therefore, the width of a track along the drift direction is correlated to the energy loss of the particle in TPC. Using such information, we made event identification as follows. The events of Type-1 is considered to be caused by the accidental coincidence of the noise of TPC and TAG, because no track of the charged particles from photonuclear reactions was observed. Type-2 is an α particle from the α-ray source, since the track is originated from the position of the α-ray source. Type-3 is possibly an event of $^{4}He(\gamma,n)^{3}He$, $^{4}He(\gamma,p)^{3}H$ or $^{4}He(\gamma,pn)^{2}H$ at relatively high excitation energy,

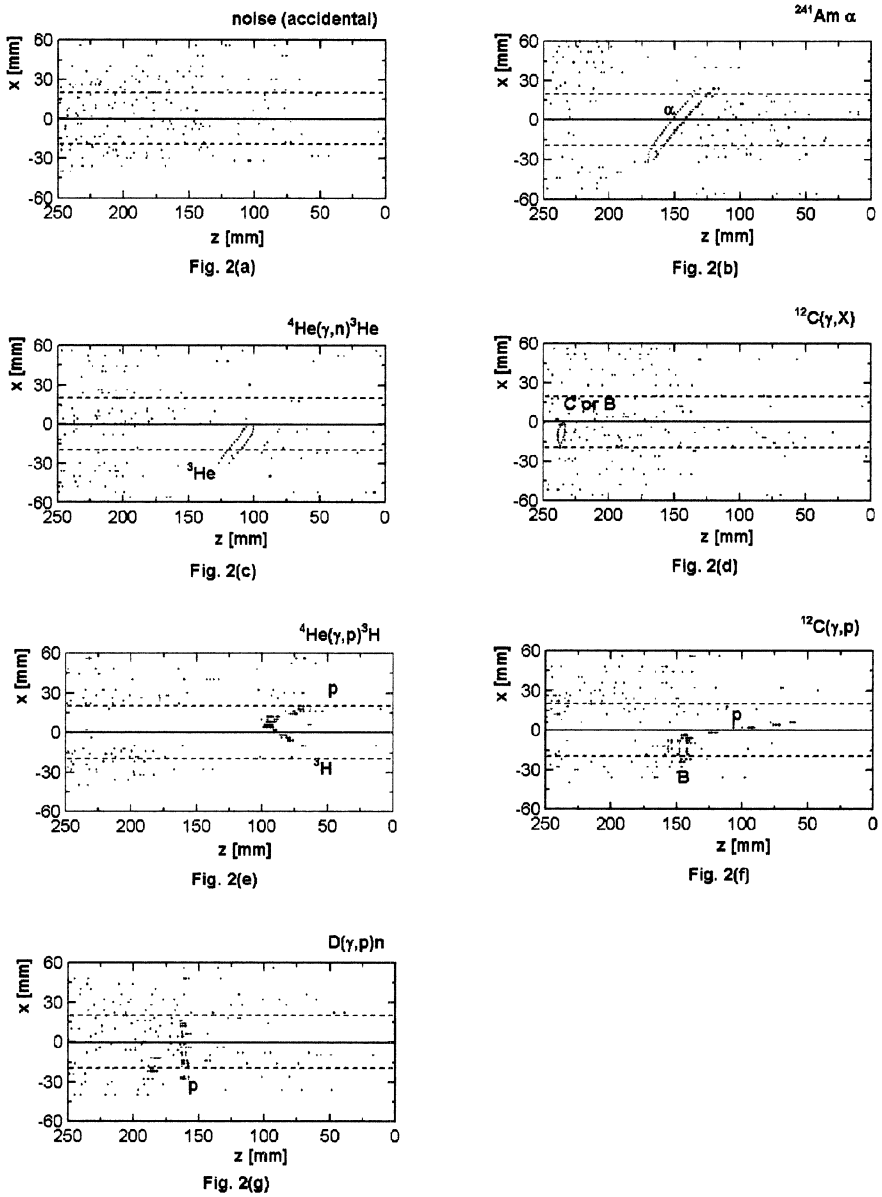

Fig.2. Examples of the observed tracks. The rectangular frames indicate the side view of the active volume of TPC. The photon beams come from the left ; (a) accidental noise, (b) α-ray from ^{241}Am source, (c) $^{4}He(\gamma,n)^{3}He$, $^{4}He(\gamma,p)^{3}H$ or $^{4}He(\gamma,pn)^{2}H$, (d) $^{12}C(\gamma,p)^{11}B$ or $^{12}C(\gamma,n)^{11}C$, (e) $^{4}He(\gamma,p)^{3}H$ or $^{4}He(\gamma,pn)^{2}H$, (f) $^{12}C(\gamma,p)^{11}B$, and (g) $^{2}H(\gamma,p)n$.

because only one track with a medium width can be found. Here, photoneutrons and photoprotons with small energy losses cannot be detected, because TPC is insensitive to them. With the similar consideration, Type-4 can be attributed to ^{11}C or ^{11}B from the photodisintegration of ^{12}C. Type-5 is a candidate of $^{4}He(\gamma,p)^{3}H$ or $^{4}He(\gamma,pn)^{2}H$. Type-6 and Type-7 are identified as (γ,p) reactions of ^{12}C and ^{2}H, respectively. Table 1 shows the number of events of Type-1～7.

The present result shows that the main background is caused by the accidental coincidence of the noise of TPC and TAG, and they can be identified and rejected by checking the track shape.

Table 1. Number of events of Type-1～7.

Event type	Number of events
Total	19,975
Type-1	17,930
Type-2	2,000
Type-3	36
Type-4	3
Type-5	3
Type-6	2
Type-7	1

Table 2. Trigger rate and dead time of data acquisition.

γ-ray intensity [photons/s]	Trigger rate [counts/s]	Dead time [%]
1×10^{6}	230	85.9
2.5×10^{5}	13.7	26.6
1×10^{4}	5.9	13.3

3.2. Trigger rate and dead time of data aquisition

To check the efficiency of the data acquisition of the present experimental system, the dead time of the system was measured as a function of the photon beam intensity, as shown in Table 2. Therefore, to make an effective measurement with the photon intensity as high as 10^{6} photons/s, the trigger rate should be decreased to about 10 counts/s. That can be achieved by requiring the coincidence of TPC, TR and TAG at the hardware level.

§ 4. Summary

In this work, the feasibility of the present experimental method was examined. We could observe the tracks of the particles emitted by the photonuclear reactions of ^{4}He, ^{12}C and ^{2}H successfully even under high radiation environment due to a high-intensity incident photon beam. The background is mainly due to the accidental coincidence between the noise signals of TPC and TAG. By requiring the coincidence of TPC, TR and TAG for the trigger condition, most of such background events can be rejected, and the efficiency of the data acquisition of ～80% can be achieved with the photon beam intensity of $\sim10^{6}$ photons/s. With the present result, we can expect our experimental method will be useful for the precise measurement of the photonuclear reactions of ^{4}He.

Acknowledgment

The authors are grateful to all the staffs of LNS of Tohoku University for their cooperation. This work was supported Grant-in-Aid for Scientific Research of the Japan Society for the Promotion of Science (JSPS).

References

[1] F.C. Barker and A.K. Mann: Philos. Mag. **2** (1957) 5.

[2] C.C. Gardner and J.D. Anderson: Phys. Rev. **15** (1962) 626.

[3] D.S. Gemmell and G.A. Jones: Nucl. Phys. **33** (1962) 102.

[4] W.E. Meyerhof, M. Suffert and W. Feldman: Nucl. Phys. **A148** (1970) 211.

[5] J.D. Irish: Phys. Rev. **C8** (1973) 1211.

[6] C.K. Malcom, D.V. Webb, Y.M. Shin and D.M. Skopik: Phys. Lett. **47B** (1973) 433.

[7] J.D. Irish *et al.* : Phys. Rev. **C8** (1973) 1211.

[8] R.C. McBroom *et al.* : Phys. Rev. **C25** (1982) 1644.

[9] J.R. Calarco *et al.* : Phys. Rev. **C28** (1983) 483.

[10] B. Wachter, T. Mertelmeier and H.M. Hofmann: Phys. Rev. **C38** (1988) 1139.

[11] B.L. Berman, D.D. Faul, P. Meyer and D.L. Olson: Phys. Rev. **C22** (1980) 2273.

[12] L. Ward *et al.* : Phys. Rev. **C24** (1981) 317.

[13] R.J. Komar *et al.* : Phys. Rev. **C48** (1993) 2375.

[14] R. Bernabei *et al.* : Phys. Rev. **C38** (1988) 1990.

[15] G. Feldman *et al.* : Phys. Rev. **C42** (1990) 1167.

[16] M. Unkelbach and H. M. Hofmann: Nucl. Phys. **A549** (1992) 550.

[17] K. Ohta: Nucl. Phys. **A495** (1989) 564, Phys. Rev. **C39** (1989) 2302.

[18] L. Van Hoorebeke *et al.* : Phys. Rev. **C48** (1993) 2510.

[19] K.I. Hahn, C.R. Brune and R.W. Kavanagh: Phys. Rev. **C51** (1995) 1624.

[20] D.P. Wells *et al.* : Phys. Rev. **C46** (1992) 449.

[21] V.D. Efros, W. Leidemann and G. Orlandini: Phys. Rev. Lett. **78** (1997) 4015.

[22] M.S. Smith, L.H. Kawano and R.A. Malaney: Astrophys. J. Suppl. **85** (1993) 219.

[23] H. Ejiri: Phys. Rep. **338** (2000) 265.

[24] L.E. Marcucci *et al.* : Phys. Rev. Lett. **84** (2000) 5959.

[25] R.I. Epstein and S.A. Colgate: Phys. Rev. Lett. **61** (1988) 2038.

[26] N. Maehara: Master thesis, Osaka University (2003).

[27] K. Maeda *et al.* : Nucl. Instr. Meth. A, in press.

[28] Y. Yasu *et al.* : IEEE Trans. Nucl. Sci. **43** (1996) 9.

The 1.2 GeV Photon Tagging System (STB-Tagger) at LNS-Tohoku

H. Yamazaki[1], T. Kinoshita[1], K. Hirota[1]*,T. Katsuyama[1], T. Itoh[1], A. Katoh[1]†, T. Nakabayashi[1], T. Shimizu[1], J. Kasagi[1], T. Takahashi[2], K. Maeda[2] and O. Konno[3]

[1]*Laboratory of Nuclear Science, Tohoku University, Mikamine, Taihaku-ku, Sendai 982-0826*
[2]*Department of Physics, Tohoku University, Aoba-ku, Sendai 980-8577*
[3]*Ichinoseki National College of Technology, Takanashi, Hagisho, Ichinoseki-shi 021-8511*

We have constructed a tagged photon beam line in the STB ring at Tohoku University. The quasi-monochromatic photon beam is produced by the internal photon tagging system (STB Tagger) which consists of a solid fiber radiator and the compact tagging counter installed in a bending magnet of the STB ring. The energy range of the tagged photon is from 2/3 E_0 to 11/12 E_0 with the electron energy of E_0.

§ 1. Introduction

At an earliest stage of the nuclear physics, the photon-induced nuclear reactions were studied by the bremsstrahlung photon beams. The bremsstrahlung photons have the continuous energy spectrum. Thus, it is impossible to determine the energy of the induced photon event by event. In order to produce the monochromatic or quasi-monochromatic photon beam, the photon tagging method has been widely used. The energy of the photon E_γ is given by the difference between the incident electron energy E_0 and the recoil electron energy E' : $E_\gamma = E_0 - E'$.

Recently a 1.2 GeV electron synchrotron called STretcher-Booster-Ring (STB-ring) has been in operation at Laboratory of Nuclear Science (LNS), Tohoku University [1]. The electrons with a maximum energy of 1.2 GeV are appropriate to study the hadron structure in the second resonance region in nuclei. Thus, the systematical studies of hadron structures in nuclei are started with the STB ring through the meson photoproduction on nuclear targets. To cover interesting nucleon resonances, the maximum photon energy of 1 GeV is necessary and the determination of the incident photon energy is essential. So, the internal bremsstrahlung tagging method with the solid fiber radiator was employed to produce the photon beam from the circulating electrons. By using the solid radiator, it is possible to make multi tagged photon beam lines in one storage ring, for example as shown in Fig. 1.

The required performance of the photon tagging system is listed as follows. First, the energy resolution of the tagged photons must be less than at least 30 MeV at 1 GeV photon energy. The widths of nucleon resonances in the second resonance region are a few hundred MeV/c^2, so it is desirable that

*Present address ; Japan Synchrotron Radiation Research Institute (JASRI),Sayo-gun, Hyogo 679-5198 Japan
†Present address ; Japan Cycle Development Institute, Tokai-mura, Igaraki 319-1194 Japan

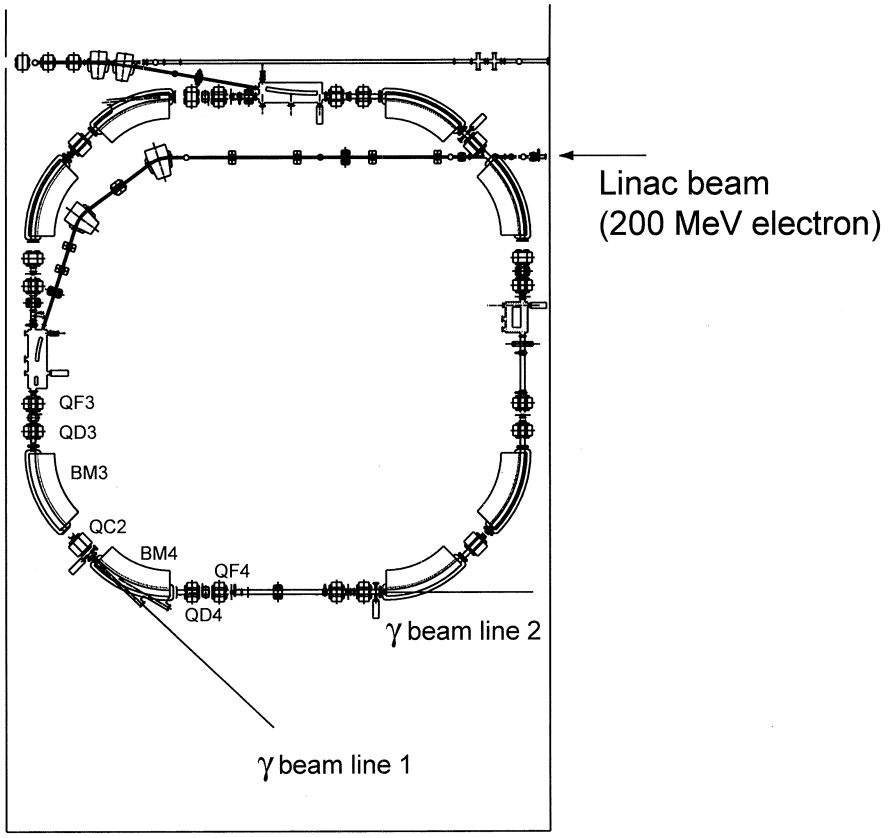

Fig.1. Layout of the STB ring in LNS, Tohoku University.

the energy resolution of the photon is a few times smaller than the resonance width. Second, the fluctuation of the photon intensity must be less than 40%, because the chance coincidence rate should be controlled low enough. Third, the tagged photon intensity must be more than 3×10^6 per second, because the cross section of the N^* formation by the photon is not so large compared with the hadronic reactions. To satisfy these requirements, we constructed the internal photon tagging system (STB Tagger), which consists of the solid fiber radiator, the compact tagging counter installed in the bending magnet.

In this report, the performance of the STB tagger and the characteristics of the tagged photon beam will be described.

§ 2. 1.2 GeV Stretcher-Booster Ring at LNS

The STB-ring is an electron synchrotron with a maximum energy of 1.2 GeV. The layout of the STB ring is shown in Fig. 1. The circumference of the STB is 49.7m. The electron beam with an energy of 200 MeV is injected into the STB from a linac and accelerated up to 1.2 GeV in about 1.2 second. The energy of the electron beam at the stored phase can be selected from 0.2 GeV to 1.2 GeV according to the experimental conditions. The duration of the energy flat top can be varied on demand. Although the maximum circulating current is about 40 mA, the typical operation current is about 10 mA from the limitation of the tagging counters. The natural emittance of the electron at 1.2 GeV is 200 nmrad. The typical size of the electron beam is about 1.0 mm and a beam divergence is about 0.7 mrad (r.m.s.) at the radiator position.

§ 3. Tagging Spectrometer

As shown in Fig. 1, a quarter of the STB ring consists of 7 magnets; BM3,4, QC2, QD3,4 and QF3,4. The STB Tagger consists of a movable carbon fiber radiator, compact tagging counters and a bending magnet (BM4) in the STB ring, which is used as the tagging spectrometer. The photon production radiator is inserted into the electron beam orbit and produces the bremsstrahlung photon duning the flat top period. The momentum of the recoil electron is analyzed in the magnetic field of BM4. An energy of the photon is determined as the energy difference between the incident and the recoil electron.

3.1 Radiator system

The radiator system in the STB-ring is placed between BM4 and QC2. It is placed at 32.5 cm from the entrance of BM4. The radiator were made from carbon fiber, which is mounted on the aluminum frame. The aluminum frame is connected with a moving rod, which is driven with a 5-phase pulse stepping motor. The diameter of the carbon fiber is 11 μ m, which is about 100 times smaller than the beam size. The electron current passed through the radiator, which is proportional to the beam density there, can be controlled by changing the radiator position. The carbon fiber was fabricated by Kureha Chemical Industry Co. from the pitch. The pitch made carbon fiber has an almost zero coefficient for thermal expansion, though the normal fibers, which are made of the poly-acrylonitrile fiber, have a slightly negative coefficient. This feature increases the heat resistivity of the radiator.

The position can be controlled automatically by the computer, which is triggered by the accelerator. The minimum moving step is 2 μ m. The movable range of the radiator is 100 mm and the maximum velocity is 80 mm/s. The radiator is installed and removed in the electron orbit with the maximum velocity, synchronized the acceleration phase of the STB ring.

3.2 Magnetic spectrometer

The energy of the recoil electron is determined by the curvature in the magnetic field of BM4. The design results of the main magnets of the STB ring are reported in reference [2]. The orbits of the main beam and the recoil electron are shown in Fig. 2. The solid curves represent the orbits of the recoil electrons with the energies from 1/12 to 1/3 E_0 with 1/24 E_0 step. The recoil electrons are extracted from the vacuum chamber through a titanium window with a thickness of 50 μ m to the air. The flight length from the window to the tagging counters in the air is about 50 mm. The spread of the recoil electron caused by multiple scattering at the exit window is estimated as 300 μ m, which is smaller than the contribution of 500 μ m estimated from the beam divergence at the radiator position .

3.3 Tagging counters

The recoil electrons are detected by the 50ch tagging counter which is installed in the bending magnet. The energies of the electrons are measured by the hit position on the tagging counter. A plastic scintillator is employed as a position detector, because it can be easily processed in any form, gives a good time resolution and is less expensive.

A detector box, in which plastic scintillators are placed in two rows near the window, is shown in Fig. 3. The plastic scintillator is in a shape of a rectangular prism with a base 3 $\sim$ 6 mm in width, 5 mm in thickness, as shown in Fig. 2, and a height of 20 mm; the 5-mm width corresponds to an energy span of 6 MeV at E_γ = 1 GeV. Each counter width has been determined so as to have the same energy width.

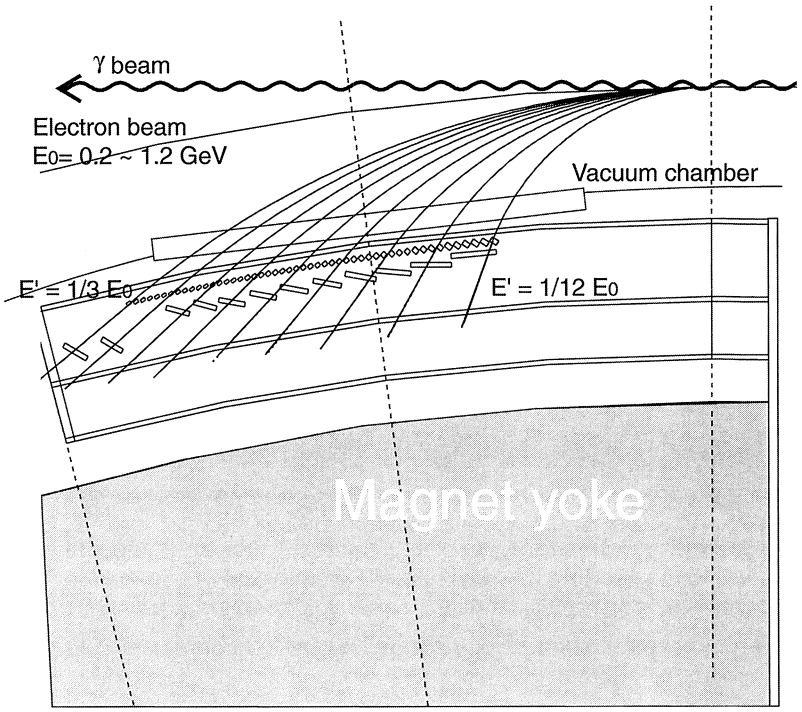

Fig.2. The orbit of the primary electron beam and recoil electrons in the STB bending magnet with the tagging counter. The orbits of the recoil electrons are displayed with the energies from 1/12 E_0 to 1/3 E_0 with 1/24 E_0 step.

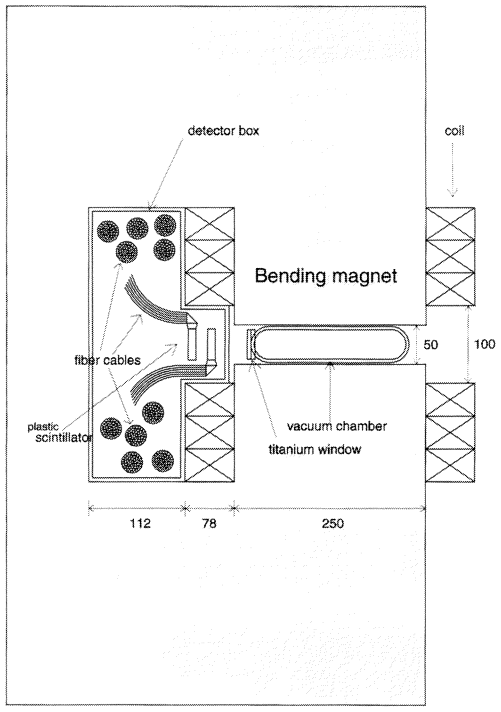

Fig.3. Cross section view of the bending magnet of the STB ring. A small detector box in which plastic scintillators and optical fiber cables are placed is designed to be inserted between the magnet chamber and the return yoke.

Fifty scintillators are placed at the front surface of the detector box and in the second raw other twelve scintillators are aligned as back counters. Each back counter covers four front counters except the one

placed at the highest energy side, which covers six front counters. The coincidence requirement between the front and the backup counter reduces the background.

The scintillation light is transmitted from each plastic scintillator to a photo-multiplier (PMT; Hamamatsu H6524-01) placed at the outside of the magnet through a bundle of 3-m long optical fiber cables. The space behind the plastic scintillator in Fig. 3 is just for 62 bundles of them. Fiber cables are quite useful to transport the light through a long path in flexible and winding. Presently employed is a optical fiber cable of 1.0 mm in diameter (Eska CK-40) manufactured by Mitsubishi Rayon Co. Sixty cables are tied up in a bundle. Both ends of the bundle are closely packed and tightly hardened; they show circular cross sections of 10.0 mm in diameter fitting to the PMT.

Losing the light intensity is inevitable for the present system, mainly due to a difficulty of light transmittal from the scintillator to the fiber cables. Thus, we have devised a light guide connecting the scintillator and the optical fiber, in order to reduce the light loss between the scintillator and the optical fiber. The light guide is in a shape combined with two geometrical parts;a trapezoidal square prism and a triangular prism. The determination of the shape has been reported in Ref. [3]

§ 4. Performance of the Tagging Counter and Photon Beam Characteristics

The test experiment has been carried out in order to check the performance of the tagging counter and the photon beam characteristics.

4.1 Performance of the tagging counter

The detector system of the final geometry was tested in an actual condition. One end of a bundle of fiber cables of 3 m in length was coupled with the light guide of the scintillator in the box, and the other end was coupled with the photomultiplier placed at about 2 m from the magnet. In Fig. 4, the measured pulse height spectrum of the tagging detector is shown. The peak at around 335ch corresponds to the electron events. The light intensity of about 65% can be obtained by using 3-m long fiber cables, in the present case.

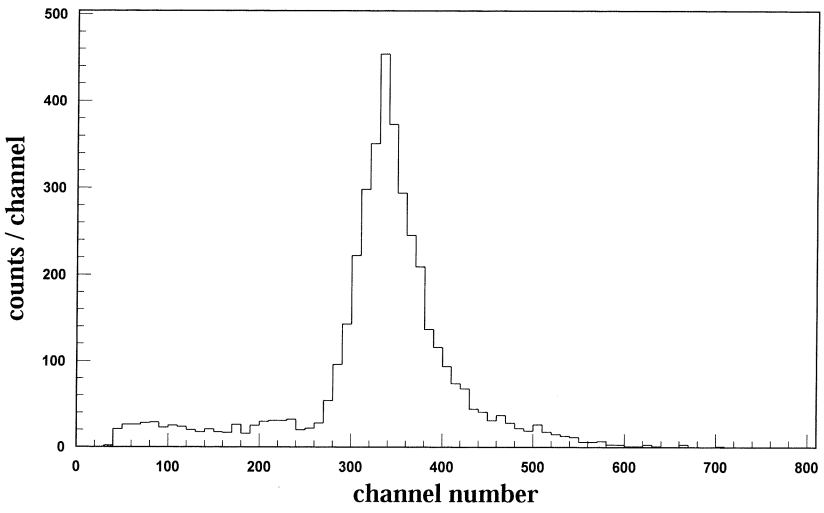

Fig.4. Pulse height spectrum of a tagging detector measured with a 1.2 GeV electron beam in an operative condition.

4.2 Photon beam profile

The beam profile of the photon beam was measured by a Polaroid film placed behind the 5 mm Pb plate at the target position of 7 m downstream from a photon production radiator. The diameter of the photon beam image was less than 20 mm. This is comparable to 5 mm (r.m.s.) which was estimated from the beam divergence and the distance between a radiator and a target.

4.3 Energy calibration

The energy of the tagged photon beam has been measured by the pair magnetic spectrometer. The tagged photon beam bombards the copper converter which is placed upstream of the pair spectrometer and produces e^+-e^- pair. The energies of e^+-e^- pair are measured simultaneously by the spectrometer. The details of the experiment have been reported in Ref. [4]. Figure 5 shows the energy spectra of the tagged photons in coincidence with three tagging counters.The single bremsstrahlung spectrum is also plotted. The peak energies shift linearly according to the tagger channel number. The energy resolution of this detector system is about 10 MeV, but the relative peak position of the photon energy can be determined within 1 MeV. Figure 6 shows the calibration curve of the tagged photon. The averaged root mean square of the deviation from the linear fit are 0.92 MeV and 0.71 MeV for 1.2 GeV and 0.93 GeV mode, respectively. The absolute value of the photon energy was also checked with the threshold energy of the $p(\gamma, \eta)$ reaction. The energy of the circulating electron can be deduced by the end point energy of the bremsstrahlung photon;1.17 GeV and 0.92 GeV are the results of the analysis.

4.4 Tagging efficiency

The tagging efficiency (ε) is defined as the ratio of the real photon numbers on target to the electron counts of the tagging counter. A CsI crystal detector was employed to count the real photon numbers on the target. The size of the CsI crystal is $50 \times 50 \times 250$ mm. It is large enough to cover the tagged photon beam profile. The pulse height data of the CsI detector output were accumulated when more than one tagging counter was fired. The tagging efficiency of the i-th counter is,

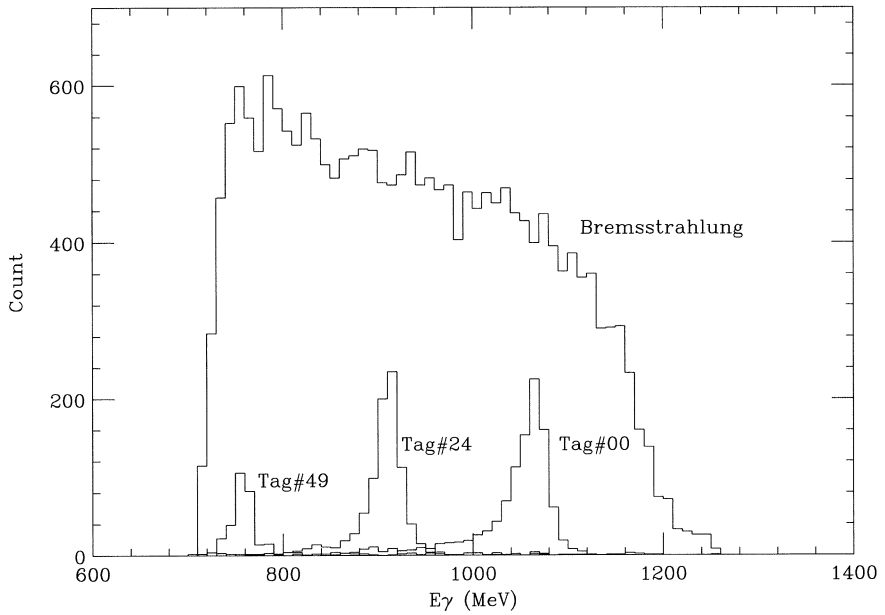

Fig.5. Bremsstrahlung spectra with three tagging counters' hits. The single bremsstrahlung pectrum is also shown.

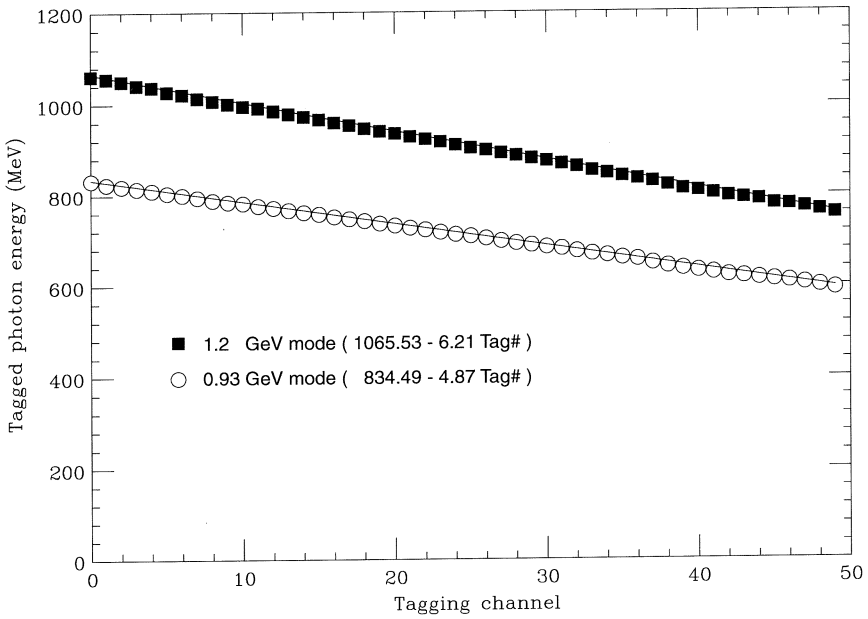

Fig.6. Energy calibration of the tagged photon measured by the pair magnetic spectrometer. The upper cluster corresponds to the electron energy of 1.2 GeV and the lower one of 0.93 GeV.

$$\varepsilon_i = \frac{N_i\,(\mathrm{on}) \otimes N\,(\mathrm{CsI})}{N_i\,(\mathrm{on}) - N_i\,(\mathrm{off})},$$

where N_i (on) is the counts of the i-th tagging counter, N (CsI) is the counts of CsI detector and N_i (off) is the counts of the i-th tagging counter when the radiator is off. $\otimes$ means in coincidence between a left and a right count. The beam intensity was controlled low enough to be able to ignore the chance coincidence between the tagging counters and a CsI detector; 10^{-4} times weaken than the normal intensity. Figur 7 shows the tagging efficiency and the radiator off/on ratio. The radiator off/on ratio with low intensity beam is a few tens times larger than that with the normal intensity beam. When the beam intensity is very low, the fluctuation of the off/on ratio is very large. The scattering points of the tagging efficiency at tagging channel of 1 and 6 are affected by this fluctuation. At the normal tagged photon intensity, the fluctuation of the radiator off/on ratio can be ignored because the absolute value is less than 1 % . The constant ε, which is the average of all ε_i, is used to count the incident photon number.

4.5 Photon flux

In Fig. 8, the typical examples of the time evolution of the tagged photon flux are shown. The former three clusters correspond to the tagged photon rates with fixed radiator positions: $3.5\,\sigma$, $3.0\,\sigma$ and $2.5\,\sigma$ far from the beam center, respectively. The photon flux increase as the radiator approach to the center orbit. The photon emission reduces the circulating electrons, so the photon flux is reduced exponentially with the fixed radiator. The size of the electron beam at the reaction point is about 1.0 mm (r.m.s.), and is about 100 larger than the radiator diameter.

By controlling the position of a radiator from $3.6\,\sigma$ to $2.5\,\sigma$ far from the electron center orbit, the almost constant tagged photon flux can be obtained during the flat top. Latter two clusters show the almost constant tagged photon intensity by controlling the radiator position. The length of the flat top is

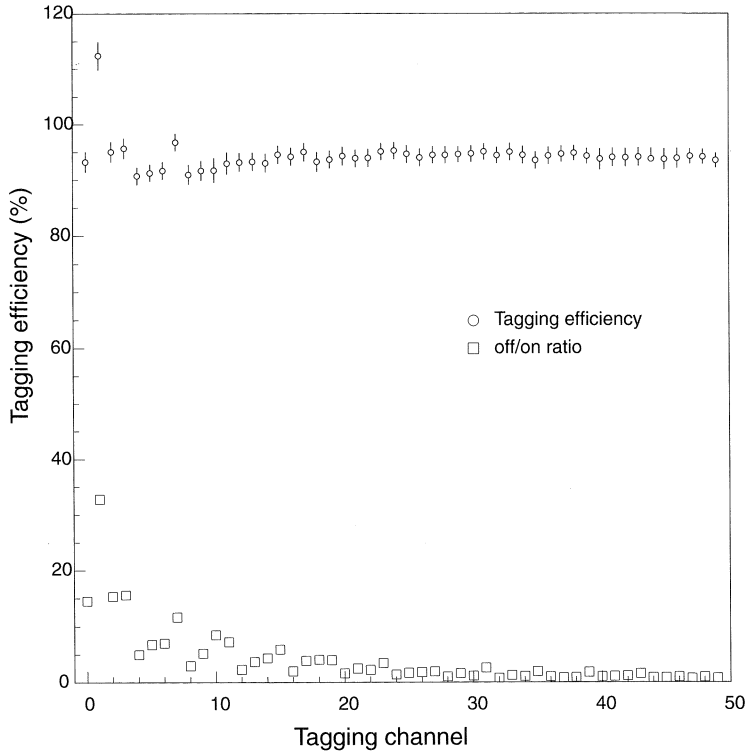

Fig.7. Tagging efficiency at the electron energy of 1.2 GeV. Open circles are the experimental results of the tagging efficiency. Open squares are the radiator off/on ratio.

typically 25 seconds. The solid line shows the tagged photon intensity, and its value is 3×10^6 / sec. The average of the counting rate of the tagging counters without a radiator is shown with a broken line, whose typical value is 1.5×10^4 / sec. The radiator off/on ratio is less than 0.5% . The duty factor (*D.F.*) is defined as the ratio of beam on time to one period. This value can be calculate from this figure: *D.F.* = 25/29 = 0.86.

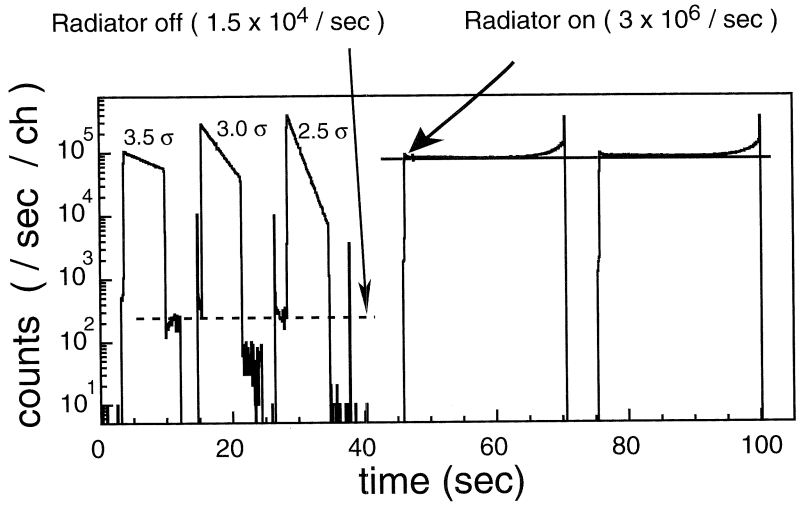

Fig.8. Time evolution of the tagged photon intensity. The radiator position has been controlled so as to keep the intensity of the tagged photon beam almost constant.

§ 5. Conclusions

The 1.2 GeV STB tagger which has the unique movable solid fiber radiator and tagging counter have been installed in the 1.2 GeV STB ring at Tohoku University. The energy range of the tagged photon beam is from 2/3 E_0 to 11/12 E_0 for the electron energy of E_0. The energy bin of the tagged photon is about 1/200 E_0, which is much smaller than the requested value of 30 MeV at 1 GeV. The position control of the solid fiber radiator made the flux fluctuation less than 30%. The maximum intensity of the tagged photon beam is 10^7 tagged photons / see. The energy calibration of the tagged photon beam has been carried out by using the pair magnetic spectrometer. The measured tagging efficiency of each counter is better than 90%. The typical duty factor is better than 0.8.

The construction of the second tagged photon beam line in the STB ring is now in progress.

References

[1] F. Hinode *et al.*: Second Asian Particle Accelerator Conference, Sep. (2001) Beijing, China.

[2] B. Feng *et al.*: Research Report of LNS, Tohoku Univ. **30** (1997) 95.

[3] T. Kinoshita *et al.*: Research Report of LNS, Tohoku Univ. **34** (2001) 25.

[4] H. Yamazaki *et al.*: Research Report of LNS, Tohoku Univ. **35** (2002) 43.

(LNS Experiment : #2432)

Energy Calibration of the STB-Tagger

T. Takahashi[1], K. Itoh[1], K. Tsukada[1], T. Watanabe[1], T. Kinoshita[2], F. Miyahara[2], T. Osaka[1], A. Matsumura[1], S. Endo[3], Y. Fujii[1], O. Hashimoto[1], H. Kanda[1], K. Maeda[1], S. N. Nakamura[1], H. Nomura[1], M. Oyamada[1], A. Sasaki[3], T. Satoh[3], T. Tamae[2], H. Tamura[1], M. Wakamatsu[1], H. Yamazaki[2] and H. Yamauchi[1]

[1]*Department of Physics, Graduate School of Science, Tohoku University, Sendai 980-8578*
[2]*Laboratory of Nuclear Science, Tohoku University, Sendai 982-0826*
[3]*Department of Electrical and Electronic Engineering, Akita University, Akita 010-0852*

The STB-Tagger was calibrated by measuring photon energies with a pair spectrometer. We conclude that the energy range of the tagged photons in the 1.2 GeV-mode is from 0.8 to 1.1 GeV.

The photon beams from the STB-Tagger system [1] are used in the neutral kaon photoproduction experiment [2]. Since the experiment focuses on the production in the threshold region, the absolute beam energy should be known as precisely as possible. We measured the photon beam energy by the pair-spectrometer system in coincidence with the STB-Tagger signal. Here the results are reported.

The experimental setup is shown in Fig. 1. Photons are converted into electron-positron pairs in a Cu converter of 0.9 mmϕ. The electrons and positrons were measured by the pair-spectrometer (PM)

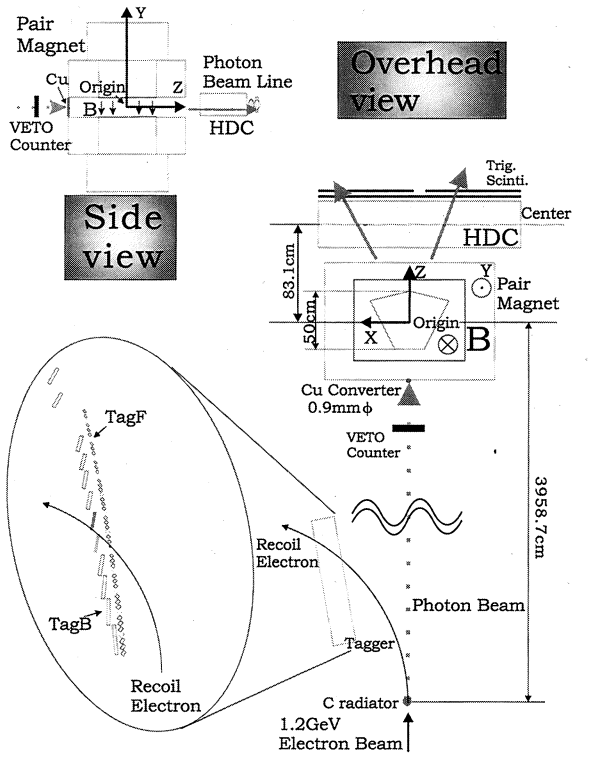

Fig.1. Experimental Setup.

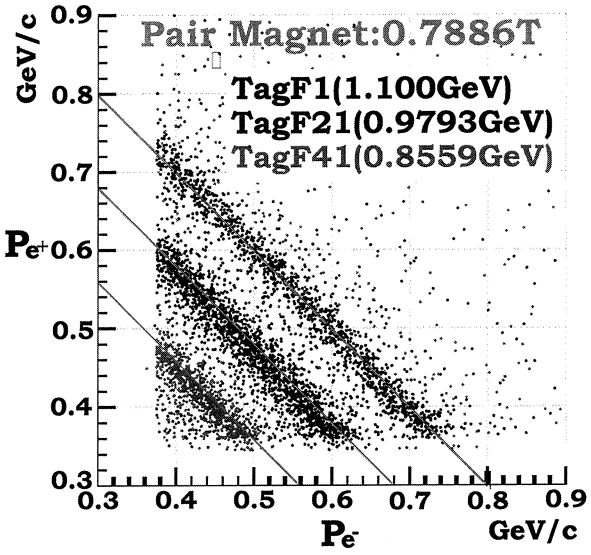

Fig.2. Correlations between momenta of e^+ and e^-.

system which consists of a dipole magnet, a drift chamber (DC), and trigger scintillators. The momenta of the electron and positron were determined by tracing back the trajectories from the DC to the converter using the PM field map. The 3-dimensional field maps were calculated by TOSCA and normalized to the measured field at the center position in each current setup. We used 4 current settings of 180, 220, 280, and 320 A, which correspond to the center field of 0.652, 0788, 1.00, and 1.14 Tesla, respectively.

As shown in Fig. 2, clear correlations between the momenta of electrons and positions were observed. Thus, energies of photons which are associated with each tagger segment were obtained. The results from different magnet setups agree with each other as shown in Fig. 3. The systematic error was

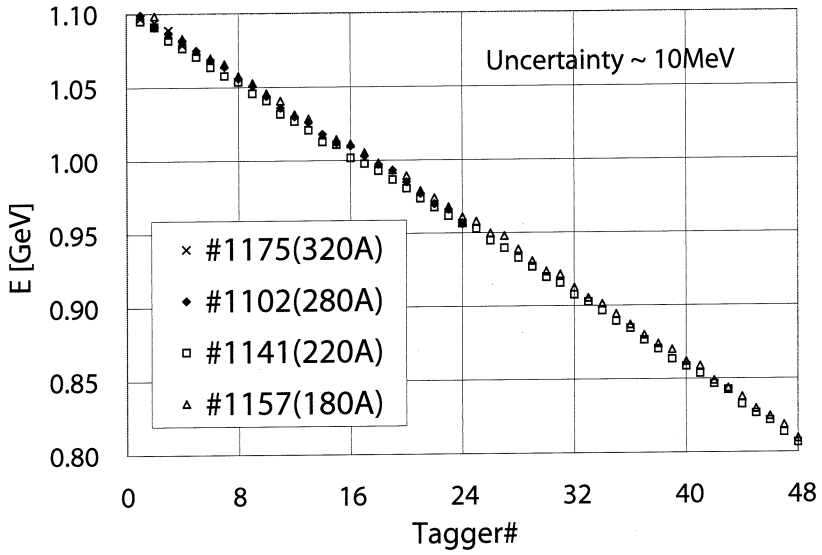

Fig.3. Determined photon energies.

estimated to be 10 MeV, which mainly comes from the field shape uncertainty in the fringing field region.

In summary, we have calibrated photon energy by measuring the electron-positron pairs after conversion with the pair-spectrometer system. We have confirmed that the STB-Tagger covers energy range from 0.8 to 1.1 GeV with the systematic uncertainty of 10 MeV.

References

[1] H. Yamazaki *et al.* : Research Report of LNS, Tohoku Univ., **34** (2001) 25, T. Kinoshita *et al.* : Research Report of LNS, Tohoku Univ., **34** (2001) 29.

[2] T. Takahashi *et al.* : Nucl. Phys. **A** (2003) 991c.

Development of High Speed γ Beam Profile Monitor

M. Nanao, T. Ishikawa and H. Shimizu
for the new GeV-γ beam line construction collaboration

Laboratory of Nuclear Science, Tohoku University, Mikamine 1-2-1, Taihaku, Sendai 982-0826

§ 1. Introduction

A new GeV-γ beam line was recently constructed at Laboratory of Nuclear Science. A GeV-γ tagging system is now under construction. The GeV-γ beam is produced by utilizing an internal radiator inserted into the circulating electron beam in the 1.2 GeV STB ring. The intensity of the γ beam is about 10^7 photons/sec. In order to use these photons as a beam in experiments, it is necessary to investigate the properties of the γ beam. As a first step, the γ beam profile is investigated at the target position in the experimental hall. Figure 1 shows the detector setup for the γ beam profile measurement.

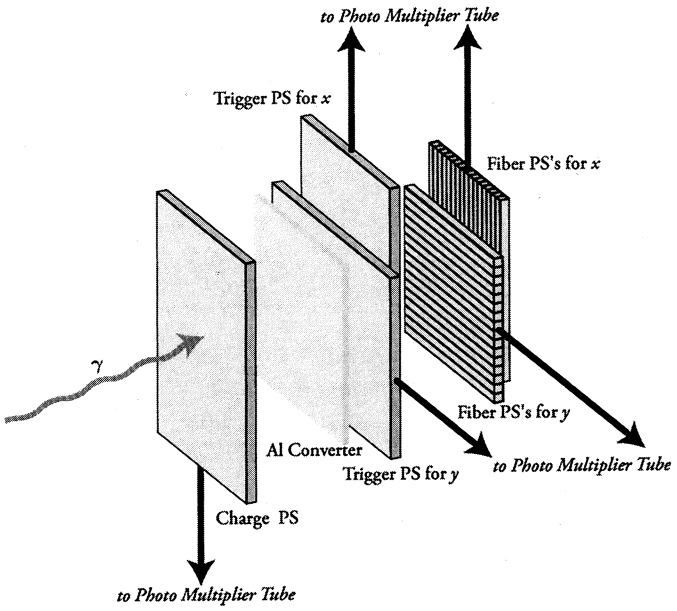

Fig.1. Detector Setup for a γ beam profile monitor system.

The detector system consists of several plastic scintillators (PS). The γ beam bombards a 1 mm thick Al converter, and some photons are converted into e^+e^- pairs. The e^+e^- pairs go straight and penetrate the trigger and fiber PS's. The trigger condition is described as

$$\overline{[\text{Charge-PS}]} \otimes \overline{[\text{Radiator-Out}]} \otimes [x \text{ trigger-PS}] \otimes [y \text{ trigger-PS}]. \quad (1)$$

Charge-PS signal vetoes e^+e^- events produced upstream. The Radiator-Out signal removes the events

taking place while the radiator is not inserted into the electron beam. The hit positions are extracted from the hit information on x and y fiber PS's.

Previously, the data were taken by a CAMAC cycle, and the typical data taking rate was about a few hundred Hz. It took about half an hour to obtain the γ beam profile. Thus we have developed a high speed γ beam profile monitor system by using a 32 bit 20 MHz sampling digital input/output PCI board PCI-2772C (Interface Corporation).

§ 2. Design of Data Acquisition System

The PCI board PCI-2772C judges each TTL signal to be high or low in the data lines responding to the leading edge of the strobe signal, for which the input response time is 20 nsec. The circuitry of the γ beam profile monitor system is simple, as shown in Fig. 2. Strobe signals are made from the coincidence

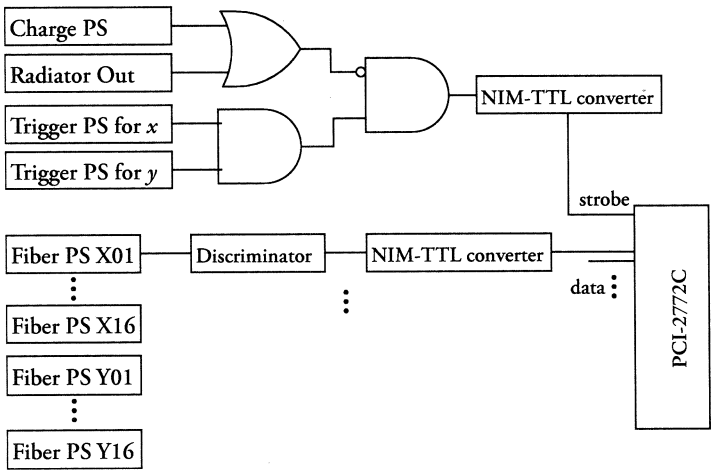

Fig.2. Logic diagram of the data acquisition system.

signals between x and y trigger-PS signals vetoed by the Charge-PS and Radiator-Out signals, and converted into TTL signals by a NIM-TTL converter. Raw signals coming from the fiber PS's are translated into NIM level signals with a width of 50 nsec by discriminators, and converted into TTL signals by NIM-TTL converters. The strobe signals are delayed by 20 nsec with respect to data signals. The host computer of this board is based on Pentium 4, 1.6 GHz (Intel).

§ 3. Perfomance of γ beam Profile Monitor

Figure 3 shows a γ-beam profile obtained while the radiator is inserted into the electron beam at 1.2 GeV. A prominent peak corresponding to the Bremsstraalung γ-beam is observed. Figure 4 shows the γ beam profile without the radiator, and the rate for reconstructed events is about 4% of that with the radiator on.

The typical data taking rate is about 40 kHz, that is limited at this moment by the program code which determines hit positions and displays the profile. Further higher data taking rate can be achieved by optimizing the program code and by introducing a faster personal computer. A set of 16-ch logic level translaters (Phillips 726) is used for NIM-TTL converters in the present measurement. We will make NIM-TTL converters of our own so that the system should be smaller and more inexpensive.

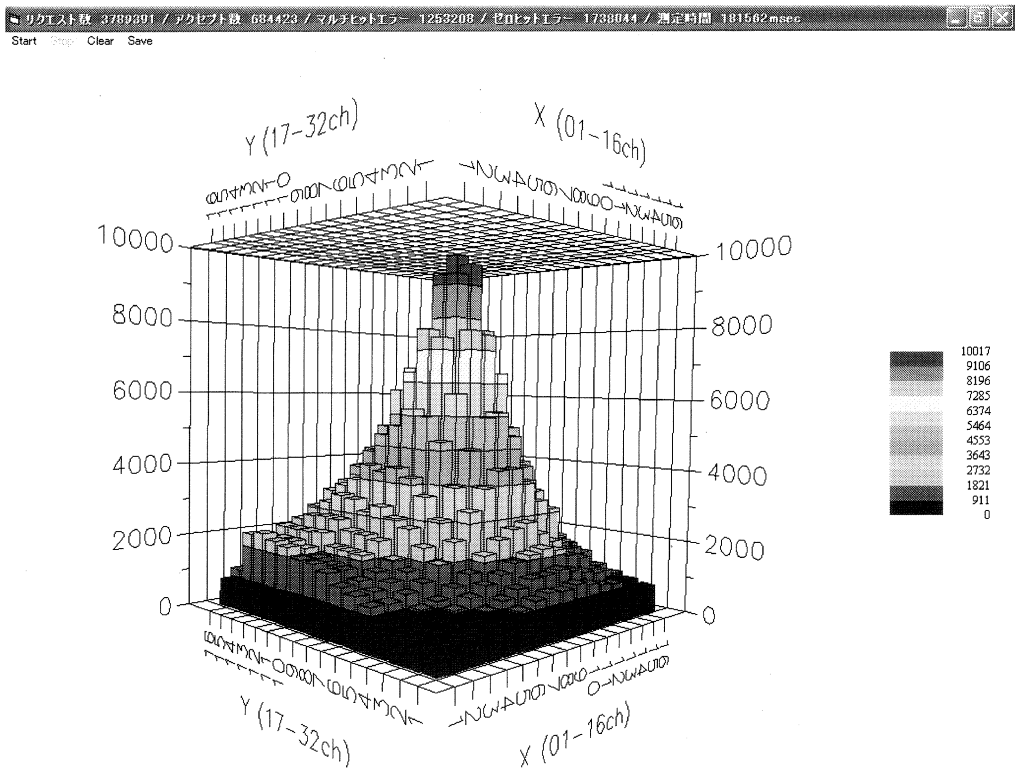

Fig3. γ beam profile obtained with the radiator on.

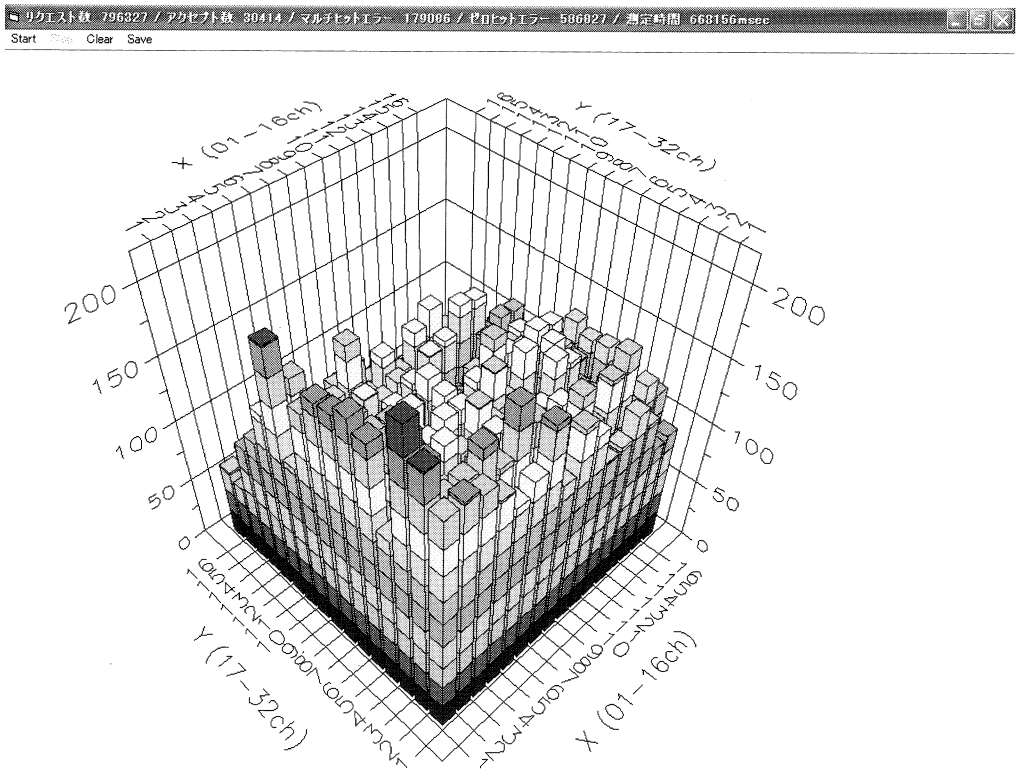

Fig4. γ beam profile obtained without the radiator.

(LNS Experiment #2451)

Performance of an Electromagnetic Calorimeter with Lead-tungstate Crystals

R. Kohara[1], T. Sugitate[1], N. Sugita[1], Y. Tsuchimoto[1], D. Toyoda[1], K. Homma[1] and H. Yamazaki[2]

[1]*Department of Physics, Graduate School of Science, Hiroshima University, Kagamiyama, Higashi-Hiroshima, Hiroshima 739-8526*

[2]*Laboratory of Nuclear Science, Tohoku University, Mikamine, Taihaku, Sendai 982-0826*

The performance of an electromagnetic calorimeter with lead-tungstate (PWO) crystals was tested by using 1 GeV photons. The calorimeter consisted of nine crystals of 20×20×200 mm in size arranged in a 3×3 array. The energy resolution was obtained to be $\sigma_E / E = (2.50 \pm 0.75\%) / \sqrt{E} \oplus (1.25 \pm 0.34\%)$ with a photomultiplier tube (PMT) reading all signals. Another setup, reading the central cell with an avalanche photo diode (APD) and the surrounding 8 cells with the PMT, was also studied, however, its energy resolution was not scaled with the stochastic function and we found the resolution of about 10 % around 1 GeV.

§ 1. Introduction

A large amount of particles is produced in ultra relativistic heavy ion collisions (Pb-Pb or Au-Au) compared with elementary reactions (p-p or e^+-e^-) in a unit solid angle. We need the electromagnetic calorimeter with high granularity in order to observe an electromagnetic particle accurately in such a high particle multiplicity environment. It is essential to seek scintillating calorimeter materials as scintillators with a small Moliere radius because the position resolution (ability to distinguish between one particle and others) strongly depends on the Moliere radius as long as we fix the total volume of the calorimeter. We also request the calorimeter with high-energy resolution to efficiently identify a particle decaying into some electromagnetic particles. It is important to increase the amount of scintillation light and to improve its uniformity and transparency because the energy resolution relies on these characteristics. The high resolution calorimeter can drastically enhance the potential to discover single photons directly emitted from a hot and dense matter created in heavy ion collisions. We made lead-tungstate ($PbWO_4$ or PWO) crystals doped yttrium at Furukawa Co., Japan. We consider the PWO crystals to be the best candidate for a high granular electromagnetic calorimeter because of its smallest Moliere radius of 2.2 cm in the inorganic scintillators. On the other hand, it is tolerable to use them at high-energy experiments because the amount of scintillation light is small. We have Y-doped PWO crystals with the dimension of 20×20×200 mm. The size is adequate for real applications. We constructed a prototype of the PWO calorimeter with 9 PWO crystals arranged in a 3×3 array and tested it with tagged photons around the energy of 1 GeV. We read out the scintillation light emitted

from the PWO crystal with photomultiplier tubes (PMT). We also tested to readout the photons with an avalanche photo diode (APD), which we can use in strong magnetic fields unlike photomultiplier. In this report, we discuss the energy resolution of the PWO calorimeter for photons of around 1 GeV with both PMT and APD readouts.

§ 2. Experiment

The measurement was performed at the second experimental hall with the 1.2 GeV electron storage ring at LNS, Tohoku University. The photon beam was produced as bremsstrahlung radiation by installing the radiator (carbon fiber of 11 micro meters in diameter) into the electron orbital and tagged by detecting the geometrical hit position of the recoiled electron corresponding to its momentum. We referred to the system as Tagger. The experimental setup is schematically shown in Fig.1. A charged

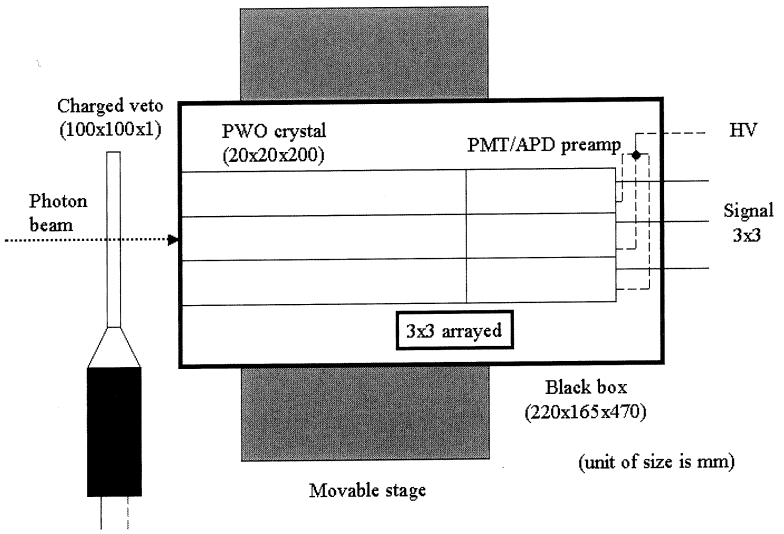

Fig.1. Experimental setup. We construct the calorimeter with 9 PWO crystals arranged in a 3×3 array.

veto counter was located at the front of the calorimeter and employed to reduce background signals. The active area of the veto counter was made of plastic scintillator with dimensions of 10×10×0.1 cm. The calorimeter consisted of 9 PWO crystals of a 3×3 array. Each crystal with a cross section of 20×20 mm^2 and a length of 200 mm (22 radiation length) was wrapped with aluminum foil. Either PMT (Hamamatsu R1450) or APD (Hamamatsu S86664-55) was attached to one end of the crystal with optical compound. The whole detector-cells were set into a light-tight box. The whole calorimeter was mounted on a stage movable in the horizontal and vertical directions. This setup enabled us to inject the incident photons onto the center of each cell. We applied negative 1.0 kV in voltage to the PMT, positive 400 V to the APD, respectively. For the test of the APD readout, we replaced the only central crystal coupled with a PMT with another crystal coupled with an APD, and the other surrounding 8 cells remained reading with the PMT. The block diagram for the electronics is shown in Fig.2. The trigger signal was obtained by a two-fold coincidence (between the signals of the radiator installation and the Tagger hit) with a veto (charged veto counter). In this test, a logic signal of each tagging counter was

digitized by a TDC. For the PMT output signal, we digitized it with a charge-sensitive ADC (LeCroy 2249A). For the APD, we put it through the shaper and digitized with a peak-holding ADC (Hoshin C008H). The ADC gate was produced by the trigger signal with a width of about 200 ns for the PMT, about 1 μs for the APD. The energy calibration of tagged photons with Tagger was performed in advance of our test as shown in Fig.3. We used 40 tagging counters of Tagger from the 1st to the 40th in total 50 ones corresponding to the tagged energy at the range between 0.85 and 1.15 GeV.

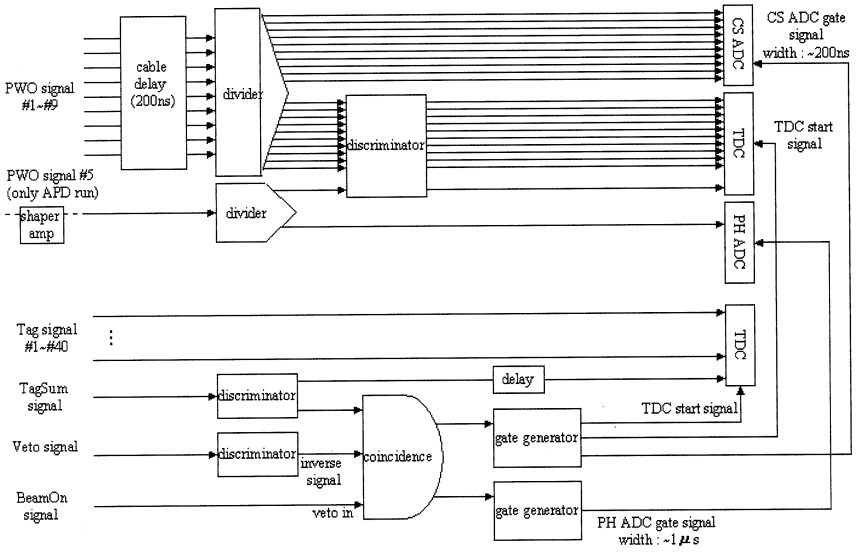

Fig.2. Block diagram of the electronics where PWO denotes the analog signal of the calorimeter, Tag is the logic signal of each tagging counter, TagSum is the logic-sum signal of Tagger, BeamOn defines the timing of the radiator installation and Veto is the analog signal of the charged veto counter.

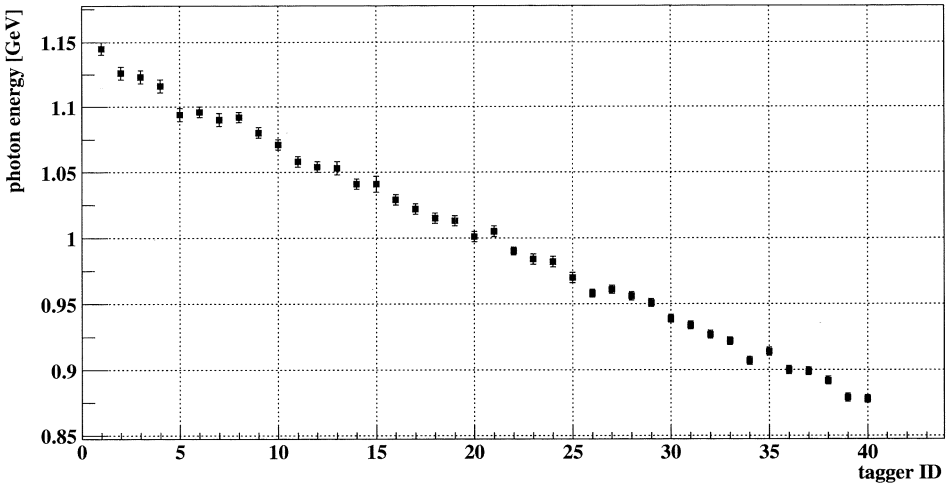

Fig.3. Tagged photon energy. It was measured and Tagger was calibrated in advance of this test. In this test experiment, we use the 40 tags from the 1st to 40th cell.

§ 3. Results

In this measurement, we saw the multiple hits on Tagger as shown in Fig.4. In the energy measurement for a single incident photon, we picked out the events where the number of hit on Tagger is 1 in order to reduce the events of multiple hit on the calorimeter during the gate period. Figure.5 shows the tagged events with the number of hits of 1. The energy calibration of the calorimeter was performed under two stages. At the first stage, we used data in which the photon beam was longitudinally injected on the center of each cell, and obtained a peak value in the ADC distribution for each incident energy. With a peak value in the deposit energy distribution obtained by the Monte Carlo simulation (GEANT4) of electromagnetic shower development for a 3×3 PWO array, we obtained a conversion factor from the ADC value to the energy. At the second stage, we used data in which the beam was injected on the center of the calorimeter (i.e., the center of the 5th cell) through the first stage. We adjusted and corrected the conversion factors taking the geometrical shower sharing into account based on the above simulation. The simulation results show the fraction of deposit energy for

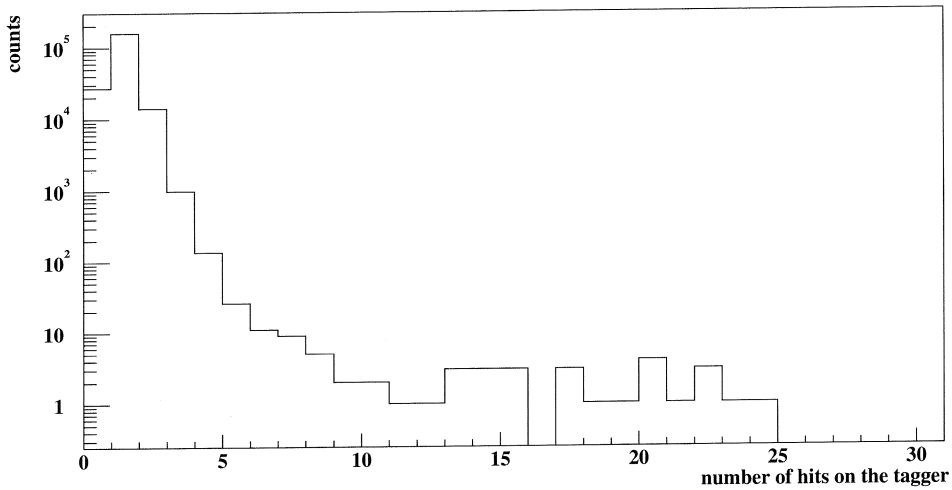

Fig.4. Number of hits on Tagger. In our analysis, we pick out the events when the number is 1. When an event is triggered and it has an overflow value of the Tagger's TDC, it is counted as zero in the number of hits

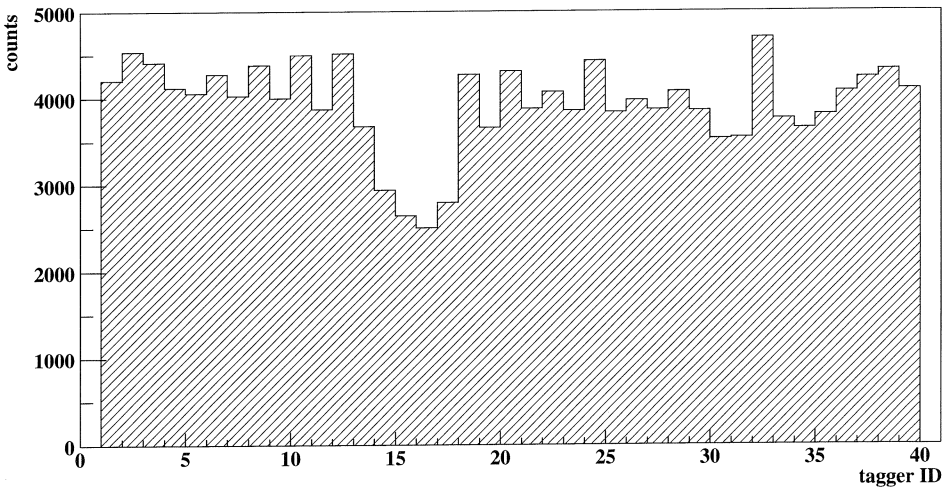

Fig.5. Tagged events when the number of hits on Tagger is 1.

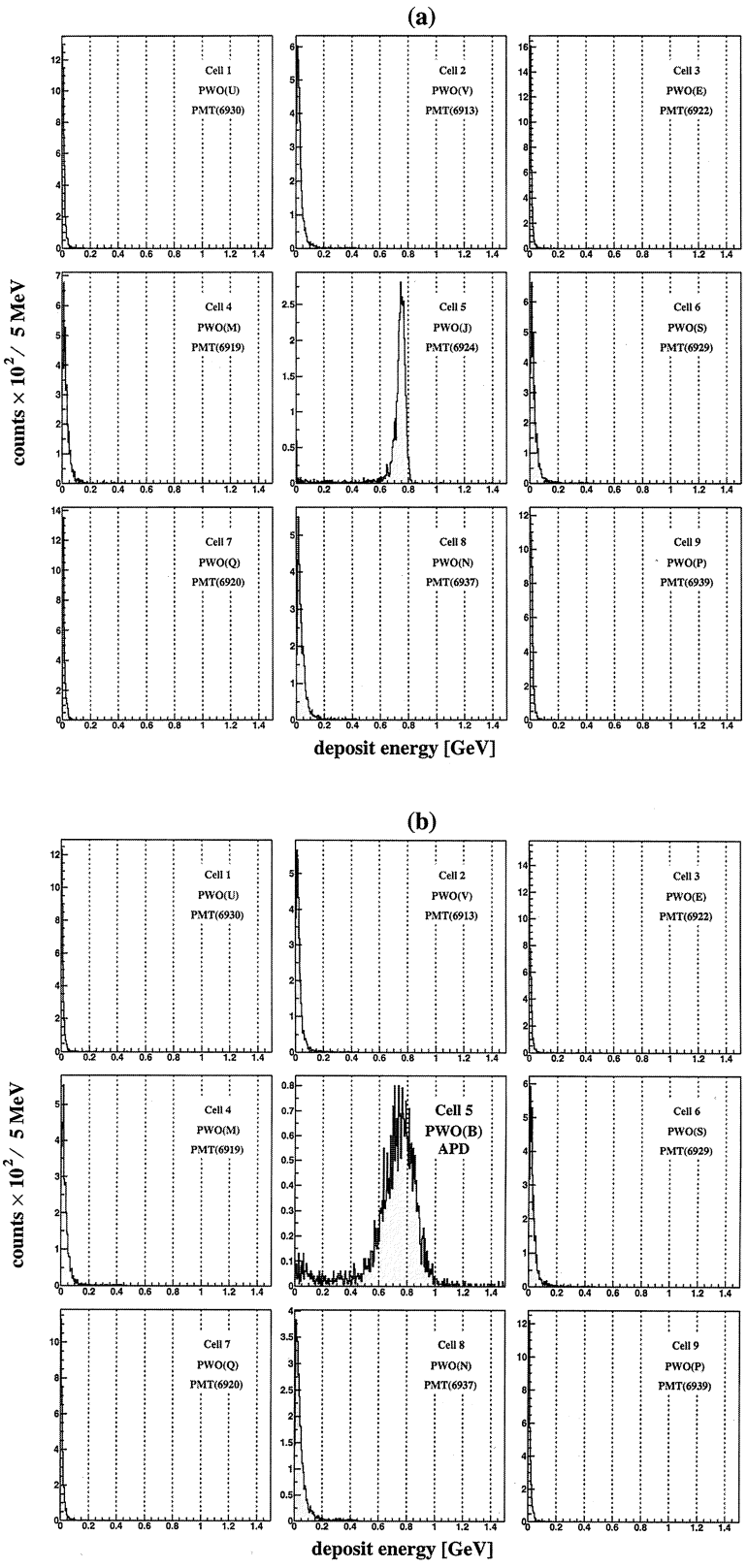

Fig.6. Deposit energy distribution in each cell of the calorimeter for 1 GeV photons incident on the center of the 5th cell (a) with PMT's and (b) with an APD for the 5th (central) cell, PMT's for the other surrounding 8 cells. The ADC values are corrected by pedestal subtraction and energy calibration.

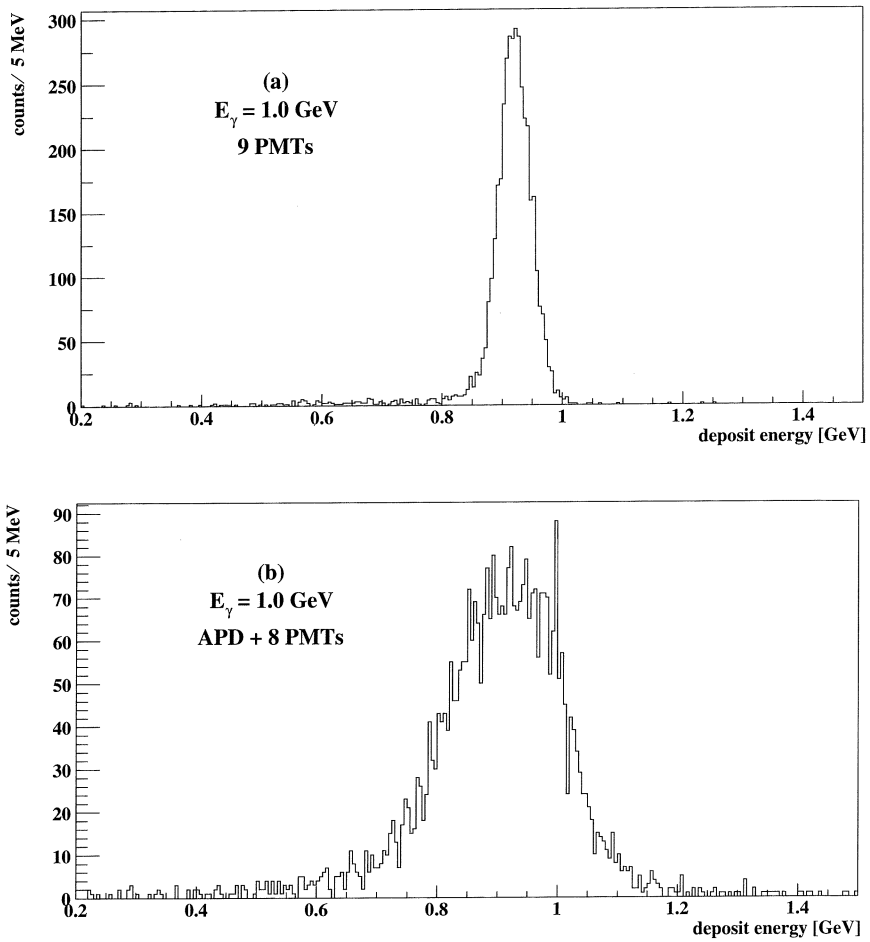

Fig.7. Deposit energy distribution measured by the PWO calorimeter for 1 GeV photons incident on the center (a) with PMT'S and (b) with an APD for the 5th (central) cell, PMT'S for the other surrounding 8 cells. The deposit energies on the 9 cells are summed up event by event.

the incident energy around 1 GeV is 75% on the central cell, 10 % on the orthogonal surrounding 4 cells and 5% on the diagonal surrounding 4 cells, respectively. After the energy calibration, we obtained measured energy spectrum for each incident energy. Figure.6 shows the deposit energy distribution in the individual cell, at 1.0 GeV photons incident (the 20th tag) on the center of the calorimeter, (a) for PMT's only and (b) for the APD scheme, respectively. By summing up all the energies deposited in the 9 cells, energy spectrum for the incident photon was obtained as shown in Fig.7. In this test, we were able to determine 40 points at the incident photon energy in the range between 0.85 and 1.15 GeV for the PMT and APD readouts, respectively. We found means and standard deviations by fitting each spectrum with a normal distribution function for the incident energy. We finally archived the energy resolution by dividing the standard deviation by the mean. For the fitting region, we truncated the lower tail seen in the deposit energy distribution. Figure.8 shows the experimental results of the energy resolution of the PWO calorimeter, (a) for the PMT's only and (b) for the APD scheme, respectively. The energy resolution, σ_E / E, is conventionally parameterized as;

$$\frac{\sigma_E}{E} = \frac{a}{\sqrt{E}} \oplus b, \tag{1}$$

where $\oplus$ denotes the square root of the quadratic summation, E is the incident energy in unit of GeV. We often call a stochastic coefficient, which means the statistical fluctuations. The stochastic coefficient

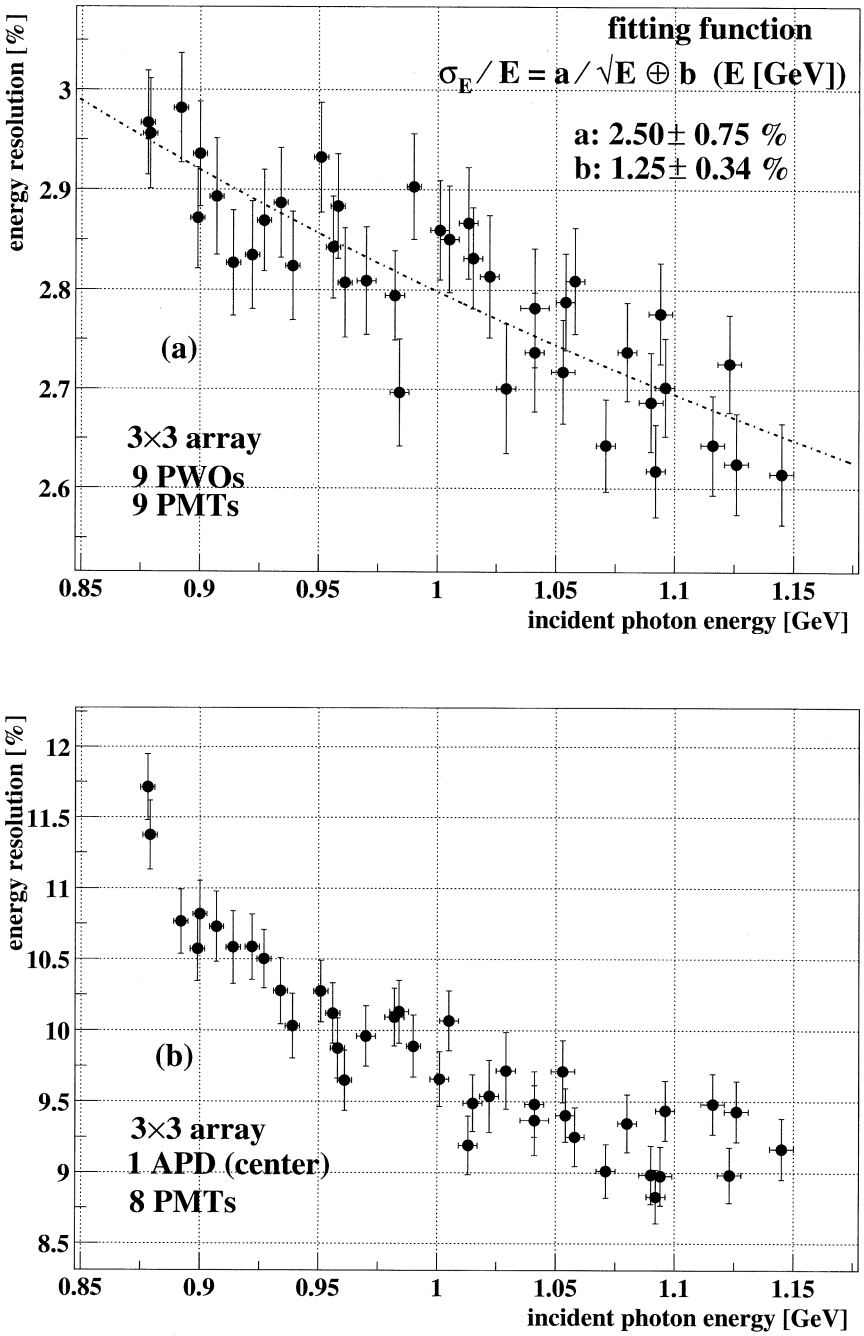

Fig.8. Energy resolution of the PWO calorimeter (a) with PMT's only and (b) with an APD for the 5th (central) cell, PMT for the other surrounding 8 cells. The energy resolution scales very well inversely as the square root of the incident photon energy for the PMT readout, however, it is not parameterized for the APD readout because of the pre-amplifier noise.

characterizes the performance of the calorimeter. The energy resolution scales well to Eq.(1) at the PMT readout, however, it is not scaled at the APD readout because of the pre-amplifier noise. By fitting data for the PMT's only, the coefficients were found to be a = 2.50±0.75 % and b = 1.25±0.34 %.

§ 4. Summary

We tested an electromagnetic calorimeter with 9 PWO crystals arranged in a 3×3 array. Each size of the crystal is 20×20×200 mm. We measured the scintillation light emitted from the PWO with PMT's or an APD. The incident photon energy was measured by summing up all the signals from the 9 cells. We evaluated the energy resolution at the incident photon energy around 1 GeV. The energy resolution for the PMT scheme was well parameterized and found that the stochastic coefficient is 2.50 ±0.75 %. Another setup, reading the central cell with an APD and the surrounding 8 cells with PMT's was also studied, but its energy resolution was not scaled with the stochastic function and we found the resolution of about 10 % around 1 GeV. We should improve the performance of the pre-amplifier for the APD, including noise rejection scheme.

Acknowledgment

We would like to thank all the staffs at LNS, Tohoku University for their supports in our beam test.

Ⅱ. Radiochemistry

(LNS Experiment : #2422, #2463)

Yield Measurements for ^{7}Be and ^{10}Be Productions from ^{nat}Cu, ^{nat}Ag and ^{197}Au by Bremsstrahlung Irradiation at E_0 = 200 MeV

H. Matsumura[1]*, T. Aze[2], Y. Oura[3], H. Kikunaga[4], A. Yokoyama[5], K. Takamiya[6], S. Shibata[6], T. Otsuki[7], H. Yuki[7], K. Sakamoto[5], H. Haba[8], K. Washiyama[9], H. Nagai[1] and H. Matsuzaki[10]

[1]*College of Humanities and Sciences, Nihon University, Setagaya-ku, Tokyo 156-8550*
[2]*Graduate School of Integrated Basic Sciences, Nihon University, Setagaya-ku, Tokyo 156-8550*
[3]*Graduate School of Science, Tokyo Metropolitan University, Hachioji, Tokyo 192-0397*
[4]*Graduate School of Natural Science and Technology, Kanazawa University, Kanazawa, Ishikawa 920-1192*
[5]*Faculty of Science, Kanazawa University, Kanazawa, Ishikawa 920-1192*
[6]*Research Reactor Institute, Kyoto University, Sennan-gun, Osaka 590-0494*
[7]*Laboratory of Nuclear Science, Tohoku University, Sendai, Miyagi 982-0826*
[8]*Cyclotron Center, RIKEN, Wako, Saitama 351-0198*
[9]*Faculty of Medicine, Kanazawa University, Kanazawa, Ishikawa 920-0942*
[10]*Research Center for Nuclear Science and Technology, The University of Tokyo, Bunkyo-ku, Tokyo 113-0032*

The yields of ^{7}Be and ^{10}Be produced by bremsstrahlung having a maximum energy (E_0) of 200 MeV in ^{nat}Cu, ^{nat}Ag and ^{197}Au targets were investigated by the AMS technique at MALT of the University of Tokyo. It was found that the yields at E_0 = 200 MeV were much lower than those at $E_0 \geqq 250$ MeV, obtained in our previous work. A change in the yields of the fragmentation component in the target-mass dependence was observed at E_0 = 200 MeV when compared with those at $E_0 \geqq 250$ MeV. However, the ratios of the fragmentation yield of ^{10}Be to that of ^{7}Be remained unchanged throughout the concerned E_0.

§ 1. Introduction

The formation of light nuclei, such as ^{7,10}Be and ^{22,24}Na, in high-energy nuclear reactions on medium-to-heavy-mass targets, called "fragmentation", is not yet clear concerning the reaction mechanisms. Therefore, no theoretical calculation code for nuclear reactions is able to satisfactorily reproduce the fragmentation. In order to provide experimental information about the fragmentation peculiarity, our group measured many yields of several light products (^{7,10}Be, ^{22,24}Na and ^{28}Mg) of bremsstrahlung-induced reactions from 23 targets ranging from ^{nat}B to ^{197}Au, the superscript (nat) being the natural isotopic abundance, at the maximum end-point energies (E_0) of 250 to 1200 MeV radiochemically in our

*Present address: Radiation Science Center, Applied Research Laboratory, High Energy Accelerator Research Organization, Tsukuba, Ibaraki 305-0801

previous works [1,2]. We successfully disentangled the contributions of photo-fragmentation from photospallation processes and found that the neutron-to-proton ratios of the targets strongly affect the formation of nuclei by fragmentation, as revealed by the yields of the isotopic pairs. In this work, the yields of the isotopic pairs of ^{7}Be and ^{10}Be from ^{nat}Cu, ^{nat}Ag and ^{197}Au at E_0 = 200 MeV (a lower energy than in the previous work) were measured in order to understand the effect of the difference in the photon energy of the initial interactions.

Although the amount of ^{7}Be produced in a target was determined by γ-ray spectrometry in the previous works, the measurements of both ^{7}Be and ^{10}Be yields were performed with the aid of AMS in this work, because it is expected that the yields of ^{7}Be from medium and heavy targets at E_0 = 200 MeV are much lower than those at $E_0 \geqq 250$ MeV. The advantage of AMS for ^{7}Be is not only high sensitivity, but also low background. Especially, it is very important that possible interference from spallation products having large yields in the γ-ray measurements at ~478 keV is avoidable in AMS.

§ 2. Experimental

Metallic plates of Cu, Ag and Au (1.7651, 2.1422, and 2.5871 g/cm^2, respectively) with a diameter of 10 mm were cut out for targets. The chemical purities of the Cu, Ag and Au plates were 99.99, 99.98 and 99.99 %, respectively. Each target was wrapped with a guard foil of the same material in order to avoid any recoil gains and/or losses of ^{7,10}Be from and/or into the surrounding materials, and stacked by sandwiching with two Al foils used as a beam flux monitor. Each stack was enclosed separately in a quartz tube evacuated by a rotary pump.

The irradiations were carried out in a water-cooled target holder with bremsstrahlung having E_0 = 200 MeV, obtained in 0.5 mm of a platinum converter at the 300 MeV electron linac of the Laboratory of Nuclear Sciences (LNS), Tohoku University. The durations of irradiation for Cu, Ag, and Au were 30, 40, and 50 minutes, respectively. The beam intensity was monitored by ^{27}Al(γ, 2pn)^{24}Na on two Al foils, as described in Ref. [3], and determined to be $(1.43\pm0.37)\times10^{12}$ for Cu, $(1.15\pm0.22)\times10^{12}$ for Ag, and $(1.76\pm0.72)\times10^{12}$ eq.q./s for Au.

After irradiation, each target was placed in a beaker containing 421 μg of Be^{2+} separately. The targets of Cu and Ag were dissolved with 16 M HNO_3, and Au with aqua regia. Copper was left in solution with excess NH_4OH. Silver was removed as AgCl with 6 M HCl. Gold was extracted into isopropyl ether after adjusting the solution to 8 M HCl. After a Fe^{3+} solution and NH_4OH were added, beryllium was collected as $Be(OH)_2$ with $Fe(OH)_3$. The precipitates free from target material were dissolved with 12 M HCl, and passed through an anion-exchange column filled with Dowex 1X8 (100-200 mesh) pretreated with 12 M HCl. The eluate with 12 M HCl was concentrated, and NH_4OH was added to the solution to precipitate $Be(OH)_2$. The precipitates were dissolved with 1 M HCl, and passed through a cation-exchange column filled with Dowex 50WX8 (100-200 mesh) pretreated with 1 M HCl. After $Be(OH)_2$ was precipitated with NH_4OH from the 1 M HCl eluate, the cation-exchange step was repeated. $Be(OH)_2$ was purified by repeated precipitations in a quartz beaker. The final beryllium solution was dried on a quartz beaker and ignited to BeO at 850℃. The BeO powder was mixed with niobium powder and pressed into a hole in an oxygen-free-copper cathode. The chemical recoveries were

about 60%.

The amounts of ^{7,10}Be were determined by AMS at MALT of the University of Tokyo. The measurement of ^{7}Be was carried out 108 days after irradiation. The ^{10}Be-AMS was performed by following the ^{7}Be-AMS. The details of the AMS for ^{7}Be at MALT are going to be reported by H. Nagai *et al.* and those for ^{10}Be were reported in [4-6]. The reproducibilities of standard samples in these measurements were ±5.8% for ^{7}Be and ±2.6% for ^{10}Be, respectively.

§ 3. Results and discussion

The measured yields of ^{7,10}Be in ^{nat}Cu, ^{nat}Ag and ^{197}Au at E_0 = 200 MeV obtained in this work are tabulated in Table 1. Those are essentially independent of the precursor decays. The half lives of ^{7}Be and ^{10}Be used for the data analysis are 53.29 d and 1.5×10^{6} y, respectively.

In Fig. 1, the yields of ^{7}Be (open squares) and ^{10}Be (closed squares) at E_0 = 200 MeV are plotted together with our previous data at $E_0 \geqq 250$ MeV (circles) as a function of E_0. It was found that all of the yields increased steeply around E_0 = 200 MeV and changed to a gradual increase at $E_0 \approx 250$ MeV. This property confirms that the (3,3) resonance in complex nuclei has the peak cross section around a photon energy of $k \approx 300$ MeV, while the threshold energy for the (3,3) resonance is ~140 MeV. This indicates

Table 1. Measured yields of ^{7}Be and ^{10}Be on ^{nat}Cu, ^{nat}Ag and ^{197}Au at E_0 = 200 MeV.

Target	Yields(μb/eq.q.)			
	^{7}Be		^{10}Be	
Cu	0.77	± 0.21	0.209	± 0.055
Ag	0.267	± 0.056	0.199	± 0.040
Au	0.052	± 0.023	0.147	± 0.061

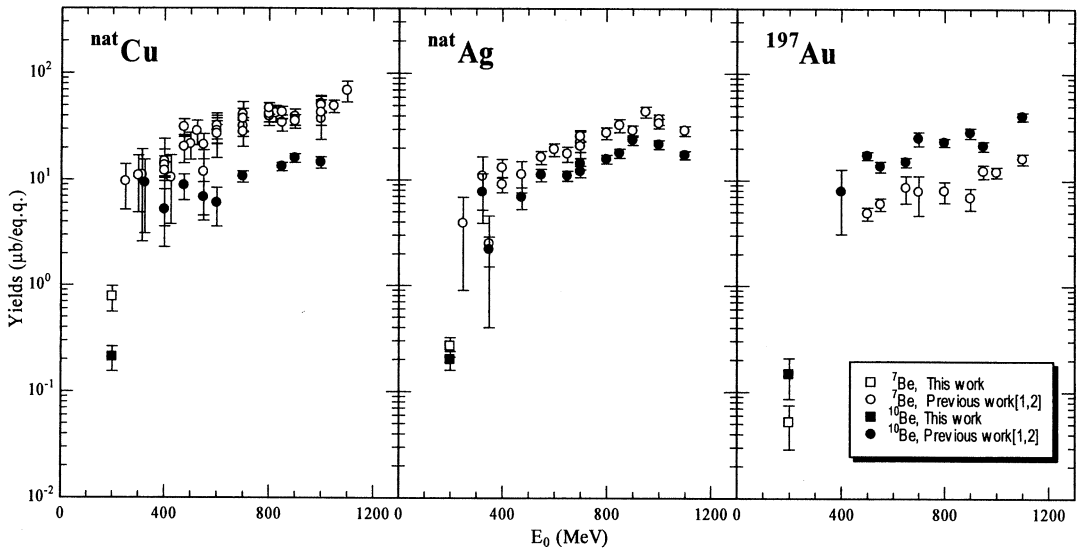

Fig.1. Yield variations for ^{7}Be and ^{10}Be productions from ^{nat}Cu, ^{nat}Ag and ^{197}Au as a function of E_0.

that the formation of beryllium nucleus is closely related to the process opened by the Δ-formation through the (3, 3) resonance.

In order to consider differences among targets at various E_0, the yield variations of ^{7}Be and ^{10}Be from E_0 = 200 to 1000 MeV in steps of 200 MeV are shown as a function of target mass (A_t) in Fig. 2. The lines from E_0 = 400 to 1000 MeV are the sum of two exponential components obtained by least-squares fits to the straight parts of the measured yield variation [1,2,7,8]. It was shown that the A_t-dependences of the yields were decomposed into spallation and fragmentation components [2]. The formation of ^{7,10}Be from the lighter targets was ascribed to spallation residues, and those from the heavier targets to fragmentation. The contribution to the yields of $^{7, 10}$Be from the spallation of ^{nat}Cu was estimated to be negligibly small by using the parameters of Rudstam's formula in Ref. [9]. The ^{7}Be yields at E_0 = 200 MeV obtained in the present work and shown by the open squares decrease with an increase in A_t more

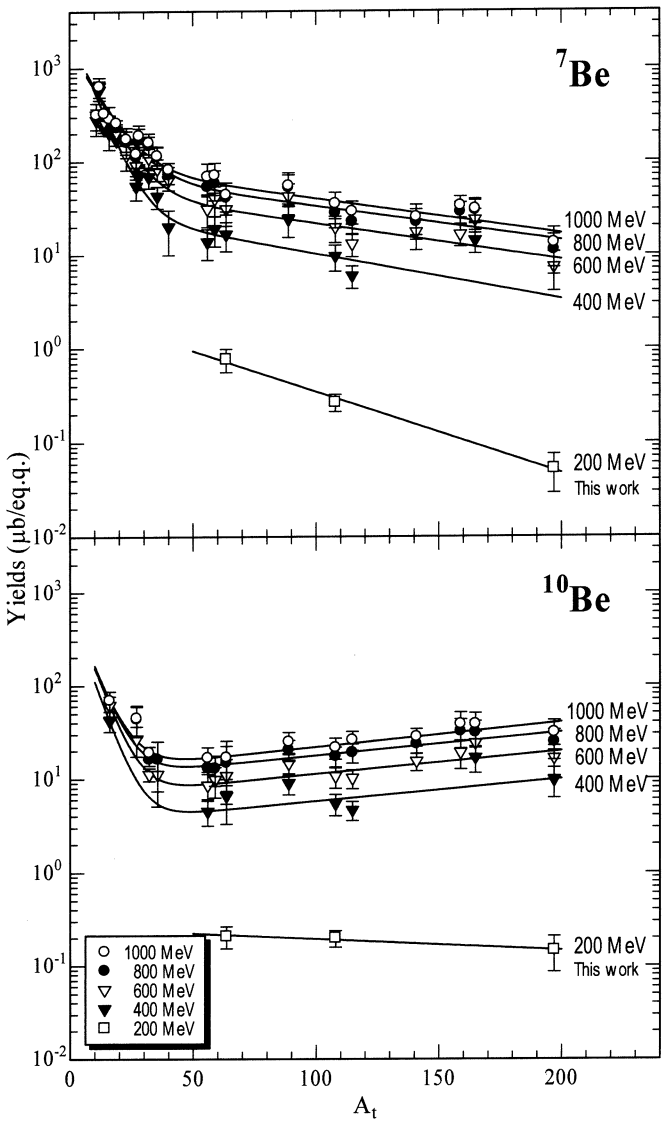

Fig.2. A_t-dependences of the yields of ^{7}Be and ^{10}Be at E_0 = 200, 400, 600, 800, and 1000 MeV.

rapidly than those at higher E_0. The fragmentation component of the ^{10}Be yields at E_0 = 200 MeV also decreases slightly with an increase in A_t in coutract to gradual increase at higher energies. What these tendencies mean is still an open question. It is considered to be a problem that needs a further study. However, it is interesting to note that the fragmentation yield ratios for the isotopic pair of ^{10}Be/^{7}Be at E_0 = 200 and 1000 MeV are quite similar to each other, as shown in Fig. 3, where the yield ratios are plotted as a function of the neutron-to-proton ratio of the target ($(N/Z)_t$). The effects on the relative production between ^{7}Be and ^{10}Be due to a difference in the energy for the initial interaction were uncertain. It was pointed out that the production ratio of ^{10}Be to ^{7}Be exceeded unity around ^{141}Pr with $(N/Z)_t$ = 1.39 and the neutron-deficient ^{7}Be (N/Z = 0.75) appeared to be formed preferably even in a

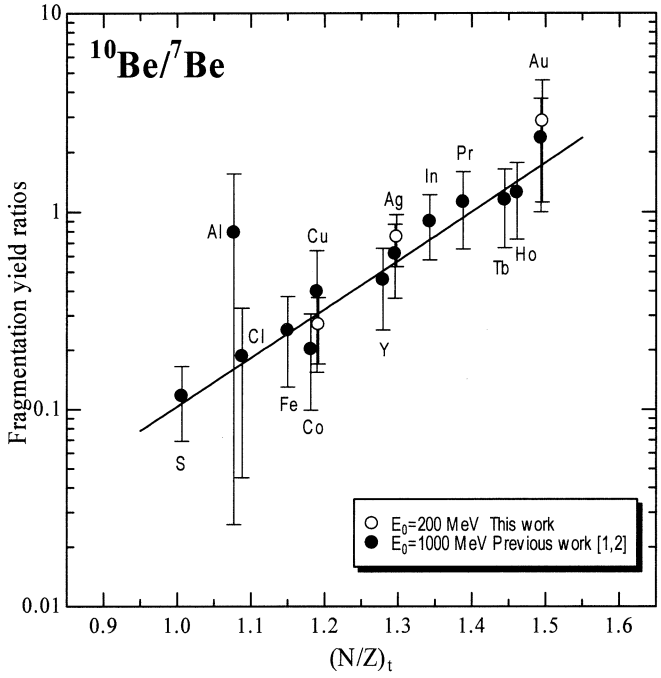

Fig.3. Fragmentation yield ratios of ^{10}Be/^{7}Be at E_0 = 200 and 1000 MeV as a function of $(N/Z)_t$.

nucleus of $(N/Z)_t$ = 1.00-1.39 compared with ^{10}Be very rich in neutron as high as N/Z = 1.50 [2]. The $(N/Z)_t$ values at which ^{24}Na/^{22}Na and ^{28}Mg/^{22}Na exceed unity are also closer to the N/Z values of ^{24}Na and ^{28}Mg, respectively. The overwhelming production of ^{7}Be and ^{22}Na from the targets with $(N/Z)_t$ larger than N/Z of these nuclides suggests that the production of these neutron-deficient nuclei occurs after some neutron emissions from the excited targets. The present study has shown that the same mechanism holds even at E_0 = 200 MeV. However further measurements for ^{7,10}Be are necessary, as well as for other light nuclei, at $E_0 \leqq 200$ MeV where the quasi-deuteron resonance or giant-resonance is effective in the photon-nucleus interactions. It was shown in the present work that the AMS technique is a powerful tool for measuring very low yields of ^{7}Be and ^{10}Be in nuclear reaction study.

Acknowledgments

The authors wish to thank the operating crews of the 300 MeV electron linac at LNS, Tohoku University. We would also like to express our thanks to the staff at the Research Center for Nuclear Science and Technology of the University of Tokyo for their helpful cooperation in the AMS measurements.

References

[1] S. Shibata *et al.*: Radiochim. Acta **80** (1998) 181.
[2] H. Matsumura *et al.*: Radiochim. Acta, **88** (2000) 313.
[3] K. Osada *et al.*: Research Report of LNS. Tohoku Univ. **20** (1987) 299.
[4] K. Kobayashi *et al.*: Nucl. Instr. Meth. **B 123** (1997) 107.
[5] K. Kobayashi *et al.*: Nucl. Instr. Meth. **B 172** (2000) 75.
[6] H. Matsuzaki *et al.*: Nucl. Instr. Meth. **B 172** (2000) 218.
[7] V. di Napoli *et al.*: Nucl. Chem. **40** (1978) 1619.
[8] V. di Napoli *et al.*: J. Inorg. Nucl. Chem. **38** (1976) 1.
[9] S. Shibata *et al.*: Phys. Rev. **C 35** (1987) 254.

(LNS Experiment : #2390, #2403, #2420, #2441, #2453, #2470)

Formation of Tc(IV) Oxide Colloids by Bremsstrahlung Irradiation of Aqueous Solutions of Pertechnetate

T. Sekine[1], H. Narushima[1], Y. Kino[1], H. Kudo[1], M. Lin[2] and Y. Katsumura[2]

[1]*Department of Chemistry, Graduate School of Science, Tohoku University, Sendai 980-8578*
[2]*Nuclear Engineering Research Laboratory, School of Engineering, The University of Tokyo, Ibaraki 319-1106*

Technetium(IV) oxide colloids ($TcO_2 \cdot nH_2O$) were formed by bremsstrahlung irradiation of aqueous solutions of pertechnetate (TcO_4^-). A transmission electron microscopy (TEM) analysis showed that the size of colloids distributed around 30 to 130 nm in diameter. The characteristic X-rays from technetium and oxygen were detected from colloid particles at the TEM measurements. Round-shaped colloids were produced by the irradiation at 40℃, whereas irregular-shaped colloid particles composed of tiny particles (2 nm in diameter) were produced at 17℃. The concentration of TcO_4^- in the target solution decreased with an increase of the absorbed dose, corresponding to an increase of the colloids yield. The yield of colloids sharply increased in the solution deaerated by Ar bubbling before irradiation, but strongly suppressed in the solution saturated with oxygen (O_2) or nitrous oxide (N_2O) gas. The fact suggests that hydrated electrons play an important role in the course of the reduction of TcO_4^- and that Tc(IV) oxide colloid is formed via successive disproportionation reactions of Tc(VI) and Tc(V).

§ 1. Introduction

Technetium-99 is a long-lived fission product with a half-life of 2.11×10^5 y. It is produced in appreciable amounts (thermal neutron fission yield = 6.1%) in nuclear fuel. Because of its long half-life, the migration of ^{99}Tc in the environment is of great importance from a viewpoint of high-level radioactive waste disposal in deep underground.

Technetium is expected to form Tc(IV) species ($TcO(OH)_2$) under a reducing condition which would not migrate due to its strong adsorption on rocks and minerals [1-4]. Therefore, $TcO(OH)_2$ is believed as a preferable species to be kept at a repository site for a long period. However, formation of colloids or pseudo-colloids facilitates a transport of radionuclides, as found in recent research on migration of Pu in groundwater at the Nevada test site [5]. Once the nuclides are incorporated into colloid particles, they travel along with a flow of groundwater. The knowledge on formation of Tc(IV) colloids and their stability in aqueous solutions is substantially limited.

Another point to be stressed is a radiation effect on the migration of radionuclides from the spent nuclear fuel contacting with groundwater, because a high dose is anticipated to its surroundings for a long period of time. Radiolytic processes cause alteration of a matrix of waste materials itself and a change of redox potentials of groundwater [6,7]. Bruno *et al.* pointed out that the release of Tc from the spent nuclear fuel would be controlled by the oxidative dissolution of metallic Tc in the fuel under

radiolytic circumstances [7].

Radiolytic processes of Tc have mainly been investigated by the pulse radiolysis of pertechnetate (TcO_4^-) in aqueous solution [8-11]. All of these reports described that hexavalent technetium, Tc(VI), was produced by a bimolecular reaction of pertechnetate with hydrated electrons (e_{aq}^-) at the rate constant of $(1.3\text{-}2.5)\times10^{10}\,M^{-1}\,s^{-1}$. However, Heller-Grossman *et al.* [10] pointed out the appearance of brownish suspension or precipitate in the electron-irradiated solution at the pulse radiolysis experiments, suggesting the formation of hydrated technetium oxide ($TcO_2\cdot nH_2O$) as a result of further reduction of Tc(VI). Recently Said *et al.* [12] observed a brown turbid solution by irradiation of aqueous pertechnetate solutions with ^{60}Co γ-rays, and they concluded the formation of Tc(IV) colloids. On the contrary, Lefort reported the redissolution of $TcO_2\cdot nH_2O$ by irradiation of ^{60}Co γ-rays [13]. Thus a study on radiolytic processes with respect to the dissolution and colloid formation of technetium species at an interface between a spent nuclear fuel and water is a current subject of interest.

In this paper, we report the formation of Tc(IV) oxide colloids in aqueous pertechnetate solutions irradiated with bremsstrahlung from an electron linear accelerator.

§ 2. Experimental

Potassium pertechnetate ($K^{99}TcO_4$) was purchased from the Radiochemical Center, Amersham. Its crystal was dissolved in triply distilled water and the TcO_4^- concentration of the solution was adjusted to the range of 5×10^{-5} - 3×10^{-4} M. The solutions were neutral and not buffered. The target solutions were prepared under aerobic and anaerobic conditions (Ar bubbling), and sealed in polypropylene vials (5 ml in volume). To the Ar-saturated solution, *t*-butyl alcohol was added to scavenge OH radicals produced by the radiolysis of water. The concentration of *t*-butyl alcohol was 0.2 M.

The target solutions were irradiated with bremsstrahlung generated by an electron linear accelerator of the Laboratory of Nuclear Science, Tohoku University. A schematic drawing for the irradiation system is shown in Fig.1. The electrons (30 MeV) were converted to bremsstrahlung by hitting a 1mm platinum converter, electrons being removed with a sweep magnet. The irradiation time ranged from 2 min to 7 h. The repetition rate of electron pulses per second (pps) was changed from 27 pps to 300 pps to adjust the absorbed dose for the target. The pulse duration was 3 μs. The dose was in the range from 0.02 to 0.08 Gy per pulse. Target temperature rose to 40℃ without a cooling system,

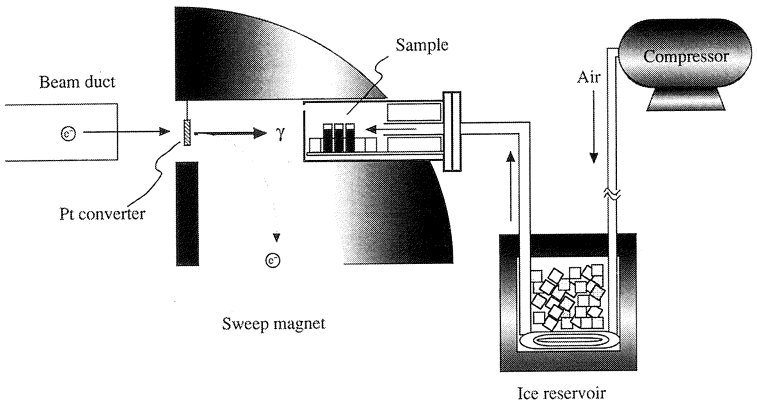

Fig.1. A schematic figure of the bremsstrahlung irradiation system.

when the target vials were situated at the end of the sweep magnet. To avoid the temperature increase, a specially designed aluminum box (70 mm width, 90 mm height, 340 mm length) was equipped (Fig.1). With this cooling system, the temperature of target vials in the box was maintained at 17±3℃ by blowing air (20 L/min) chilled with ice during irradiation. Target temperature was measured with a chromel-alumel thermocouple (in a quartz tube) dipped in a vial containing water (a dummy target) in the box. The signal from the thermocouple was monitored in a short period of time when a beam was off. The irradiated solutions were kept in an ice reservoir until analysis.

Dose monitoring was performed with a cerium dosimeter [14]. A polypropylene vial containing an acidic solution of cerium(IV) sulfate (0.1 or 0.05 M $Ce(SO_4)_2$, in 0.4 M H_2SO_4) was placed beside the target solutions. Correction for the absorbed dose was made by monitoring radioactivity of ^{64}Cu produced by the $^{65}Cu(\gamma,n)^{64}Cu$ reaction in the copper tips (20-100 mg) attached to each vial. The radioactivity of ^{64}Cu was determined by measuring γ-rays (1345 keV) from ^{64}Cu with a γ-ray spectrometer with a Ge detector equipped with a 4 k multichannel analyzer.

A transmission electron microscope (TEM, JEOL JEM-2000 EXII) was used for evaluation of a mean size of colloids. Characteristic X-rays emitted from the colloid particle were simultaneously monitored by the energy dispersive X-ray spectroscopy (EDXS; Oxford Instruments Link-ISIS).

The amount of Tc(IV) colloids was determined by ultrafiltration (Ultra Filter UK-10, Molecular cut off 10000, Toyo Roshi Kaisha. Ltd.). UV-visible spectra were recorded on a Shimadzu MultiSpec-1500 in the range of 190-800 nm before and after ultrafiltration. The concentration of ^{99}Tc was measured with a liquid scintillation counter (Aloka LSC 5100).

The surface charge of Tc(IV) colloids was determined by electrophoresis (moving boundary method) for the colloids produced in the Ar-saturated solutions, because these colloids were stable against coagulation for years. The colloidal solution (130 μL) was poured into a glass U-tube (height 30 mm, ϕ 1.5 mm). Platinum electrodes were used and the electric potential between platinum electrodes was 6 or 12 V. The operation time was within 1 h. The pH of technetium colloidal solution was changed in the range from pH 7 to 1.5 by addition of HCl to determine isoelectric point (point of zero charge).

§ 3. Results

The color of irradiated solutions gradually changed to brownish black with an increase of absorbed dose, resulting in turbid solutions of $TcO_2 \cdot nH_2O$ colloids. Figures 2(a) and 2(b) show typical TEM images for colloidal particles. The size of colloids was distributed in the range from 30 to 130 nm as a whole. Characteristic X-rays originated from technetium and oxygen were observed when an electron beam was focused on one particle at the TEM analysis. Electron diffraction of the colloid particles showed no clear patterns, indicating an amorphous structure.

As shown in Figs.2(a) and 2(b), the shape of particles varies with the temperature of the target solution. The colloids particles shown in Fig.2(a) were formed at 40℃ (without a cooling system), and the others (Fig.2(b)) were formed at 17℃ (with a cooling system). In the former case, we always observed round-shaped particles especially after the long time irradiation (3 h to 7 h). However, only particles with an irregular surface feature were found in the latter case. The particles with irregular

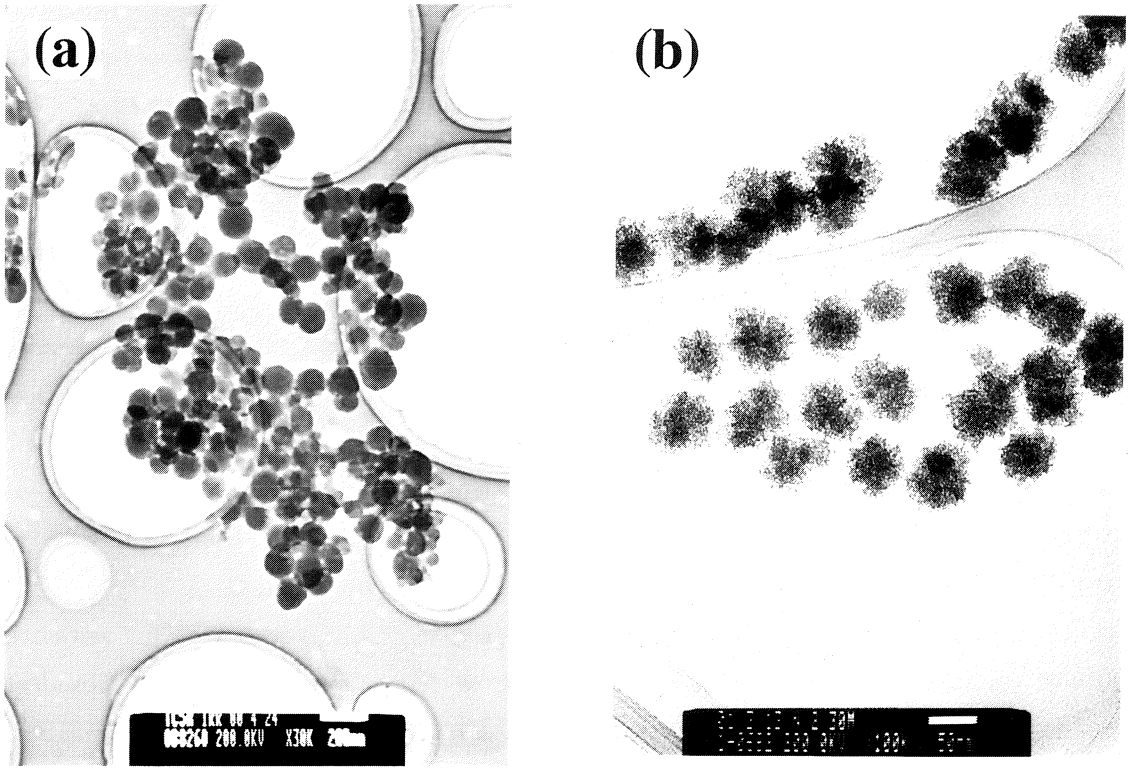

Fig.2. TEM images for Tc(IV) oxide colloid particles radiolytically produced in aerated solutions.
(a) produced at 40℃. Irradiation time: 4.75 h. A white bar indicates 200 nm in length.
(b) produced at 17℃. Irradiation time: 0.5 h. A white bar indicates 50 nm in length.

surfaces were formed as an aggregate of a number of tiny particles (Fig. 2(b)) with the diameter of 2 nm. This is true for almost all particles that were produced at 17℃ irrespective of absorbed dose or irradiation time. About 30 thousands of tiny particles are estimated to aggregate in a large particle with a diameter of 70 nm. The fact suggests that the small particles of 2 nm in diameter were firstly produced in the solution and they coagulated giving larger particles with irregular surfaces during irradiation at 17℃. In the irradiation at 40℃, the small particles were dissolved and precipitated on the surface of other particles just like the Ostwald ripening process, finally giving round-shaped spherical particles.

UV-vis spectra for the irradiated solution gave a continuous absorption in the range from 200 nm to 800 nm owing to light scattering by colloid particles [15]. Our spectra were similar to those reported by Said *et al.*, for aqueous pertechnetate solutions irradiated with ^{60}Co γ-rays [12], except for an absorption peak around 480 nm that they observed.

The TcO_4^- concentration in the filtrate was spectrophotometrically determined after ultrafiltration of the irradiated sample. The radioactivity of ^{99}Tc was simultaneously measured. The concentrations determined by both the spectrophotometric and radioactivity measurements agreed within 10% of fluctuation. The concentrations obtained by ultrafiltration for the targets irradiated at 17℃ are chosen for further quantitative analysis, because a poor reproducibility of the yields of $TcO_2 \cdot nH_2O$ colloids against absorbed dose was observed for irradiation without temperature control.

The fractions of TcO_4^- in the target are plotted against the absorbed dose up to 100 kGy in Fig.3 for

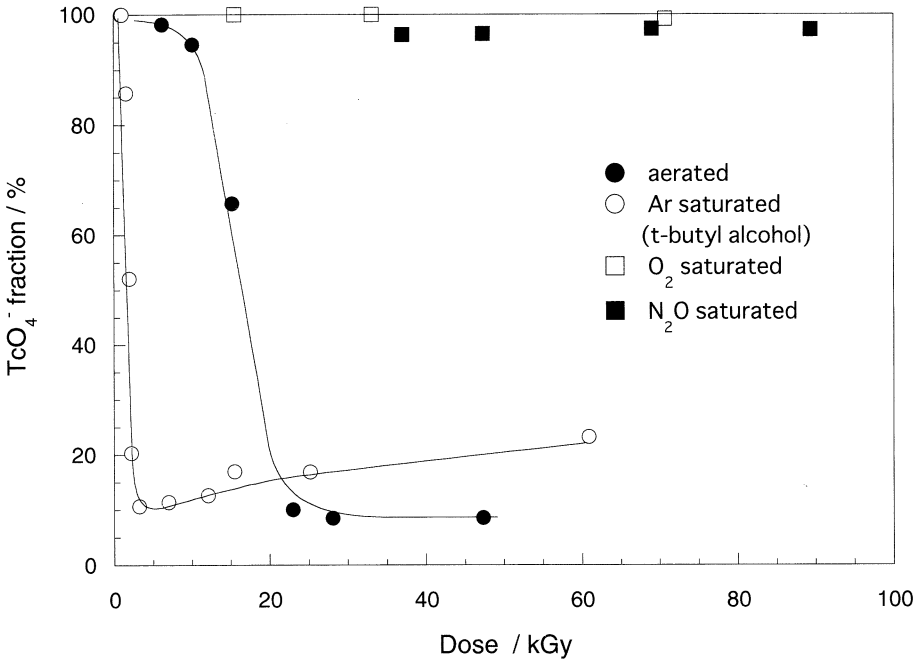

Fig.3. Fraction of TcO_4^- by the bremsstrahlung irradiation for different conditions of the target. Initial concentration of TcO_4^- ($[TcO_4^-]_{initial}$) is 0.1 mM.

●: aerated target, ○: Ar-saturated target (0.2 M *t*-butyl alcohol), □: O_2-saturated target, ■: N_2O-saturated target. Irradiation temperature : 17±3 ℃.

samples with an initial TcO_4^- concentration of 0.1 mM. The consumption of pertechnetate is strongly affected by the presence of radical scavengers and generators, as shown in Fig.3. The TcO_4^- concentration sharply decreases in the Ar-saturated target solution (0.2 M *t*-butyl alcohol) even in the low dose range, while the decrease is gradual in the aerated solution. No colloid generation was found both in the O_2-saturated and N_2O-saturated solutions up to 200 kGy.

Gradual coagulation of the colloids was sometimes observed in a few days after irradiation, resulting in precipitate of $TcO_2 \cdot nH_2O$. However, it was not always observed and a reason why the colloids were kept in a turbid solution was not clear. We found that the colloids formed in Ar-saturated solution were quite stable, and electrophoretic analysis of this turbid solution revealed a negative charge on the colloid particle in pH range from 7 to 3. The charge was turned into positive at pH 1.5, indicating that a point of zero charge of $TcO_2 \cdot nH_2O$ colloids should lie in pH between 1.5 and 3. The charge on the particles should play an important role on the stability based on the DLVO (Derjaguin-Landau-Verwey-Overbeek) theory [16].

§ 4. Discussion

4-1. Reduction processes of TcO_4^-

The $TcO_2 \cdot nH_2O$ colloid formation should be initiated by reduction of TcO_4^- ions with the radiolytic products of water. The radiolysis of water gives following products within 100 ns after radiation is absorbed [17],

$$H_2O \rightarrow e_{aq}^-, H, OH, H_2, H_2O_2, H_3O^+, \quad (1)$$

with *G*-values as $G(e_{aq}^-) = G(OH) = G(H_3O^+) = 2.7$, $G(H) = 0.6$, $G(H_2) = 0.45$, and $G(H_2O_2) = 0.7$. The

hydrated electrons (e_{aq}^-) and both OH and H radicals are strong single electron redox reagents. In the O_2-saturated solution, e_{aq}^- and H are effectively scavenged by O_2 to give O_2^- ions. In the N_2O-saturated solution, N_2O rapidly reacts with e_{aq}^- giving an OH radical which is a strong oxidant. Because hydrated electrons of a strong reducing reagent are effectively removed by dissolved O_2 and N_2O, the reduction of TcO_4^- to produce colloids does not occur (Fig.3). Namely, hydrated electrons play an important role in the course of the reduction of TcO_4^-, as described for results of pulse radiolysis of TcO_4^- in the literature [8-11]. The $TcO_2 \cdot nH_2O$ colloids suddenly appeared at a higher dose (> 200 kGy) even in the N_2O-saturated solution. Taking into account the solubility of N_2O (2.8×10^{-2} M at 20℃) and G-value of e_{aq}^-, we can consider that all the N_2O in the target solution is consumed by e_{aq}^- up to 200 kGy.

We discuss the reduction processes of TcO_4^- on the data obtained for the Ar-saturated solution with 0.2 M *t*-butyl alcohol, which eliminates the oxidative OH radicals from the system. Figure 4 shows the fraction of TcO_4^- obtained for the lower dose range. It is noted that the fraction of TcO_4^- smoothly decreases depending on the absorbed dose, but not on the irradiation time and a repetition rate of pulses. Because the G-value for formation of Tc(IV) oxide colloids might be equivalent to the consumption rate (the number of decreasing TcO_4^- ions per an absorbed dose of 100 eV), we can estimate the G-value for the colloid formation from the slope of each curve in Fig.4. The G-value is 0.4± 0.1, in agreement with the value of 0.37 reported by Said *et al.* [12]. If all hydrated electrons are consumed in the reduction process of Tc(VII) to Tc(IV) through a three-electron process, a G-value for the production of Tc(IV) species should be 0.9 that is one third of $G(e_{aq}^-)$ = 2.7. The G-value (0.4±0.1) obtained in the present experiment is smaller than 0.9, indicating that all of the hydrated electrons do not necessarily contribute to the complete reduction of Tc(VII) to Tc(IV).

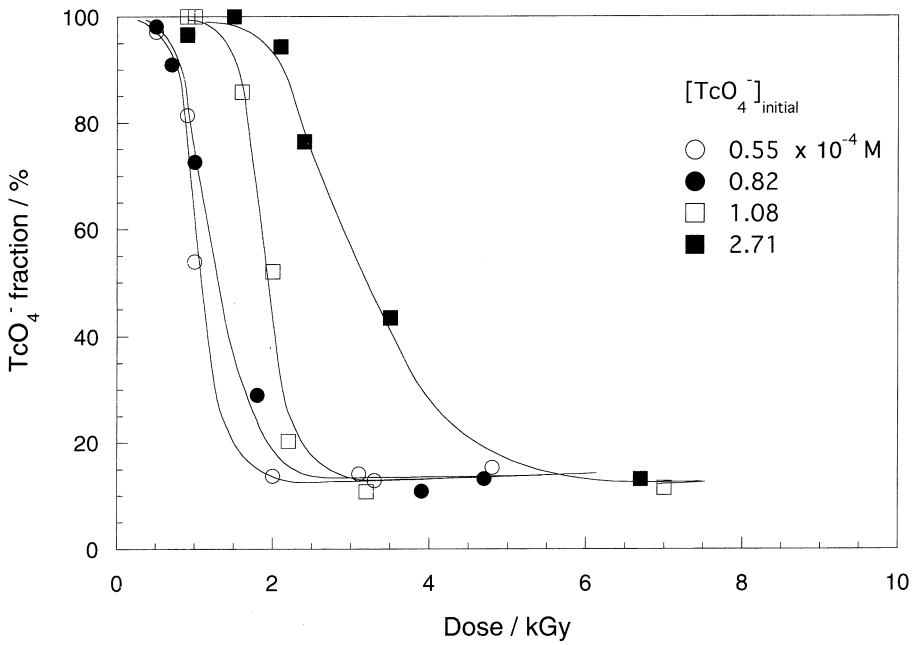

Fig.4. Fraction of TcO_4^- for the Ar-saturated solutions (0.2 M *t*-butyl alcohol) against dose. Initial concentration of TcO_4^- ($[TcO_4^-]_{initial}$), ○: 0.55×10^{-4} M, ●: 0.82×10^{-4} M, □: 1.08×10^{-4} M, ■: 2.71×10^{-4} M. Irradiation temperature : 17±3 ℃. Solid lines are a guide for eyes.

From knowledge of aqueous chemistry of Tc, it is reasonable to consider that both Tc(VI) and Tc(V) species undergo disproportionation reactions; Tc(VI) + Tc(VI) → Tc(VII) + Tc(V) and Tc(V) + Tc(V) → Tc(VI) + Tc(IV) [18]. Hence, we consider the following scenario for the production of $TcO_2 \cdot nH_2O$ colloids from TcO_4^-; 1) the reduction of TcO_4^- by e_{aq}^- to produce Tc(VI), 2) a disproportionation reaction of Tc(VI) giving Tc(V), 3) Tc(IV) formation by a disproportionation reaction of Tc(V), and 4) solidification of $TcO(OH)_2$ as colloids. In the solidification, the concentration of the product Tc(IV) (as $TcO(OH)_2$) of the latter disproportionation reactions increases and exceeds its solubility.

To estimate the consumption quantity of TcO_4^- ions in the reduction processes along with the above mentioned scenario, we simulated the radiolysis process by using the software FACSIMILE (AEA Technology). In principle, the program translates sequences of chemical reactions into a set of differential equations. These equations are solved by numerical integration after specifying initial concentrations, radiolytic yields of chemical species, rate constants, doses per pulse, pulse durations, *etc.* The pulsed irradiation by the LINAC with pulse duration of 3 μs is simulated by the FACSIMILE code. The data set for radiolysis of water is given by Sunder *et al.*[19] and Mezyk *et al.* [20]. When *t*-butyl alcohol is contained in the target solution in sufficient amounts, OH radicals are effectively scavenged by *t*-butyl alcohol. This scavenging eliminates unknown oxidation reactions of Tc(VI), Tc(V) and Tc(IV) with OH, giving a more simple system for the simulation. As for the reduction of pertechnetate, the following reaction sets were used :

$$Tc(VII) + e_{aq}^- \rightarrow Tc(VI) \qquad (k = 2.5\times10^{10}\ M^{-1}\ s^{-1}\ [11]) \qquad (2)$$

$$Tc(VI) + Tc(VI) \rightarrow Tc(VII) + Tc(V) \qquad (k = 1.3\times10^{8}\ M^{-1}\ s^{-1}\ [11]) \qquad (3)$$

$$Tc(V) + Tc(V) \rightarrow Tc(VI) + Tc(IV) \qquad (k = 1.3\times10^{8}\ M^{-1}\ s^{-1}) \qquad (4)$$

The rate constants for Reactions (2) and (3) are taken from the literature [11]. The unknown rate constant for Reaction (4) was assumed to be equal to that of (3). The scenario for the reduction of pertechnetate is triggered by the bimolecular reaction of TcO_4^- with e_{aq}^-, and Tc(IV) is finally produced by successive disproportionation reactions of Tc(VI) in Eq. (3) and Tc(V) in Eq. (4). The number of Tc(IV) species experimentally found as colloids is plotted in Fig. 5 against the calculated number of TcO_4^- ions consumed in units of mM. The data scattered around the solid line of the 1:1 relation between the experimental and calculated data, revealing that above mentioned scenario for the reduction of TcO_4^- ions should be a main route for the Tc(IV) production. In Fig.5, however, the experimental values seem to be slightly larger than the calculated value giving a higher slope compared to the 1:1 line. Other possible reduction reactions of TcO_4^- ions would be initiated with H radicals that were not effectively scavenged by *t*-butanol, because the reduction reaction of TcO_4^- ions with H radicals was not involved in the above simulation. The rate constant of the reaction between H radicals and *t*-butanol is comparatively small ($k = 8\times10^4\ M^{-1}\ s^{-1}$ [21]) and unscavenged H radicals might reduce TcO_4^- ions partly. However, the principal reduction process of TcO_4^- ions should be governed by hydrated electrons because of the large *G*-value.

4-2. Colloid generation process

The tiny $TcO_2 \cdot nH_2O$ particle of 2 nm in diameter shown in Fig. 2(b) must be a particle that is

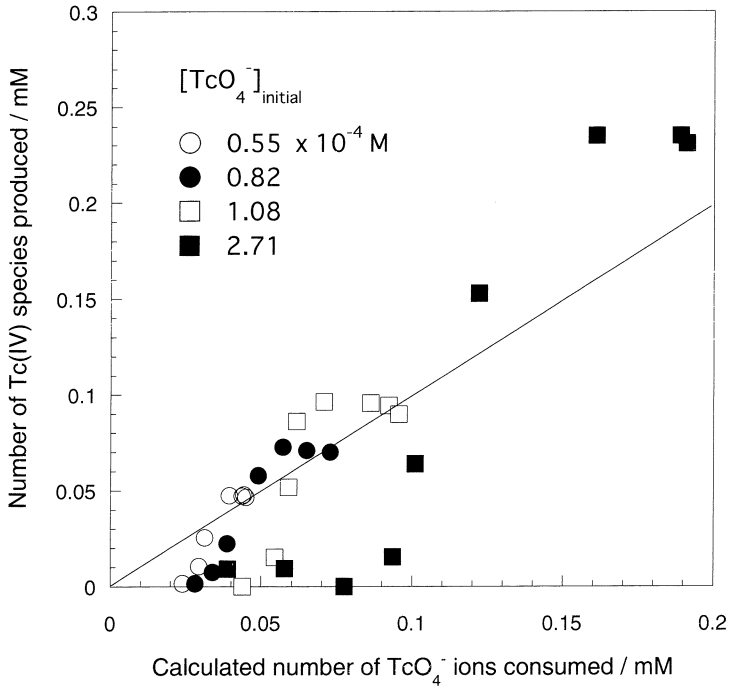

Fig.5. Number of Tc(IV) species experimentally obtained as colloids produced in the Ar-saturated target (0.2 M *t*-butyl alcohol) vs. calculated number of TcO_4^- ions consumed (in units of mM). Initial concentration of TcO_4^- ($[TcO_4^-]_{initial}$), ○: 0.55×10^{-4} M, ●: 0.82×10^{-4} M, □: 1.08×10^{-4} M, ■: 2.71×10^{-4} M. A solid line shows the 1 : 1 relationship between experimental and calculated values.

stabilized in the solution immediately after the colloid generation. Generation of such tiny particles would be explained by a mechanism proposed by LaMer [22]. The LaMer mechanism describes that solidification of solute in a solution is initiated at the solute concentration much higher than the solubility; so-called supersaturation. A fingerprint of the supersaturation of Tc(IV) species, which would be a precursor of the tiny $TcO_2 \cdot nH_2O$ particles, is the existence of a threshold dose seen in Fig.4. The colloid formation is clearly detected as the fraction of TcO_4^- just begins to decrease at the threshold dose. Namely, radiolytic reduction of Tc(VII) to Tc(IV) proceeds to attain the supersaturation condition. The concentration of Tc(IV) or consumed amounts of TcO_4^- even at 0.01 kGy obtained by radiolysis simulations with the FACSIMILE program was higher than the solubility of $TcO(OH)_2$; i.e. in the range between 10^{-8} and 10^{-7} M [23, 24]. The value of 0.01 kGy is quite small compared to the threshold of 0.4 kGy seen in Fig.4. This implies that the concentration of the Tc(IV) species at the threshold is much higher than the solubility of $TcO(OH)_2$, attaining the supersaturation condition. The chemical form of this highly soluble Tc(IV) species is unknown, although Vichot suggested that soluble Tc(IV)-O polymers would be a precursor of $TcO_2 \cdot nH_2O$ [25].

Based on the LaMer model, Sugimoto [26] described a colloid generation mechanism that dealt with emergence of nuclei with sizes distributed around a thermodynamically stable critical size would appear under the supersaturation condition. Nuclei smaller than the critical size quickly dissolve again, while larger nuclei grow through the Ostwald ripening, resulting in the colloids having suitable sizes

stabilized in the solution. In the present case, it is speculated that the concentration of the Tc(IV)-O polymer species increases with an increase of absorbed dose, and that the stabilized colloids or tiny particles of 2 nm in diameter of $TcO_2 \cdot nH_2O$ appear through the above mentioned processes. Finally the aggregated colloids consisted of the tiny particles are formed as shown in Fig.2(b). Although much remains to be solved to understanding of generation mechanisms of $TcO_2 \cdot nH_2O$ colloids, it is to be noted that identification of Tc(IV)-O polymer species and the determination of the critical size of the $TcO_2 \cdot nH_2O$ colloids are essential subjects of matter.

§ 5. Conclusion

The $TcO_2 \cdot nH_2O$ colloid was radiolytically formed by the irradiation of TcO_4^- solution with bremsstrahlung from a LINAC. The colloid particle produced at 17±3℃ consisted of tiny particles of 2 nm in diameter, whereas round-shaped particles were formed by the irradiation at 40℃. The reduction of TcO_4^- proceeded mainly through processes involving a bimolecular reaction of TcO_4^- with e_{aq}^- followed by successive disproportionation reactions of Tc(VI) and Tc(V).

The colloids produced in the Ar-saturated solution were very stable (more than 8 months at least) against further coagulation. The colloids in neutral solution had a negative charge that would stabilize them in the dispersed solution. The occurrence of tiny particles of $TcO_2 \cdot nH_2O$ of 2 nm should be a clue to understanding its generation mechanism. Such tiny particles would be stabilized in solution immediately after the generation of nuclei of colloids.

Acknowledgment

The authors acknowledge to Prof. T. Ohtsuki and machine group members of the Laboratory for Nuclear Science, Tohoku University, for their assistance for bremsstrahlung irradiation. They also wish to thank Prof. T. Mitsugashira and Dr. K. Yubuta in the Institute for Materials Research, Tohoku University, and to Mr. Y. Hayasaka in the High Voltage Electron Microscope Laboratory, Tohoku University, for their help in the TEM measurements of colloid particles.

References

[1] E.A. Bondietti and C. W. Francis : Science **203** (1979) 1337.

[2] K.H. Lieser and Ch. Bauscher : Radiochim. Acta **42** (1987) 205.

[3] K.H. Lieser and Ch. Bauscher : Radiochim. Acta **44/45** (1988) 125.

[4] S. Kunze, V. Neck, K. Gompper and Th. Fanghänel : Radiochim. Acta **74**, (1996) 159.

[5] A.B. Kersting, D.W. Efurd, D.L. Finnegan, D.J. Rokop, D.K. Smith and J.L. Thompson : Nature **397** (1999) 56.

[6] D.W. Shoesmith and S. Sunder : J. Nucl. Mater. **190** (1992) 20.

[7] J. Bruno, E. Cera, U.-B. Ekfund, T. Eriksen, M. Grivé and K. Spahiu : Radiochim. Acta **88** (2000) 513.

[8] A.K. Pikaev, S.V. Kryuchkov, A.F. Kuzina and V.I. Spitsyn : Dokl. Phys. Chem. **236** (1977) 992.

[9] E. Deutsch, W.R. Heineman, R. Hurst, J.C. Sullivan, W.A. Mulac and S. Gordon : J. Chem. Soc. Chem. Commun. (1978) 1038.

[10] L. Heller-Grossman, S. Abrashkin, A. Shafferman, M.A. Davis and R.A. Taube : Int. J. Appl. Radiat. Isot. **32** (1981) 501.

[11] K. Libson, J.C. Sullivan, W.A. Mulac, S. Gordon and E. Deutsch : Inorg. Chem. **28** (1989) 375.

[12] K.B. Said, Y. Seimbille, M. Fattahi, C. Houee-Lévin and J.C. Abbé : Appl. Radiat. Isot. **54** (2001) 45.

[13] M. Lefort : Bull. Chem. Soc. Chim. Fr. (1963) 882.

[14] G.R.A. Johnson and J. Weiss : Proc. Roy. Soc. (London) **240A** (1957) 189.

[15] P.W. Barber and S. X. Hill : "*Light Scattering by Particles*", Wiley, New York, 1957.

[16] R.J. Hunter : "*Foundations of Colloid Science*". Vol. 1., Oxford Univ. Press, (Clarendon), London/New York, 1986.

[17] G.V. Buxton : "*Radiation Chemistry—Principles and Applications*", ed. Farhataziz and M. A. J. Rodgers, VCH Pub., Weinheim, 1987, chap. 10.

[18] J.A. Rard, M.H. Rand, G. Anderegg and H. Wanner : "*Chemical Thermodynamics of Technetium*", M. C. A.Sandino, E. Osthols, ed., Elsevier, Amsterdam, 1999.

[19] C. Sunder and H. Christensen : Nucl. Tech. **104** (1993) 403.

[20] S.P. Mezyk and Z.D. Bartels : J. Chem. Soc. Faraday Trans. **91** (1995) 3127.

[21] P. Neta, R.W. Fessenden and R.H. Schuler : J. Phys. Chem. **75** (1971) 1654.

[22] V.K. LaMer and R. Dinegar : J. Am. Chem. Soc. **72** (1957) 4847.

[23] R.E. Meyer, W.P. Arnold, F.I. Case and G.D O'Kelley : Radiochim. Acta **55** (1991) 11.

[24] T E. Eriksen, P. Ndalamba, J. Bruno and M. Caceci : Radiochim. Acta **58/59** (1992) 67.

[25] L. Vichot : PhD thesis, the University of Paris XI Orsay (2001).

[26] T. Sugimoto : J. Colloid Interface Sci. **150** (1992) 208.

(LNS Experiment : #2462, #2479)

ニッケルアルギネートマイクロカプセルによる放射性核種の除去

折谷貴幸，三村　均

東北大学大学院工学研究科　量子エネルギー工学専攻
核エネルギーフロー環境工学分野（〒980-8579　仙台市青葉区荒巻字青葉01）

Removal of Radioactive Nuclides with Nickel Alginate Microcapsules

T. Oritani and H. Mimura

Environmental Perspective on the Energy Flow, Department of Quantum Science of Energy Engineering, Graduate School of Engineering, Tohoku University, Aoba Aramaki, Aoba-ku, Sendai 980-8579

Nickel Alginate microcapsules enclosing inorganic ion-exchangers (ferrocyanide and clinoptilolite) and organic extractant (DEHPA) were prepared by gelling the kneaded sols. The metal ions of Cs^{+}, Sr^{2+}, Y^{3+}, Eu^{3+} and Am^{3+} were readily absorbed on the microcapsule within 6 h and relatively high uptake percentages above 90% was obtained. The uptake of metal ions followed a Lamgmuir-type absorption equation and uptake capacities of Cs^{+}, Sr^{2+}, Y^{3+} and Eu^{3+} were estimated to be 6.27×10^{-2}, 1.11×10^{-2}, 5.09×10^{-2} and 1.73×10^{-1} mmol/g, respectively. The microcapsules were thus effective for the simultaneous removal of radioactive nuclides from waste solutions.

§ 1．序

JOC 事故，チェルノブイリ事故，TMI 事故もしくは，原子力施設での小規模トラブル（冷却水漏れ）では，液性，核種の種類および溶液の濃度が不明瞭で複雑な組成の事故廃液が発生する。これらの事故廃液は高減容化および被曝低減化といった観点から見ても迅速な処理が求められる。過去の事故例を調べると，事故廃液を回収後，液性，核種の種類および溶液濃度を測定し，最も適した吸着除去剤を選択し処理している。このような方法では除去手順からみても迅速な処理にはならない。

以上の観点から，従来型の特定の核種に選択性を持つ吸着除去剤ではなく，あらゆる状況にも瞬時にかつ柔軟に対応でき，しかも全放射能を効率的に吸着除去できる“多元機能”を有する吸着剤が望まれている。

前報[1]では，このような吸着剤は，複数の選択性吸着剤を，バイオポリマーであるアルギネートゲルの高い包括固定能を利用し，“多元機能”を有する複合吸着剤を調製することが可能であることを示した[2-5]。

今年度の研究では，包括固定させる吸着剤および抽出剤は同一の試料を用い，攪拌法およびゲル化溶液を変化させて調製した複合吸着剤の吸着特性，キャラクタリゼーションに関しての基礎的な検討を行った。

§2. 実　　験

2.1 吸着剤および抽出剤

使用した吸着剤および抽出剤としては，前年度の研究で最も吸着効率が優れた組み合わせを用いた。Cs 選択性吸着剤としては，フェロシアン化物である NiFC，Sr および Co の吸着剤として，天然ゼオライトである Clinoptilolite（以下 CP），Y，Eu および Am の抽出剤として，DEHPA 抽出剤を使用した。第1表には，使用した交換体および抽出剤の種類と化学組成を示す。

第1表　Inorganic ion-exchangers and organic extractants enclosed in the microcapsules.

[Inorganic ion-exchangers for Cs uptake]
-Ni-ferrocyanides (NiFC) :$K_{2-x}Ni_{x/2}[NiFe(CN)_6]\cdot nH_2O$, x = 1.22

[Inorganic ion-exchangers for Sr-Co uptake]
-Clinoptilolite (Natural zeolite, CP)[a] :$Na_6[(AlO_2)_6(AiO_2)_{30}]\cdot 24H_2O$

[Organic extractants for Y-Eu-Am extraction]
-DEHPA :di-(2-ethylhexy) phosphoric acid

2.2 アルギネートによる包括固定化

アルギン酸ナトリウム（NaALG）は，和光純薬工業一級品で，粘度が500-600 cP の試薬を使用し，混練は以下の手順で行った。

1.5 wt.% NaALG（500-600 cP）溶液50cm^{3}に対して所定量の上記吸着剤（各0.1g）を混練したのち，高速遊星運動式脱泡混練装置（日本精機製作所 NBK-1）を使用し，回転数1,000 rpm，10 min で攪拌を2回行った。上記吸着剤を分散させた混練ゾルを調製し，0.5 M $NiCl_2$ 溶液に滴下した。滴下と同時に瞬時に生成したゲルポリマーを一晩熟成し，水洗後，40℃で風乾した。調製したマイクロカプセル試料の SEM 像を

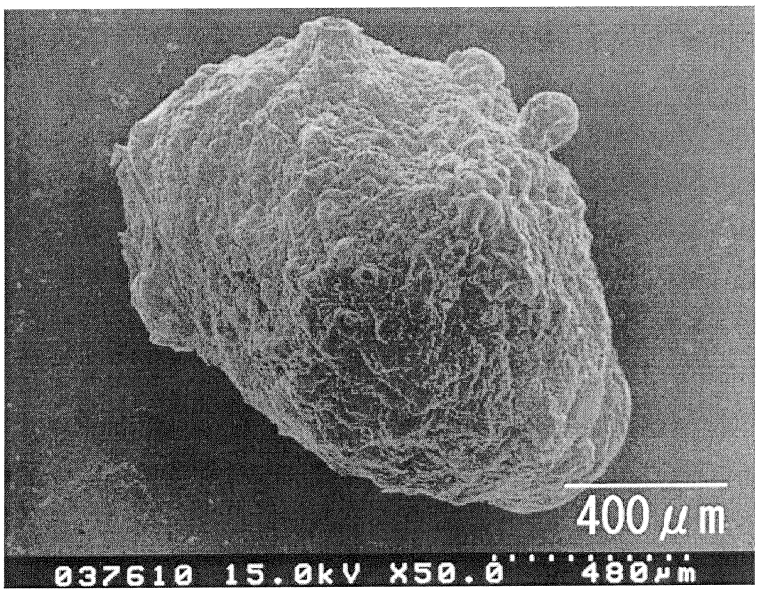

第1図　SEM image of spherical microcapsule (NiFC/CP/DEHPA/NiALG) prepared from the kneaded sol consisting of 0.1 g NiFC - 0.1 g CP - 0.1 g DEHPA and 50 cm^3 of NaALG solution (1.5 wt.%, 500～600 cP).

第1図に示す。調製したマイクロカプセルは，吸着剤および抽出剤を包括固定した直径 1 mm 程度の粒状であった。

2.3 分配実験

マイクロカプセル粒子への放射性核種の吸着率および分配係数は，バッチ法により以下の手順で求めた。ポリプロピレン製遠沈管内で，各核種の硝酸溶液（5 cm^3）とマイクロカプセル（50 mg）を25℃で1日間振とうし，上澄み液のγ放射能を NaI（Tl）シンチレーションカウンター（応用光研 Model RC-101-A）により測定した。核種の吸着率（R，%）および分配係数（K_d，cm^3/g）は，次式により算出した。

$$R = \frac{A_i - A_t}{A_i} \times 100 \ (\%) \tag{1}$$

$$K_d = \frac{A_i - A_f}{A_f} \times \frac{V}{m} \ (cm^3/g) \tag{2}$$

ここで，A_i，A_t および A_f は，初期，時間 t および平衡後の液相の放射能濃度（cpm/cm^3），m(g) はマイクロカプセルの重量，V(cm^3) は溶液の体積である。各核種の吸着速度は，一定時間毎に上澄み液をサンプリングし，その放射能を測定し，吸着率（%）の時間変化を調べた。また，V/m を変化させることで吸着等温線を作成し，マイクロカプセルの飽和吸着量を算出した。

単独溶液の測定後，今回使用した6種類の RI をすべて混合した溶液での核種の吸着率および分配係数を求めた。混合溶液の放射能は pure Ge 半導体検出器（CANBERRA, SERIES 35 PLUS）により測定し，単独溶液と同様に算出した。

実験し使用した RI として，^{137}Cs，^{60}Co および ^{152}Eu は日本アイソトープ協会から購入したものを希釈して用いた。^{241}Am は Radiochemical Center（UK）から購入した Am 酸化物を溶解して用いた。^{85}Sr および ^{88}Y は，東北大学原子核理学研究施設の LINAC の 50 MeV 制動放射線を用いて，$^{86}Sr(\gamma, n)^{85}Sr$ および $^{89}Y(\gamma, n)^{88}Y$ 反応により製造した。

§ 3．結果と考察

3.1 マイクロカプセルの分配係数（K_d）値

今回調製した Ni アルギネートで包括固定したマイクロカプセルと前年度調製した Ca アルギネートで包括固定したマイクロカプセルの K_d 値の比較を第2図に示す。1価のカチオンおよび3価のカチオンの K_d 値はほぼ同程度であるが，2価のカチオンでは大幅な改善が見られ，特に Sr に関しては K_d 値は大きく向上した。これはゲル化溶液を Ca から Ni 溶液に変えることにより，クリノプチロライトの2価カチオンに選択性が向上したためと考えられる[6]。

3.2 吸着速度

上記2種類のマイクロカプセルへの，各金属イオンの吸着速度の比較を第3図に示す。機械的な混練を行った Ni 型のマイクロカプセルでは吸着速度の改善が見られる。これは機械的な混練により吸着剤および抽出剤の粒子がより微細化し，カプセル内でより均一に分散した結果，吸着剤および抽出剤の反応面積が増加したためと考えられる。

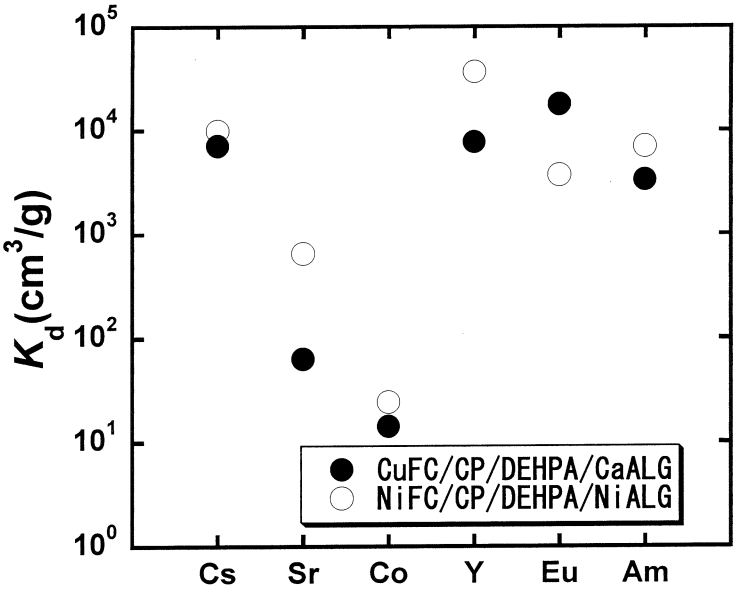

第2図 Uptake rate of various metal ions for CuFC/CP/DEHPA/CaALG (close) and NiFC/CP/DEHPA/NiALG (open) microcapsules in the presence of 10^{-2} M HNO_3. *V/m* 100 cm^3/g; carrier concn. 10 ppm, [Am^{3+}]: 2.1×10^{-9} M; 25℃.

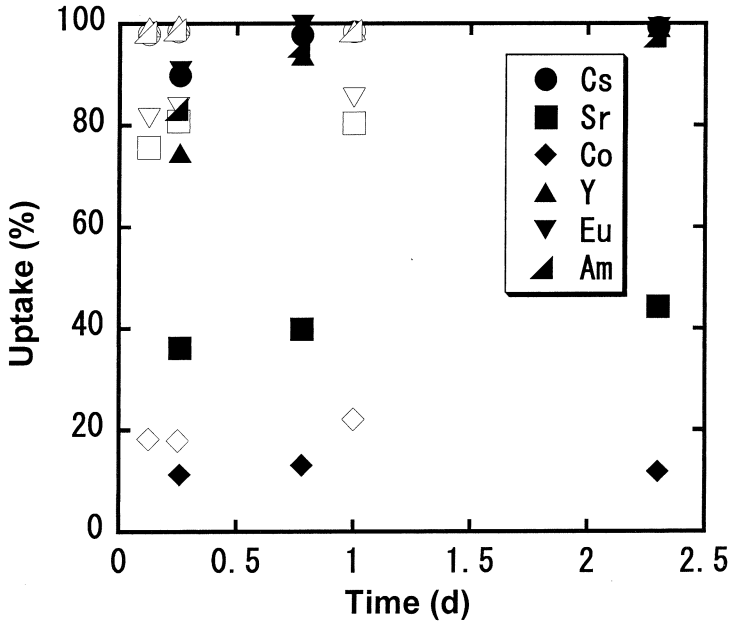

第3図 Uptake percentage of various metal ions for CuFC/CP/DEHPA/CaALG (close) and NiFC/CP/DEHPA/NiALG (open) microcapsules in the presence of 10^{-2} M HNO_3. *V/m* 100 cm^3/g; carrier concn. 10 ppm, [Am^{3+}]: 2.1×10^{-9} M; 25℃.

3.3 カプセル内での金属イオンの吸着および分布

調製したマイクロカプセルに金属イオンを吸着させ，アクリル樹脂で固定化した後，粒子断面の SEM（日立, 4100L）観察および EPMA（日立, X-650S）による EDS 分析を行った。マイクロカプセル断面の SEM 像を第４図に示し，各吸着剤および抽出剤の EDS 分析の結果を第５図に示す。各吸着剤および抽出剤は Ni アルギネートによって均一に包括固定されていることが分かる。EDS スペクトルから，各吸着剤および抽出剤への金属イオンの吸着は，NiFC および CP に Cs，CP に Sr，DEHPA に Y および Eu，ニッケルアルギネート担体に Y および Eu が取り込まれていることが分かった。なお Co に関しては EDS の定量分析の検出限界以下であった。

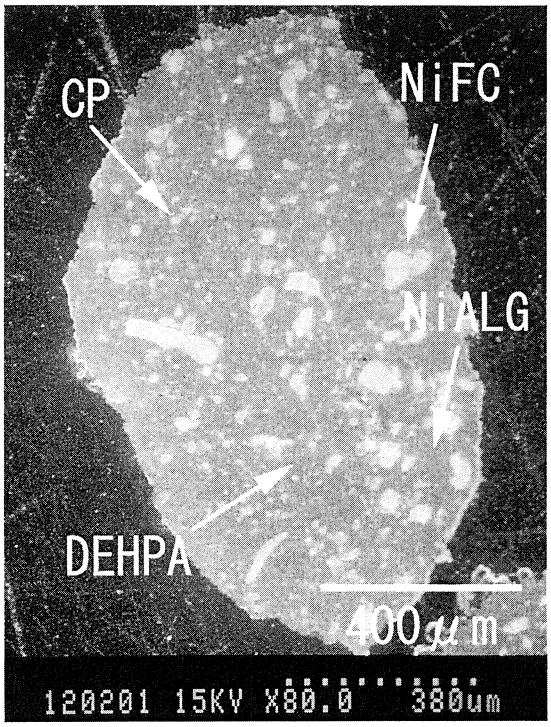

第４図　SEM image of the cross section of NiFC/CP/DEHPA/NiALG microcapsule.

3.4 飽和吸着量

第６図は各金属イオンの吸着等温線を示す。吸着等温線の形より，４種類の金属イオンの吸着は，全てラングミューア型吸着等温式に従うと推測される。ラングミューア型吸着等温式は以下の式で示される。

$$Q = \frac{KQ_{max}[M]_{eq}}{1 + K[M]_{eq}} \tag{3}$$

ここで M, Q, K および Q_{max} は，金属イオン，M イオンの平衡濃度 $[M]_{eq}$ における平衡吸着量，ラングミューア定数および M イオンの飽和吸着量である。これを展開すると以下の式で整理される。

$$\frac{[M]_{eq}}{Q} = \frac{1}{KQ_{max}} + \frac{[M]_{eq}}{Q_{max}} \tag{4}$$

この式に基づいて，各金属イオンに対しラングミューアプロットを作成し，その傾きの逆数から金属イオ

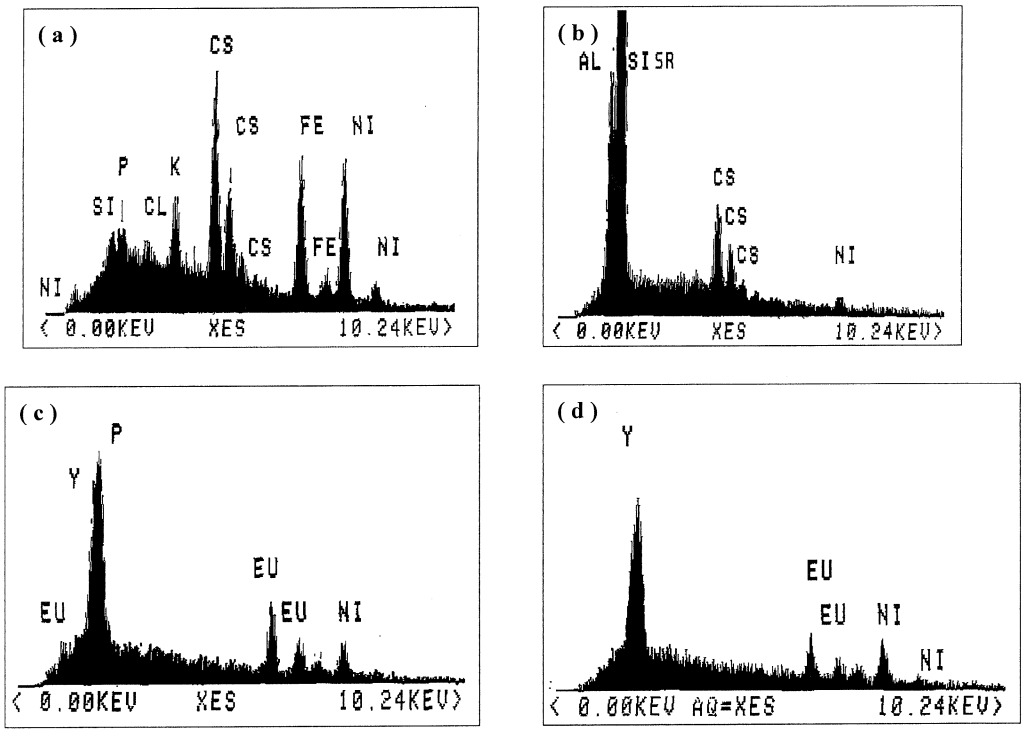

第5図　EDS spectrum of metal ions adsorbed on NiFC/CP/DEHPA/NiALG microcapsule. (a: NiFC, b: CP, c: DEHPA, d: NiALG)

ンの飽和吸着量を求めた。一例として，Yイオンのラングミューアプロットを第7図に示す。金属イオンの飽和吸着量は，Cs : 6.27×10^{-2} mmol/g，Sr : 1.11×10^{-2} mmol/g，Y : 5.09×10^{-2} mmol/g および Eu : 1.73×10^{-1} mmol/g であった。

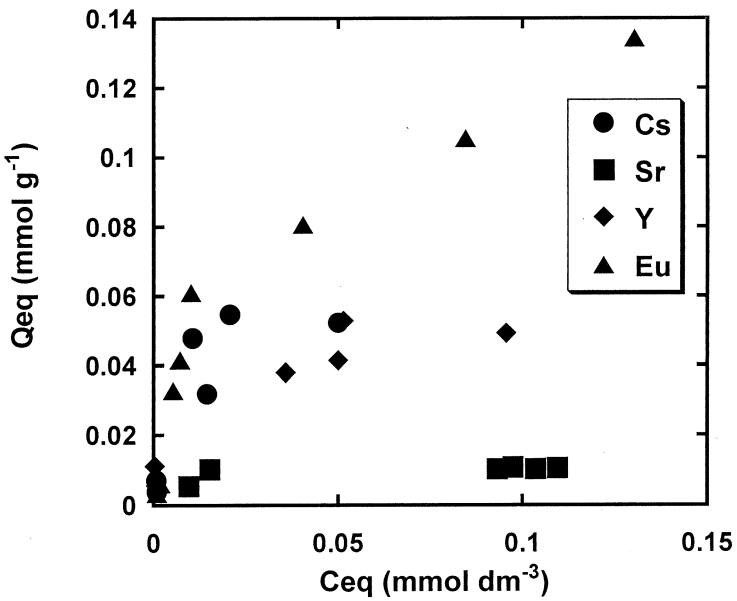

第6図　Adsorption isotherms of various metal ions for NiFC/CP/DEHPA/NiALG microcapsule.

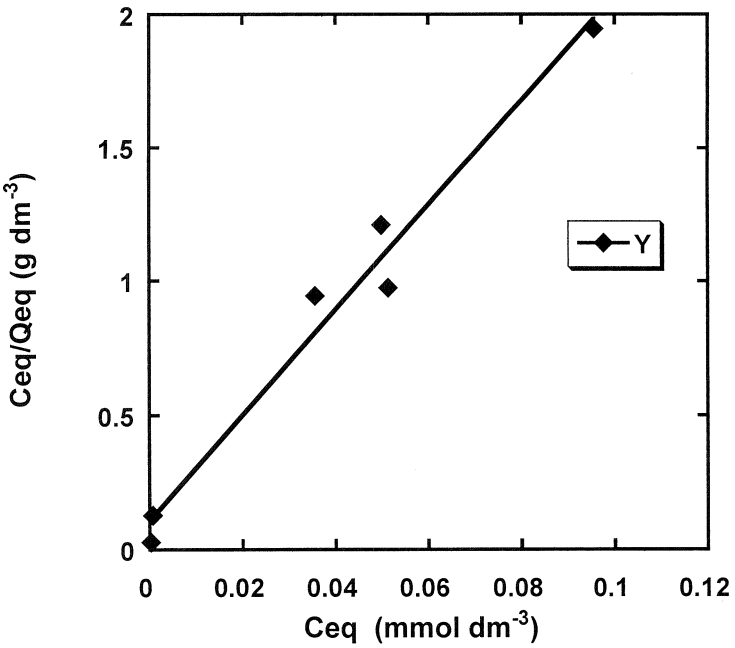

第7図　Langmuir plots for uptake of Y.

3.5　飽和吸着量の比較

EPMA の分析から，Cs の吸着に関しては DEHPA およびアルギネート部分には吸着せず，NiFC および CP のみに吸着している。このため，これらの吸着剤の飽和吸着量とアルギネートへの充填率を比較することにより，飽和吸着量の比較を行った。

アルギネートへの充填率は，アルギネートゲルの含水率を測定することにより求めた。アルギン酸ナトリウムの添加量を変化させた場合のマイクロカプセルの含水率変化を第8図に示す。

1.5 wt.% のアルギン酸ナトリウムを0.5 M $NiCl_2$ 溶液でゲル化したマイクロカプセルの含水率は約88％である。アルギネート溶液50ml に対して，各吸着剤および抽出剤を0.1g ずつ添加しているため，マイクロカプセル中の吸着剤および抽出剤の充填率は5.1％と求められる。

文献値から NiFC および CP の飽和吸着量は，1.0 - 1.5 mmol/g［7］および1.46 mmol/g［8］である。測定した Cs の飽和吸着量および吸着剤の充填率から包括固定されている吸着剤の飽和吸着量は，

$$0.063\times\frac{1}{0.034}=1.85\ (\mathrm{mmol/g})$$

と見積もることができ，吸着剤の飽和吸着量と同程度であることがわかる。この結果より，アルギネートで包括固定した場合であっても，吸着剤の性能は維持されていると考えられる。

3.6　混合溶液での吸着特性

単独溶液でのマイクロカプセルへの核種に対する吸着特性に関する結果を示したが，現実的な事故廃液では複数の核種が混合して存在していると考えられる。複数の核種が共存する場合にも吸着性能が維持されることが望ましい。

それぞれ単独の核種の溶液で求めた吸着率と，今回使用した6種類の核種を混合した溶液で求めた吸着速

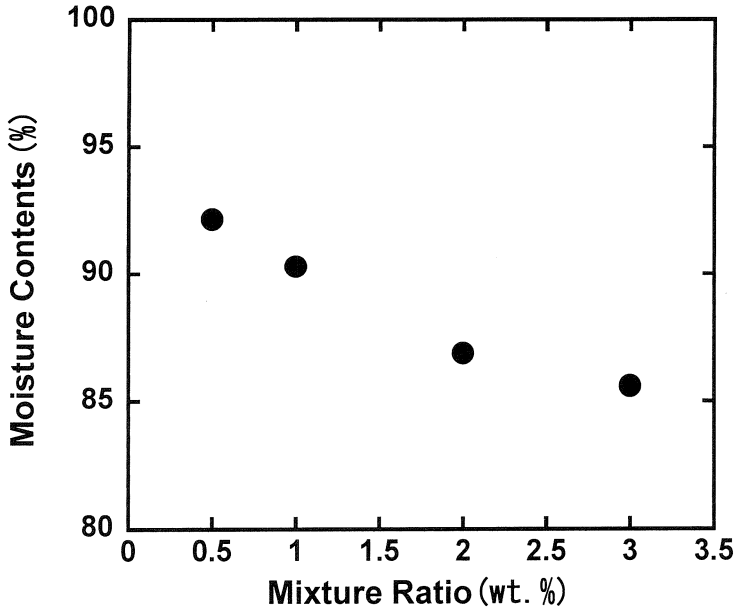

第8図　Moisture contents of gel particle (without inorganic-exchangers and organic-extractant).

度の比較を，第9図に示す。測定は NaI(Tl) シンチレーションカウンターおよび pure Ge 半導体検出器を用いており，検出効率の違いはあるが，ほぼ同程度の分配係数および吸着速度が得られた。以上のことから，本研究で調製したマイクロカプセルは，全ての放射性核種を除去できる可能性がある。

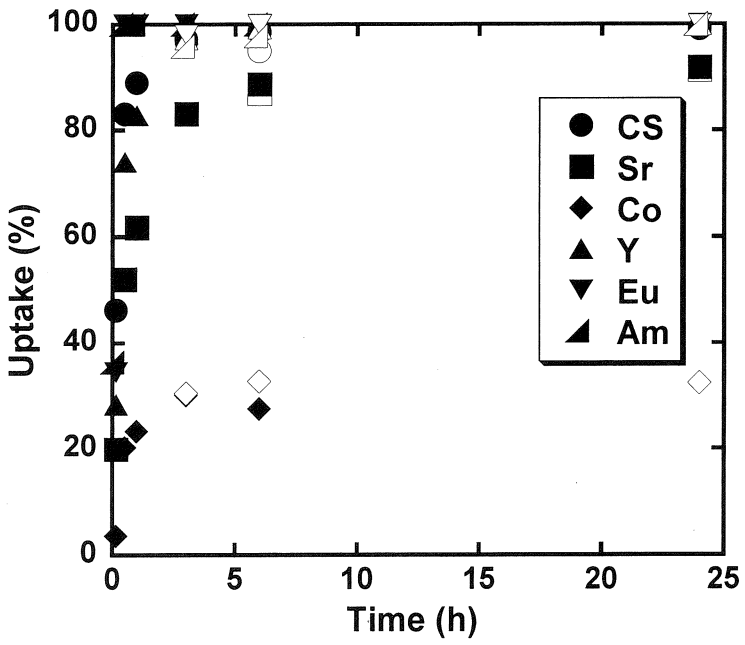

第9図　Uptake rate of various metal ions for microcapsule in the single (open) and mixed solutions (close).

§4. まとめ

（1） ゲル化溶液および混練法を変化させることにより，吸着速度および核種の分配係数を向上させることが可能であった。

（2） 吸着速度および分配係数を測定した結果，すべての核種は6時間程度で平衡に到達した。Cs，Sr，Y，Eu および Am の吸着率は90％以上の高い値が得られたが，Co の吸着率は40％程度であった。10^{-3} M HNO_3 共存下での K_d 値は，Cs: 1.1×10^4, Sr: 1.0×10^3, Co: 4.7×10, Y: 5.1×10^4, Eu: 6.5×10^4 および Am: 9.8×10^4 cm^3/g であった。

（3） マイクロカプセル断面の EDS スペクトル分析から，NiFC および clinoptilolite に Cs^+，clinoptilolite に Sr^{2+}，DEHPA に Y^{3+} および Eu^{3+}，NiALG に Y^{3+} および Eu^{3+} が取り込まれていることが確認された。

（4） マイクロカプセルの飽和吸着量は，Cs：6.27×10^{-2} mmol/g，Sr：1.11×10^{-2} mmol/g，Y：5.09×10^{-2} mmol/g および Eu：1.73×10^{-1} mmol/g であった。また包括固定した吸着剤と調製したマイクロカプセルの飽和吸着量の比較から，アルギネートで包括固定した場合でも吸着剤の性能は維持されていることが分かった。

（5） 複数の核種を混合した溶液と，単独溶液での吸着結果はほとんど差が認められなかった。

（6） 今後の課題としては，飽和吸着量をより向上させるためマイクロカプセルに固定する吸着剤および抽出剤の限界量を明らかにする必要がある。

§5. 謝　辞

本研究を行うにあたり，RI の製造でお世話になった東北大学原子核理学研究施設の大槻勤博士およびマシングループの皆様方に感謝したします。また，マイクロカプセル試料の SEM および EPMA 測定に際し，東北大学多元物質科学研究所技術室の佐藤雄孝，釜谷隆技官に協力していただき，感謝いたします。

参　考　文　献

[1] H. Mimura, T. Oritani and K. Akiba : Research Report of Laboratory of Nuclear Science, Tohoku University **35** (2002) 56.

[2] D.A. Rees and E.J. Welsh : Angew. Chem Int. Ed. Engle. **16** (1997) 214.

[3] H. Mimura and Y. Onodera : "*Proc. of ICEM'01*" (2001).

[4] H. Mimura, H. Ohta, H. Hoshi, K. Akiba and Y. Onodera : Sep. Sci. Technol. **36** (2001) 31.

[5] H. Mimura, K. Akiba and Y. Onodera : "*Proc.of WM'02*" (2002).

[6] D. W. Breck : "*Zeolite Molecular Sieves*", Robert. E, Krieger Publishing Compary Florida, 1984, p559.

[7] H. Mimura, N. Kageyama, K. Akiba, M. Yoneya and Y. Miyamoto : Solvent Extraction and Ion Exchange, **16** (1998) 1013.

[8] H. mimura and T. kannno : SCI. REP. RITU, A-Vol. **30**, No.1 (1981).

(LNS Experiment : #2454, #2471)

アトミックトランスポート機構に依存する銅の自己拡散パラメーター

藤川辰一郎

東北大学大学院工学研究科 (980-8579 宮城県仙台市青葉区荒巻字青葉02)

Diffusion Parameters Dependent on Atomic Transport Mechanism for Self-diffusion in Copper

S.-I. Fujikawa

Graduate School of Engineering, Tohoku University, Sendai 980-8579

The self-diffusion coefficients of Cu in copper single crystals in the temperature range from 980 K to 1351 K were determined by the serial sectioning method using the self-made tracer ^{67}Cu. The temperature dependence is expressed by $D = 2.62\times10^{-5}\ \exp(-199\ \mathrm{kJmol^{-1}}/RT)\ \mathrm{m^2/s}$. A slight curvature was observed in the Arrhenius plot of the self-diffusion coefficients near the melting of copper. The result was analyzed using the monovacancy-divacancy model, showing that the contribution of divacancy to the self-diffusion in copper at high temperature range near the melting of copper cannot be ignored. The self-diffusion coefficients in the present work were compared with the other copper self-diffusion works for volume diffusion, grain boundary diffusion, surface diffusion, diffusion in nanocrystal and liquid of copper.

§ 1. はじめに

原子の拡散は基本的な物性現象の一つであり，あらゆる材料の製造工程および使用条件下において重要な役割を担っている。銅および銅合金の分野においても，拡散に関する情報が役に立つ研究テーマとしては，鋳塊の熱処理，加工熱処理，伸銅品の熱処理，焼結，拡散接合，クラッド材製造，各種の脆化，回復・再結晶，結晶粒微細化，時効析出，酸化，腐食，応力腐食割れ，ハンダ接合での界面反応，不純物の粒界偏析，表面偏析，熱間加工時の組織制御，超微細結晶粒組織の熱的安定性，銅配線膜でのエレクトロマイグレーションおよびSn合金メッキの密着性など多岐に亘っている。その場合に関係する拡散としては，純銅および銅合金中の自己体拡散および自己粒界拡散だけでなく，純銅および銅合金と他金属との相互拡散および反応拡散，純銅および銅合金中の合金元素および不純物元素の不純物体拡散および不純物粒界拡散ならびに水素および酸素の拡散などがある。

本研究では最も基本的なデータである銅の自己体拡散係数の精密測定を行うことを目的としている。銅の自己体拡散係数に関しては，すでにいくつか発表されているが[1,2]，いずれも古く再測定が必要になっている。実験的には，銅の自己拡散の研究にとっては最適であるが，市販されておらず，極めて入手が困難な放

射性トレーサー ^{67}Cu（半減期62時間）を電子ライナックによって自ら製造し，それを用いて拡散係数を測定する。さらに，得られた結果とすでに発表されている銅の各種の自己拡散，すなわち体拡散，粒界拡散および表面拡散ならびにナノ結晶および液体銅中の銅の拡散と比較検討した。

§ 2．実験方法

2.1 拡散実験用の銅試料の作製

純銅の単結晶を純度99.999%の銅のインゴットから，第1図に示した自作の装置を用い，細心の注意を払ってブリッジマン法で作製した。育成した単結晶の形状は丸棒であり，その直径は 6 mmそして長さは130 mm

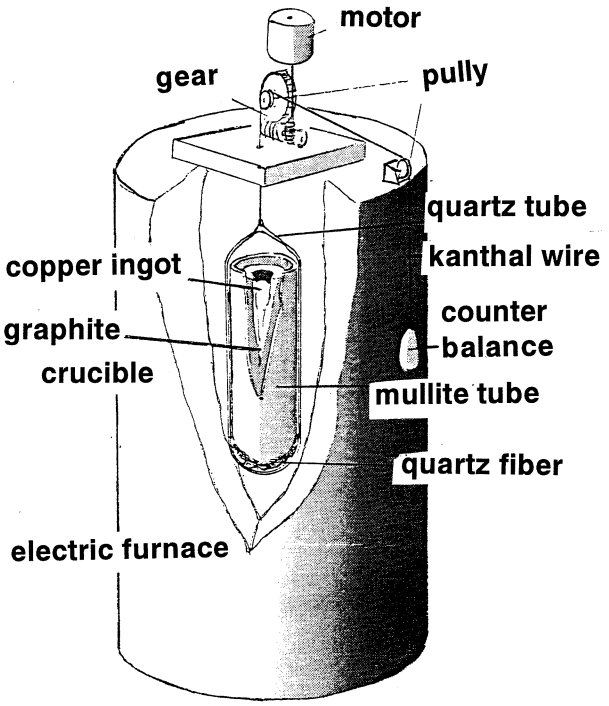

第1図　Schematic diagram the equipment for Bridgman process used in the present work.

である。さらに，精密切断機により長さ11 mmの円柱状の拡散試料を作製した。背面反射 Laue 法により，単結晶であることを確認した。転位拡散の影響を最小限にするために，1300 K で H_2 ガス中 10^5s の予備焼鈍を行った。ダイヤモンドペーストを用いた機械的な研摩，$H_3PO_4 : HNO_3 : H_2O = 4 : 3 : 3$ の組成の水溶液による化学研摩および最終的に $H_3PO_4 : H_2O = 8 : 2$ の組成の水溶液を用いた電解研摩を行い拡散試料とした。

2.2 放射性トレーサーの調製

本研究で用いた放射性トレーサー ^{67}Cu は，天然同位体組成を持つ99.999%の純度の Zn 金属の小片を照射ターゲットとして用い，^{68}Zn（γ，p）核反応で製造した。東北大学原子核理学研究施設に設置されている電子ライナック加速器による制動輻射の方法を用いた。γ線照射したままの Zn ターゲット中には，極微量の Cu の同位体が含まれるため，本研究では溶媒抽出法およびイオン交換法で純粋の銅同位体を無担体で分離精製した[3,4]。その分離精製過程の各段階のチエックには，高性能の Ge (Li) 半導体検出器によるγ線スペクトルの測定によって行った。第2図および第3図は，それぞれ照射直後および最終的に精製した銅同位体のγ線スペクトルを示している。第2図と第3図との比較から，分離精製によって，Zn 金属が完全に除去

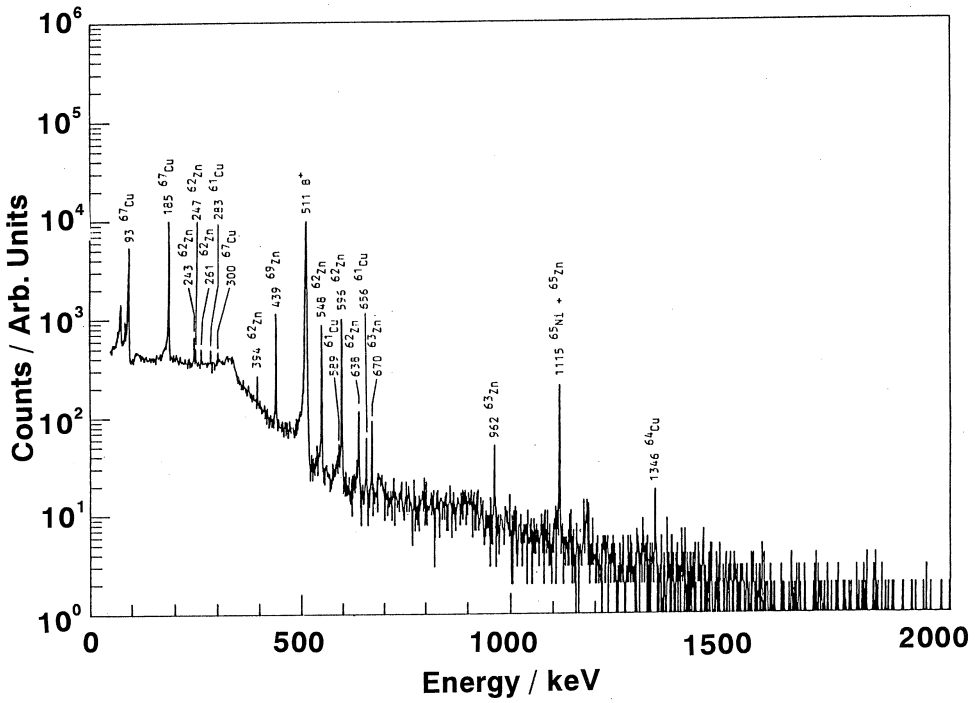

第２図　γ-ray spectrum measured for initial zinc target after bremsstrahlung irradiation.

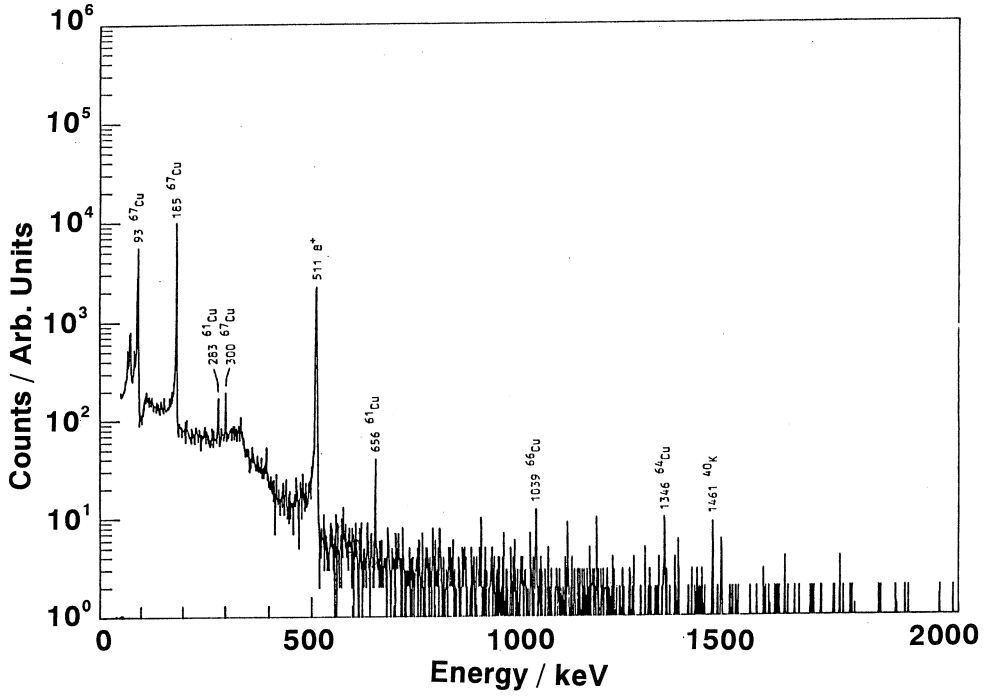

第３図　γ-ray spectrum measured for finally purified radioactive tracer of copper.

されていることが，Zn の同位体の有無からわかる。さらに，Cu の同位体として，^{67}Cu 以外により短寿命の ^{61}Cu および ^{64}Cu が同時に生成していることがわかる。その３種の同位体を利用して，銅における自己拡散の同位体効果の研究をすることが出来る。本研究では，^{61}Cu および ^{64}Cu が十分に減衰した時点で，^{67}Cu を用いて自己拡散係数を決定した。

2.3 拡散実験

電解研摩された試料端の片面に放射性トレーサーを電着法で薄く付着させた。トレーサーを付着した試料を，高真空にした後に高純度の He ガスを少量入れた石英管中に封入した。980～1351 Kの温度範囲で拡散焼鈍を行った。その場合，試料温度を正確に測定するために，熱電対が石英管内の試料に密着するような工夫を行った。拡散焼鈍後のトレーサーの濃度分布の測定はシリアルセクショニング法で行った。なおこの方法では，拡散試料を拡散方向に垂直に少しずつ多段階に亘ってセクショニングし，その削りとつた薄片の放射能強度を測定し，トレーサー分布を決定する。セクショニングは第４図に示した金属試料用の大型滑走式精密ミクロトームで行った。削りとつた薄片の質量を精密天びんで測定し，それと試料直径および銅の密度の値からセクショニング距離を計算した。さらに，その薄片に含まれるトレーサーの量を Ge (Li) 半導体検出器で，第５図に示したような決定法で正味の ^{67}Cu の放射能強度を試料オートチエンジャーで測定した。

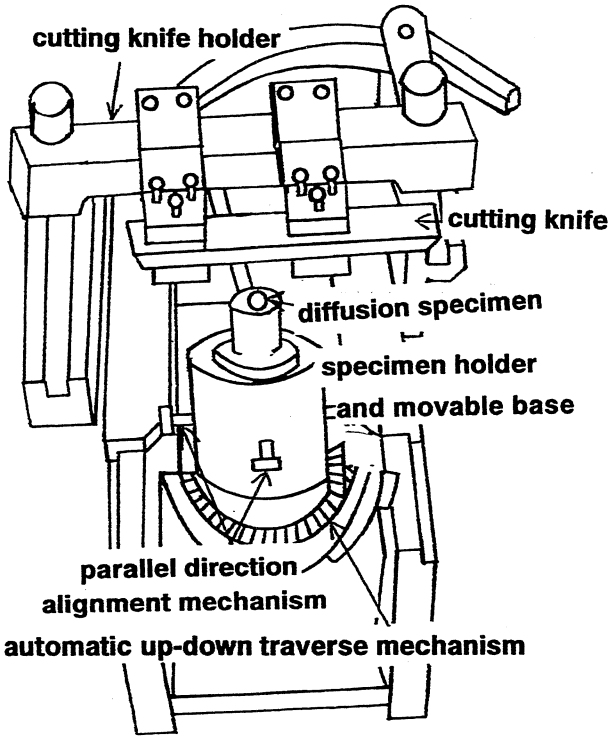

第４図　The schematic diagram of microtome equipment for serial sectioning of diffused specimens.

§ 3．実験結果

本研究のような拡散の薄層源の初期条件に対しては，Fick の拡散の第２則の解は次式で与えられる：

$$c\,(x, t) = c_0 \exp(-x_n^2/4D^*t), \tag{1}$$

ここで $c\,(x, t)$ は削りとった薄片の非放射能強度，x_n は薄片の中心位置から最初の表面までの距離，そして D^* は拡散係数である。さらに，t は拡散時間，そして c_0 は定数である。式 (1) によれば，拡散浸透曲線すなわち $c\,(x, t)$ 対 x_n^2 プロットは直線になり，その傾きから D が得られる。第６図はセリアルセクショニング法で測定した ^{67}Cuの拡散浸透曲線の典型的な結果の例である。第７図はそのようにして得られた銅の自己拡散係数の温度依存性をアレニウスプロットとして示した。そのような拡散係数の温度依存性を１本のアレニウ

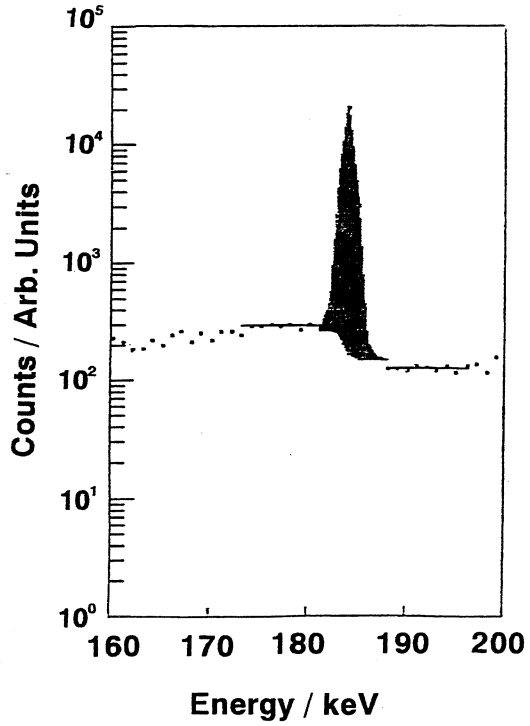

第5図　Net γ-peak area of ^{67}Cu used for diffusion study.

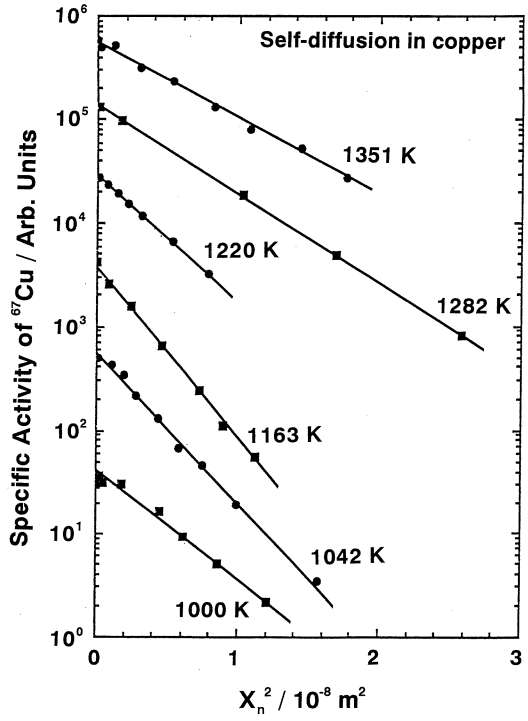

第6図　Typical penetration profiles of diffusion of ^{67}Cu in copper single crystals.

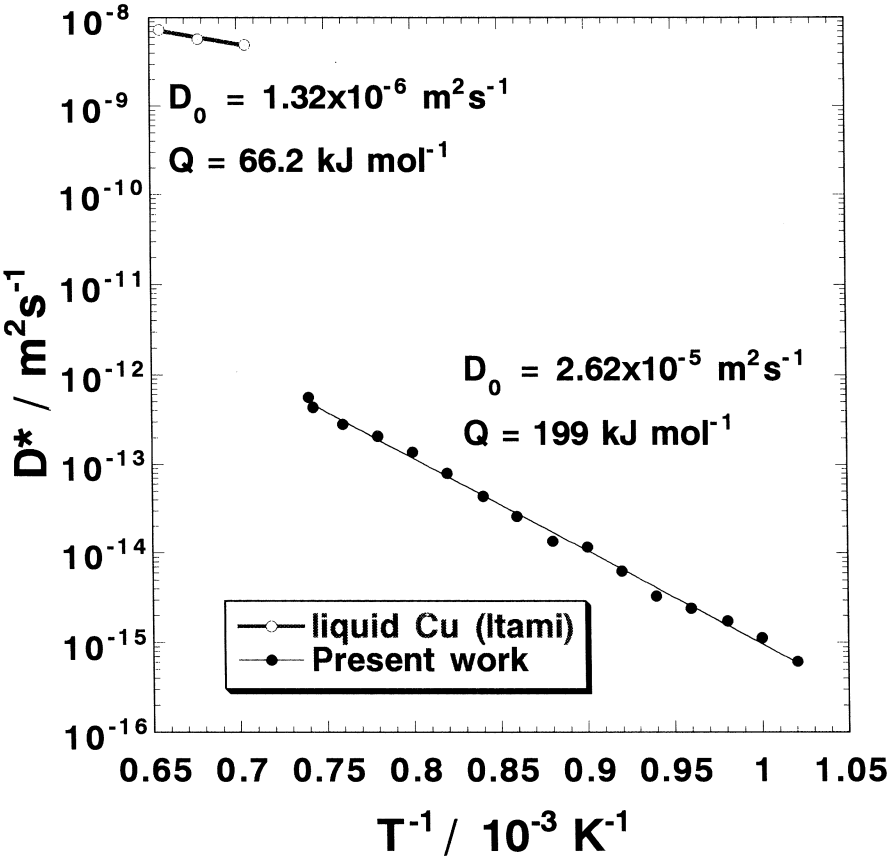

第7図　Temperature dependence of self-diffusivities of copper obtained in the present work, in comparison with the data for self-diffusivities in liquid copper.

スプロットで表現できるとした結果を，よく知られた次式に当てはめて得られた振動数項 (D_0) および拡散の活性化エネルギー (Q) を第1表に示した。

$$D^* = D_0 \exp(-Q/RT) \ \mathrm{m^2/s} \tag{2}$$

§4．考　　察

4.1　各種の銅の自己拡散と本研究結果との比較

第1表には，本研究結果とともに，銅における各種の自己拡散に関する現在信頼できると思われる結果[5-9]と比較して示した。ここで液体拡散係数 (D_l)，表面拡散係数 (D_s) およびナノ結晶での拡散係数 (D_n) の温度依存性は，式(2)に類似した式で表される。一方，粒界拡散係数 (D_b) の温度依存性は以下のように表される[10,11]。

$$\delta D_b = (D_b)^0 \exp(-Q_b/RT) \ \mathrm{m^3/s} \tag{3}$$

ここで δ は粒界の幅であり，$(\delta D_b)^0$ は振動数項である。$(D_b)^0$ は粒界拡散の活性化エネルギーである。さらに，通常は δ =0.5nm として D_b が計算される。第1表から，本研究で得られた自己体拡散の D_0 および Q は他研究者によるそれとほぼ一致しているが，それらより若干小さい値になっている。銅における自己体拡散の Q はその粒界拡散，および表面拡散ならびに銅のナノ結晶における自己拡散係数および無対流の下で測

Table 1. The diffusion parameters for various self-diffuson of copper

diffusion	purity	prexponential factor, D_0 (m^2/s)	Q (kJ/mol)	temperature range (K)	references
volume	5N	2.62×10^{-5}	199	980 - 1351	Present work
volume	5N	7.8×10^{-5}	211	973 - 1333	Ref. 1
volume	Al<10 ppm, Zn<10 ppm, Mo<5 ppm	8.70×10^{-5}	212	1010 - 1352	Ref. 2
grain boundary	5N8	$3.89\times10^{-16*}$	72.5	993 - 1339	Ref. 5
grain boundary	5N	$1.16\times10^{-15*}$	84.8	1057 - 1246	Ref. 5
surface		2.6×10^{-5}	86.6	773 - 1233	Ref. 6
surface	4N7	6.3×10^{-5}	114	1163 - 1288	Ref. 7
nanocrystal		3×10^{-9}	61.8	293 - 393	Ref. 8
liquid copper		1.32×10^{-6}	61.8	1419 - 1525	Ref. 9

*$(\delta D_b)^0$, (m^3/s)

定された液体銅における真の自己拡散係数よりもかなり大きく，体拡散速度が極めて小さいことがわかる。第１表に示した各種の拡散パラメーターを用いて，銅における低温（573K）および融点での各種の拡散係数を計算した結果を第２表に示した。この結果によると，本研究で得られたD_0およびQから計算した低温でのD^*は他の研究者によるD_vよりも僅かながら大きいが，D_b, 表面拡散係数D_s, およびナノ結晶中の拡散係数D_nよりもかなり小さいことがわかる。またD_nはD^*よりも極めて大きく，D_bおよびD_lよりも僅かながら小

Table 2. Comparison of various self-diffusivities of copper.

diffusion	D (m^2/s)		references
	573 K	1356 K	
volume	1.9×10^{-23}	5.66×10^{-13}	Present work
volume	4.27×10^{-24}	5.66×10^{-13}	Ref. 1
volume	4.20×10^{-24}	5.99×10^{-13}	Ref. 2
grain boundary (5N8)	1.93×10^{-13}	1.26×10^{-9}	Ref 5
grain boudary (5N)	4.36×10^{-14}	1.26×10^{-9}	Ref. 5
surface	3.3×10^{-13}	2.58×10^{-9}	Ref. 6
nanocrystal	6.98×10^{-15}		Ref. 8
liquid copper		3.72×10^{-9}	Ref. 9

さいことは興味深い。融点では，３種のD^*はほぼ一致している。その場合，D_b, D_sおよびD_lがオーダー的に一致していることは拡散機構を考える上で重要と思われる。

4.2 アレニウスプロットの曲がりおよび複空孔の寄与

一般にfcc金属の単結晶における自己体拡散係数の温度依存性は，いわゆる単空孔-複空孔モデルによると，式(2)のような１本のアレニウス式に代わって，厳密には次式で表される[12]。

$$D^* = D^{1V} + D^{2V}$$
$$= D_0{}^{1V} \exp(-Q^{1V}/RT) + D_0{}^{2V} \exp(-Q^{2V}/RT) \quad (4)$$

ここではD^{1V}およびD^{2V}は単空孔および複空孔による自己体拡散係数である。式(4)の後半の式はD^{1V}およびD^{2V}に対応するアレニウス式である。式(5)を第7図に示した測定結果に当てはめ，回帰分析によって 式(5)の各パラメーターを求めると，次式のようになる。

$$D^{1V} = 1\times10^{-5} \exp(-192\ \mathrm{kJmol^{-1}}/RT)\ \mathrm{m^2/s} \quad (5)$$

$$D^{2V} = 8\times10^{-2} \exp(-300\ \mathrm{kJmol^{-1}}/RT)\ \mathrm{m^2/s} \quad (6)$$

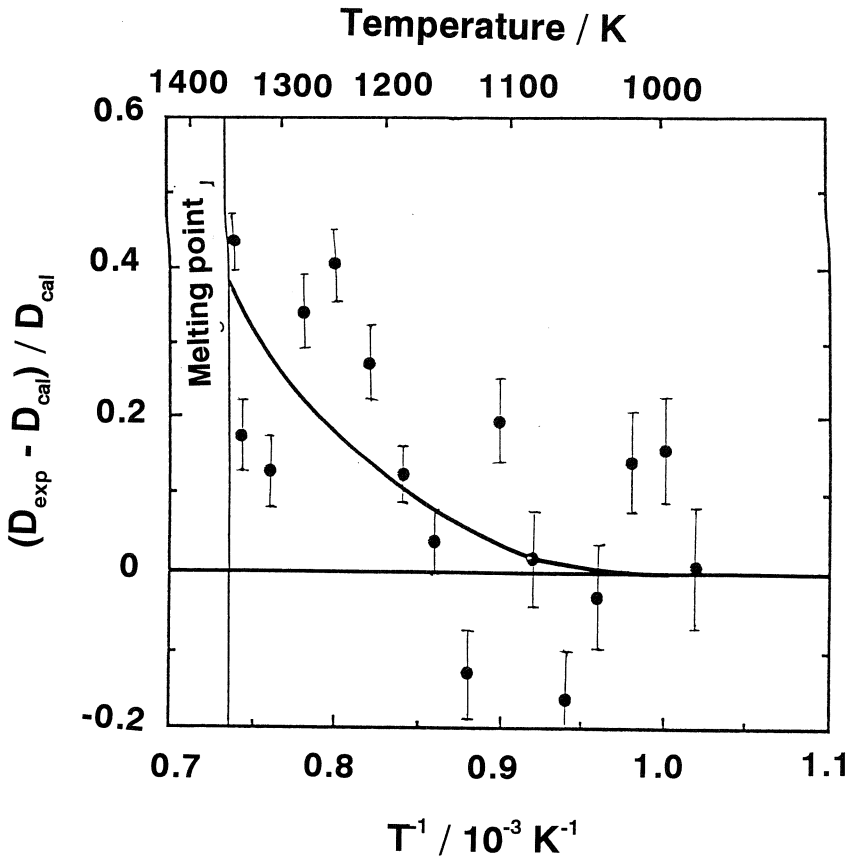

第8図　The deviation of the individual experimental self-diffusivities from the calculated values for monovacancy diffusion.

式(5)を用いて第7図中の測定データを解析した結果を第8図に示した。縦軸は$(D_{exp}-D_{cal})/D_{cal}$である。ここで$D_{exp}$および$D_{cal}$はそれぞれ測定値および式(5)による計算値である。約1200K以上の温度で誤差範囲を考慮しても，複空孔の寄与が無視できないことがわかる。この結果から融点での複空孔の寄与(D^{2V}/D^*)を見積もると，それは最大で約40％になる。本研究と関連して行った結果を第3図に示した3種の銅の同位体を用いて，同じ試料について測定した同位体効果係数（E）の温度依存性の結果[13,14]によると，銅の自己拡散に対するEは1250 K以上の温度では温度の上昇につれて徐々に減少する。この結果は第8図から予想された結果と対応している。

§5. 結　論

ブリッジマン法を用いて99.999%Cuから銅単結晶を作製し，さらにCuの拡散係数の測定に適した放射性トレーサー^{67}Cuを調製し，Cuの自己体拡散を細心の注意を払って研究した。得られた結果は次の通りである。

(1) セリアルセクショニング法で980～1351Kの温度範囲で自己体拡散係数を決定した。

(2) 拡散係数の温度依存性を1本のアレニウスプロットで表現できるとした求めた結果によると，その温度依存性は，$D = 2.62\times10^{-5}\exp(-199\ \mathrm{kJmol^{-1}}/RT)\ \mathrm{m^2/s}$ で表される。

(3) 単空孔 - 複空孔モデルで自己体拡散係数の温度依存性を解析し，融点近傍の高い温度ではCuの自己拡散への複空孔機構の寄与が無視できないという結果を得た。

(4) 本研究で得られた自己体拡散係数と他研究者によるCuの自己体拡散係数，自己粒界拡散係数および自己表面拡散係数ならびに液体銅および銅のナノ結晶における自己体拡散係数とを比較検討した。

謝　辞

銅の放射性同位元素の製造は，東北大学大学院理学研究科原子核理学研究施設の電子ライナックを用いて行ったものであり，同施設のマシングループに支援を頂いた。さらに，本研究の一部は㈱日本伸銅協会内伸銅技術研究会の「銅及び銅合金研究助成」の援助を受けて行ったものである。

参　考　文　献

[1] S.J. Rothman and N.L. Peterson : Phys. Stat. Sol., 35 (1976), 305.

[2] D. Bartdorf, G. Neumann and P. Reimers, Phil. Mag., 38 (1978), 157.

[3] M. Yagi and K. Kondo : Int. J. Appl. Radiat Isotopes, 29 (1978), 756.

[4] 藤川辰一郎：核理研報告, 12 (1979), 229.

[5] T. Surholt and C. Herzig : Acta Mater., 45 (1997), 3817.

[6] H.P. Bonzel and N.A. Gjostein : cited in "*Diffusion in Copper and Copper Alloys, Part. 1. Volume and Surface Self-diffusion in Copper*", ed. D.B. Butrymowicz *et al.*, J. Phys. and Chem. Ref. Data, 2 (1974), 64.

[7] K. Hohne and R. Sizmann : Phys. Stat. Sol. A 5 (1971), 577.

[8] J. Horva'th, R. Birringer and H. Gleiter : Sol. State Comm., 62 (1987), 319.

[9] 伊丹俊夫ら：「高融点金属複雑融体の拡散の研究」,宇宙開発事業団技術報告, TR-IAロケット微小重力実験 - 7号機実験成果報告, (2001), 宇宙開発事業団.

[10] 藤川辰一郎：「拡散の基礎（その1）」,（その2）, 軽金属, 46 (1996), 202, 254.

[11] LANDOLT-BORNSTEIN, New Series, Group III, vol. 26, "*Diffusion in Solid Metals and Alloys*", ed. H. Mehrer, Springe-Verlag, p 630, p 717.

[12] 例えば，藤川辰一郎：「金属における拡散」, シュプリンガー・フェアラーク東京, 近刊, 全350頁. 原著作（Th. Heumann : *Diffusion in Metallen, Grundlagen, Theorie, Vorgaenge in Reinmetallen und Legierungen, Unter Mitarbeit von H. Mehrer*, Springer-Verlag, 1992）の完訳.

[13] 藤川辰一郎：第42回銅及び銅合金技術研究会講演会講演概要集, (2002)163.

[14] S. Ushino and S.-I. Fujikawa：submitted to Phil. Mag.

(LNS Experiment : #2311, #2329, #2346, #23681, #2382, #2402, #2421, #2439)

Chemistry of Carrier-free ^{7}Be Isotope for Diffusion in Metals

S.-I. Fujikawa[1], H. Yuki[2] and T. Ohtsuki[2]

[1]*Department of Material Science, Faculty of Engineering, Tohoku University, Aramaki, Aoba, Sendai 980-8579*
[2]*Laboratory of Nuclear Science, Tohoku University, Mikamine, Taihaku, Sendai 982-0826*

Carrier-free ^{7}Be has been produced respectively by ^{7}Li(p,n)^{7}Be and ^{10}B(γ,p2n)^{7}Be (as well as ^{11}B(γ,p3n)^{7}Be) reactions using the Cyclotron and Electron Linear Accelerator. Radiochemical methods for purification of the carrier-free radioactive ^{7}Be isotope from the irradiated lithium and boron compounds
have been investigated. A simple separation scheme is proposed.

§ 1. Introduction

The ^{7}Be radioisotope (53.2 days of half-life and γ emitter of 478 keV γ-ray) is a greatly important radioisotope for physical and/or chemical studies as a tracer for a diffusion process [1] in materials science and environmental research [2], etc. due to the appropriate half-life and the simple nuclear structure. The ^{7}Be isotope can be produced by using nuclear reactions, namely ^{7}Li(p,n)^{7}Be with a Cyclotron, ^{12}C(γ,α)^{7}Be or ^{10}B(γ,p2n)^{7}Be (a photonuclear reaction) with an electron linear accelerator, respectively. For a separation method of ^{7}Be radioisotope produced from a irradiated target, several methods have been presented so far, however, the methods are including complex procedures and needs a longer time in some cases [3-5]. Therefore, it is desired that an easier and less troublesome technique is developed to separate the carrier-free ^{7}Be isotope from the target materials.

In the present work, we show a convenient method for the preparation of carrier-free ^{7}Be isotope by using a cation-exchange column alone, for the samples produced by ^{7}Li(p,n)^{7}Be and ^{10}B(γ,p2n)^{7}Be (^{11}B(γ,p3n)^{7}Be) reactions.

§ 2. Experimental Procedure

Two different reactions were used in order to produce the carrier-free ^{7}Be isotope, one for the ^{7}Li(p,n)^{7}Be with a cyclotron and another for ^{10}B(γ,p2n)^{7}Be (as well as ^{11}B(γ,p3n)^{7}Be) with Linear electron accelerator, respectively.

1) For the ^{7}Li(p,n)^{7}Be reaction, about 50 mg of a highly purified lithium carbonate, a powder form of Li_2CO_3 (99.997 mass %), was pressed in a disk form and used as a target. The Li_2CO_3 disk was wrapped in a pure aluminum foil of 10 μm in thickness for irradiation. The irradiation with 16 MeV protons was performed at the Cyclotron Radio-Isotope Center, Tohoku University. The beam current was typically 1 μA and the irradiation time was about 6 hours. The sample was cooled with He-gas during irradiation.

2) For the ^{10}B(γ,p2n)^{7}Be (^{11}B(γ,p3n)^{7}Be) reaction, about 50 mg of boric acid, a powder form of

H_3BO_3 (99.997 mass %), was also wrapped in a pure aluminum foil of 10 μm in thickness and sealed in a quartz tube of 10 mm in diameter as a target. The irradiation with the bremsstrahlung (50 MeV electrons) was carried out at the Electron Linear Accelerator, Laboratory of Nuclear Science, Tohoku University. The pulse width of the electron beam was 3 μs, and the repetition rate was 300 pulses/s. The sample in a quartz tube was placed horizontally on the axis of the electron beam in close contact with the back of a platinum converter with 2 mm in thickness and cooled by running tap water. The average beam current was 130 μA for 50 MeV-electrons during the irradiation for 6 hours.

The irradiated Li_2CO_3 (^{7}Be) and H_3BO_3 (^{7}Be) targets were transferred into separate beakers of 100 ml and were dissolved in a small volume of 6N hydrochloric acid (HCl). Then, two solutions were evaporated to dryness by using an infrared lamp and a hot plate to convert to the chlorides. The chlorides, namely Lithium chlorides and Boron chlorides, were found to have a white porous crystal. Both the chlorides were dissolved again in 3 ml of 0.05 N HCl to charge the column. A Dowex 50W × 8 (100-200 meshes) resin was used in H^+-form which had previously been equilibrated with 0.05 N HCl. The resin column used here was 10 mm in diameter and 100 mm in length.

Firstly, for the irradiated sample of Li_2CO_3 (^{7}Be), the solution of 3 ml (0.05 N HCl) included the irradiated materials was charged in the column and added 5-column volumes of 0.05 N HCl. All elution treatments were performed at a constant flow rate of 1 ml/min. While the solution was passed through the cation-exchange column, the ^{7}Be and Li ions were absorbed on the resin bed. Then, after adding 5-column volumes of 0.7 N HCl for the column of Li_2O_3 (^{7}Be), the eluted fraction was collected in a beaker and dried up to check whether a residue has remained in the bottom. A white porous crystal of the Li chlorides was also remained in the beaker. The radioactivities of the porous crystal were measured with a high-pure Ge-detector. It was found that no activities were observed in the residue crystal (the Li chlorides). Finally, 3-column volumes of 3N HCl was added in the column to elute the ^{7}Be isotope. All the fraction was collected in the test tube by 4 ml and evaporated to dryness. No residue such as a white-porous crystal of Li chlorides was seen in the bottom of the test tubes. However, the radioactivities (^{7}Be) alone were observed in the test tubes.

Similar procedures were applied for the irradiated sample of H_3BO_3 (^{7}Be). After adding 5-column volumes of 0.05 N HCl for the column, the eluted fraction was collected in a beaker and dried up to check the Boron crystal. A white porous crystal was also confirmed in the beaker. The radioactivities were measured with a Ge-detector, but no activities were also observed in the crystal. We found that the ^{7}Be isotope alone was kept in the resin bed with 0.05 N HCl. After the ^{7}Be isotope was eluted into the test tubes with 5-column volumes of 3N HCl, the radioactivities of the fractions were also measured. It was also found that the ^{7}Be isotope were observed in the test tubes.

§ 3. Results and Discussion

The γ-ray of each eluted fraction in samples was measured with a Ge-detector. One of the spectra for the ^{7}Be fractions from the column of Li_2O_3 (^{7}Be) was shown in Fig. 1. The photopeak corresponding to ^{7}Be (the 478 keV γ-ray) was observed and no other radioactivities from the impure materials (a contaminant such as copper, iron, etc.) were seen in the spectrum except the natural radioactivities of

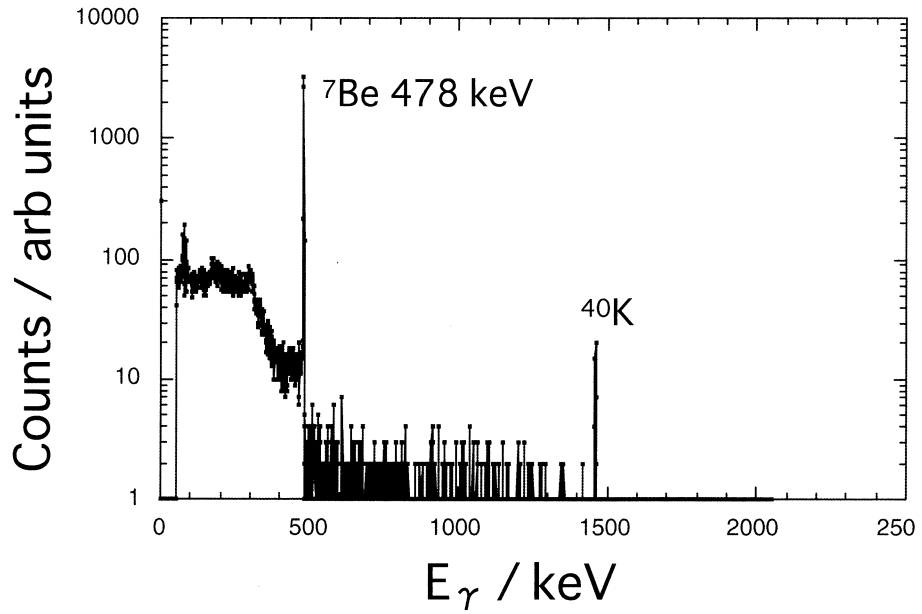

Fig.1. Typical γ-ray spectrum of the ^{7}Be fraction, an eluate of 4 ml in the test tube, from the column of Li_2O_3 (^{7}Be).

^{40}K from the environment (background radioactivity). Therefore the radiochemical purity of each final product was ascertained by measuring the γ-ray spectrum. Similar γ-ray spectra for the ^{7}Be fractions from the column of H_3BO_3 (^{7}Be) were observed.

The elution behavior of ^{7}Be isotope is shown in Figs. 2 and 3 for the irradiated samples of Li_2CO_3 and H_3BO_3, respectively. As can be seen in the figures, radioactivities of the carrier-free ^{7}Be radioisotope from the target materials were observed in the fractions (No. 24-34 in Fig. 2 and No. 19-24 in Fig. 3). Furthermore, no residue was observed in the test tubes of the fractions after dry-up. The facts suggest that only the ^{7}Be radioisotope populated the fractions with no contaminant.

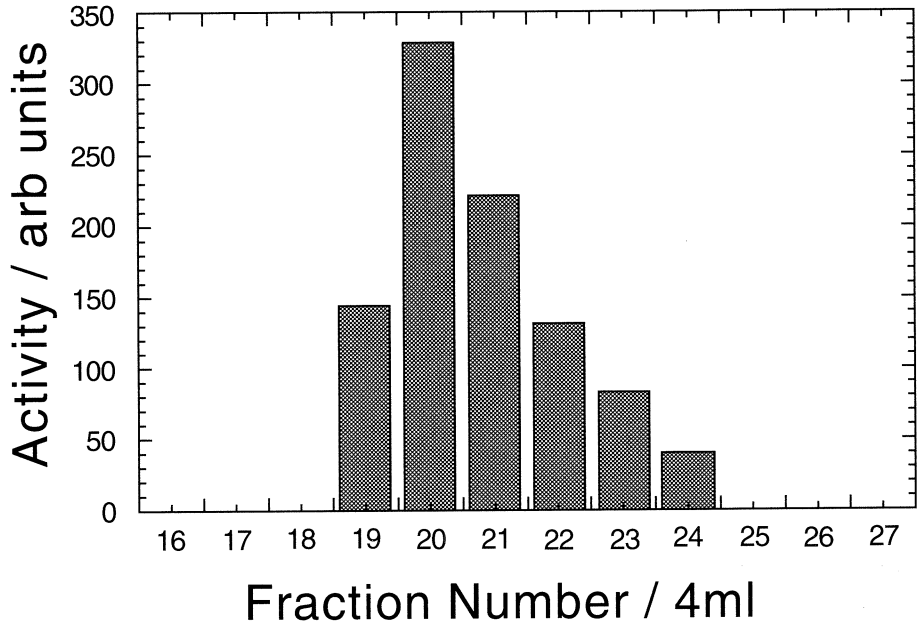

Fig.2. The elution behavior, a radioactivities measured with a Ge-detector, of ^{7}Be isotope with 3N HCl as a function of fraction number for the sample of Li_2O_3 (^{7}Be).

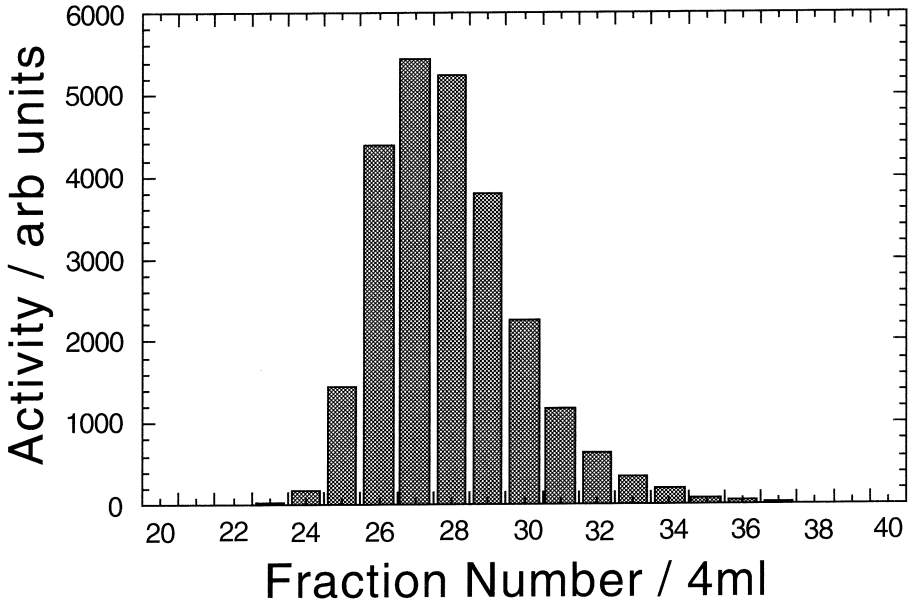

Fig.3. The elution behavior, a radioactivities measured with a Ge-detector, of ^{7}Be isotope with 3N HCl as a function of fraction number for the sample of H_3BO_3 (^{7}Be).

The total activities of the ^{7}Be isotope produced by ^{7}Li(p,n)^{7}Be reaction is estimated to be about twenty times greater than that produced by ^{10}B(γ,p2n)^{7}Be reaction (see Figs.2 and 3). The difference in the specific activities of the ^{7}Be isotope produced depends on the cross section of ^{7}Li(p,n)^{7}Be and ^{10}B(γ, p2n)^{7}Be reactions. Even though the specific activities produced by the photonuclear reaction are smaller than those produced by the proton-induced reaction, the bremsstrahlung irradiation makes it possible to produce a large quantity of sample.

In the previous work, a precipitation method for the removal of some impurities (a contaminant such as copper, iron, etc.) was adopted in the chemical separation procedures even if an ion-exchange method was used [5]. Highly purified target materials, such as samples of 99.997% for Li_2CO_3 and/or H_3BO_3, can be obtained commercially at present. Therefore, an easier procedure for the preparation of the carrier-free ^{7}Be isotope is getting developed.

§ 4. Conclusion

The results suggest that ^{7}Be isotope can be produced by the ^{7}Li(p,n)^{7}Be and ^{10}B(γ,p2n)^{7}Be (^{11}B(γ, p3n)^{7}Be) reactions. A chemical separation procedure using a cation-exchange method for the preparation of the carrier-free ^{7}Be isotope can be successfully applied even for the separation of neighbor atoms such as Li, Be, and B. The chemical yield of carrier-free ^{7}Be isotope throughout the separation procedure was proved experimentally to be more than 98 %.

Acknowledgements

The authors are grateful to the technical staffs of Laboratory of Nuclear Science, and the Cyclotron, Tohoku University for beam-handling. One of authors (S.-I. Fujikawa) is supported by the Japan Copper and Brass Research Association.

References

[1] For example, A. Rehmet, K. Rätzke, F. Faupel, P.D. Eversheim, K. Freitag, U. Geyer and S. Schneider: Appl. Phys. Lett. **79** (2001) 2892.

[2] For example, J.M. Kaste, S.A. Norton and C.T. Hess: Rev. in Mineralogy and Geochemistry **50** (2002) 271.

[3] E. Segre and C.E. Wiegand: Phys. Rev. **75** (1949) 39.

[4] H.R. Haymond, W.M. Garrison and J.G. Hamilton: UCRL-920 (1950).

[5] D.C. Aumann: Radiochimica Acta **7** (1967) 64.

(LNS Experiment : #2455, #2472)

SNC隕石Y000593の化学組成の特徴

白井直樹, 大浦泰嗣, 海老原充

東京都立大学大学院理学研究科 (192-0397 東京都八王子市南大沢 1-1)

Chemical Characteristic of Antarctic SNC Meteorite Y000593

N. Shirai, Y. Oura and M. Ebihara

Graduate School of Science, Tokyo Metropolitan University, 1-1 Minami-Osawa, Hachioji, Tokyo 192-0397

Three activation analysis methods, that is, prompt gamma ray analysis, instrumental neutron activation analysis and instrumental photon activation analysis, were applied to Antarctic nakhlite, Yamato-000593 together with Nakhla and other shergottites for the non-destructive determination of major and trace elemental contents. Powder samples representing six different portions within Y000593 were analyzed for discussing the chemical heterogeneity. As a result, major elements are homogeneously distributed within ±7%, and trace elements are homogeneously distributed within ±11% except for H, B, Cl, Br and rare earth elements. Based on similarity of chemical composition, crystallization age and cosmic-ray exposure age between Y000593 and Nakhla, these two meteorites were estimated to leave same meteoroid and to fall at separate point of the Earth.

§ 1. はじめに

隕石は, 小惑星や他の惑星の破片と考えられている。その中で, SNC 隕石と呼ばれるグループは shergottite, nakhlite, chassignite の3つのサブグループに分類され, 酸素同位体組成などから同一母天体からきたものと考えられている。そして, SNC 隕石に含有されている希ガスの同位体組成が火星に着陸したバイキング探査機によって測定された火星大気中の希ガス同位体組成とよく一致していることや, 結晶化年代が他の隕石に比べて若いことなどの理由により SNC 隕石は火星起源の隕石であると考えられている。

2000年に南極大陸にて発見された Yamato-000593 は nakhlite に属する隕石である。これまでに nakhlite は Nakhla をはじめ計6個しか見つかっておらず, Y000593 は南極大陸ではじめて発見された nakhlite である。

本研究では, 3種類の非破壊放射化分析法, 即ち即発γ線分析法 (PGA), 機器中性子放射化分析法 (INAA) 及び機器光量子放射化分析法 (IPAA) を用いてY000593の化学組成を求めた。Y000593 は 13.7kg 回収されており, 元素分布の均一性を検討するには最適の試料である。そこでY000593の数箇所の異なる位置で試料を採取し, それぞれ分析を行い, 元素分布の均一性について検討した。また, 得られた化学組成に基づき, Y000593 と Nakhla の関係について検討した。

§2．実　　験

本研究で用いた試料は，国立極地研究所から提供された南極隕石 Y000593 である。Y000593 全岩の中でそれぞれ数 cm から10数 cm 離れた位置で重さ２g～3.5g の試料６個（それぞれ Y000593，40~Y000593，45と呼ぶ）を採取した。各試料をめのう乳鉢を用いて均一に粉末にした後，分析に用いた。また同時に Nakhla，55（nakhlite）の分析も行った。PGA，INAA 及び IPAA による定量のための比較標準として，産総研地質総合研究センターから配布されている JB-1（玄武岩）または Smithsonian Institution から配布されている Allende 隕石試料を用いた。また，一部の元素については高純度試薬を比較標準試料とした。以下に，各放射化分析法の概略を示す。

PGA：粉末状試料約100mgを四フッ化エチレン六フッ化プロピレンフィルム袋に入れ，日本原子力研究所 JRR-3M 実験ホール内の即発γ線分析装置により，約１時間冷中性子照射しながら即発γ線を測定した。

INAA：粉末状試料約50mgをポリエチレン袋に入れ JRR-3 PN-3 にて10秒間中性子を照射し，ただちにγ線を測定した。その後，同試料を JRR-4 T パイプにて１分ならびに20分間照射し，東京都立大学 RI 研究施設にて適当な時間間隔で数回γ線を測定した。

IPAA：PGA により分析した試料のうち約50mg を純度99%の Al 箔で二重に包み，直径１cm のペレット状に整形して照射試料とした。これを，flux を補正するための金箔と一緒に石英管内に常圧封入した。これを東北大学原子核理学研究施設電子線形加速器にて最大エネルギー 30MeVの制動放射線で30分間照射し，ただちにγ線を測定した。その後，同試料を３時間30分照射し，東京都立大学RI研究施設にて INAA と同様な測定を行った。

§3．結果と考察

３つの非破壊放射化分析法を組み合わせることにより28元素が定量できた。第１図と第２図に，Y000593，40からY000593，45それぞれの定量値をそれらの平均値で規格化した値を示した。図中に６試料間での定量値の変動幅を標準偏差１σで帯により示した。これらの定量値のばらつきには試料間の不均一性によるものと測定統計変動の両方が含まれている。主要元素濃度はその値によらずどの元素も試料２~3.5g 単位では±６%以内で均一に分布していることがわかった。また Mn は特に均一に分布していた。微量元素濃度は主要元素より試料間のばらつきが大きい。特に Cl と Br のばらつきが大きいが，γ線測定による相対統計誤差が約60%あり，ばらつきの主な原因の一つと考えられる。H は Y000593，45のみ他の５つの試料より1.7倍大きく，これを除くと±７%内で均一であった。Y000593，45中の他の微量元素濃度は概して他の５つの試料中で一番小さい。一方，Y000593，42は，他の試料より微量元素濃度は大きく，この傾向は特に希土類元素で著しい。Y000593，45とY000593，42を除くとB，Cl，Br，H 以外の微量元素は±11%内で均一であった。なお６試料では±17%内で均一であった。

第１表に Nakhla，55と Y000593 の定量値を Lodders [1] による Nakhla の編集値とともに示した。Nakhla，55の本研究による定量値は Lodders [1] による編集値とほとんどの元素で誤差範囲内でよく一致したが，Na，Br，Rb は編集値より20~30%大きい。さらに，Cl は編集値よりも10倍以上大きい。Nakhla，55は NASA の月試料取扱施設にて塊の内部から採取された後，分析試料調製直前まで不活性ガス中に密封されていたため，地球上での汚染は非常に考えにくい。本研究での Y000593 中の Cl 濃度が約80から110ppm

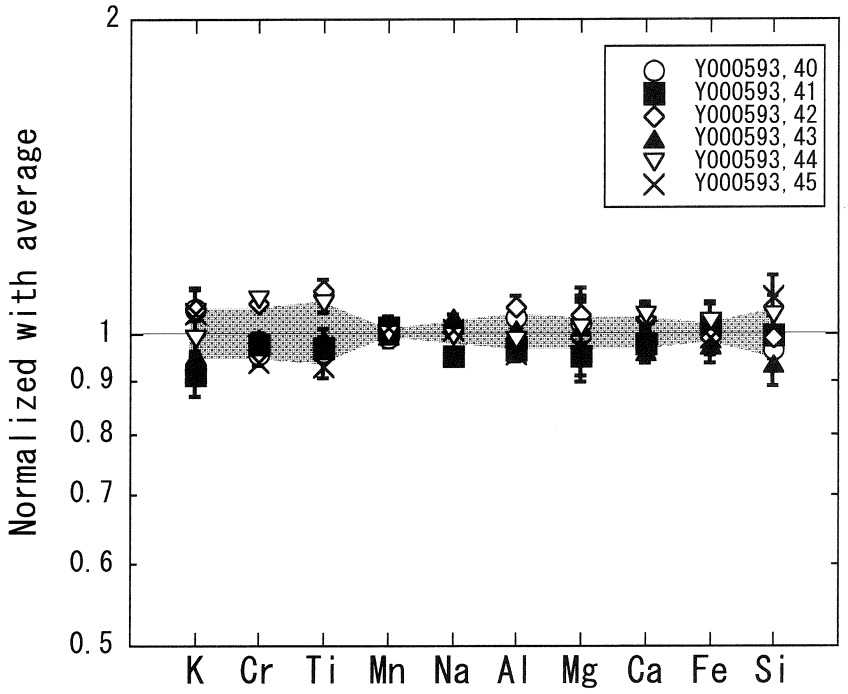

第１図　Y000593 の主要元素分布の均一性。 帯は各元素の試料間のばらつきを標準偏差（1σ）で示した。横軸には濃度が低い元素から順に並べた。

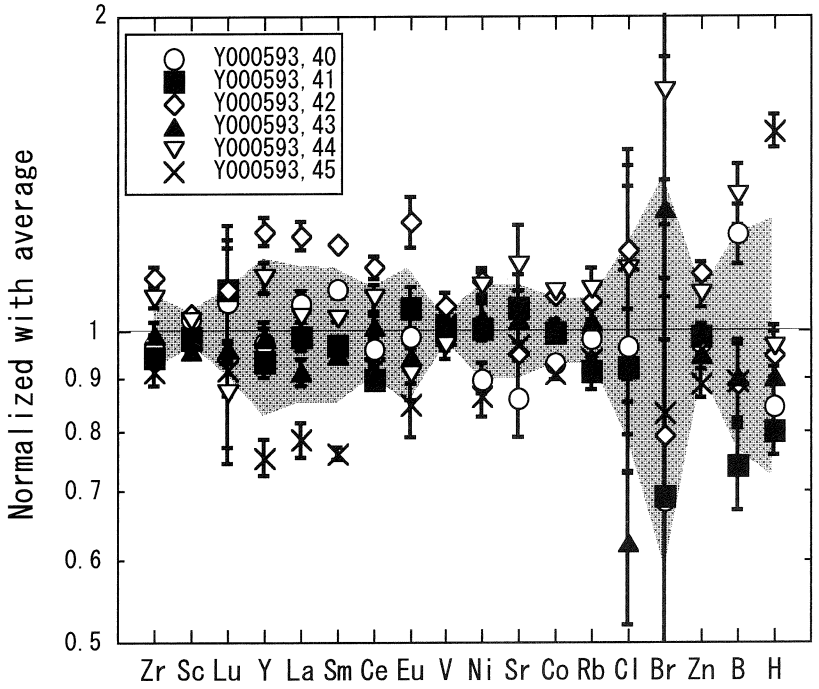

第２図　Y000593 の微量元素分布の均一性。 帯は各元素の試料間のばらつきを標準偏差（1σ）で示した。横軸には宇宙化学的凝縮温度が高い元素から順に並べた。

まで変動していることを考えると，Cl は非常に不均一に分布していることを示唆しているのであろう。Cl の報告値はほとんどなく，Br とともに今後さらなる分析が必要である。

Nakhla と Y000593 の 6 試料の平均値は，多くの元素において誤差範囲内でよく一致した。また，いくつかの元素では Nakhla の定量値は Y000593 の 6 試料の定量値の変動内におさまった。ただし，Y000593 中のBrはNakhlaの約1/5倍，Znは約1.5倍高かった。Y000593とNakhlaの化学組成は，特定元素の不均一性を

第1表　NakhlaとY000593の定量結果

		Nakhla,55 本研究	Nakhla Lodders (1998)	Y000593 平均値	Y000593 最大値[1)]	Y000593 最小値[2)]
主要元素 (%)	Na	0.459 ± 0.003	0.34 ± 0.05	0.452 ± 0.013	0.468 ± 0.003	0.430 ± 0.003
	Mg	7.15 ± 0.43	7.3 ± 0.2	6.25 ± 0.22	6.49 ± 0.39	5.95 ± 0.35
	Al	1.02 ± 0.02	0.89 ± 0.11	1.12 ± 0.05	1.19 ± 0.02	1.07 ± 0.02
	Si	22.9 ± 1.0	22.7 ± 0.8	22.8 ± 1.2	24.7 ± 1.1	21.3 ± 1.1
	K	0.114 ± 0.005	0.107 ± 0.019	0.120 ± 0.007	0.126 ± 0.006	0.109 ± 0.006
	Ca	11.0 ± 0.3	10.5 ± 0.5	10.1 ± 0.3	10.5 ± 0.3	9.7 ± 0.3
	Ti	0.210 ± 0.005	0.202 ± 0.025	0.224 ± 0.015	0.246 ± 0.006	0.207 ± 0.005
	Cr	0.197 ± 0.002	0.177 ± 0.028	0.177 ± 0.011	0.191 ± 0.001	0.165 ± 0.001
	Mn	0.407 ± 0.009	0.382 ± 0.31	0.423 ± 0.004	0.428 ± 0.010	0.421 ± 0.009
	Fe	15.6 ± 0.6	16.0 ± 1.2	17.4 ± 0.4	17.8 ± 0.7	16.8 ± 0.7
微量元素(ppm)	H	560 ± 32		842 ± 233	1305 ± 48	673 ± 37
	B	2.47 ± 0.20	4.6	2.53 ± 0.60	3.41 ± 0.23	1.87 ± 0.17
	Cl	1053 ± 101	80	91.3 ± 19.8	159 ± 8	79.9 ± 3.6
	Sc	55.4 ± 0.1	51 ± 4	56.2 ± 1.9	58.3 ± 0.1	53.5 ± 0.1
	V	211 ± 6	192	197 ± 6	208 ± 6	191 ± 6
	Co	49.8 ± 0.6	48 ± 5	49.5 ± 3.7	53.7 ± 0.6	44.8 ± 0.5
	Ni	71.0 ± 2.4	90	65.2 ± 6.7	72.6 ± 2.1	56.3 ± 2.4
	Zn	56.8 ± 1.7	54 ± 11	75.7 ± 6.8	85.6 ± 2.3	67.1 ± 2.1
	Br	5.32 ± 0.53	4.5 ± 0.2	1.01 ± 0.42	1.72 ± 0.63	0.61 ± 1.32
	Rb	5.02 ± 0.21	3.8 ± 0.8	3.19 ± 0.23	3.49 ± 0.16	2.90 ± 0.12
	Sr	58.5 ± 7.4	59 ± 10	67.5 ± 2.80	88.1 ± 7.6	65.5 ± 5.5
	Y	3.93 ± 0.16	3.3 ± 1.1	4.75 ± 0.80	5.91 ± 0.19	3.58 ± 0.15
	Zr	9.99 ± 0.29	8.8 ± 1.0	10.7 ± 0.9	12.0 ± 0.3	9.78 ± 0.28
	La	2.37 ± 0.05	2.06 ± 0.33	2.52 ± 0.34	2.94 ± 0.05	1.97 ± 0.06
	Ce	6.01 ± 0.17	5.87 ± 0.37	6.93 ± 0.67	7.96 ± 0.19	6.22 ± 0.16
	Sm	0.856 ± 0.009	0.77 ± 0.08	1.02 ± 0.15	1.23 ± 0.01	0.777 ± 0.010
	Eu	0.255 ± 0.013	0.235 ± 0.030	0.300 ± 0.045	0.381 ± 0.022	0.254 ± 0.018
	Lu	0.055 ± 0.008	0.055 ± 0.007	0.068 ± 0.007	0.074 ± 0.009	0.059 ± 0.007

1) 6試料の中での最大濃度
2) 6試料の中での最小濃度

第2表　Y000593とNakhlaの結晶化年代と宇宙線照射年代

	Y000593	Nakhla
結晶化年代	1.33Ga (K-Ar)[1)]	1.3Ga (Ar-Ar)[2)]
宇宙線照射年代	12.16Ma (^{21}Ne)[1)]	11Ma (^{3}He)[3)] 12Ma (^{21}Ne)[4)]

1) R. Okazaki et al. (2002) [2]　K-Ar法、^{21}Ne法による年代
2) D. D. Bogard (1995) [3]　Ar-Ar法による年代
3) M. J. Drake et al. (1994) [4]　^{3}Heに基づく年代
4) M. J. Drake et al. (1994) [4]　^{21}Neに基づく年代

除けば，ほぼ一致していると見なしてよいであろう。また，Y000593とNakhlaの結晶化年代（第２表）はともに1.3Gaであることから，両隕石は火星の同じ位置からもたらされたlaunching pairであると考えられる。又，Y000593とNakhlaの宇宙線照射年代（第２表）はそれぞれ12.2Maと11~12Maであり，ほぼ等しいことから，両隕石が同一meteoroidに属し，各隕石に分かれた後，相ついで地球の別々の地点に落下したと考えられる。

謝　辞

本研究は Yamato nakhlite consortium 研究の一つとして行われ，Y000593 は国立極地研究所より提供していただいた。Nakhla, 55は M. Gardy により提供していただいた。PGA と INAA は原研施設共同利用制度により行われた。IPAA を行うにあたり制動放射線照射ならびに放射線測定において東北大学核理研助教授・大槻勤氏と結城秀行博士にご協力いただいた。深く感謝する。

参　考　文　献

[1] K. Lodders: Meteorit. Planet. Sci. 33 (1998) A183.

[2] R. Okazaki, K. Nagao, N. Imae and H. Kojima: Antarctic Meteorites. XXVⅡ (2002) 134.

[3] D.D. Bogard: Lunar Planet. Sci. XXVI (1995) 143.

[4] M.J. Drake, T.D. Swindle, T. Owen and D.S. Musselwhite: Meteoritics. 29 (1994) 854.

(LNS Experiment #2480)

A Test of Radiation Hardness of Magnetic Fluid

A. Yoshida [1], T. Suda [1], T. Kubo [1], T. Ohtsuki [2], H. Yuki [2]

[1] *RIKEN(Institute of physical and Chemical Research), 2-1 Hirosawa, Wako, Saitama 315-0198*
[2] *Laboratory of Nuclear Science, Tohoku University, Mikamine, Taihaku, Sendai 982-0826*

The radiation hardness of a magnetic fluid used for a vacuum-tight rotating actuator was investigated. A high intense electron beam of 50 MeV with 140 μA was converted to γ-rays with the dose rate of approximately 50-150 kGy/hour and irradiated to a sample of the magnetic fluid. No significant change on the viscosity was observed up to the total dose of 0.5-1.5 MGy.

§ 1. Introduction

The in-flight radioactive-isotope (RI) beam separator BigRIPS [1] is being built at RIKEN for the RI-beam factory (RIBF) project [2]. The power deposit in the RI-beam production target of the BigRIPS is quite high. It is expected to be 22 kW, for the case of ^{238}U primary beam at 350 AMeV bombarding a Be target of 5.4 mm (1.0 g/cm^2) in thickness. The beam spot size is expected to be as small as 1 mm in diameter. The power density on the target surface becomes quite high as 28 GW/m^2. In order to avoid the target melting, a water-cooled rotating-disk target is being developed [3]. Since the estimated dose at the target system is high as a few MGy/year, we must know the radiation hardness of the materials, which will be used in the system. A vacuum-tight rotating actuator is indispensable for this system. In the actuator, the magnetic fluid is used as liquid "O-ring" to keep the vacuum. There is, however, no data on its radiation hardness as far as the authors know. The compositions of the magnetic fluid are metal powder of magnetite and organic materials of solvent and surfactant. The critical dose of the magnetic fluid is estimated as several 100 kGy up to a few MGy that corresponds to the critical dose of vacuum oil reported in the reference [4]. In order to make it clear, a high radiation test was performed at LNS, Tohoku University.

§ 2. Experimental Procedures and Results

The experimental setup is displayed in Fig.1. A high intense electron beam of 50 MeV with 140 μA was bombarded on a water-cooled Pt radiator with the thickness of 1 mm and was converted to γ-rays. The charged particles are swept out by using a magnet located at down stream of the radiator. The γ-ray was collimated by the Pb slit and irradiated a sample of the magnetic fluid. The magnetic fluid sample used [5] was a composite consists of ferromagnetic ultra-fine particles, which chemically adsorbed surfactant and are well dispersed by the base liquid of perfluoro-polyether in order to form a stable colloidal liquid. It is pointed out [6] that the magnetic fluid used to be damaged by high temperature as higher than 80°C. In order to avoid heating up of the sample by irradiation, the fluid of

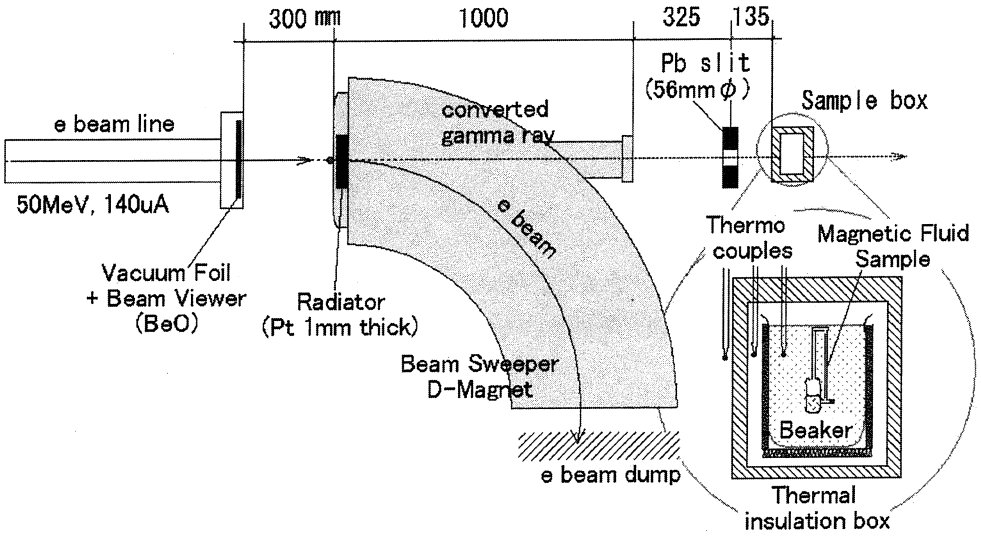

Fig.1 Experimental setup.

1cc in volume was sealed in a small glass cell and was sunk in a beaker with flowing cooling-water. The temperature of the sample was kept at 20 - 30°C.

The dose rate was measured by using two methods. First, two types of radiation sensitive color films [7] that has a sensitivity for electrons, γ-rays and X-rays were used and were stuck just behind the Pb beam collimator. From the observation of the change of the color, the dose rate was estimated to be 50-60 kGy/h and had uniform intensity distribution in a round shape slit of 56 mm in diameter. Secondly, a calorimetric measurement was performed. We measured the temperature increase of the water in the beaker that was well covered by a thermo insulator box. A gradual rise in temperature was observed. It was 0.06°C/min of 1 litter water corresponding to 3.5 Watt heat loss by irradiation. The volume of water irradiated was 250 cc defined by the Pb collimator and thus indicated the dose rate of 3.5 W / 0.25kg = 50 kGy/h (Gy = J/kg). Both results agree well.

A simulation study to estimate the dose rate was also performed using the GEANT code. In the first place, an energy distribution of the emitted γ-ray flux at the sample position was calculated considering the experimental geometry. In order to check the reliability of this simulation, the γ-ray flux was measured by using the ^{197}Au(γ, n)^{196}Au reaction. We put several pieces of thin Au foil just behind the Pb beam collimator. After a series of irradiation, the γ-decay (E_γ= 357 keV) originated from ^{196}Au was measured in the offline analysis. The cross section of this reaction had been measured by Livermore group [8] and has a large peak of giant resonance in the energy region of E_γ= 8 - 20 MeV. By integrating the product of this cross section and the γ-ray flux of the simulation, the yield of ^{196}Au was calculated and compared with the obtained one. There was a good agreement. In the second place, an energy loss of γ-ray in the water filled in the beaker was simulated by the GEANT code. The result gives the temperature increase of 0.16°C/min of 1 litter water, which is 2.7 times larger value compared to the observed value. It must be noted that a small peak of E_γ= 413 keV originating from the reaction of ^{197}Au(n, γ)^{198}Au was also observed, but the γ-decay yield was 1/10 of the (γ, n) reaction. Further simulation work considering the dose rate of neutron flux is in progress.

From the results of these measurements, the sample of the magnetic fluid was irradiated at the dose

rate of 50 k to 150 kGy/h, approximately. The total irradiation time was 10 hours, thus the total dose became 0.5 M to 1.5 MGy, approximately.

After the irradiation, the degradation of the magnetic fluid was tested by using two methods. First, we observed a formation of magnetic fluid spikes. A normal magnetic fluid placed near the magnet shows a pattern of spikes on its surface. This is due to the growth of the surface instability. The spike grows until achieving a balance of surface tension, magnetic force and gravity. The observation of these spikes is one of the indirect methods to check the properties of the magnetic fluid such as surface tension, viscosity and stability of colloid. Two pictures before and after the irradiation are compared in Fig.2. We could not observe any difference between those two. Secondly, the viscosity of the magnetic fluid was measured by using a thin tube viscosity meter. The magnetic fluid of 1 cc was injected into a thin tube of 3 mm in diameter and was sealed in the tube in order to avoid scattering out during irradiation. The thin tube sample was irradiated in a beaker with flowing cooling-water. A fall time of the liquid through the thin tube was measured at room temperature of 20°C and compared in Fig.3. The viscosity of the magnetic fluid is large as 3500~4500 mPa.sec, thus the fall time in the tube was slow as 40 sec. We could not observe also a big change.

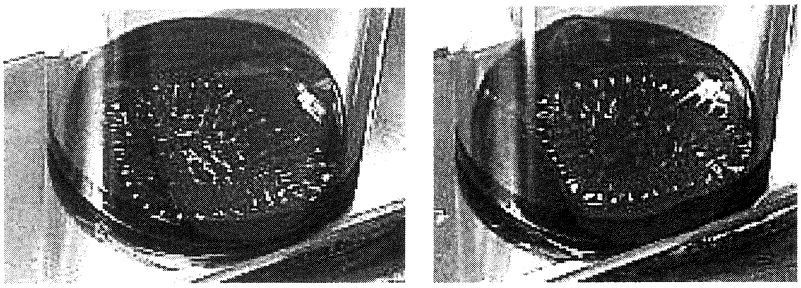

Fig.2. Observation of the formation of magnetic spikes, before (left) and after (right) the irradiation.

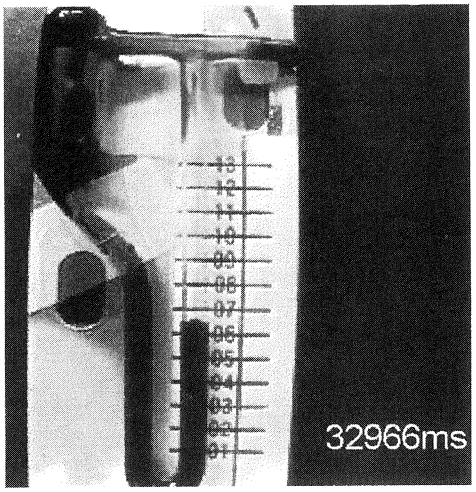

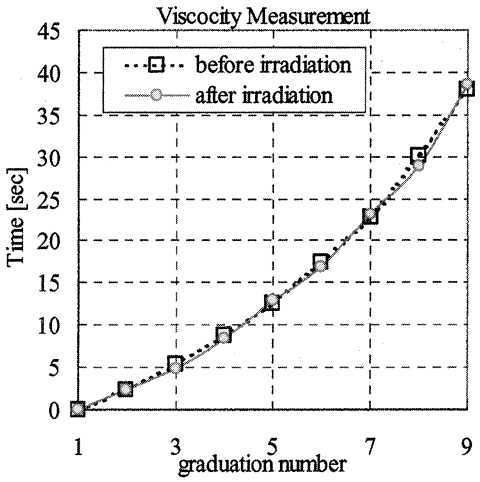

Fig.3. Viscosity measurement of the magnetic fluid using a thin tube viscosity meter (left).
A fall time of the liquid through a thin tube was measured at each graduation (right).

§ 3. Summary

Radiation hardness of a magnetic fluid was investigated by irradiating an intense γ-ray converted from an electron beam of 50 MeV with 140 μA. The dose rate was measured by using radiation sensitive color films, a calorimetric method and a radio chemical method. It was determined as 50-150 kGy/hour, approximately. After the irradiation, the degradation of the magnetic fluid was tested by observing a formation of spikes and by measuring a viscosity of the magnetic fluid. No significant change was observed up to the total dose of 0.5-1.5 MGy. A further high radiation test is under consideration by changing the distance between the radiator and the magnetic fluid sample shorter than those of present work.

References

[1] T. Kubo *et. al.*: Nucl. Instr. Meth. **B204** (2003) 97.

[2] Y. Yano *et al.*: "*Proc. 16th Int. Conf. on Cyclotrons and their Applications*", East Lansing, Michigan, ed. F. Marti (American Institute of Physics, 2001) p. 161.

[3] A. Yoshida *et al.*: RIKEN Accel. Prog. Rep., **35** (2002)152; **34** (2001)188; Nucl. Instr. Meth. A(2003), in press.

[4] P. Beynel *et al.*: CERN 82-10 (1982).

[5] The sample was supplied by Rigaku Co. http://www.rigaku.co.jp/. Its commercial fluid type code is F-310 produced by Sigma Hi-Chemical INC., http://www.sigma-hc.co.jp/.

[6] private comunication with Rigaku Co.

[7] RADCOLOR Film No.381, Nitto-denko Co., dose range of 10 k - 50 kG, and BEAM COLOR Film OG/10 NM-15B, Simitomo-denko Co. http://www.sei.co.jp/, dose range of 1k-30 kGy.

[8] B.L. Berman: PrePrint UCRL-78482.

Ⅲ. Accelerator, Synchrotron Radiation, and Instrumentation

(LNS Experiment : #2483)

フォトニック結晶からのスミス・パーセル放射スペクトル測定

大原直人[1]，近藤泰洋[1]，神戸　亮[1]，宮嵜博司[1]，柴田行男[2]，伊師君弘[2]，
蔦谷　勉[2]，日出富士雄[3]，瀬川勇三郎[4,5]，山本貴一[4]，堀内典明[4]，
大高一雄[6]，山口修一[7]

[1]東北大学大学院工学研究科（980-8579　仙台市青葉区荒巻字青葉 08）
[2]東北大学多元物質科学研究所（980-8577　仙台市青葉区片平 2-1-1）
[3]東北大学原子核理学研究施設（982-0826　仙台市太白区三神峯 1-2-1）
[4]理化学研究所フォトダイナミクスセンター（980-0845　仙台市青葉区荒巻字青葉 519-1399）
[5]東北大学大学院理学研究科（980-8578　仙台市青葉区荒巻字青葉）
[6]千葉大学先進科学教育センター（263-8522　千葉市稲毛区弥生町 1-33）
[7]千葉大学工学部（263-8522　千葉市稲毛区弥生町 1-33）

Measurement of Smith-Purcell Radiation Spectrum from a Photonic Crystal

N. Ohara[1], Y. Kondo[1], M. Kanbe[1], H. Miyazaki[1], Y. Shibata[2], K. Ishi[2],
T. Tsutaya[2], F. Hinode[3], Y. Segawa[4,5], K. Yamamoto[4], N. Horiuchi[4],
K. Ohtaka[6] and S. Yamaguchi[7]

[1]*Department of Applied Physics, Advanced School of Engineering, Tohoku University, Aramaki, Aoba-ku, Sendai 980-8579*
[2]*Institute of Multidisciplinary Research for Advanced Materials, Tohoku University, 2-1-1 Katahira, Aoba-ku, Sendai 980-8577*
[3]*Laboratory of Nuclear Science, Tohoku University, 1-2-1 Mikamine, Taihaku-ku, Sendai 982-0826*
[4]*Photodynamics Research Center, The Institute of Physical and Chemical Research (RIKEN), 519-1399 Aoba, Aramaki, Aoba-ku, Sendai 980-0845*
[5]*Department of Physics, Graduate School of Science , Tohoku University ,Aoba ,Aramaki, Aoba-ku, Sendai 980-8578*
[6]*Center for Frontier Science, Chiba University, 1-33 Yayoi-cho, Inage-ku, Chiba 982-0826*
[7]*Graduate School of Science and Technology, Chiba University, 1-33 Yayoi-cho, Inage-ku, Chiba 982-0826*

When the electron beam of high energy (150MeV) passes near the surface of a photonic crystal at uniform velocity, optical radiation in a millimeter wave region is observed. It turns out that this light is converted from the evanescent wave emitted by the electrons into propagating waves through the photonic band modes in resonance. Since the previous measurements showed that a radiation peak appeared in out of region above the mechanism, the experiments for specifying the origin of this radiation was conducted. It was observed that intensity of the radiation increased for a 3D photonic crystal of double layers.

フォトニック結晶の表面近傍を高エネルギー（150MeV）の電子ビームが等速度で通過する時に，ミリ波領域の光放射が観測される。この光は，電子から放射されたエバネッセント波（減衰波）が進行波に変換されたものであり，フォトニックバンドモードを共鳴的に励起した際に放出される光であることがわかった。しかしそのメカニズムに対応しない放射ピークが出現したため，この光放射起源を特定するための実験を行った。また，２層の３次元フォトニック結晶を用いて放射強度を増幅させることに成功した。

§ 1．序

電子線が金属回折格子の表面近傍を通過するときに光を放出する現象がある。この光放射現象は1953年に Smith と Purcell によって報告されスミス・パーセル放射と呼ばれている[1]。スミス・パーセル放射とは等速度で運動する電子から放射される減衰波が回折格子により散乱を受け，遠方でも観測可能な進行波が放射される現象である。前回の実験では金属回折格子の代わりにフォトニック結晶を用いてスミス・パーセル放射を発生させるという実験を行った。その結果，フォトニックバンドモードの共鳴励起による光放射を観測することができたが，このメカニズムに対応しない原因不明の放射ピークも観測され，その起源を特定することはできなかった[2]。したがって今回はその放射ピークの起源を特定するための実験をテフロン球で構成された２種類のフォトニック結晶（単層）を用いて行った。また，２層の３次元フォトニック結晶を用いた実験も行った。本稿ではこれらの実験結果について報告する。

§ 2．光放射メカニズム

フォトニック結晶中では，その固有状態を励起する光だけが存在可能であり，それ以外の光は結晶中に存在することができない。さらに，運動量- エネルギー空間（(k, ω) 空間）においてバンド中で真空中の光の分散関係 $\omega = ck$ であらわされるライトコーンの内側の光だけが進行波となり，遠方でも観測できる光となる（第１図)。従って，本実験ではライトコーンの内側のフォトニックバンドモードが共鳴的に励起された際に放出される光を観測している。その放射メカニズムについて以下に示す。

等速度で x 方向に運動する電子は電磁波を放射している。その波の波数ベクトルは以下の式で定義される。

$$k_i = (k_x, q_y, \Gamma_i) \tag{1}$$

ここでは，x 軸を電子ビームの進行方向，z 軸をフォトニック結晶と垂直な方向としている。電子から放射される光は，(k, ω) 空間においてはその分散平面がライトコーンの外側に位置するため，遠方では観測できない減衰波である。しかし，減衰波がフォトニック結晶や回折格子のような周期構造物に入射すると，減衰波の波数ベクトルはウムクラップモーメントを得てライトコーンの内側へ逆格子ベクトルの線形和だけシフトする。その結果，減衰波が進行波へと変換され，遠方でも観測可能な光となる(第１図)。ウムクラップ散乱によって逆格子ベクトル（mK_1+nK_2）を受け取り，進行波となった波数ベクトルは

$$k_s = (k_x+mK_{1x}+nK_{2x}, q_y+mK_{1y}+nK_{2y}, \Gamma_{mn}) \tag{2}$$

と表される[2]。今後，（mK_1+nK_2）だけシフトした減衰波の分散平面を H_{mn} 平面と呼ぶことにする。周期構造物が金属回折格子の場合は観測される光放射に特異性は無いが[3]，フォトニック結晶を用いた場合はフォトニックバンドによる分散を有するため，バンド分散線上で特異的な放射が観測される。実際，(k, ω) 空間においてこの H_{mn} 分散線がフォトニックバンドを横切る際に励起が起こるため，鋭く高強度な放射ピークが観測される[4, 5]。

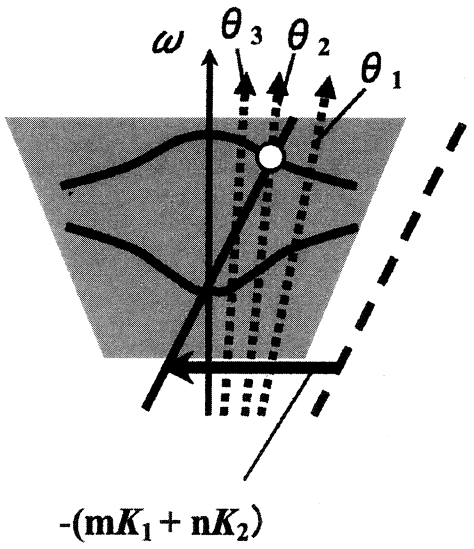

第１図　(k, ω) 空間における散乱過程の模式図。減衰波の分散直線（破線）がウムクラップ散乱をうけ，ライトコーン（影をつけた部分）の内部へシフトし，（実線）となる。実曲線はフォトニックバンドを模式的に表したもの。点線矢印は放射角度θを固定したときのスペクトルに相当する。

§ 3．実　　験

核理研に設置した測定系の概略を第２図に示す。フォトニック結晶の表面近傍を，電子線加速器から放出された電子ビーム（150MeV）が通過する。ビームの平均電流は1.5μA，電子ビームの断面は直径10mm の円形であり，ビーム高さはフォトニック結晶から10mm 離れた位置に固定されている。フォトニック結晶から放射された光は，光学系の中を第２図の点線で示した経路を通って干渉分光計に導かれる。平面鏡 M1 は可動鏡になっており，干渉計への光学軸が変わらない設計になっている。M1 を動かすことで放射角度θ依存性を測定することができ，θは50°＜θ＜110°の範囲で測定した。

実験では直径3.2mm のテフロン球（ε＝2.05）を六方最密構造で配列させたフォトニック結晶（PhC）を

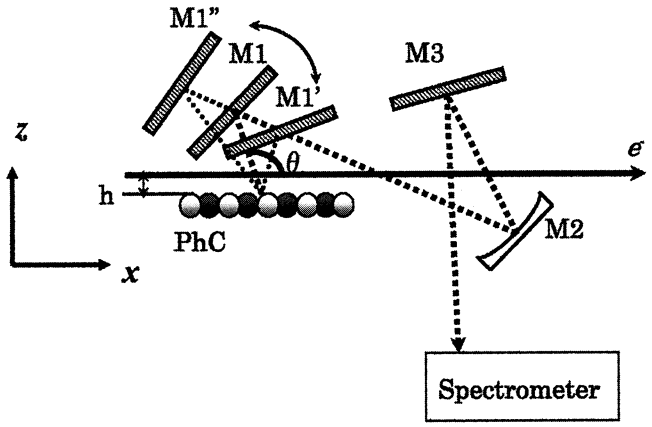

第２図　実験に用いた光学系。M1，M3：平面鏡，M2：凹面鏡，h：ビーム高さ，θ：放射角度。

用いており，単層の２次元 PhC と２層の３次元 PhC を用意した。なお，単層の２次元 PhC については，前回の実験で出現した H_{mn} 線上に乗らない放射ピークの起源を調べるために２種類の試料を用意した。

§ 4．実験結果と考察

4-1　テフロン球　単層

原因不明の放射ピークを観測した前回の実験では，テフロン球を粘着フィルムで支えているフォトニック結晶を用いており，そのフィルムに撓みが生じていた。この撓みが原因不明の放射ピークを発生させる原因ではないかと予測し，十分撓ませたフォトニック結晶とテフロン球を平面上に配列させた撓みの無いフォトニック結晶についてその放射起源を特定するための実験を行った。十分撓ませた試料からの光放射スペクトルを第３図に示す。実線が今回のスペクトル，点線が前回のスペクトルであり，H_{mn} ピーク（矢印）と原因不明のピーク（※印）ともに検出され，再現性の良い結果が得られた。第４図に十分撓ませた試料から放射された光のスペクトルの放射角度 θ 依存性を示す。図中の矢印で指しているピークは第２節で紹介したメカニズムによりフォトニック結晶からウムクラップ散乱を受けて生成された光であり，H_{mn} 分散線上に分布するピークである。※印で指しているピークは原因不明の放射ピークに対応している。どちらのピークも鋭いピーク構造を持っており，強い角度依存性を有している。

次に平面上に配列させた試料の（k，ω）空間における光放射強度分布を第５図に示す。今回の実験では，放射角度 θ が110°～50°と，広範囲に及ぶ測定を行った。なお，横軸の $(k_s)_x$ は放射角度 θ を用い，以下の関係式により求めた。

$$(k_s)_x = \frac{\omega}{c}\cos\theta \qquad (3)$$

H_{mn}［(−1,0)，(−2,0)，(−3,0)］線上に分布している放射ピークは前号で報告したとおり，フォトニックバンドモードの共鳴的な励起により生成された光である。また，テフロン球を平面上に配列させた試料からも H_{mn} 分散線上に分布しない原因不明な放射ピークが観測されたため，その放射起源が撓みによる影響で

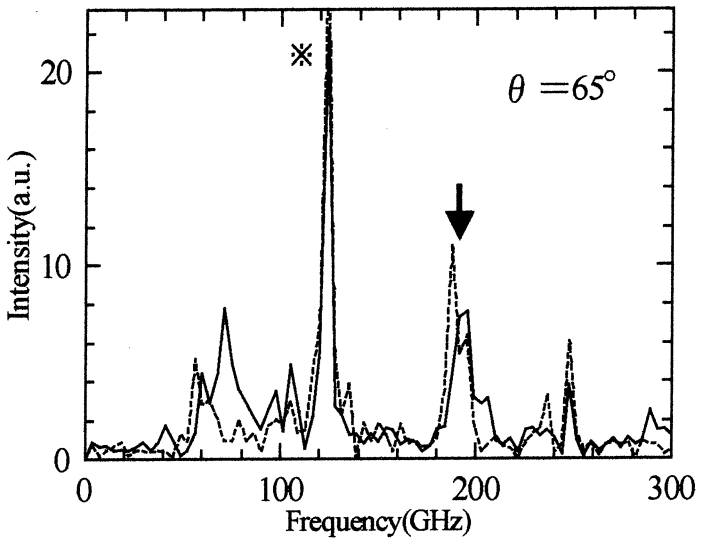

第３図　テフロン球単層の撓んだ試料からの光放射スペクトル（実線）と前回測定したスペクトル（点線）。矢印で示してあるピークは（k，ω）空間で H_{mn} 線上に分布するピーク，※で示してあるピークが原因不明のピークである。

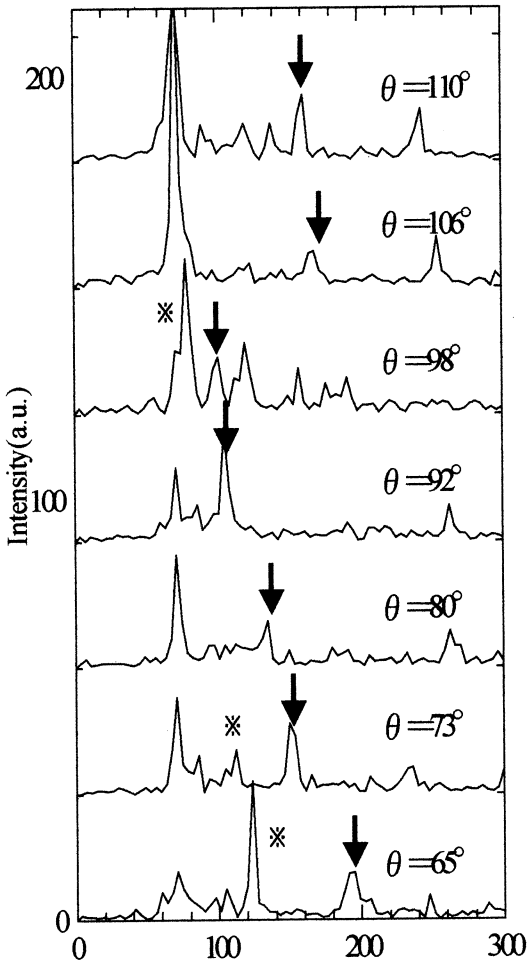

第４図　テフロン球単層の撓んだ試料からのスペクトルの放射角度依存性。

はないことがわかった。さらにこの放射ピークは，(k，ω）空間においてH_{mn}分散線の約0.8倍の傾きを持つ線上に分布していることがわかった。よって，今後この分散平面を$0.8H_{mn}$，その線上に分布する放射ピークを$0.8H_{mn}$放射ピークと呼ぶことにする。$0.8H_{mn}$分散線上に分布するピーク構造は単色性と指向性という点でH_{mn}ピークと酷似しており，それと似た過程で何らかの物質から散乱を受け，生成された光である可能性が高い。散乱物としてはフォトニック結晶やそれを支持しているアクリル枠の端面，エコソーブなどが考えられるが現時点でその原因を特定することはできなかった。

4-2　テフロン球　２層

２次元単層の試料を重ね，２層にしたフォトニック結晶について実験を行った。第６図は，２層フォトニック結晶の（k，ω）空間における光放射強度分布である。２層の場合フォトニックバンドの密度が増すため，放射ピークは単層のときよりも多く観測される。第７図に単層と２層のスペクトルの比較図を示す。単層に比べ，２層のフォトニック結晶では放射強度が増大した。単層の場合，電子ビームから発生するエバネッセント波はフォトニック結晶の外側（下方）への漏出が大きい。だが，２層（多層）のフォトニック結晶では，１層目から漏出した光をその下層で受け取り，散乱が起こることでエネルギーの漏出が減り，効率よく光を生成することができる。その結果，共鳴的に放射強度が増幅される[5]。ただし，漏出した光の散乱は上層の数層においてのみ発生するため無闇に層を増やしても意味が無い。

なお，$0.8H_{mn}$放射ピークについては２層のフォトニック結晶でも増強していることから，フォトニック結

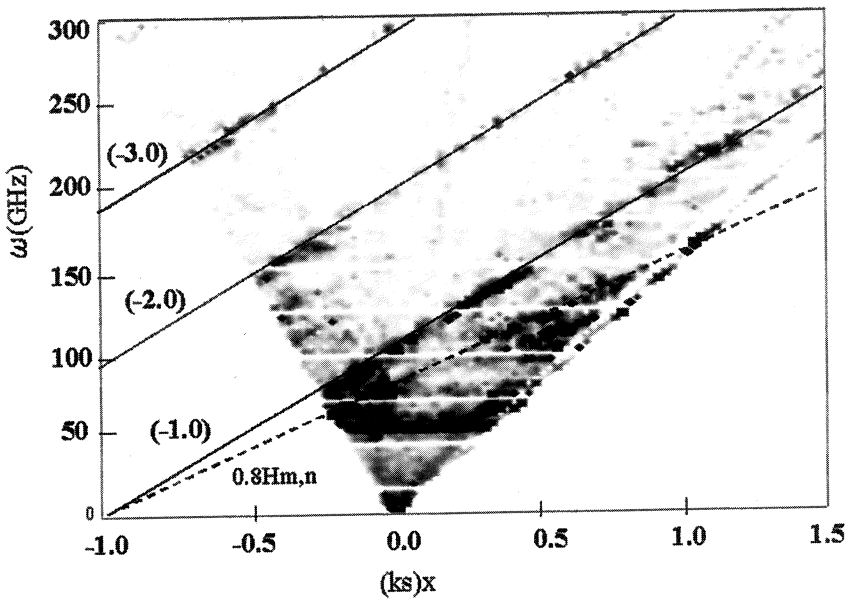

第５図　配列させた試料の（k，ω）空間における光放射強度分布。実線がそれぞれH_{mn}［(−1,0)，(−2,0)，(−3,0)］分散線に対応している。点線は$0.8H_{mn}$線である。

晶自身からの散乱が原因である可能性が高いと考えられる。

§４．ま と め

電子がフォトニック結晶の表面近傍を等速度で通過するときに，単色性に優れ，強い角度依存性を持つ特異な光放射が観測された。その他に光速度$0.8c$に対応する$0.8H_{mn}$放射ピークが観測され，このピークの原因として試料の撓みが疑われていた。しかし，２種類の撓みの異なるフォトニック結晶を用いた実験により，

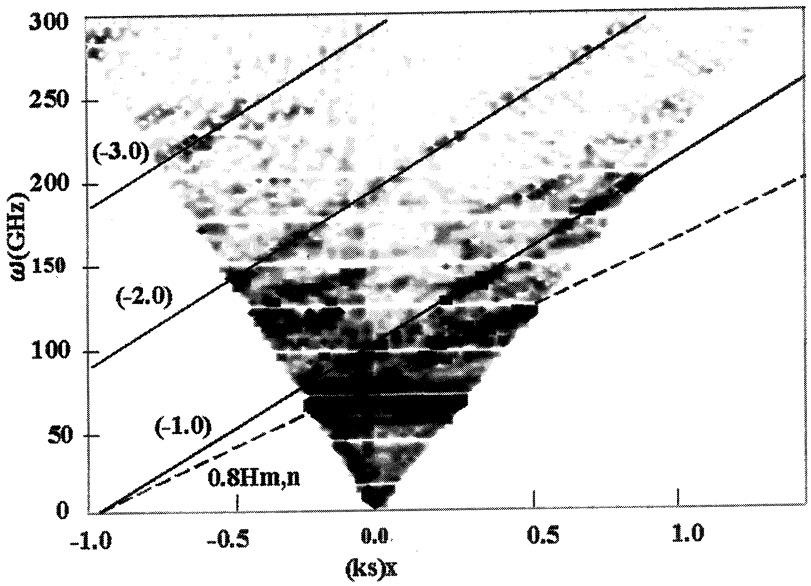

第６図　２層フォトニック結晶の（k，ω）空間における光放射強度分布図。

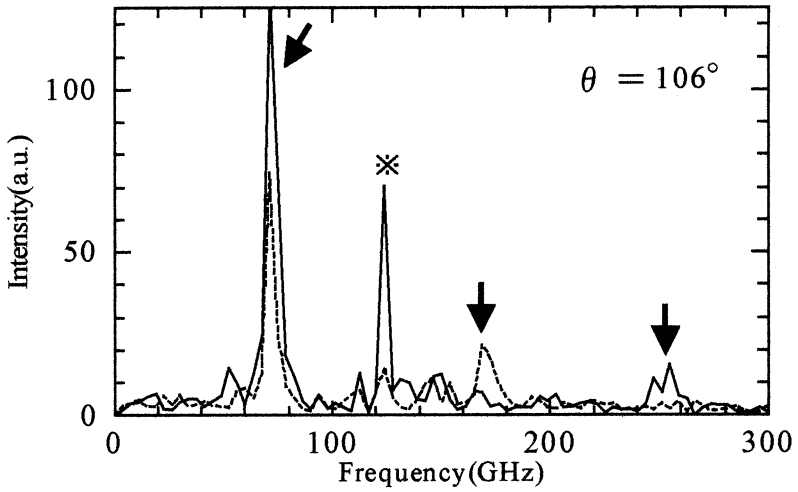

第7図　2層（実線）と単層（点線）の光放射スペクトル。矢印で示すピークは H_{mn} 分散線上に分布する。$0.8H_{mn}$ ピークを※で示す。

撓みによるものではない事がわかり，この放射ピーク発生の原因を特定することはできなかった。また，フォトニック結晶を2層にすることで単層の時よりもシャープで強い強度を持つ光を発生させることに成功した。

参　考　文　献

[1] S.J. Smith and E.M. Purcell : Phys. Rev. **92** (1953) 1069.

[2] K. Yamamoto *et al.*: Research Report of LNS, Tohoku University, **35** (2002) 90.

[3] Y. Shibata *et al.*: Phys. Rev. E **57** (1998) 1061.

[4] K. Ohtaka and S. Yamaguti : Optics and Spectroscopy **91** (2001) 506.

[5] K. Ohtaka and S. Yamaguti : Optics and Quantum Electronics **34** (2002) 235.

管理区域入退管理システムの開発

宮本 篤，山崎寛仁，結城秀行，七尾晶士，菅原由美，大槻 勤

東北大学大学院理学研究科原子核理学研究施設
(982-0826 仙台市太白区三神峯 1-2-1)

Development of the Radiation Control System for Personal Permission, Status and Record

A. Miyamoto, H. Yamazaki, H. Yuki, M. Nanao, Y. Sugawara and T. Ohtsuki

Laboratory of Nuclear Science, Tohoku University, Mikanine 1-2-1, Taihaku-ku, Sendai 982-0826

The radiation control system for automated locks, personal status, and recordings in the database was developed at Laboratory of Nuclear Science (LNS), Tohoku University. It consists of the Programmable Logic Controllers (PLC) for the entrance system and Windows PC. The PLC is controlled with Fins Gateway and Compolet on the Windows PC through an ethernet. The SQL Server 2000 was also installed on the Windows PC for database management. In the system, personal data such as destination, purpose, working hours and radiation dose are stored in the database. Furthermore, monthly report of personal data can easily be printed out by using the system. Personal status can be checked by a status monitor of the accelerator in the operation room and the entrance of the radiation controlled area, etc.

§ 1. はじめに

加速器を有する共同利用施設のような比較的規模の大きい放射線取扱施設では，日々の入退者を把握するために入退管理システムがなくてはならないものとなっている。このような施設での管理区域入退管理システムは，その放射線取扱事業所の特殊性（管理区域の配置や取扱従事者の流れ，放射線管理者や加速器オペレータによる状況の把握，記帳，適切なデータベースの保存や作成等）を考慮しなければならない。しかしながら，施設の特殊性にあわせて，入退システムを独自に開発して利用している例は少ない。

東北大学大学院理学研究科原子核理学研究施設では，これまでの入退管理システムの老朽化と1.2 GeV の光子を用いた原子核実験室の完成により新入退管理システムの導入を行った。本システムでは入退情報の入力ばかりでなく，データベースの作成，加速器運転状況画面を利用した入退者の表示など，効率的に入退管理が行えるようになった。本稿では当施設で独自に組み上げた入退管理システムの概要を紹介する。

§ 2. 管理区域

当施設は放射線発生装置として300 MeV 電子ライナックおよび1.2 GeV ストレッチャーブースタリング（STB リング），非密封放射性同位元素 111 核種と 密封放射性同位元素 ^{241}Am-Be（中性子校正用線源

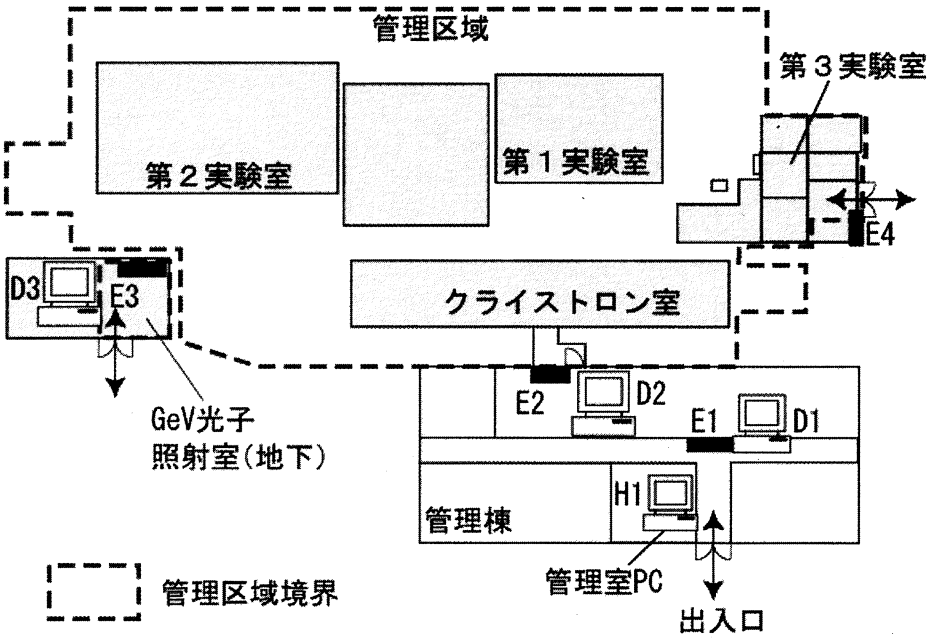

第１図　核理研管理区域の概要および管理区域入退管理システムの配置図。入退システムは，管理棟出入口部 (E1)，管理区域出入口部；クライストロン出入口部 (E2)；GeV 光子照射室出入口部 (E3)；第３実験室出入口部 (E4)，管理室 PC (H1)，および自動表示装置 (D1, D2, D3) から構成される。

370MBq）の使用承認を受けている。また，管理区域内建屋の広さは約 5,000m^2 に及ぶ。管理区域内はクライストロン室，電子ライナック本体室，第１および第２電磁石室，低エネルギー実験に使用される第１実験室，高エネルギー実験に使用される第２実験室，非密封放射性同位元素使用室の第３実験室，さらに新設の GeV 光子照射室がある。管理区域の入退チェックは主に地上のクライストロン室出入口ゲートの１ヶ所で行っていたが，新設の GeV 光子照射室出入口の入退域ゲートが加わった。第１図に管理区域全体の概要と管理区域入退システムの設置場所を示す。

§ 3．管理区域入退管理システムの概要

放射線安全管理室で開発した管理区域入退管理システム（入退システム）の構成を第２図に示す。入退システムは，管理棟出入口部 (E1)，管理区域出入口部のクライストロン室出入口 (E2) および GeV 光子照射室出入口 (E3)，管理室 PC (H1)から構成され，これに自動表示画面による入退者表示 (第１図のD1, D2, D3) が加わる。非密封放射性同位元素使用室である第３実験室の出入口部 (E4) 入退管理は入域の制限から別にシステムを設けている。

3.1　ハードウエアおよびソフトウエアの構成

第３図にハードウエアの構成を示す。(a)は管理棟出入口部，(b)はクライストロン室および GeV 光子照射室出入口部の構成である。各部にはそれぞれ一般に使用されている信頼性の高い PLC（Programmable Logic Controllers, OMRON社製）[1] を使用している。各々の PLC 間および PLC- ホストコンピュータ間の通信は，専用に敷設した Ethernet (10Base-T) によって行なわれている。各部とも，制御用 CPU ユニットを中心に，ID カードの入出力を行う Read write head（アンテナ），情報の表示および入力を行うためのタッチパネルから構成される。クライストロン室出入口部と，GeV 光子照射室出入口部に関しては，入口側および出口側に各々 Read write head を持ち，インターロック機能を備えた扉の施錠・解錠操作を行う点が管理棟出入口部と異なる。

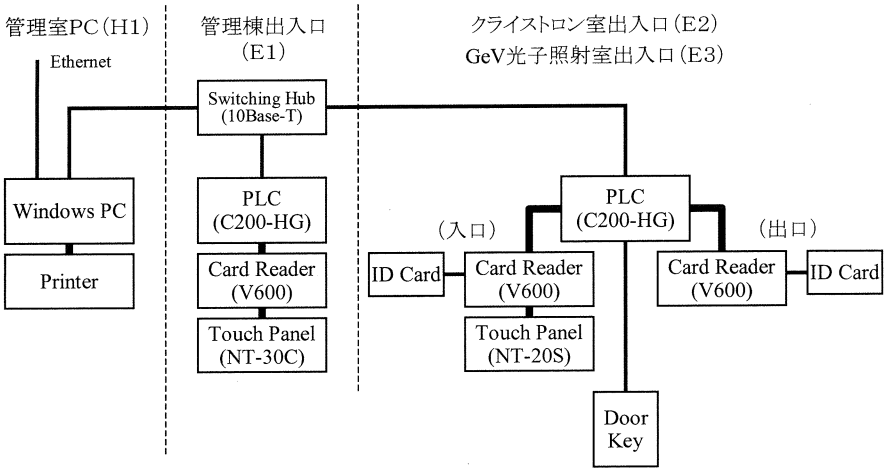

第２図　管理区域入退管理システムの構成図。Windows PC, PLC, 電気錠から構成され，PC-PLC 間の通信は専用の Ethernet で行う。

第４図にソフトウエアの構成を示す。PLC 間および PLC- ホストコンピュータ間の通信は，OMRON 標準プロトコル FINS によって行われる。ホスト上のアプリケーションから PLC を制御するには，FinsGateway, Compolet（共に OMRON 社製）を使用した。FinsGateway はホストコンピュータから各種 FINS コマンドを発行するためのミドルウエアであるが，簡単な制御を行う場合にも FINS コマンドを組み立て，PLC からのレスポンスを解釈する手続きを指定する必要がある。Compolet はこれらの処理を自動で行うActiveXコンポーネントであり，Visual Basicで記述されたアプリケーションから簡単に呼び出す事ができる。Compolet 経由で収集した入退域に関する情報はホストコンピュータのデータベースに格納される。

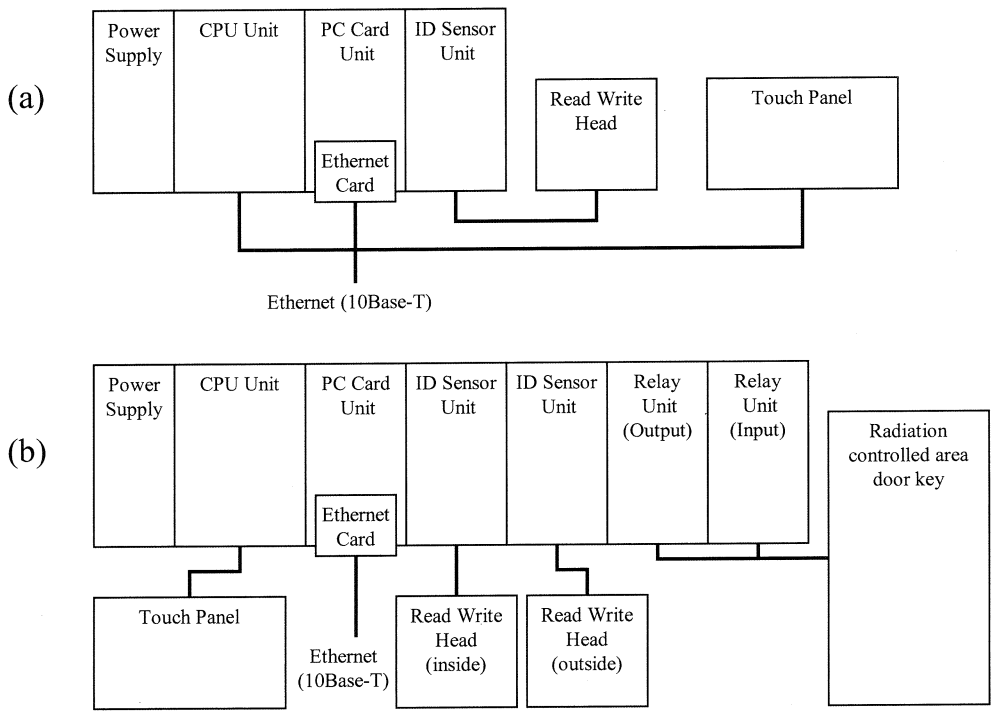

第３図　ハードウエアの構成図。(a)管理棟出入口部 (E1)，(b)クライストロン出入口部 (E2) および GeV 光子照射室出入口部 (E3) の構成。

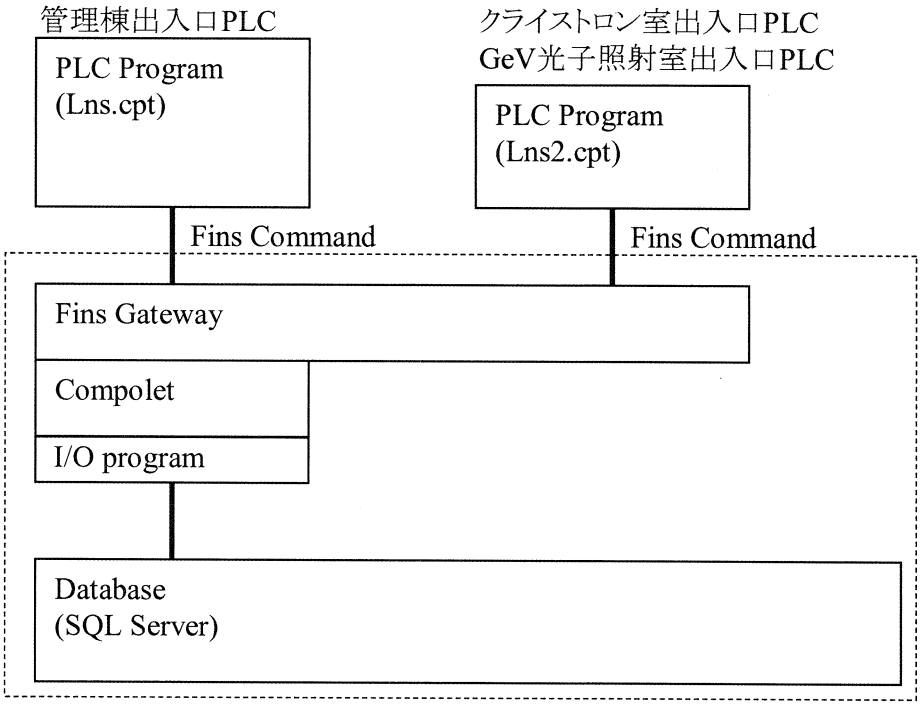

第４図　ミドルウエアおよびソフトウエアの構成図。

データベースは Microsoft 社 SQL Server 2000[2] を使用した。

3.2　管理棟出入口部

管理棟出入口部は，個人の管理区域への入域手続き（名前，入室範囲の確認，および退域時の被曝線量の登録）を行う。この操作はすべて放射線作業従事者全員に配布されている作業従事者 ID カード（以後 ID カードとする）を使用して行う。管理区域内では加速器電磁石や実験機器等で強磁場を使用することが多いため，電波を使用して読み出しおよび書き込みを行う非接触式タイプの ID カードを採用した。また，新規の作業従事者に対する ID カードの登録もここで行う。第５図に管理棟出入口部に設置されているシステム（タッチパネル）の概略を示す。

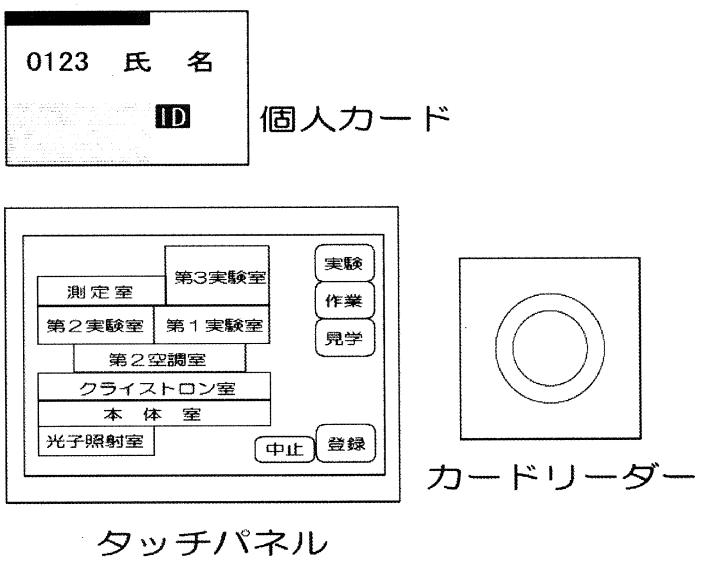

第５図　個人 ID カード，タッチパネル（入力画面），カードリーダの概略。

3.3 管理区域出入口部

クライストロン室出入口およびGeV光子照射室出入口は管理区域への入域および退域のゲートとなっている。出入口扉は常時，電気錠により施錠され，入退域時の開錠操作はIDカードによって行う。

3.4 管理室PC

管理室内には入退管理システムのホストコンピュータが設置されている。ホストコンピュータは，OSにWindowsXP Professionalを採用したPCを使用しており，このOS上で動作するアプリケーションは，入退域および入退情報の収集とデータベースの更新を行う。また，クライストロン室出入口およびGeV光子照射室の電気錠を開錠する際の，PLCからの問い合わせを処理している。また入退域ログや，被曝線量の集計結果を帳票出力する事が可能であり，個人別の入退域記録や被曝線量の月報の作成を行うことができる。

3.5 動　　作

管理棟出入口部のPLCの動作フローチャートを第6図に示す。管理区域に入域しようとする作業従事者は，まず最初に管理棟出入口部で入域手続きをする必要がある。PLC Read write headにIDカードの入力があると，PLCはホストにそのIDカードが登録済みか否かの問い合わせを行う。入域処理ではタッチパネルより入力される入域範囲および入域目的（作業，見学等）を，その時間とともにホストに送信する。

管理棟出入口部での入域手続きが終了した従事者が管理区域へ入域するには，IDカードで管理区域入口側Read write headに入力する。入力があると，PLCはホストに，該当するIDカードが管理棟出入口部での入域手続きが終了しているか否かの問い合わせを行う。条件を満たしている場合には管理区域出入口の電気錠を開錠し，入域した旨をホストに送信する。条件を満たさない場合にはその理由がタッチパネルに出力さ

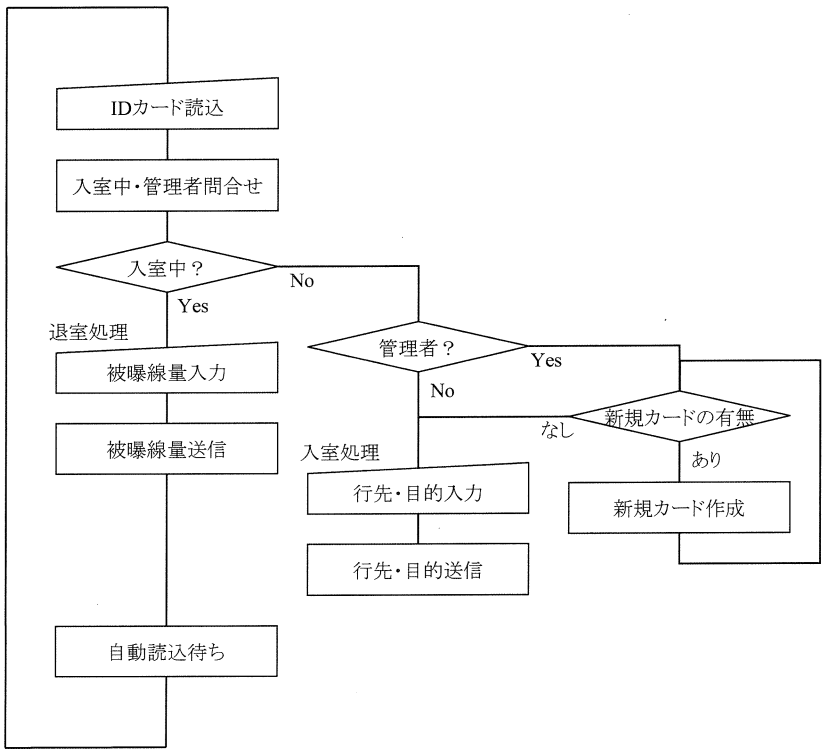

第6図　E1部LCの動作フローチャート。管理者は新規カードの発行を行い，作業従事者は入退手続を行う。

れる。

作業を終えた従事者が退域するには，管理区域内側扉のRead write headにIDカードを近づけると電気

錠を開錠し，退域した旨の情報をホストに送信する。

管理区域内作業が終了し，管理棟を出る場合には管理棟出入口部で退域手続きをする必要がある。退域処理は Read write head に ID カードで入力をし，タッチパネル被曝線量入力画面を表示させる。携帯したポケット線量計の被曝線量を入力すると，退域時間とともにホストに線量が送信され，退域手続きが終了する。

3.6 自動表示画面による入退者表示

これらとは独立に管理棟出入口，クライストロン室および GeV 光子照射室それぞれの出入口には自動表示装置（モニタ画面）が設置されている。この自動表示装置は，入退管理システムとは独立にビームコース・インターロックの状態が表示されている。このモニタ画面の一部を用いて，入退情報取得部から得た入域登録者の一覧（氏名，行先および入域時間）を表示している。この自動表示モニタ画面によって，加速器オペレータや管理区域外の者が管理区域内作業者の確認を行うことができる。自動表示装置に表示される情報は，ホストコンピュータのデータベースより取得するため，常に最新の情報を表示する事が可能である。

§4. まとめ

本研究施設では，比較的安価で管理区域増設にも対応しやすい管理区域入退管理システムを独自に開発した。本システムでは非接触型の ID カードを用いて入退域登録（各個人の入域先および入域目的，作業時間，被曝線量），管理区域出入口ドアの開錠を行うことができる。また本システムは加速器の運転状況を表示した画面（自動表示画面）を用いて入域者リストの表示を行い，加速器運転時の安全確認の一端としている。管理室ホストコンピュータはデータベースの帳票管理（個人管理データ月報作成）など，保存用データの帳票作成も可能となった。

参　考　文　献

[1] たとえば S. Brian Morriss : Programmable Logic Controllers, Prentice Hall ; ISBN : 0-130-95565-5 (1999).

[2] M.F. Garcia : Microsoft SQL Server 2000 オフィシャルマニュアル（上，下），日経 BPソフトプレス, ISBN : 4-891-00204-2, 4-891-00210-7 (2001).

IV. Status Report of LNS Accelerator Complex in 2002

Status Report of LNS Accelerator Complex in 2002

H. Hama, F. Hinode, A. Kurihara, M. Mutoh, M. Nanao, Y. Shibasaki, K. Shinto and S. Takahashi

Laboratory of Nuclear Science, Tohoku University, 1-2-1 Mikamine, Taihaku-ku, Sendai 982-0826

Operation status of an electron accelerator complex at Laboratory of Nuclear Science, Tohoku University is reported. After a completion of a new building containing an experimental vault, the inspection for the radiation safety was done in the beginning of October, 2003, so that most of user machine time was consumed in the latter half of the fiscal year 2002.

§ 1. Operation Statistics

Experiments at the low energy beam line of the linac were performed through the entire FY. Total machine time consumed in the FY 2002 is summarized in Table 1.

Table 1. Details of the linac operating mode and total operation times in the FY2002. Available period for the user machine time except the low-energy high-intensity mode was about 6 months.

Mode	Energy (MeV)	Repetition (Hz)	STB ring mode	Typical experiment	Time (h)
High intensity	< 50	300	(linac alone)	RI-production	266
Pulse-beam	150	50	(linac alone)	synchrotron radiation	144
Stretcher injection (I)	140	100	Pulse-stretcher	nuclear physics	97
Stretcher injection (II)	150	100	Pulse-stretcher	nuclear physics	139
Booster injection (I)	150	50*	1.2 GeV Booster	nuclear physics	320
Booster injection (II)	200	50*	1.2 GeV Booster	nuclear physics	584
Machine study	-	-	-	-	181
Tuning & conditioning	-	-	-	-	371
				(total)	2102
				unscheduled shut-off	417

A large portion of the machine time was allocated to the 1.2 GeV booster operation. A nominal energy of the linac beam for the booster injection is 200 MeV, which is the maximum available energy of the linac. However the linac is often likely to loose one of five klystron modulators because of decrepit devices, so that a procedure of lower energy injection has been previously established. For the efficient beam injection, the higher energy beam is preferred because of transverse emittance and the stability of the magnetic field in the STB ring. Below 150 MeV, it, however, seems to be very difficult to inject the

beam, which is mainly due to ripples of the excitation current for the STB dipoles. Actually, in the FY2003, we once lost a modulator due to malfunction of the thyratron during a long-term machine time. A half-day work successfully reduced the interruption of the machine time employing the 150 MeV beam injection.

Figure 1 shows shared time portion of each operating mode of the LNS linac. Since we have permitted many options in the beam supply, i.e., the energy, the macropulse current, the macropulse duration and the repetition rate, the operation mode has been widely spread and become complicate. Totally 31-time mode change was urged for the user machine time.

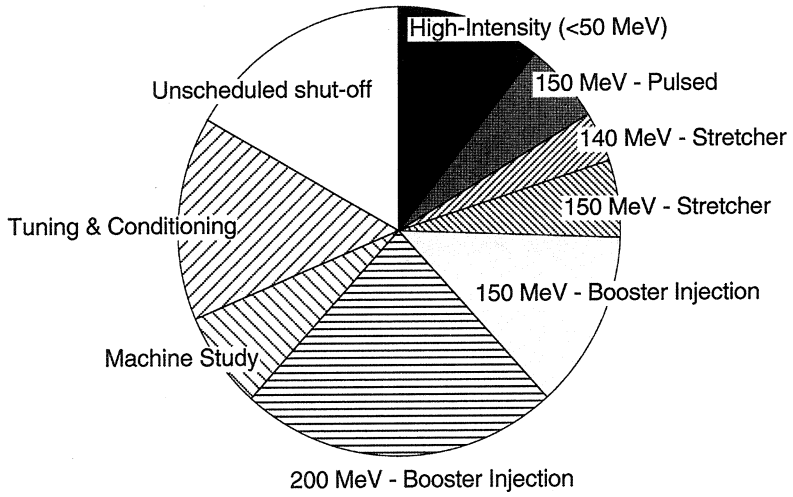

Fig. 1 Shared time portion of each operating mode of the LNS linac integrated over the FY2002. See Table 1 for detail of the operating mode.

§ 2. Major Troubles

We have been still very anxious about fatal malfunction of the 36-year-old linac system, because the unscheduled shut-off occupied more than 16 % of the total time as shown in Fig. 1. In the FY2002, significant troubles occurred to the vacuum system of the linac frequently. In addition, cooling water leaks also happened to the waveguides and every kind of the beam pipes and the slits. Radical modification or replacing of the vacuum chambers is highly required to save the linac from the risk of long-term shut-off. Because the linac was designed with the very early days manner, no sufficient length is left between the accelerating structures and other components, re-construction of the whole system including the beam transport optics is possibly necessary to improve the vacuum.

§ 3. Development

Because the maximum repetition rate of the LNS linac is 300 Hz which is much higher than other conventional linacs, the klystron (collector) cooling is very important. An independent heat-exchanger has been employed since the machine was commissioned. A 25 MW klystron (PV2012B) generates the

heating power of 27 kW on the average at the collector, meanwhile the cooling capacity of the independent system is only 24 kW. As a result, a part of the cooling water has to be evaporated to bring additional cooling effect (evaporative cooling effect). Because the system is now getting much degraded and some water leaks are frequently occurred, a prototype of the new collector cooling system employing a 100 kW plate-type heat-exchanger was installed on a klystron modulator. It has seemed to be working well, so that other old cooling systems will be replaced in near future.

The linac control system is now completely re-constructed by using a PC based control system kernel "COACK", which has been developed by collaboration of KEK, LNS and other laboratories. The biggest advantage of the new control system has resulted from a function of save-and-load of entire machine parameters administered by the software. Device failures are also quickly detected. Further development, particularly improvement of the person-machine interface, is under way.

Operation of the booster synchrotron, STB ring, has been much improved by the machine study. Number of corrections, i.e., closed obit correction, tune stabilization in ramping and etc., were applied and consequently the maximum 50 mA beam is now able to be accelerated up to 1.2 GeV at one linac beam burst (no beam stacking). However such a large beam current causes serious instabilities of the coupled-bunch, the ion-trap and the microwave. The collective synchrotron oscillation driven by the coupled-bunch instability is occurred at higher beam currents than 8 mA, which is a crucial obstacle for generation of the high quality beam. We are going to investigate higher order mode (HOM) excitation in the main accelerating cavity and a cure of the instability.

V. List of Publication

List of Publication（論文リスト）（2002.1～2002.12）

Papers Published in Refereed Journals

Measurement of the Angular Correlations for the $^{16}O(e, e'n)^{15}O$ Reaction in the Giant Resonance Region.

K. Kino, T. Saito, Y. Suga, M. Oikawa, T. Nakagawa, T. Tohei, K. Abe, H. Ueno

Phys. Rev. **C65** (2002) 024604.

Reaction Mechanism for $^{12}C(e, e'n)^{11}C$ in the Continuum above the Giant Resonance.

K. Takahisa, T. Saito, S. Suzuki, C. Takakuwa, M. Oikawa,

T. Nakagawa, T. Tohei and K. Abe

Phys. Rev. **C66** (2002) 014605.

Strongly Enhanced D D Fusion Reaction Observed for keV D^+ Bombardment on PdO, Pd and Fe.

J. Kasagi, H. Yuki, T. Baba, T. Noda, T. Ohtsuki, A.G. Lipson

J. Phys. Soc. Japan. **71** (2002) 2881-2885.

Performance of a Compact Detector Package for the Out-of-plane Spectrometer System.

Z.-L. Zhou, S. Sirca, W. Boeglin, A.J. Sarty, R. Alarcon, R. Beck, A. Bernstein, W. Bertozzi, T. Botto, P. Bourgeois, J. Calarco, F. Casagrande, J. Chen, J.R. Comfort, D. Dale, M.O. Distler, G. Dodson, S. Dolfini, A. Dooley, K. Dow, M. Epstein, M. Farkhondeh, S. Georgakopoulos, S. Gilad, R. Hicks, M. Holtrop, A. Hotta, X. Jiang, K Joo, D. Jordan, N. Kaloskamis, A. Karabarbounis, J. Kirkpatrick, S. Kowalski, C. Kunz, N. Liyanage, J. Mandeville, D.J. Margaziotis, T. McIlvain, C. Mertz, R. Milner, R. Miskimen, I. Nakagawa, C.N. Papanicolas, M. Pavan, G. Peterson, A. Ramirez, D. Rowntree, Y. Sato, J. Shaw, E. Six, S. Sobczynski, S.-B. Soong, N. Sparveris, S. Stave, S. Stiliaris, T. Tamae, D. Tieger, C. Tschaler, D. Tsentalovich, W. Turchinetz, C. Vellidis, G.A. Warren, L.B. Weinstein, S.E. Williamson, A. Young, J. Zhao, T. Zwart

Nucl. Instr, Meth. **A487** (2002) 365-380.

Se-atom Incorporation in Fullerene by Using Nuclear Recoil and Ab Initio MD Simulations.

T. Ohtsuki, K. Ohno, K. Shiga, Y. Kawazoe, H. Yuki

Phys. Rev. **B65** (2002) 073402-(1-4).

Development of Flow Extraction and Detection Method of Radiocarbon for Activation Analysis of High Pure Materials.

K. Masumoto, K. Shikano, T. Ohtsuki, Y. Ito

Analytical Sciences **17** (2002) 641-643.

Charged-particle Activation Analysis of Oxygen in Fluoride and Chalocogenide Glasses Used for Fiber-amplifiers.

K. Shikano, Y. Nishida, K. Kobayashi, T. Kanamori, M. Shimizu, K. Masumoto, T. Ohtsuki

J. Radioanal. Nucl. Chem. **253** (2002) 25-29.

Study of Metallofullerenes Encapsulating Actinides.

K. Akiyama, Y. Zhao, K. Sueki, K. Tsukada, H. Haba, Y. Nagame, S. Suzuki, T. Ohtsuki, M.

Sakaguchi, K. Kikuchi, M. Katada, H. Nakahara

J. Nucl. Radiochem. Sci. **3** (2002) 151-154.

Papers Published in International Conference Proceedings

Medium Effects on Nuclear Reactions: DD Fusion Reactions in Metals with keV Deuteron Bombardment.

J. Kasagi, H. Yuki, W. Galster, T. Shimizu

Proceedings of Multilateral Symposium between the Korean Academy of Science and Technology and the Foreign Academies (KAST, 2002) 411-421.

S_{11} Resonance in Nuclear Medium Observed with the (γ, η) Reactions.

H. Yamazaki, T. Kinoshita, K. Hirota, K. Kino, T. Nakabayashi, T. Katsuyama, A. Katoh, T. Terasawa, J. Kasagi, T. Takahashi, H. Kanda, K. Maeda, Y. Tajima, H.Y. Yoshida, T. Noma, Y. Aruga, A. Iijima, Y. Ito, T. Fujinoya, T. Yorita, O. Konno

Proceedings of International symposium on "Electromagnetic Interactions in Nuclear and Hadron Physics, Edited by M. Fujiwara and T. Shima, (World Scientific, 2002) 265-270.

Physics in $2\pi^0$ Measurements

H. Shimizu, T. Matsumura, P. Shagin, T. Yorita

International Workshop on "Nuclear Physics in Different Degrees of Freedom", (Institute of Basic Science, 2002) 1-10.

Expariments at LNS Sendai.

H. Shimizu

International Workshop on "Quark Nuclear Physics", (Pusan National University Press, 2002) 173-187.

Review

低温核融合とサイエンス.

笠木治郎太

現代化学 **7** (2002) 22.

核的反跳によるフラーレンへの異原子挿入とその理論的考察 (Insertion of foreign-atoms in fullerenes by nuclear recoil and their MD simulation).

大槻　勤, 大野かおる

The Bulletin of the Cluster Science and Technology **5** (2002) 23-29.

VI. Approved Experiments

平成14年度前期採択課題一覧表

課題番号	課題名	申込責任者	採択シフト数
原子核関連分野			
2446	Photoproduction of Neutral Kaons on Deuterium Target near Threshold Region	橋本　治	60
2447	^{12}C および ^{27}Al の全光吸収断面積の測定	寺沢　辰生	8
2448	新実験室へのガンマビーム入射	清水　肇	施設実施
2449	低移行運動量領域における ^{16}O (e,e′p) 実験	玉江　忠明	24
2451	タングステン酸鉛結晶電磁カロリメータの性能評価実験	杉立　徹	4
放射光関連分野			
2452	フォトニック結晶からのスミス・パーセル放射スペクトル測定	近藤　泰洋	4
放射化学・物性関連分野			
2453	長寿命放射性核種の環境中移行における基礎化学反応研究	関根　勉	1
2454	銅における拡散	藤川辰一郎	1
2455	宇宙・地球化学的試料の光量子放射化分析	海老原 充	1
2456	ファイバアンプ用ガラス中の炭素の光量子放射化分析	鹿野　弘二	1
2457	標識化による金属内包フラーレン及びヘテロフラーレンの研究及びその応用	大槻　勤	1
2458	^{230}Th (γ, n) 反応で生成する $^{229m,g}Th$ の反跳捕集と ^{146}Sm の製造	中西　孝	1
2459	電子ビームによるフリーラジカル生成の研究	結城　秀行	1
2460	Th-229mの製造とその崩壊特性	三頭　聡明	1
2461	金属および半導体材料中の軽元素の定量のための分離，補集法の開発	桝本　和義	1
2462	アルギネートマイクロカプセルによる放射性核種の一括除去	秋葉　健一	1

平成14年度後期採択課題一覧表

課題番号	課　　題　　名	申込責任者	採　択 シフト数
原子核関連分野			
2464	水素，重水素原子核標的での２π光生成反応の研究	前田　和茂	8
2465	30～100MeV 領域における ^{4}He 光核反応	嶋　　達志	10
2466	CCD の電子線による放射線損傷の研究	杉本　康博	1
2467	^{24}Mg (e,e′ α) ^{20}Ne反応の研究	坪田 博明	10
放射光関連分野			
2468	フォトニック結晶からのスミス・パーセル放射のスペクトル測定	近藤　泰洋	4
2469	マイクロバンチ FEL の基礎研究（4）矩形閉鎖共振器の場合	柴田　行男	2
放射化学・物性関連分野			
2470	長寿命放射性核種の環境中移行における基礎化学反応研究	関根　　勉	2
2471	銅中の不純物拡散	藤川辰一郎	1
2472	宇宙・地球化学的試料の光量子放射化分析	海老原　充	2
2473	ファイバアンプ用ガラス中の軽元素の光量子放射化分析	鹿野　弘二	1
2474	標識化による金属内包フラーレン及びヘテロフラーレンの研究及びその応用	大槻　　勤	1
2475	^{230}Th (γ, n) 反応で生成する ^{229m,g}Th の反跳捕集と ^{147}Sm (γ, n) 反応による ^{146}Sm の製造	中西　　孝	1
2476	電子ビームによるフリーラジカル生成の研究	結城　秀行	1
2478	金属および半導体材料中の軽元素の定量のための分離，補集法の開発	桝本　和義	2
2479	アルギネートマイクロカプセルによる放射性核種の一括除去	秋葉　健一	1
2480	磁性流体の耐放射線強度のテスト	吉田　　敦	2

核理研研究報告　第36巻

2003年11月発行

発行所　東北大学大学院理学研究科
附属原子核理学研究施設
仙台市太白区三神峯1-2-1（郵便番号982－0826）
電話　022－743－3400

印刷所　株式会社　東北プリント
仙台市青葉区立町24番24号
TEL　022（263）1166㈹

RESEARCH REPORT OF
LABORATORY OF NUCLEAR SCIENCE
TOHOKU UNIVERSITY

Volume 36 November 2003

Laboratory of Nuclear Science, Tohoku University,
1-2-1, Mikamine, Taihaku, Sendai 982-0826, Japan

東北大学大学院理学研究科

原 子 核 理 学 研 究 施 設